A thesis submitted to the

University of Glasgow

in candidature for the degree of

Doctor of Philosophy

AC Electrokinetic Studies of Virus Host Interactions

Acknowledgements

In the course of working towards this thesis I have been grateful for the help of a large number of people and I would like to thank them for their help and support:

I would like to start by thanking my supervisor, Dr. Hywel Morgan, to whom I am grateful for his help and guidance. I am also grateful to Dr. Frazer J. Rixon, MRC Virology Unit, Glasgow for his help in improving my understanding of cells and viruses. As well as J. Mitchell and M. Robertson for their help in supplying cells and viruses needed in this work.

I would also like to thank Dr Steven Britland, School of Pharmacy, University of Bradford as well as A. Tudor Evans of the same institution and Tong-Tong Li, Centre of Cell Engineering, University of Glasgow for their help in studying the cellular effects of Dielectrophoresis.

I would like to thank my friends and colleagues at the Departments of Electronics and Electrical Engineering, the University of Glasgow: W. Monaghan, C. Cotton, D. Bakewell, N.G. Green and CL Chan as well as all the technicians in Dry etch and the clean rooms for their advice and help. Special thanks to Dr. M. P. Hughes for many helpful conversations over coffee, and Pam Foreman for having the patience to put up with me.

Finally I would like to thank my family for their help and support though the years of study I have undertaken.

Summary

AC electrokinetics is the phenomenon of induced motion in polarisable particles by the use of alternating electric fields. Rotational motion, referred to as electrorotation, is induced by rotating electric fields, whilst lateral motion, referred to as dielectrophoresis, is induced by non-uniform electric fields.

The work presented in this thesis covers a range of applications of AC electrokinetics. Electrorotation was used to investigate the changes in the gross biophysical properties of fibroblast like cells following infection with Herpes Simplex Virus type 1. Changes in the biological properties of the cells were correlated with the known biophysical life-cycle of the virions. Electrorotation was also used to study the effect of using antibodies to couple virions to the surface of polystyrene beads. The results indicated that electrorotation was likely to be applicable to the detection of virus using appropriate antibody-coated polystyrene beads. Analysis of the experimental results showed that dielectrophoretic methods would be better suited to the detection of virus complexed polystyrene beads.

To obtain accurate results from electrorotation spectra requires that the electric field distribution in the electrorotational electrode is known. An experimental map of the torque distribution within an electrode array showed good correlation with a numerical model in which the both the phase and magnitude of the electric field was taken into account.

Dielectrophoresis has been used for the separation and enrichment of cell populations. However, such separation techniques require exposure of the cells to high electric fields that could affect the normal physiology of the cells. To test for this, a range of possible biological effects were screened for. The results indicate that electric fields are possibly associated with the perturbation of cellular events. These results are considered to be the first step in understanding the effects of dielectrophoresis on the biological and biochemical properties of cells.

Index

Acknowledgements ii

Summary iii

Index iv

Chapter 1: Introduction and scope of work 1

1.1 Introduction 1

1.2 Scope of work 3

1.2.1 Electrorotation studies of Baby Hamster Kidney fibroblasts infected with the Herpes Simplex Virus, type 1. 4

1.2.2 Attachment of HSV-1 to polystyrene beads. 5

1.2.3 Rotation mapping of planar microelectrodes 5

1.2.4 Cellular effects of electric fields. 6

1.3 Summary 8

1.4 References 9

Chapter 2: AC Electrokinetics – Theoretical Aspects 13

2.1 Introduction 13

2.2 Polarisation 14

2.2.1 Electric polarisation 14

2.2.2 Basic polarisation processes 14

2.2.3 Gauss's Law 15

2.2.4 Laplace's and Poisson's equations 16

2.2.5 Electric flux density 16

2.2.6 Electric susceptibility and relative permittivity 17

2.2.7 Real dielectrics and complex permittivity 17

2.3 Further Polarisation processes 20

2.3.1 Debye relaxations 21

2.3.2 Interfacial Dielectric Phenomena: Maxwell-Wagner Polarisation 24

2.4 Dielectric Particles in an external electric field 28

2.4.1 Potential of a particle in an electric field. 28

2.4.2 Potential of a particle in an electric field - lossy dielectrics. 31

2.4.3 Effective dipole moment - The Clausius-Mossotti factor 32

2.5 Dielectrophoresis 34
2.5.1 Derivation of force on a particle 35
2.5.2 Time averaged dielectric force 37
2.6 Electrorotation 40
2.6.1 Derivation of torque on a particle 40
2.6.2 Time averaged torque 42
2.6.3 Steady state rotation rate 44
2.7 Modelling dielectric particles 46
2.7.1 Spherical dielectric models 46
2.7.2 Elliptical shell model 49
2.7.3 Mixture theory 53
2.7.4 Curve fitting 54
2.7.5 Electric field distribution in electrodes 55
2.8 Electric field simulation 60
2.8.1 Finite element method 60
2.8.2 Method of moments 62
2.9 References 67
Chapter 3: Electrorotation measurements of the virus life cycle of Herpes Simplex Virus Type 1 infected Baby Hamster Kidney Fibroblasts. *I. Background and Methods.* 70
3.1 Summary 70
3.2 Introduction 71
3.3 Virus life-cycle 75
3.4 Importance of dielectric parameters 78
3.5 Materials and Methods 79
3.5.1 Cell culture and virus infection. 79
3.5.2 Electrorotation measurements 79
3.5.3 Scanning Electron Microscope (SEM) images 81
3.5.4 Protein profiles 82
3.5.5 Data analysis and Theory 82
3.5.6 Verification of Membrane conductivity using Dielectrophoretic Crossover Frequency Measurements 84
3.5.7 Determination of virus surface coverage 86

3.5.8 Determination of the bound structures within the cytoplasm 88
3.6 References 90

Chapter 4: Electrorotation measurements of the virus life cycle of Herpes Simplex Virus Type 1 infected Baby Hamster Kidney Fibroblasts. *II Results*...95
4.1 Electrorotation 95
4.1.1 Electrorotational data 95
4.1.2 Verification of cell model 98
4.2 Protein profiles 101
4.3 Membrane conductivity 102
4.4 Specific membrane capacitance 106
4.5 Surface morphology and membrane composition 108
4.6 Scanning Electron Microscopy 112
4.7 Mixture theory applied to progeny virions 115
4.8 Internal permittivity 117
4.9 Internal conductivity 119
4.10 Mixture theory applied to cell interior 120
4.11 References 124

Chapter 5: Electrorotation measurements of the virus life cycle of Herpes Simplex Virus Type 1 infected Baby Hamster Kidney Fibroblasts. *III Discussion and Conclusions.* 126
5.1 Discussion 126
5.1.1 Virus life-cycle and cell ultrastructure 126
5.1.2 Membrane capacitance 127
5.1.3 Membrane permeability and internal conductivity 128
5.1.4 Internal permittivity 128
5.1.5 Prospects 130
5.2 Conclusions 132
5.3 References 133

Chapter 6: Determination of the dielectric properties of polystyrene beads complexed with herpes simplex virus 135
6.1 Summary 135
6.2 Introduction 136
6.3 Theory 139

6.4 Materials and Methods 141
6.4.1 Electrodes and Electrorotational Measurements 141
6.4.2 Binding protocol of carboxylate modified beads 141
6.4.3 Virus cultivation and preparation 142
6.4.4 Complexing of HSV-1 with antibody coated polystyrene beads 142
6.5 Results 145
6.5.1 Electrorotation of untreated carboxylate modified beads 145
6.5.2 Electrorotation of EDAC treated carboxylate modified beads 146
6.5.3 Electrorotation of protein coated carboxylate modified beads 148
6.5.4 Attachment of HSV-1 to protein coated carboxylate modified polystyrene beads 148
6.5.5 Electrorotation of protein coated carboxylate modified beads complexed with HSV-1 156
6.6 Discussion 157
6.6.1 Data analysis 157
6.6.2 Dielectric mixture theory applied to virions on the surface of polystyrene beads 158
6.7 Conclusions 163
6.8 References 164

Chapter 7: Mapping the Electrorotational Torque in Planar Microelectrodes ... 166
7.1 Summary 166
7.2 Introduction 167
7.3 Theory 169
7.4 Materials and methods 170
7.4.1 Electrodes 170
7.4.2 Experimental 171
7.5 Results 172
7.6 Discussion 175
7.6.1 Data analysis 175
7.6.2 Comparison with theoretical model 179
7.7 Conclusions 183
7.8 References 184

Chapter 8: Cell reactions to dielectrophoretic manipulation. 186

8.1 Summary 186
8.2 Introduction 188
8.2.1 Cellular responses to dielectrophoresis 188
8.3 Experimental methods 189
8.3.1 Fabrication and electrode design 189
8.3.2 Cell handling during dielectrophoresis 190
8.3.3 Electric field mapping and membrane potential calculations 190
8.3.4 Cell culture. 191
8.3.5 Analysis of cell division parameters. 192
8.3.6 Examination of cell morphology. 192
8.3.7 Mitochondrial stress (MTT) assay. 193
8.3.8 fos-protein Western blotting and immunodetection. 193
8.3.9 mRNA fingerprinting - Experimental Design. 194
8.3.10 mRNA fingerprinting - isolation of mRNA. 194
8.3.11 mRNA fingerprinting - first-strand cDNA synthesis 195
8.3.12 PCR for mRNA fingerprinting - cDNA amplification. 196
8.4 Results. 197
8.4.1 Dielectrophoresis 197
8.4.2 Electric field and power dissipation simulation. 199
8.4.3 Membrane potential calculations 204
8.4.4 Steady-state temperature measurements. 205
8.4.5 Cell morphology 206
8.4.6 Mitochondrial stress 211
8.4.7 Expression of fos-protein. 211
8.4.8 mRNA fingerprinting. 213
8.5 Discussion. 215
8.6 Conclusion 219
8.7 References. 221

Chapter 9: Conclusion and future work 224
9.1. Conclusions 224
9.2. Future work 225
9.3. References 228

Publications arising from this work 230

Chapter 1: Introduction and scope of work

1.1 Introduction

AC electrokinetics is the motion induced on micron and sub-micron particles through the application of alternating electric fields. The study of this phenomena is of interest to researchers in a wide range disciplines and the topic is being pursued for its potential applications in areas such as medical diagnostics and treatment, as well as for example, the detection of parasites in water supplies.

It has long been known that electric fields can induce lateral motion in particles, for example Hatescheck and Thorne [1] observed the motion of nickel particles that was suspended in toluene and benzene, when exposed to a non-uniform electric field. Pohl named this type of motion dielectrophoresis in 1951 [2], and later wrote a detailed study of the phenomena [3]. Another type of motion was observed by Lang [4] in 1906, who was able to demonstrate that the direction of rotation of an insulating dielectric cylinder exposed to a rotating electric field depended on the conductivity of the suspending medium. It was not until 1982 that Arnold and Zimmermann [5] used this method for inducing rotation of single cells, thus making it possible to obtain reproducible measurements of cell response to rotating electric fields. Leading to the development of the method of electrorotation for single cell dielectric measurements. Electrorotational and dielectrophoretic motion are closely connected, with electrorotation having its physical origin in the phase component of the effective dipole moment of a particle, while dielectrophoresis arises from the real component of such a dipole moment.

Dielectrophoresis can be explained by considering a polarisable particle exposed to an electric field. The electric field causes charge to build up at the interface between the surface of the particle and its surroundings, causing it to polarise. The nature of the charge build-up is determined by the dielectric properties of the

particle and its surroundings. If the polarisibility of the particle is greater than its surroundings, then the dipole moment will be in the direction of the applied electric field and the resulting motion is referred to as positive dielectrophoresis. Conversely, if the polarisibility of the particle is less than its surroundings, the dipole moment will be in the opposite direction to the applied electric field and the resulting motion is referred to as negative dielectrophoresis.

If the electric field is uniform then the charges will be arranged in such a manner that the forces on a dielectric particle cancel each other out and the particle will not experience a net force. Thus, in order for a polarisable particle to experience a net force it needs to be exposed to a non-uniform electric field. As a result of variations in the electric field gradient, the particle will experience different charge densities at different points. The result is that the individual forces no longer cancel each other out and the particle experiences a net force induced by the non-uniform electric field [3, 6-10]. This motion has become the focus of numerous attempts at developing new methods of cell sorting and differentiation [11-13].

Electrorotation is the continuous rotation of a polarisable particle exposed to a rotating electric field. Reproducible experiments of rotation of particles during dielectrophoretic pearl chain experiments was observed by Zimmermann *et al* [14]. This was later suggested to be a result of dipole-dipole interaction between adjacent particles [15] as a result of a phase delay in the dipoles with respect to the applied field. These observations lead to the realisation that rotating electric fields could cause single cells to rotate. Leading Arnold and Zimmermann [16] to introducing the technique of suspending particles in a rotating field, creating a practical method of inducing rotational motion of single cells, from which information of the cell's dielectric parameters can be obtained.

Electrorotation occurs when a dipole is induced in a particle by a rotating electric field. When an external electric field is applied to a polarisable particle the dipole moment induced in the particle will initially not be aligned with the electric field. After a given time, the dipole moment will align with the electric field. If the electric field is rotating the induced dipole moment will continuously

be trying to align with the electric field, causing the particle to experience a continuous torque (e.g. [17]). The direction of the rotation is determined by the phase angle between the dipole moment and the electric field. If the phase difference is less than 180° the particle rotation will follow the applied electric field, this is referred to as co-field rotation. However, if the phase difference is greater than 180° the quickest way for the dipole moment to relax is by rotating counter to the electric field, causing the particle rotation to be in the opposite direction of the applied electric field, this is referred to as anti-field rotation.

The rate and the direction of rotation of a particle exposed to rotating electric fields depends on the dielectric properties of the particle and its surrounding medium. Since the dielectric parameters of a particle will, in general, exhibit frequency dependent behaviour, electrorotation can be used as a means of studying the dielectric properties of individual particles. This has proved to be a useful tool in the characterisation of the dielectric properties of a range of biological particles.

1.2 Scope of work

In this thesis the effect of infecting Baby Hamster Kidney fibroblasts with Herpes Simplex Virus, type 1 was investigated using electrorotational methods. The results of the investigations are analysed with respect to the known life-cycle of the virus. The rapid detection of the Herpes Simplex Virus, type 1 would be a valuable contribution to the treatment of virus. To this end experiments were performed in which the virus was attached to polystyrene beads so that the effect of the virus can be studied with a view to the development of electrorotational or dielectrophoretic detection methods. The electrodes used in this work generate non-uniform electric fields and knowledge of the electric field distribution is important in order to obtain accurate results. Therefore torque mapping in an electrode was performed and the results used to verify the numerical model proposed by Hughes *et al* [18]. Electrorotation measurements are often used in the development of dielectrophoretic cell sorting systems (e.g.[19]). In such a

system cells are exposed to electric fields at high frequencies and such fields might affect the physiology of cells. It is therefore of importance to determine the cellular effects of exposing cells to dielectrophoresis, and measurements of such effects were made.

1.2.1 Electrorotation studies of Baby Hamster Kidney fibroblasts infected with the Herpes Simplex Virus, type 1.

The technique of electrorotation has been used to study the dielectric properties of a number of biological particles [17, 19-33]. There are a number of examples where electrorotation has been used as a non-invasive method to probe the changes in the dielectric properties of cells and micro-organisms when subjected to stimuli or challenged by infection or parasitic invasion. Some examples include observations of the differences in the membrane capacity and conductivity of fertilised and unfertilised rabbit oocytes [30], the time-dependent interaction of erythrocytes with influenza virus [27], as well as the changes in the dielectric properties of lymphocytes following stimulation with mitotic agents [32].

In this thesis the time dependent changes in the dielectric properties of Baby Hamster Kidney fibroblasts (BHK(C-13)) following infection with the Herpes Simplex Virus, type 1 (HSV-1) were observed using electrorotation. The aim of this study was to determine if viral infection of a cell manifests itself in changes in the gross physiological parameters of the cells. The study was expanded to include measurements of protein profiles and scanning electron microscope images of cells. The results were analysed in terms of the known biophysical life-cycle of the virus. The possibility of developing methods for the separation of infected and non-infected cells is also discussed.

1.2.2 Attachment of HSV-1 to polystyrene beads.

When a polystyrene bead is coated with a protein layer, the surface properties of the bead changes. These changes are reflected in the dielectric properties of the bead, which in turn produces changes in the electrorotation spectrum of the bead. In this work beads were first coated with anti-mouse IgG, then with monoclonal mouse anti-HSV-1 IgG to which HSV-1 virions were attached. At each stage the electrorotational spectra of the beads were obtained. The results of each stage were analysed with a view to ascertaining the possibility of developing a method for detecting HSV-1 virions in solution.

Classical diagnostic procedures for the detection of HSV-1, such as direct visualisation of virus particles by electron microscopy, virus growth characteristics on susceptible cells and immunofluorescent detection, often necessitates isolation and cultivation of the virus, which is usually a long and uncertain procedure. These methods have to a large extent been superseded by immunological and in particular by nucleic acid based techniques. All these current methods have some drawbacks and most require skilled operators. Therefore approaches based on changes in the AC electrokinetic properties of particles promise a rapid, sensitive and quantitative new method.

1.2.3 Rotation mapping of planar microelectrodes.

During electrorotation measurements it is important to know the electric field distribution across the electrode. Time-invariant electrostatic field mapping have been performed [18, 34, 35] and there have also been attempts at field mapping using cm scaled electrodes [34, 35]. A more comprehensive numerical study of the electric field generated by electrorotation electrodes was presented by Hughes *et al* [18] and in this study both the magnitude and phase of the electric fields were taken into account. In order to verify this simulation experimentally, measurements of the spatial variation of electrorotational torque within a polynomial electrode [36] were performed. The rotation rate of elliptical latex beads was measured at a large number of different discrete positions within an

electrode. The spatial variation in rotation rate was analysed and the results compared to the predictions made by Hughes *et al* [18].

1.2.4 Cellular effects of electric fields.

With dielectrophoretic methods it is possible to move cells towards high field regions or away from high field regions and the method can be used as a tool to separate different cell types or to enrich cell sub-populations. This technique holds great promise for the development of new cell sorting technologies and in recent times several systems of cell separation have been developed. For example, Talary *et al* [11] used dielectrophoretic methods to obtain a six-fold enrichment of CD34+ cell subpopulation from bone marrow and peripheral blood stem cells without the need for initial chemical treatment associated with immunoadsorption techniques. Gascoyne *et al* [12] reported dielectrophoretic separation of MDA-231 human breast cancer cells from blood with 100% efficiency, while the tumour to normal cell ratio was reported to be in excess of $1{:}1x10^5$.

If dielectrophoresis is to be used to manipulate cells that may subsequently be used for clinical proposes it is important to investigate the nature and extent of any cellular responses to dielectrophoretic manipulation. Identifying such effects is clearly important in ascertaining the viability of dielectrophoretic cell sorting technologies. It is well known that cells are capable of exhibiting very rapid and quantifiable responses to a range of stimuli. Since there are not any appropriate precedents that suggest an obvious subcellular system as a potential target for the dielectrophoretic field, a spectrum of possible resultant effects were investigated using a range of different biological investigations. These include scanning electron microscopy, alterations in cell-cycle control system dynamics and a MTT mitochondrial stress assay. Alterations in gene expression was tested at two levels. Firstly, expression of the intermediate-early gene c-fos was investigated and secondly, mRNA fingerprinting was carried out using sets of random primers as an assessment of non-specific gene transcription. This work was performed in colaboration with Dr S. Britland (University of Bradford,

School of Pharmacy), T.T. Li (University of Glasgow, Department of Cell Biology) and Dr A.T. Evans (University of Bradford, School of Pharmacy).

1.3 Summary

In order to determine if viral infection of a cell manifests itself in changes in the gross physiological parameters of the cells, electrorotational measurements were performed on BHK(C-13) cells at different times after infection with HSV-1. The results of these measurements, as well as of scanning electron microscopy and protein profiles were analysed in terms of the known biophysical life-cycle of the virus. HSV-1 virions were attached to antibody coated polystyrene beads and the effect on the dielectric properties of the beads were investigated using electrorotational methods. The results were analysed with a view of developing a new method for detection of HSV-1 in solution. The electric field distribution in an electrorotational electrode was measured using an experimental torque map and the distribution was favourably compared to a numerical model presented by Hughes *et al* [18]. Exposing cells to electrical fields raises concerns about possible cellular effects of such manipulation. In order to quantify the possible cellular effects of dielectrophoretic manipulation of cells, a spectrum of possible resultant effects were investigated using a range of different biological investigations.

1.4 References

1. Hatschek, E. and P.C.L. Thorne, *New solutions in Non-Dissociating Liquids I - Nickel in toluene and Benzene*. Royal Society Procedings, 1923. **103**: p. 276-284.
2. Pohl, H.A., Journal of Applied Physics, 1951. **22**: p. 869-871.
3. Pohl, H.A., *Dielectrophoresis*. 1978, Cambridge: Cambridge University Press.
4. Lang, V.V., Versuche im elektrostatishen Drehfelde, Wien. Ber., 1906. **115**: p. 211-222.
5. Arnold, W.M. and U. Zimmermann, *Rotation of an isolated cell in a rotating electric field.* Naturwissenschaften, 1982. **69**: p. 297.
6. Pethig, R., *Dielectrophoresis: Using Inhomogeneous AC Electrical Fields to Separate and Manipulate Cells.* Critical Reviews in Biotechnology, 1996. **16**(4): p. 331-348.
7. Wang, X.B., R. Pethig, and T.B. Jones, *Relationship of dielectrophoretic and electrorotational behaviour exhibited by polarized particles.* Journal of Physics D: Applied Physics, 1992. **25**: p. 905-912.
8. Jones, T.B. and M. Washizu, *Multipolar dielectrophoretic and electrorotation theory.* Journal of Electrostatics, 1996. **37**: p. 121-134.
9. Jones, T.B., *Dielectrophoretic force calculation.* Journal of Electrostatics, 1979. **6**: p. 69-82.
10. Denner, V. and H.A. Pohl, *Dielectrophoretic force in electrostatic fields.* Journal of Electrostatics, 1982. **13**: p. 167-174.
11. Talary, M.S., K.I. Mills, T. Hoy, A.K. Burnett, and R. Pethig, *Dielectrophoretic separation and enrichment of CD34+ cell subpopulation from bone marrow and peripheral blood stem cells.* Medical and Biological Engineering and Computing, 1995: p. 235-237.
12. Gascoyne, P.R.C., X.-B. Wang, Y. Huang, and F.F. Becker, *Dielectrophoretic Separation of Cancer Cells from Blood.* IEEE Transactions on Industry Applications, 1997. **33**: p. 670-678.
13. Wang, X.B., J. Vykoukal, F.F. Becker, and P.R.C. Gascoyne, *Separation of polystyrene microbeads using dielectrophoretic/gravitational field-flow-fractionation.* Biophysical Journal, 1998. **74**: p. 2689-2701.

14. Zimmermann, U., J. Vienken, and G. Pilwat, *Rotation of cells in an alternating electric field: the occurrence of a resonance frequency.* Z. Naturforsch, 1981. **36**: p. 173-177.

15. Holzapfel, C., J. Vienken, and U. Zimmermann, *Rotation of cells in an alternating electric field: theory and experimental proof.* Journal of Membrane Biology, 1982. **67**: p. 13-26.

16. Arnold, W.M. and U. Zimmermann, *Rotating-field-induced rotation and measurement of the membrane capacitance of single mesophyll cells of Avenia sativa.* Z. Naturforsch., 1982. **37c**: p. 908-915.

17. Arnold, W.M. and U. Zimmermann, *Electro-rotation: Development of a technique for dielectric measurements on individual cells and particles.* Journal of Electrostatics, 1988. **21**: p. 151-191.

18. Hughes, M.P., X.B. Wang, F.F. Becker, P.R.C. Gascoyne, and R. Pethig, *Computer-aided analysis of electric fields used in electrorotation studies.* Journal of Physics D: Applied Physics, 1994. **27**: p. 1564-1570.

19. Gimsa, J., T. Schnelle, G. Zechel, and R. Glaser, *Dielectric Spectroscopy of Human Erythrocytes: Investigations under the influence of Nystatin.* Biophysical Journal, 1994. **66**: p. 1244-1253.

20. Fuhr, G., J. Gimsa, and R. Glaser, *Interpretation of Electrorotation of Protoplasts II. Interpretation of Experiments.* Studia Biophysica, 1985. **109**: p. 5-14.

21. Fuhr, G., J. Gimsa, and R. Glaser, *Interpretation of Electrorotation of Protoplasts I. Theoretical Considerations.* Studia Biophysica, 1985. **108**(3): p. 149-164.

22. Wicher, D., J. Gundel, and H. Matthies, *Electrorotation of Liposomes in the α- and β- Dispersion range.* Studia Biophysica, 1987. **119**(1-3): p. 103-104.

23. Gimsa, J., P. Marszalek, U. Loewe, and T.Y. Tsong, *Dielectrophoresis and electrorotation of neurospora slime and murine myeloma cells.* Biophysical Journal, 1991. **60**: p. 749-760.

24. Becker, F.F., X.B. Wang, Y. Huang, R. Pethig, J. Vykoukal, and P.R.C. Gascoyne, *Separation of human breast cancer cells by differential*

dielectric affinity. Proceedings of the National Academy of Science, 1995. **92**: p. 860-864.

25. Huang, Y., X.B. Wang, R. Holzel, F.F. Becker, and P.R.C. Gascoyne, *Electrorotational studies of the cytoplasmic dielectric properties of Friend murine erythroleukaemia cells.* Physics in Medicine and Biology, 1995. **40**: p. 1789-1806.

26. Wang, J., V.L. Sukhorukov, C.S. Djuzenova, U. Zimmermann, T. Muller, and G. Fuhr, *Electrorotational spectra of protoplasts generated from giant marine alga Valonia utricularis.* Protoplasma, 1997. **196**: p. 123-134.

27. Gimsa, J., C. Pritzen, and E. Donath, *Characterisation of Virus-Red-Cell interaction by electrorotation.* Studia Biophysica, 1989. **130**(1-3): p. 123-131.

28. Gimsa, J., T. Muller, T. Schnelle, and G. Fuhr, *Dielectric Spectroscopy of Single Human Erythrocytes at Physiological Ionic Strength: Dispersion of the Cytoplasm.* Biophysical Journal, 1996. **71**: p. 495-506.

29. Zhou, X.F., G.H. Markx, and R. Pethig, *Effect of biocide concentration on electrorotation spectra of yeast cells.* Biochimica et Biophysica Acta, 1996. **1281**: p. 60-64.

30. Arnold, W.M., R.K. Schmutzler, S. Al-Hasani, D. Krebs, and U. Zimmermann, *Differences in membrane properties between unfertilised and fertilised single rabbit oocytes demonstrated by electro-rotation - Comparison with cells from early embryos.* Biochimica et Biophysica Acta, 1989. **979**: p. 142-146.

31. Gascoyne, P., R. Pethig, J. Satayavivad, F.F. Becker, and M. Ruchirawat, *Dielectrophoretic detection of changes in erythrocyte membranes following malarial infection.* Biochimica et Biophysica Acta, 1997. **1323**: p. 240-252.

32. Hu, X., W.M. Arnold, and U. Zimmermann, *Alterations in the electrical properties of T and B lymphocyte membrane induced by mitognic stimulation. Activation monitored by electro-rotation of single cells.* Biochimica et Biophysica Acta, 1990. **1021**: p. 191-200.

33. Huang, Y., X.B. Wang, F.F. Becker, and P.R.C. Gascoyne, *Membrane changes associated with the temperature-sensitive P85$^{gag-mos}$- dependent*

transformation of rat kidney cells as determined by dielectrophoresis and electrorotation. Biochimica et Biophysica Acta, 1996. **1282**: p. 76-84.

34. Gimsa, J., R. Glaser, and G. Fuhr, *Remarks on the field distribution in four electrode chambers for electrorotational methods.* Studia Biophysica, 1988. **125**: p. 71-76.

35. Holzel, R., *Electric field calculation for electro-rotation electrodes.* Journal of Physics D: Applied Physics, 1993. **26**: p. 2112-2116.

36. Huang, Y. and R. Pethig, *Electrode design for negative dielectrophoresis.* Measurement Science and Technology, 1991. **2**: p. 1142-1146.

Chapter 2: AC Electrokinetics – Theoretical Aspects

2.1 Introduction

AC Electrokinetics describes how externally applied alternating electric fields can induce motion in particles. Cell and particle movement occurs as a result of externally applied time varying electric fields and is dependent on the induced polarisation of the field-exposed cells or particles. By using micro-fabrication methods it is possible to create electrodes that generate electric fields capable of inducing motion in dielectric particles, the motion can be lateral if the electric field generated is non-uniform or rotational if a rotating electric field is employed. The direction and speed of the resulting motion is dependent upon the properties of the dielectric particle and its suspending electrolyte, as well as the applied electric field. Using a suitable dielectric model for the particle and analysing the response of a particle to an applied electric field, information can be obtained about the nature of the dielectric particle upon which motion is imparted.

2.2 Polarisation

Polarisation is the ability of materials to acquire a dipole through the action of an external electric field [1]. Materials in which an external electric field can induce dipoles are referred to as dielectrics. In a dielectric material there are charges bound to atoms or molecules and these can only be forced to move minute distances by the application of an external electric field. The field causes positive charges to move one way and negative charges to move in the opposite direction, a dielectric in which such a displacement has taken place is said to be polarised. Some molecules possess a permanent dipole and in a material consisting of such molecules the dipoles align with an externally applied electric field, causing the net dipole moment of the material to increase.

2.2.1 Electric polarisation

In a material, where the average dipole moment vector is $\boldsymbol{p}$ and there are N dipoles per unit volume, then

$$\boldsymbol{P} = N\boldsymbol{p} \tag{1}$$

is the *electric* polarisation. Within a dielectric, polarisation causes charges to accumulate. These are referred to as bound charges; the bound volume charge density ρ_b of a dielectric is given by:

$$\rho_b = -\nabla \cdot \boldsymbol{P} \tag{2}$$

2.2.2 Basic polarisation processes

There are three basic mechanisms by which an external electric field can induce dipoles in a homogeneous dielectric material. *Electronic* polarisation occurs when the centre of charge of the electron cloud in a molecule moves slightly with respect to the centre of charge of the nuclei. The displacement is minute, even on an atomic scale, typically 10^{-8} times the diameter of an atom. *Atomic*

polarisation is a result of ions, of different signs, moving in different directions as a result of an applied electric field. *Orientaional* polarisation occurs when polar molecules align in an applied electric field, causing the dielectric to become further polarised. The alignment is partially disrupted by collisions caused by thermal agitation.

2.2.3 Gauss's Law

In a volume ν that contains various dielectrics, the total charge Q within ν is given by $Q = Q_f + Q_b$, where Q_f is the total free charge and Q_b is the total bound charge. When there are no surface charges on ν then *Gauss's* law relates the outward flux of the electric field E through the surface of area A to the net enclosed charge Q by:

$$\int_A \boldsymbol{E} \cdot d\hat{\boldsymbol{A}} = \frac{Q}{\varepsilon_0} \tag{3}$$

where $d\hat{A}$ is the vector normal to a small element of the surface and ε_0 is the permittivity of free space.

In the case where the volume ν lies inside the dielectric, Gauss's law can be expressed in differential form:

$$\nabla \cdot \boldsymbol{E} = \frac{\rho}{\varepsilon_0} \tag{4}$$

where $\rho = \rho_f + \rho_b$ is the total charge density.

2.2.4 Laplace's and Poisson's equations

If $\boldsymbol{E} = -\nabla V$ is substituted in to the differential form of Gauss's law. then it follows that

$$\nabla^2 V = -\frac{\rho}{\varepsilon_0} \tag{5}$$

This is *Poisson's* equation for the potential V in dielectrics. In a region where the total charge density $\rho = \rho_f + \rho_b$ is zero

$$\nabla^2 V = 0 \tag{6}$$

This is *Laplace's* equation for dielectrics.

2.2.5 Electric flux density

Combining the differential form of Gauss's law and the expression for the bound charge density within a dielectric gives:

$$\nabla \cdot (\varepsilon_0 \boldsymbol{E} + \boldsymbol{P}) = \rho_f \tag{7}$$

The vector $\boldsymbol{D}$ is defined as

$$\boldsymbol{D} = \varepsilon_0 \boldsymbol{E} + \boldsymbol{P} \tag{8}$$

and is such that its divergence is equal to that of the volume free charge density. It is referred to as the electric flux density. As a result:

$$\nabla \cdot \boldsymbol{D} = \rho_f \tag{9}$$

2.2.6 *Electric susceptibility and relative permittivity*

In most dielectrics $\boldsymbol{P}$ is proportional to $\boldsymbol{E}$ and points in the same direction, such dielectrics are linear and isotropic. Then

$$\boldsymbol{P} = \varepsilon_0 \chi_e \boldsymbol{E} \tag{10}$$

for which χ_e is electric susceptibility of the dielectric. In linear and isotropic dielectrics

$$\boldsymbol{D} = \varepsilon_0 \boldsymbol{E} + \boldsymbol{P} = \varepsilon_0 (1 + \chi_e) \boldsymbol{E} = \varepsilon_0 \varepsilon_r \boldsymbol{E} \tag{11}$$

where $\varepsilon_r = 1 + \chi_e$ is a dimensionless number, the relative permittivity of a dielectric.

2.2.7 *Real dielectrics and complex permittivity*

Some dielectrics are close to ideal, they are homogeneous, linear, and isotropic, their conductivity is close to zero and their relative permittivity is virtually independent of frequency, i.e. they have a constant permittivity. However, this is generally not the case.

Consider a parallel plate capacitor of surface area A, where the plates are separated by a distance s, connected to a voltage source with a potential V and frequency f as illustrated in figure 1:

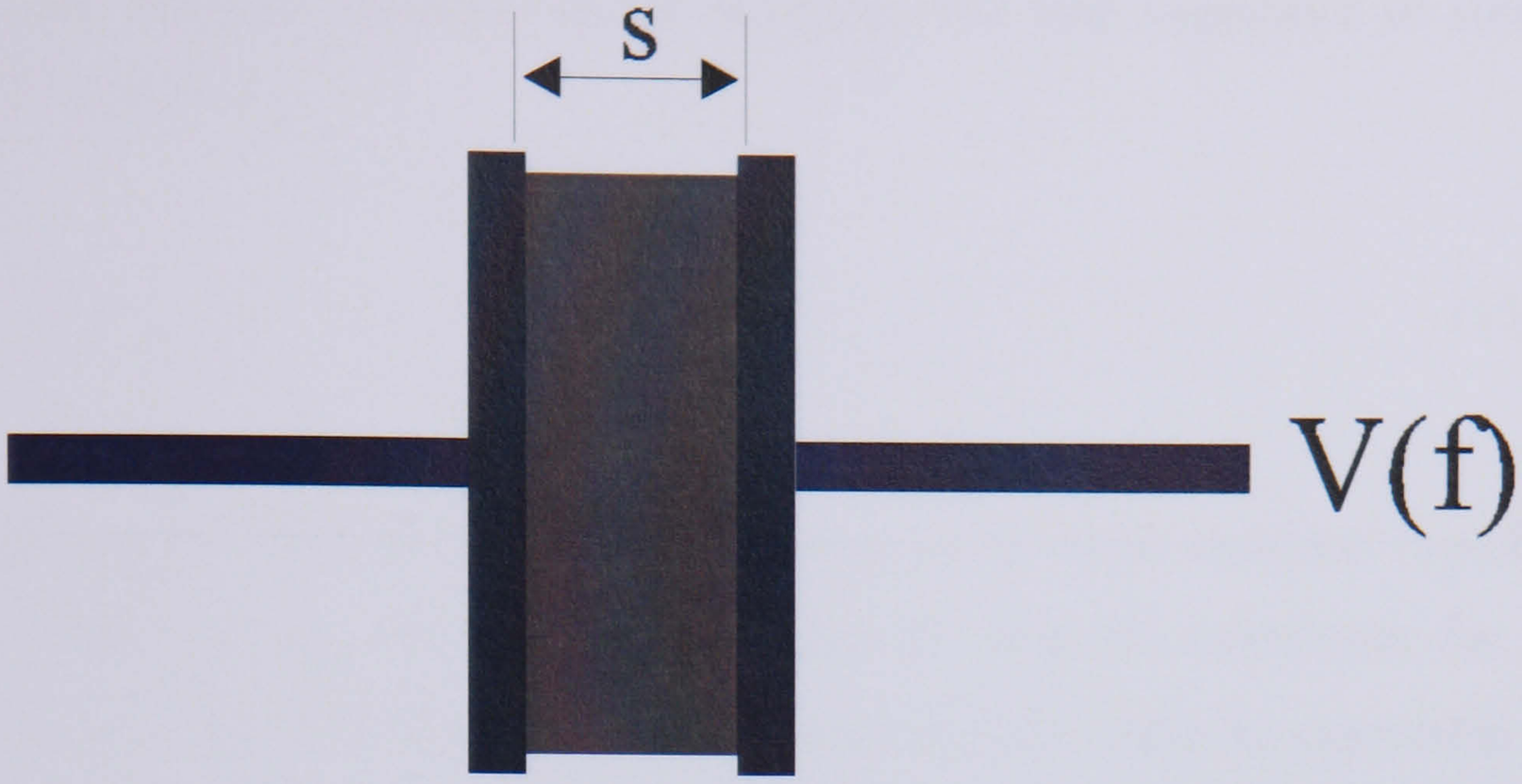

Figure 1: Parallel plate capacitor with an applied voltage of frequency f. The plates are of area, A separated by a distance s, the gap is filled by an ideal dielectric.

For a capacitor that consists of an ideal dielectric, the impedance is given by:

$$Z = \frac{1}{j\omega C} \tag{12}$$

where $j = \sqrt{-1}$, ω is the angular velocity of the potential and the capacitance C is given by

$$C = \varepsilon_0 \varepsilon_r \frac{A}{s}. \tag{13}$$

Most real dielectrics exhibit more complicated behaviour. They are partially conducting and as such are said to be lossy. If a parallel plate capacitor, as illustrated in figure 1, contains a lossy dielectric then the capacitor is equivalent to a circuit containing an ideal non-conducting dielectric of capacitance C_1, in parallel with a resistor of resistance R_1, where the resistance is given by:

$$R_1 = \frac{s}{\sigma A} \tag{14}$$

where σ is the conductivity of the dielectric. The total impedance of such a circuit is given by:

$$Z = \frac{R_1}{1 + j\omega R_1 C_1} \tag{15}$$

Comparing this expression to the impedance of an ideal capacitor (equation (12)); replacing R_1 with equation (14) and C_1 with the expression for the capacitance of a parallel plate capacitor (equation (13)), yields an expression for the capacitance of a parallel plate capacitor consisting of a lossy dielectric:

$$C = \varepsilon^* \frac{A}{s} \tag{16}$$

where the term ε^* replaces the permittivity $\varepsilon = \varepsilon_0 \varepsilon_r$ in equation (13). The term ε^* is referred to as the *complex permittivity* of a lossy dielectric, and is:

$$\varepsilon^* = \varepsilon_0 \varepsilon_r - j\frac{\sigma}{\omega} \tag{17}$$

This is a convenient to way express the conductivity terms of a dielectric exposed to an alternating electric field [2].

If the complex permittivity has an imaginary component then there is and absorption of energy and associated joule heating in the dielectric. The rate of conversion of electrical energy to heat is proportional to the imaginary component.

2.3 Further Polarisation processes

The rate at which polarisation occurs is finite, so if an external electric field is changing rapidly then the dipole may no longer be able to keep up with the electric field. This leads to a reduction in the polarisibility of a material compared to low frequency values [3]. Such a reduction in polarisibility is referred to as a dielectric relaxation, and this depends on the nature of the dielectric material as well as on the way a dielectric system is assembled.

In a dielectric system consisting of different dielectrics there are several different processes that cause the dielectrics to polarise as a result of an applied electric field. These include the three basic polarisation processes: orientational, atomic and electronic polarisation, as well as polarisation caused by interfacial processes in heterogeneous materials. Therefore variations in the permittivity of a dielectric occur as the frequency of the applied electric field changes. Atomic relaxations occur at the same frequencies as the natural vibrations of a molecule (infrared range at about 10^{14}Hz), electronic relaxations occur at the higher frequencies of the electronic transitions within an atom (visible and higher). Orientational polarisation processes will in general have a relaxation frequency that is lower than that of the atomic and electronic polarisations. The orientational relaxations depend largely on the immediate environment of the molecular dipole, as described by Debye [4] type relaxations. An example of these dielectric relaxation processes is illustrated in figure 2.

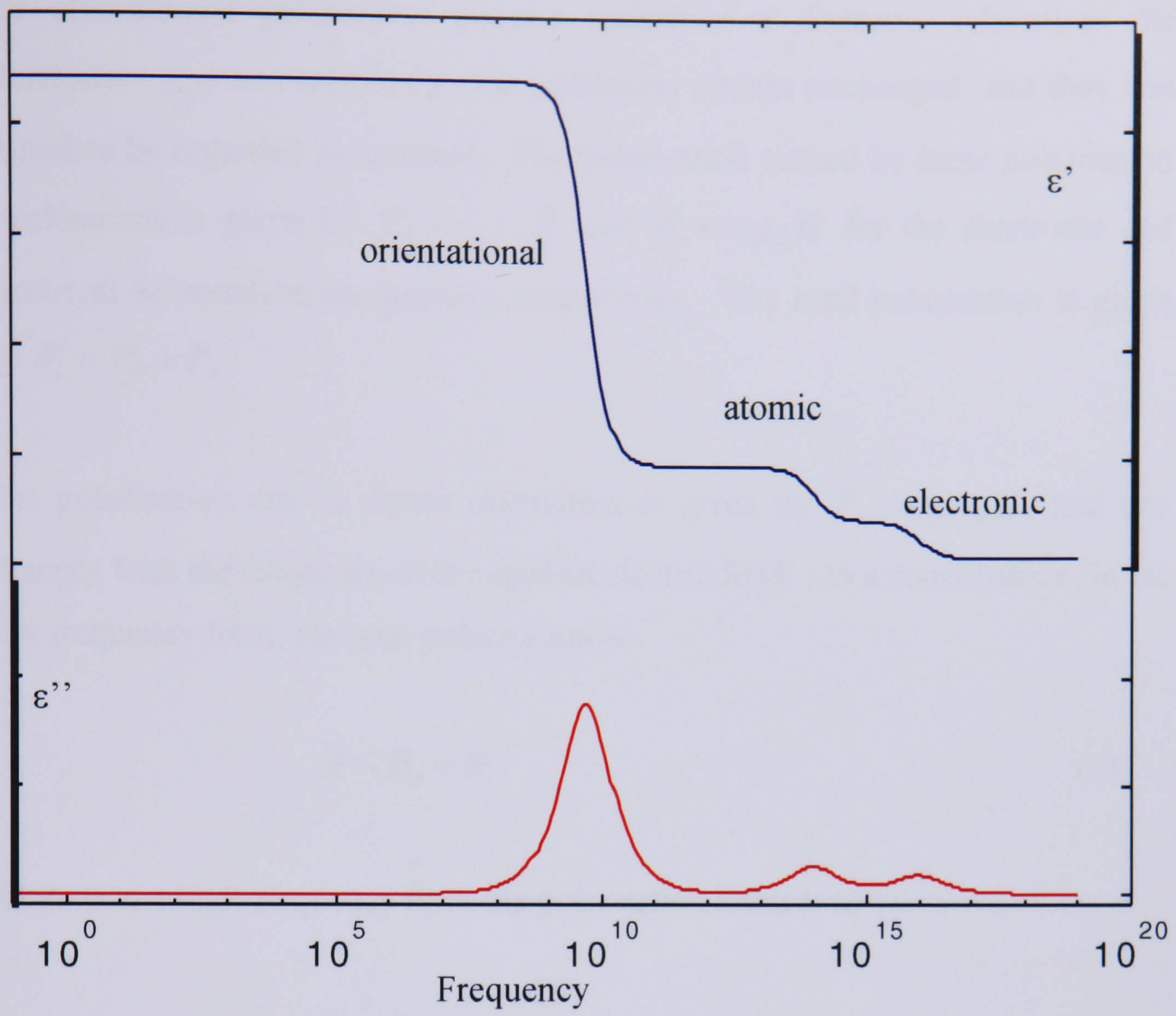

Figure 2: Variations of the dielectric parameters $\varepsilon', \varepsilon''$ with the frequency for the interfacial, orientational atomic and electronic dielectric dispersion processes. The frequencies shown are examples for the different relaxations. The figure is not to scale.

The atomic and electronic polarisations processes have relaxation frequencies that are high enough for the polarisation they cause to be unaffected by the angular velocity of the electric fields used in this work. They can therefore be considered to be constant at all the frequencies of the applied electric field.

2.3.1 Debye relaxations

In a homogeneous dielectric material, polarisation is caused by the movement of charge to create dipoles or by alignment of individual dipole moments. As the slowest polarisation mechanism in a *homogeneous* dielectric material is usually dipole reorientation, it is usually the first polarisation term to disappear as the

frequency of an applied electric field is increased. In the frequency range where the orientational polarisation process undergoes a dielectric relaxation. the electronic (χ_{el}) and atomic (χ_a) polarisations remain unchanged, and they can therefore be regarded as constant. The polarisation caused by these polarisation mechanisms is given by $\boldsymbol{P}_{el} = \varepsilon_0 \chi_{el} \boldsymbol{E}$ and $\boldsymbol{P}_a = \varepsilon_0 \chi_a \boldsymbol{E}$ for the electronic and electrical polarisation mechanisms respectively. The total polarisation is given by $\boldsymbol{P}_c = \boldsymbol{P}_{el} + \boldsymbol{P}_a$.

The polarisation due to dipole orientation is given by $\boldsymbol{P}_{or} = \varepsilon_0 \chi_{or} \boldsymbol{E}$, and this changes with the frequency of the applied electric field. As a consequence, in the low frequency limit, the total polarisation is:

$$\boldsymbol{P} = \boldsymbol{P}_{or} + \boldsymbol{P}_c \tag{18}$$

While in the high frequency limit the polarisation reduces to

$$\boldsymbol{P} = \boldsymbol{P}_c \tag{19}$$

as a result of the orientational polarisation term disappearing.

It can be shown [3] that this change can be described as a frequency dependent polarisation:

$$\boldsymbol{P}(\omega) = \boldsymbol{P}_{or}(\omega) + \boldsymbol{P}_c = \varepsilon_0 \left(\frac{\chi_{or}}{1 + j\omega\tau_{or}} + \chi_c \right) \boldsymbol{E} \tag{20}$$

corresponding to the dielectric having a complex permittivity given by:

$$\varepsilon^* = \varepsilon_\infty + \frac{\varepsilon_l - \varepsilon_\infty}{1 + j\omega\tau_{or}}. \tag{21}$$

where τ_{or} is the characteristic relaxation time of the macroscopic dielectric relaxation mechanism. ε_l is the permittivity at the low frequency limit. while ε_∞

is the permittivity at frequencies high enough for orientational polarisation to have disappeared. The complex dipole moment consists of a real and an imaginary component:

$$\varepsilon^* = \varepsilon' - j\varepsilon'' \tag{22}$$

The real component is given by:

$$\varepsilon' = \varepsilon_\infty + \frac{(\varepsilon_l - \varepsilon_\infty)}{1 + \omega^2 \tau_{or}^2} \tag{23}$$

While the imaginary component is given by:

$$\varepsilon'' = \frac{(\varepsilon_l - \varepsilon_\infty)\omega\tau_{or}}{1 + \omega^2 \tau_{or}^2} \tag{24}$$

These are known as the Debye equations, an example of the frequency dependence of ε' and ε'' is illustrated in figure 3.

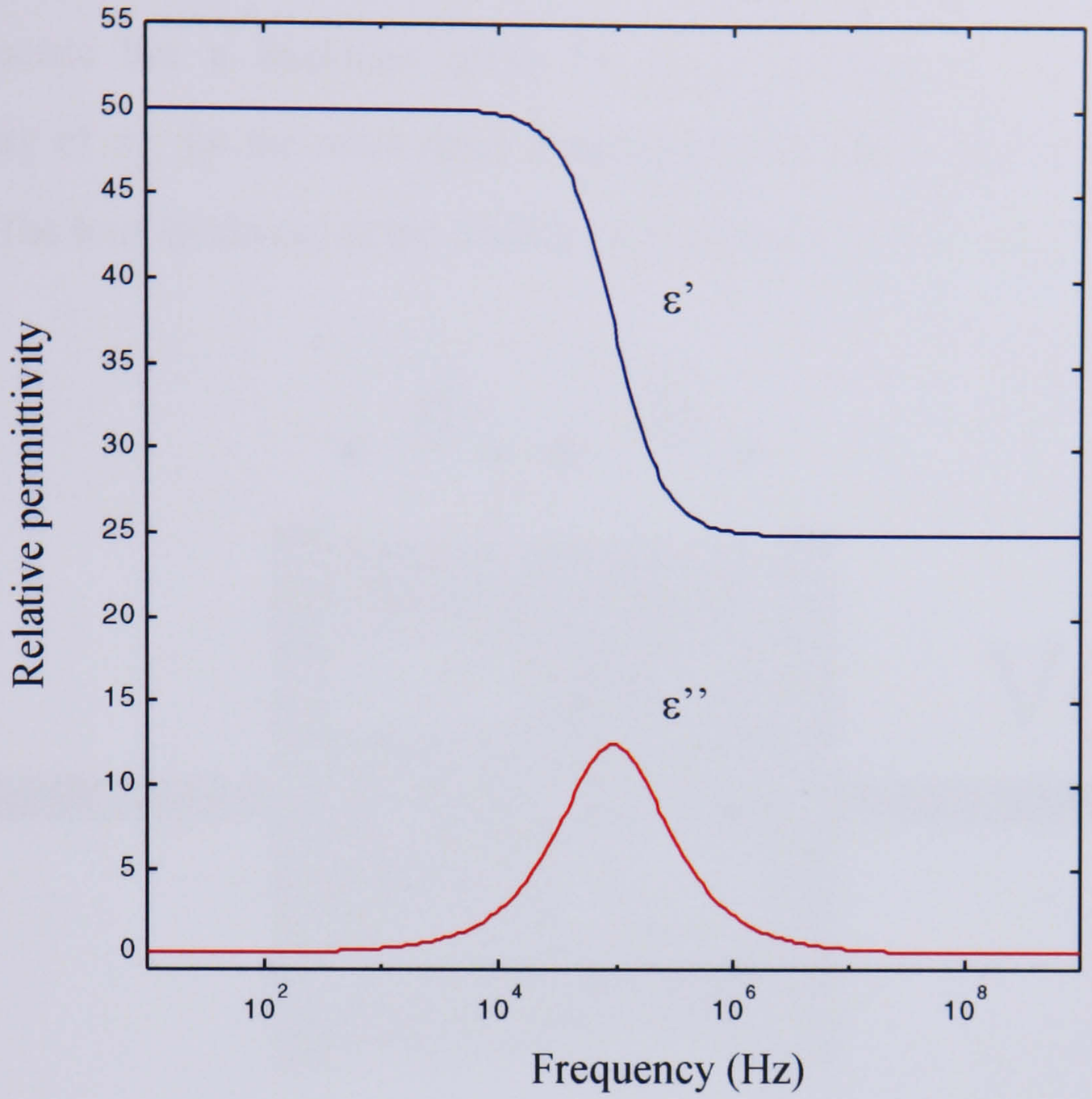

Figure 3: Variations in the real and imaginary components of the complex permittivity with frequency of an applied electric field, as given by equations (23) and (24) respectively. The low and high frequency limits were set to $\varepsilon_l = 50$ and $\varepsilon_\infty = 25$ and the characteristic relaxation time to $\tau_0 = 1.67 \times 10^{-6}$ seconds.

2.3.2 Interfacial Dielectric Phenomena: Maxwell-Wagner Polarisation

Debye relaxations occur in homogeneous media. However, many systems are not homogeneous, but contain several different dielectrics and as such are heterogeneous. In general, a heterogeneous medium exhibits frequency dependent dielectric and conductive properties that are different from those of the constituent components. Such dispersions are known as Maxwell-Wagner or interfacial polarisations [3].

The simplest example of such a heterogeneous system is a parallel plate capacitor that consists of two parallel slabs of different dielectrics, as illustrated in figure 4. One dielectric has a thickness given by d_1, a conductivity of σ_1 and a permittivity of ε_1, for the other these parameters have values given by d_2, σ_2 and ε_2. The total thickness of the dielectrics is given by $d = d_1 + d_2$.

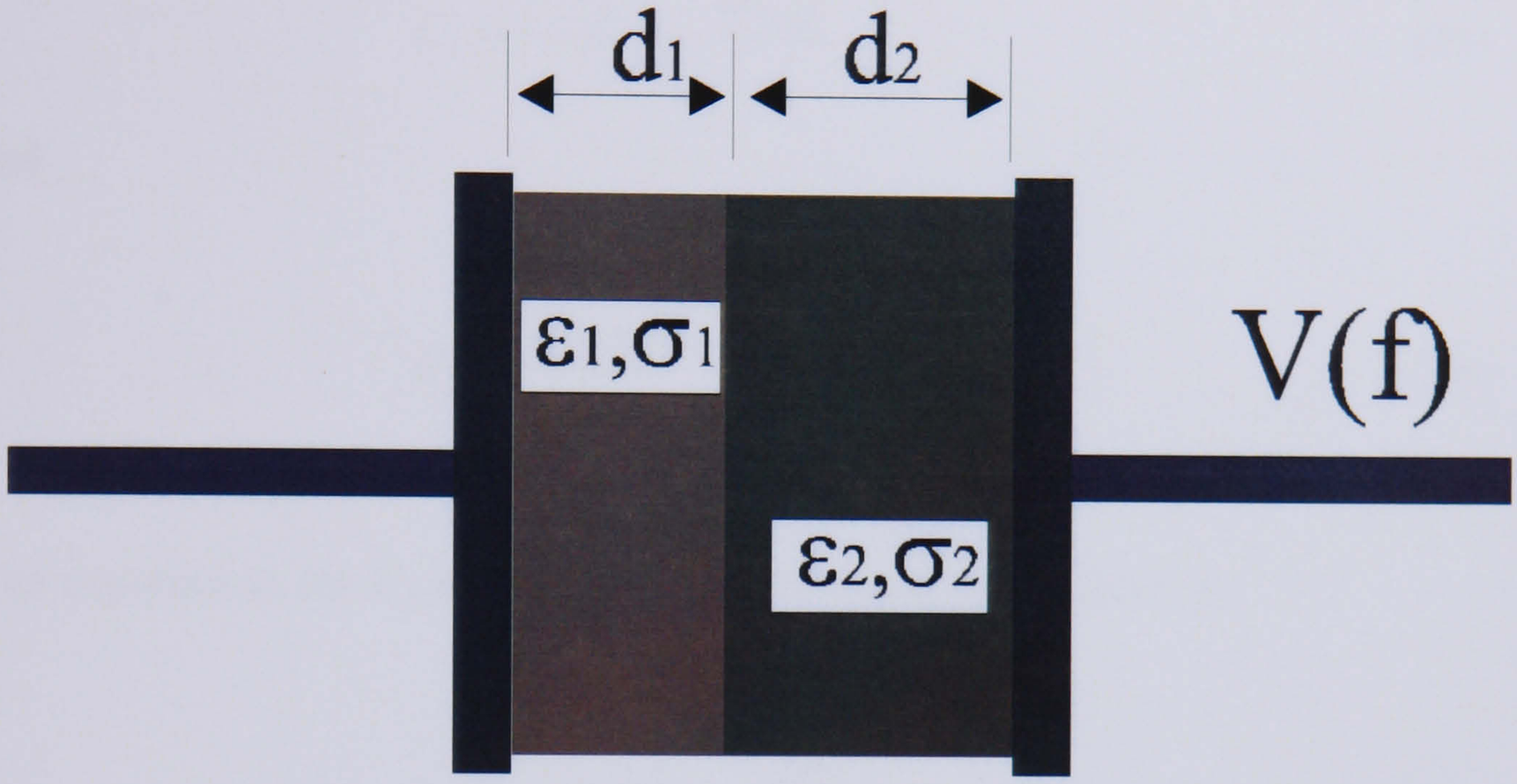

Figure 4: Parallel plate capacitor with an applied voltage of frequency *f*. The plates are of surface area *A*. The gap is filled by two real dielectrics of thickness d_1 and d_2, the dielectrics are defined by the permittivities $\varepsilon_1, \varepsilon_2$ and conductivities σ_1, σ_2 respectively.

The physical mechanism by which interfacial polarisation occurs can be explained in terms of the non-uniform distribution of charges across the interface between the two differing dielectrics. In order to achieve continuity of current in the differing dielectrics is a charge carrier discontinuity exists at the boundary of the two dielectrics. The build-up of charge at the interface causes polarisation in the dielectric system, this polarisation is frequency dependent and is the origin of interfacial relaxations for a heterogeneous system.

By assuming that σ_2 is negligibly small and that ε_1, σ_2 and ε_2 are frequency independent, it is possible to obtain a simple expression for the behaviour of the dielectric system. The system can be regarded as two capacitors in series, for which the total capacitance can be found by using [3]:

$$\frac{1}{C}=\frac{1}{C_1}+\frac{1}{C_2} \tag{25}$$

The capacitance of the two capacitors are given by:

$$C_1=\frac{A\varepsilon_0\left(\varepsilon_1-\frac{j\sigma_1}{\omega\varepsilon_o}\right)}{d_1} \tag{26}$$

and

$$C_2=\frac{A\varepsilon_0\varepsilon_2}{d_2} \tag{28}$$

The expressions for C_1 and C_2 gives a total capacitance given by:

$$C=\frac{A\varepsilon_0\varepsilon_2\left(\varepsilon_1-\frac{j\sigma_1}{\omega\varepsilon_0}\right)}{d_2\left(\varepsilon_1-\frac{j\sigma_1}{\omega\varepsilon_0}\right)+d_1\varepsilon_2} \tag{29}$$

From which it can be seen that in the low frequency limit ($\omega\to 0$) the effective permittivity is given by:

$$\varepsilon_l=\frac{\varepsilon_2 d}{d_2} \tag{30}$$

for $d=d_1+d_2$.

While for the high frequency limit ($\omega\to\infty$) the effective permittivity is given by:

$$\varepsilon_\infty=\frac{\varepsilon_1\varepsilon_2 d}{d_2\varepsilon_1+d_1\varepsilon_2} \tag{31}$$

from which it can be seen that $\varepsilon_l > \varepsilon_\infty$ indicating that the system exhibits a dielectric dispersion.

From a full analysis of the two layer system it can been shown that the dielectric dispersions of a two layer system can be described in terms of Debye equations [5], leading to the following expressions for the dielectric parameters in the two layer system:

$$\varepsilon' = \varepsilon_\infty + \frac{\varepsilon_l - \varepsilon_\infty}{1+\omega\tau} \tag{32}$$

and

$$\varepsilon'' = \frac{(\varepsilon_l - \varepsilon_\infty)\omega\tau}{1+\omega^2\tau^2} \tag{33}$$

with

$$\varepsilon_l = \frac{d(\varepsilon_1 d_1 \sigma_2^2 + \varepsilon 2 d 2 \sigma_1^2)}{(\sigma_1 d_2 + \sigma_2 d_1)^2}, \tag{34}$$

$$\varepsilon_\infty = \frac{d\varepsilon_1\varepsilon_2}{(\varepsilon_1 d_2 + \varepsilon_2 d_1)} \tag{35}$$

and

$$\tau = \frac{\varepsilon_0(\varepsilon_1 d_1 + \varepsilon_2 d_2)}{\sigma_1 d_2 + \sigma_2 d_1} \tag{36}$$

The conductivity of the interfacial system as a whole is given by [5]:

$$\sigma = \frac{d\sigma_1\sigma_2}{\sigma_1 d_2 + \sigma_2 d_1} \tag{37}$$

2.4 Dielectric Particles in an external electric field

When a polarisable particle is exposed to an electric field, charge builds up at the interface between the surface of the particle and its surroundings, causing the particle to polarise. As a result of the polarisation of the particle, the electric field is perturbed in the vicinity of the particle. By studying the effect the polarised particle has on the electric field an expression for the effective permittivity of the particle can be obtained.

2.4.1 Potential of a particle in an electric field.

When a dielectric material is exposed to an external electric field it polarises (as described in section 2.3 above). For the case of a dielectric particle suspended in a dielectric medium the medium/particle interface is polarised by Maxwell-Wagner type interfacial polarisation. As a result, surface charge is induced, and the particle acquires an induced dipole moment. This dipole moment depends not only on the properties of the dielectric particle, but also on its interaction with the medium in which it is suspended. If the particle is spherical then it can be described by a co-ordinate system as illustrated in figure 5.

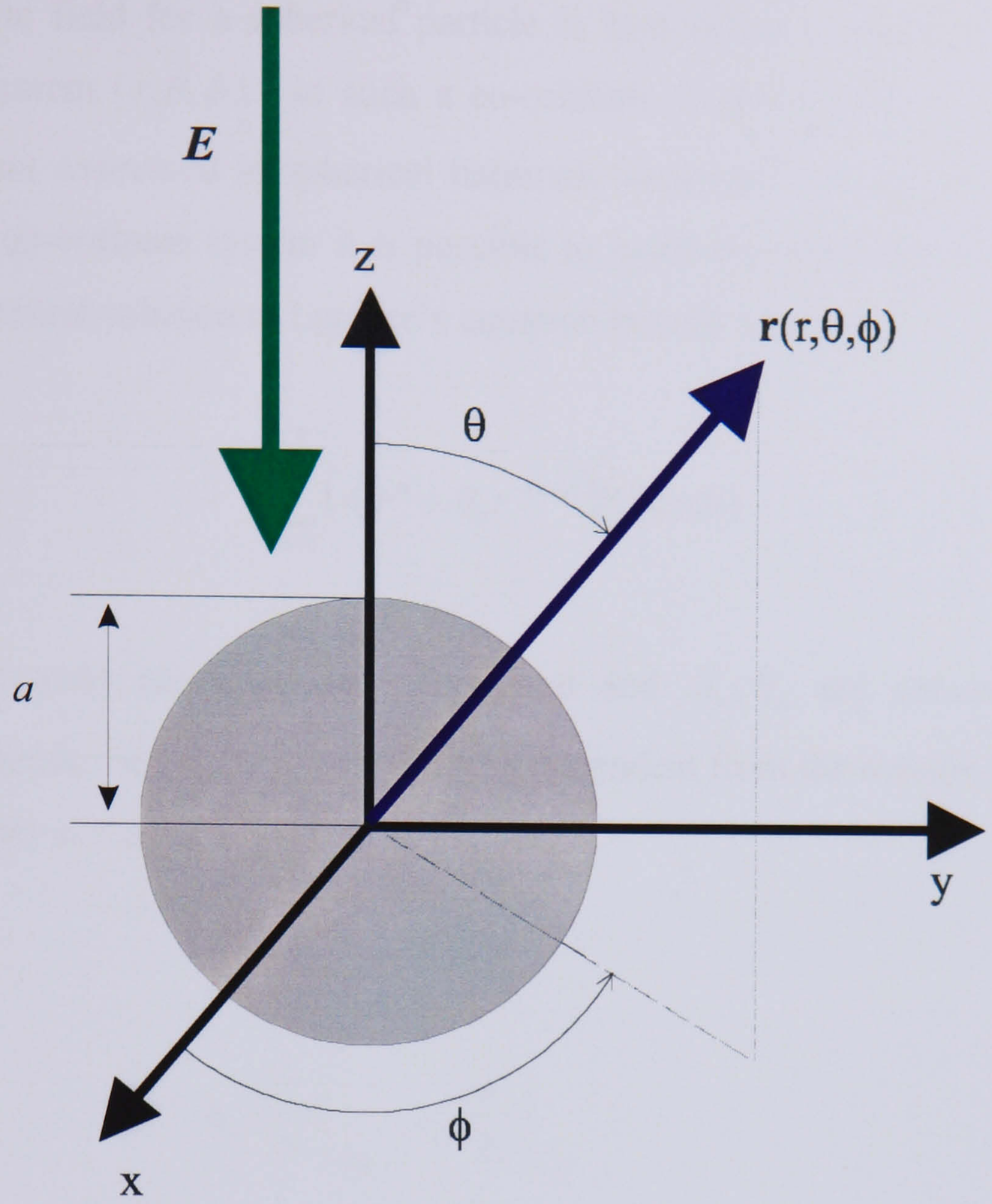

Figure 5: Co-ordinate system used to solve the potential arising from a spherical dielectric sphere of radius a suspended in an electric field $\boldsymbol{E}$.

To calculate the induced dipole moment, Laplace's equations must be solved for a spherical particle. If the particle is insulating and suspended in a dielectric medium, with the electric field $\boldsymbol{E}_0$ uniform and the dielectric particle spherical with radius a, then the following boundary conditions must be satisfied [1]:

(1) The potential V is continuous at $r = a$

(2) The normal component of $\boldsymbol{D}$ is continuous at $r = a$

(3) When $r \to \infty$, $V = \boldsymbol{E}_0 r\cos\theta$

The electric field for a spherical particle is best solved using a spherical co-ordinate system (r,θ,ϕ). In such a co-ordinate system solutions to Laplace`s equation are expressed in spherical harmonic functions. Using an appropriate choice of co-ordinate system it is possible to make the solution independent of ϕ. The general solution to Laplace's equation in such a case is:

$$V=\sum_{n=0}^{\infty}\left(A_n r^n + B_n r^{-(n+1)}\right)P_n(\cos\theta) \tag{38}$$

where $P_n(\cos\theta)$ are Legendre polynomial and A_n, B_n are constants. The potential inside the sphere is considered independent from the outside. This leads the boundary conditions being expressed as:

$$V_m\big|_{r=a} = V_p\big|_{r=a} \tag{39}$$

$$\varepsilon_m \left.\frac{\partial V_m}{\partial r}\right|_{r=a} = \varepsilon_p \left.\frac{\partial V_p}{\partial r}\right|_{r=a} \tag{40}$$

where V_m and V_p are the potentials in the suspending medium and the particle respectively, while ε_m and ε_p are the permittivities of the suspending medium and the particle respectively. The field outside the sphere must satisfy boundary condition (c). Therefore the solution for the potential outside the sphere must contain the term $V_m = -\boldsymbol{E}_0 r\cos\theta$ and no other positive power of r. As the potential inside the sphere is finite at $r=0$ there cannot be any negative powers of r. From this it can be shown that solutions for the potentials outside and inside the sphere take the form:

$$V_m = \boldsymbol{E}_0 r\cos\theta\left(\frac{a^3}{r^3}\left(\frac{\varepsilon_p-\varepsilon_m}{\varepsilon_p+2\varepsilon_m}\right)-1\right) \tag{41}$$

$$V_p = -\frac{3\varepsilon_m}{\varepsilon_p+2\varepsilon_m}\boldsymbol{E}_0 r\cos\theta \tag{42}$$

2.4.2 Potential of a particle in an electric field - lossy dielectrics.

If the dielectric is now conducting, the boundary conditions (a) and (c). and general solutions still hold. The presence of conductivity terms and charge transport to the dielectric interface, which in turn affects the electric flux density $\boldsymbol{D}$ in the dielectric must be included. In such a scenario applying Gauss's law changes boundary condition (b) to become:

$$\varepsilon_p \left.\frac{\partial V_p}{\partial r}\right|_{r=a} - \varepsilon_m \left.\frac{\partial V_m}{\partial r}\right|_{r=a} = \rho_s \tag{43}$$

where ρ_s is the free surface charge density at the interface, which is governed by time dependent charge carrier transport. The charge conservation equation can be used to relate the rate of change of charge in a volume to the flux of charges through the surface bounding the volume:

$$\frac{\partial q}{\partial t} = -\nabla \cdot \boldsymbol{J} \tag{44}$$

The current density in a dielectric can be related to the electric field strength:

$$\boldsymbol{J} = \sigma \boldsymbol{E} \tag{45}$$

Combining the above two equations and using Gauss's law in differential form gives a new form for the second boundary condition:

$$\frac{\partial \rho_s}{\partial t} = \sigma_m \left.\frac{\partial V_m}{\partial r}\right|_{r=a} - \sigma_p \left.\frac{\partial V_p}{\partial r}\right|_{r=a} \tag{46}$$

In the case of time varying electric fields of the form $\boldsymbol{E} = \boldsymbol{E}_0 e^{j\omega t}$, then the potential V and the surface charge density ρ_s are also time dependent. The time dependent derivative of ρ_s is then $j\omega\rho_s$. The two equations that describe the second boundary condition can then be combined to give:

$$\varepsilon_p^* \left.\frac{\partial V_p}{\partial r}\right|_{r=a} - \varepsilon_m^* \left.\frac{\partial V_m}{\partial r}\right|_{r=a} = 0 \tag{47}$$

where ε_p^* and ε_m^* are the complex permittivities of the particle and the medium respectively. The difference between this equation and the boundary condition for an ideal dielectric does not depend on position, so the solution to the potentials are given by the same equations as for an ideal dielectric, i.e.:

$$V_m = \boldsymbol{E}_0 r \cos\theta \left(\frac{a^3}{r^3} \left(\frac{\varepsilon_p^* - \varepsilon_m^*}{\varepsilon_p^* + 2\varepsilon_m^*} \right) - 1 \right) \tag{48}$$

$$V_p = -\frac{3\varepsilon_m^*}{\varepsilon_p^* + 2\varepsilon_m^*} \boldsymbol{E}_0 r \cos\theta \tag{49}$$

2.4.3 Effective dipole moment - The Clausius-Mossotti factor

The potential induced by a dipole of moment $\boldsymbol{p}_{eff}$ suspended in a dielectric medium of permittivity ε_{med} is given by [6]:

$$V_{dipole} = \frac{\boldsymbol{p}_{eff} \cos\theta}{4\pi\varepsilon_m r^2} \tag{50}$$

Comparison of the dipole potential with the potential V_m around a dielectric sphere gives the following expression for the dipole moment:

$$\boldsymbol{p}_{eff} = 4\pi\varepsilon_m \left(\frac{\varepsilon_p^* - \varepsilon_m^*}{\varepsilon_p^* + 2\varepsilon_m^*} \right) a^3 \boldsymbol{E} \tag{51}$$

The effective dipole moment of a sphere suspended in a dielectric medium is frequency dependent due to Maxwell-Wagner relaxation at the particle-medium

interface. The frequency dependence of the effective dipole moment is described by the expression:

$$K(\omega) = \frac{\varepsilon_p^* - \varepsilon_m^*}{\varepsilon_p^* + 2\varepsilon_m^*} \tag{52}$$

This expression is known as the *Clausius-Mossotti* factor. The Clausius-Mossotti factor is correct under conditions where the characteristic size of the electric field is large compared to the size of the sphere and the sphere is sufficiently far away from other dielectric objects so that it is not influenced by the potential induced by their dipole moments.

2.5 Dielectrophoresis

When a polarisable particle that is suspended in a dielectric medium is exposed to an electric field, the particle polarises. The nature of the polarisation is determined by differences in the dielectric properties of the particle and its surroundings. If the polarisibility of the particle is greater than its surroundings, then the resulting polarisation will be in the direction of the applied electric field. Conversely, if the polarisibility of the particle is less than its surroundings, the resulting polarisation will be in the opposite direction of the applied electric field.

When a particle is polarised by an applied electric field, the charges that give rise to the polarisation will experience a force. If the electric field is uniform then the forces on the charges in the dielectric particle balance out and the particle will not experience a net force. However, if the electric field is non-uniform, then there will be an imbalance of forces and the particle will experience a net force. The induced force on the particle is referred to as dielectrophoresis [7-12]. The direction of the dielectrophoretic force is towards the high field regions if the polarisibility of the particle is greater than the surroundings and away from the high field regions if the polarisibility of the particle is less than the surroundings as illustrated in figure 6.

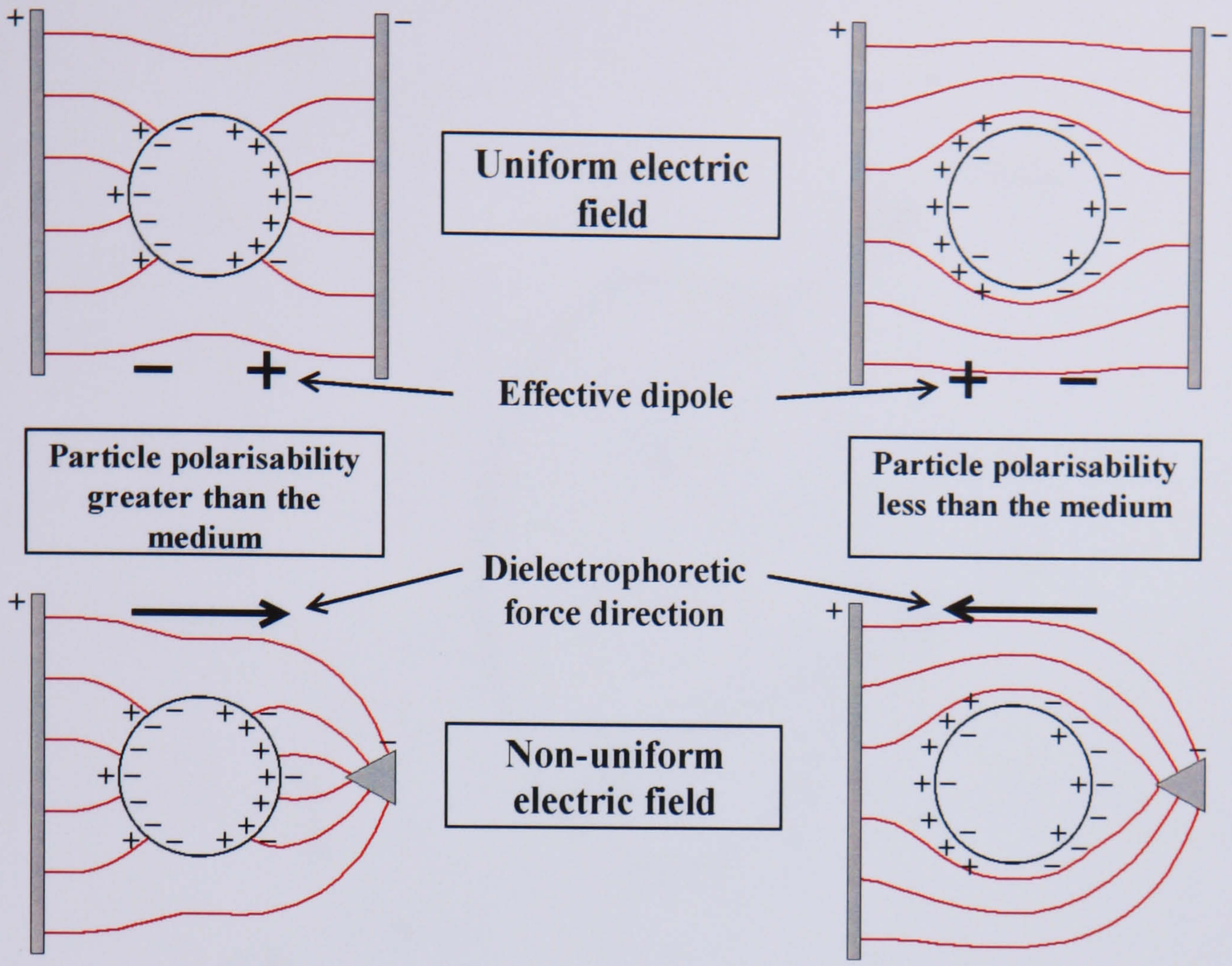

Figure 6. Schematic representation of the polarisation of a spherical particle in a dielectric medium in a uniform and in a non-uniform electric field. The case of a particle with polarisibility greater than the medium polarisibility is shown on the left and the case of a particle with polarisibility less than the medium polarisibility is shown on the right. When the electric field is uniform the forces on the charges in the dipole balance and there is no movement. But if the electric field is non-uniform there is an imbalance in the force on the charges in the dipole and the particles move in the direction of the dielectrophoretic force. If the particle polarisibility is greater than the medium, the force is in the direction of the high-field regions, in the case when particle polarisibility is less than the medium the force is towards low field regions.

2.5.1 Derivation of force on a particle

When a particle is subjected to conditions that causes it to experience a net dipole moment, it will have centres of positive and negative of charges that are equal but separated by a distance ***d*** as illustrated in figure 7. The electric field is assumed to contain no contributions from the dipole itself.

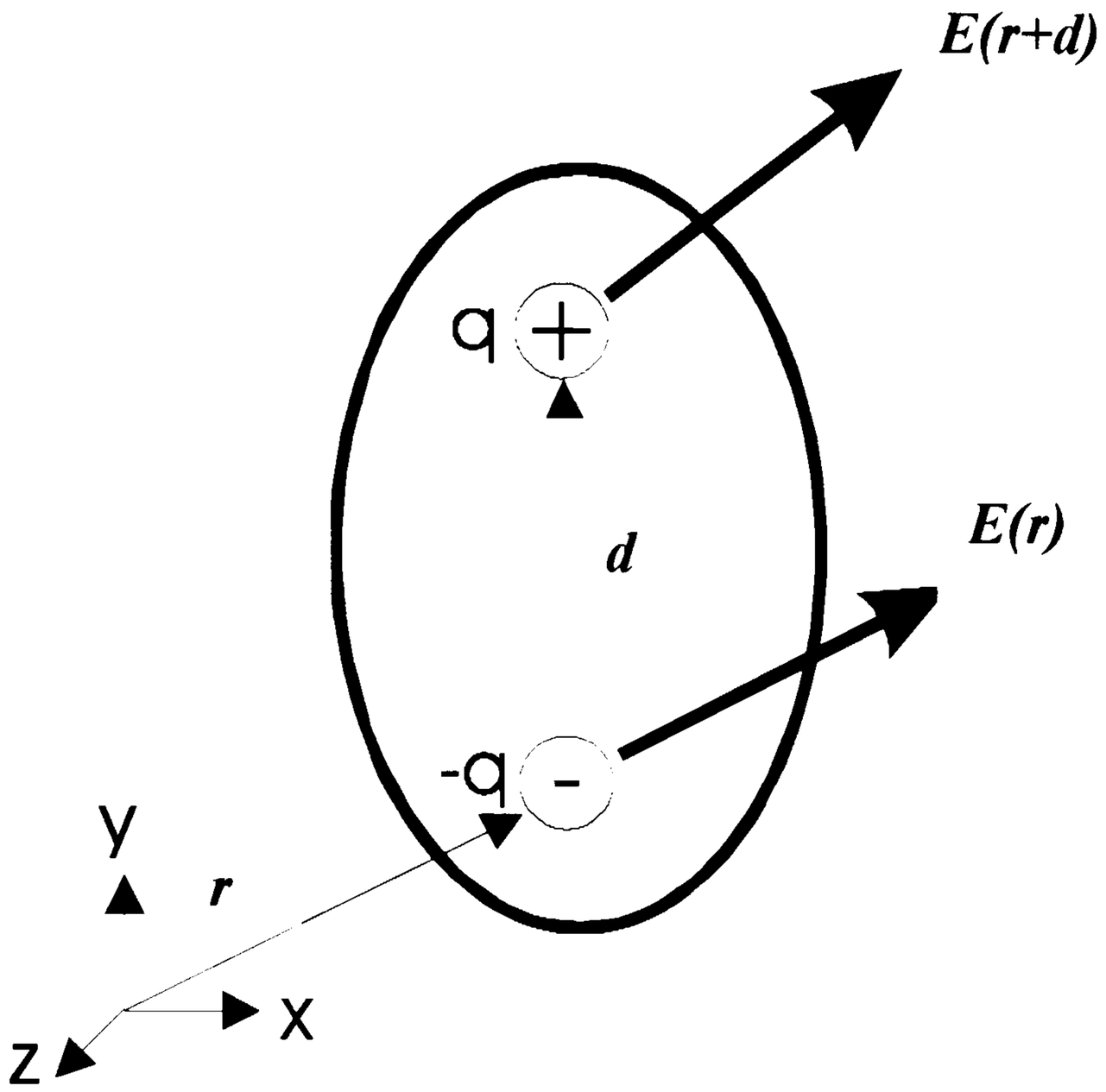

Figure 7: The net force on a small dipole given by $\boldsymbol{p} = q\boldsymbol{d}$ in a non-uniform electric field. The electric field vectors show the direction and magnitude of the electric field at the positive and negative charge.

If the electric is non-uniform then the positive and negative charges will experience different electric field strengths [6], giving rise to a total force on the particle of:

$$\boldsymbol{F} = q\boldsymbol{E}(\boldsymbol{r}+\boldsymbol{d}) - q\boldsymbol{E}(\boldsymbol{r}) \tag{53}$$

where $\bar{r}$ is the position vector of $-q$. For the case where the magnitude of $\boldsymbol{d}$ is small compared to the non-uniformity of the electric field, a Taylor series can be used to describe the electric field about the position $\boldsymbol{r}$ as:

$$\boldsymbol{E}(\boldsymbol{r}+\boldsymbol{d}) = \boldsymbol{E}(\boldsymbol{r}) + \boldsymbol{d}\cdot\nabla\boldsymbol{E}(\boldsymbol{r}) \tag{54}$$

where terms of order d^2 and higher are ignored. In this manner the force on the particle can be written as:

$$\boldsymbol{F} = q\bar{d} \cdot \nabla \boldsymbol{E} \tag{55}$$

From which the force on a dipole due to the applied electric field can be found:

$$\boldsymbol{F}_{dipole} = (\boldsymbol{p} \cdot \nabla)\boldsymbol{E} \tag{56}$$

The above derivation is usually accurate for calculations of the force on single particles in a non-uniform electric field where the dimensions of electrodes are usually much larger than that of the dielectric particle.

2.5.2 Time averaged dielectric force

We have shown that the instantaneous force on a dipole subjected to an applied electric field is given by:

$$\boldsymbol{F} = (\boldsymbol{p} \cdot \nabla)\boldsymbol{E} \tag{57}$$

If the force depends on time as a result of the electric field being time varying ($\boldsymbol{E} = \boldsymbol{E}_0 e^{j\omega t}$) the dipole moment will vary at the same angular velocity as the electric field, but will lag by an angle θ. The time-averaged force can be found using [6]:

$$\langle \boldsymbol{F} \rangle = \frac{1}{2}\mathrm{Re}\left[(\boldsymbol{p} \cdot \nabla)\boldsymbol{E}^*\right] \tag{58}$$

where $\boldsymbol{E}^*$ indicates the complex conjugate of $\boldsymbol{E}$.

The time-averaged force can be calculated using the vector identity that states that for two vectors $\boldsymbol{A}$ and $\boldsymbol{B}$:

$$\nabla(\boldsymbol{A}\cdot\boldsymbol{B}) = (\boldsymbol{B}\cdot\nabla)\boldsymbol{A} + (\boldsymbol{A}\cdot\nabla)\boldsymbol{B} + \boldsymbol{B}\times(\nabla\times\boldsymbol{A}) + \boldsymbol{A}\times(\nabla\times\boldsymbol{B}) \tag{59a}$$

If the vectors $\boldsymbol{A}$ and $\boldsymbol{B}$ are electric fields then by the Maxwell's equation that states that

$$\nabla\times\boldsymbol{E} = 0 \tag{59b}$$

then the vector identity becomes:

$$\nabla(\boldsymbol{A}\cdot\boldsymbol{B}) = (\boldsymbol{B}\cdot\nabla)\boldsymbol{A} + (\boldsymbol{A}\cdot\nabla)\boldsymbol{B} \tag{59c}$$

The electric field used was of the form:

$$\boldsymbol{E} = \boldsymbol{E}_0 e^{j(\omega t - \boldsymbol{k}\cdot\boldsymbol{x})} \tag{59d}$$

where $\boldsymbol{E}_0$ is real and depends only on position, t is time, ω is the angular velocity of the electric field, $\boldsymbol{k}$ is the wave number and $\boldsymbol{x}$ is the position of the vector.

Also we can write:

$$\nabla e^{j(\omega t - \boldsymbol{k}\cdot\boldsymbol{x})} = -j\boldsymbol{k}e^{j(\omega t - \boldsymbol{k}\cdot\boldsymbol{x})} \tag{59e}$$

According to equation (51) $\boldsymbol{p}$ is proportional to $\boldsymbol{E}$. The dipole moment can therefore be expressed as:

$$\boldsymbol{p} = \alpha(\omega)\boldsymbol{E} \tag{59f}$$

if $\alpha(\omega)$ is a scalar:

$$\alpha(\omega) = 4\pi\varepsilon_m a^3 K(\omega) \tag{59g}$$

Using the above relationships is written as [6-8]:

$$\begin{aligned}(\boldsymbol{p}\cdot\nabla)\boldsymbol{E}^{*} &= \alpha(\omega)e^{j(\omega t-\boldsymbol{k}\cdot\boldsymbol{x})}\{(\boldsymbol{E}_0\cdot\nabla)\boldsymbol{E}_0\}e^{-j(\omega t-\boldsymbol{k}\cdot\boldsymbol{x})} \\ &\quad + j\alpha(\omega)e^{j(\omega t-\boldsymbol{k}\cdot\boldsymbol{x})}(\boldsymbol{E}_0\cdot\boldsymbol{k})\boldsymbol{E}_0 e^{-j(\omega t-\boldsymbol{k}\cdot\boldsymbol{x})}\end{aligned} \tag{59h}$$

For transverse propagating electromagnetic fields:

$$\boldsymbol{E}_0\cdot\boldsymbol{k}=0 \tag{59i}$$

As a result:

$$(\boldsymbol{p}\cdot\nabla)\boldsymbol{E}^{*} = \alpha(\omega)e^{j(\omega t-\boldsymbol{k}\cdot\boldsymbol{x})}\{(\boldsymbol{E}_0\cdot\nabla)\boldsymbol{E}_0\}e^{-j(\omega t-\boldsymbol{k}\cdot\boldsymbol{x})} \tag{59j}$$

from which it can be shown that

$$(\boldsymbol{p}\cdot\nabla)\boldsymbol{E}^{*} = \alpha(\omega)(\boldsymbol{E}_0\cdot\nabla)\boldsymbol{E}_0 \tag{60a}$$

Using the same method it can be shown that

$$(\boldsymbol{p}^{*}\cdot\nabla)\boldsymbol{E} = \alpha(\omega)(\boldsymbol{E}_0\cdot\nabla)\boldsymbol{E}_0 \tag{60b}$$

which demonstrates that the position of the complex conjugate does not affect the final result.

Using the vector identity in equation (59c) and the results in equations (60a) and (60b), the time averaged can be shown to be:

$$\langle\boldsymbol{F}\rangle = 2\pi\varepsilon_m a^3\,\mathrm{Re}\{K(\omega)\}\nabla\boldsymbol{E}_0^2 \tag{61}$$

Where Re{ } indicates the real part of the Clausius-Mossotti factor. The sign of the real part of the Clausius-Mossotti can be either positive or negative. indicating that particles can be moved towards high or low field regions

2.6 Electrorotation

The action of an externally applied electric field on a dielectric particle results in the particle experiencing an induced dipole moment. Initially the dipole moment will not be aligned with the electric field vector and a time delay clearly exists between the establishment of the field and the dipole. The induced dipole moment vector tries to align itself with the electric field vector, giving rise to a torque on the particle. In a static electric field the induced dipole will quickly be able to align itself with the electric field, causing the torque to disappear rapidly. However, if the electric field is rotating, the dipole will continuously be attempting to align itself with the electric field vector. As a result, a dielectric particle exposed to a rotating electric field will experience a continuous torque [6, 13, 14].

When a particle such as a cell is suspended in a dielectric medium and is exposed to a rotating electric field it experiences an induced dipole moment. There will be a phase difference between the field vector and the dipole moment vector resulting in the particle experiencing a torque tending to align the particle's polarisation vector with the field. This torque is zero when the phase angle between the particle's polarisation vector and the applied field is zero and maximum when the phase angle is $\pm 90^0$. If the induced dipole moment lags behind the field then the direction of rotation is with the field and vice versa for a moment that leads the field. A theoretical treatment of this effect can be found in a number of publications [9, 15-18].

2.6.1 Derivation of torque on a particle

Consider a particle that is exposed to an externally applied electric field that causes the particle to have centres of positive and negative charge equal in magnitude but separated by a distance ***d***, as illustrated in figure 8(a). The centres of positive and negative charge give rise to a dipole moment. Initially this dipole moment will not be aligned with the electric field, causing the dipole to experience a torque. The torque is caused by the centres of positive and negative

charge experiencing a force ($\boldsymbol{F} = q\boldsymbol{E}$) that are equal in magnitude but that act in opposite directions. These forces causes the dipole to experience a torque and therefore to align with the electric field.

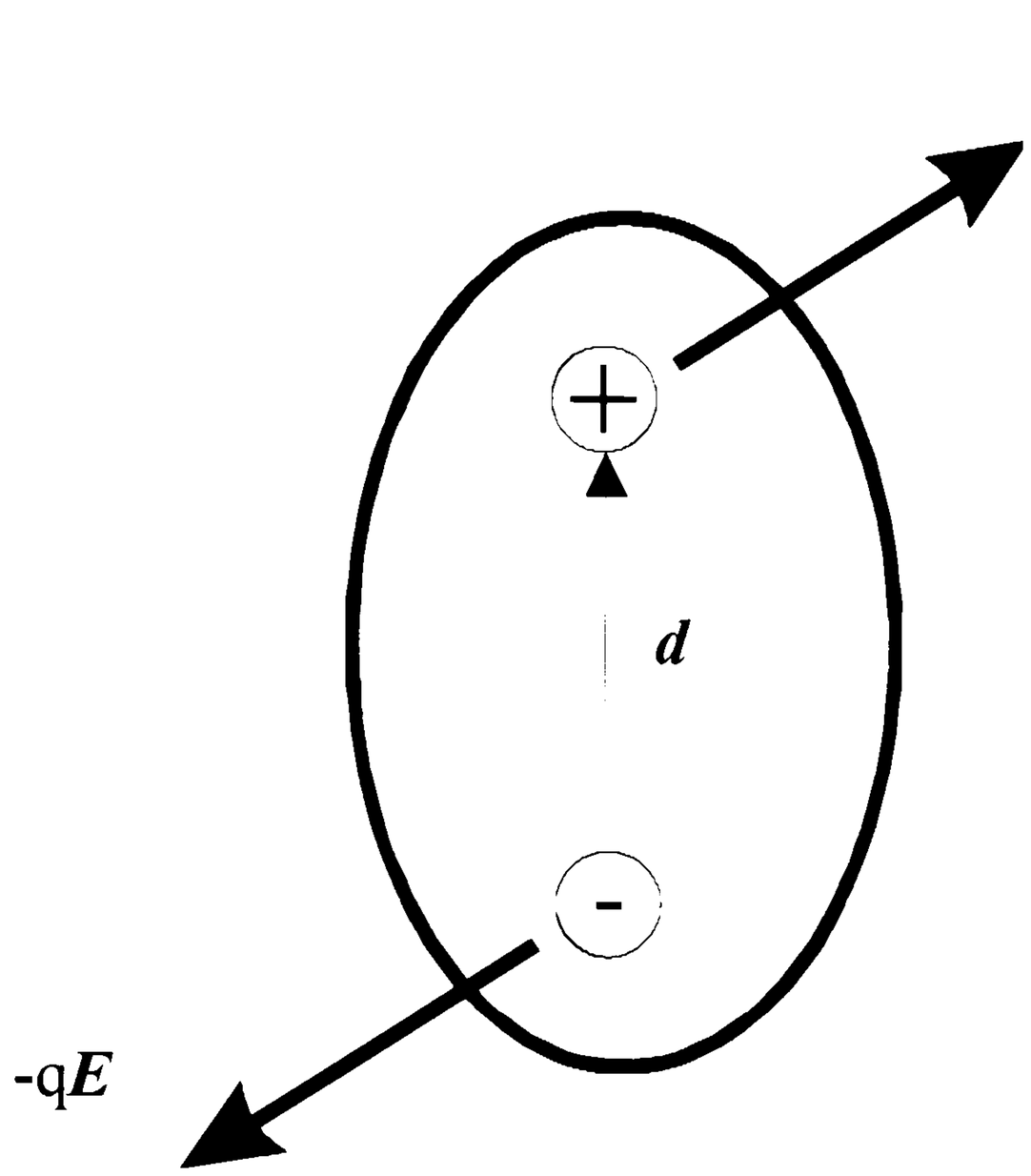

Figure 8(a): Force components creating a net torque on a small dipole given by $\boldsymbol{p} = q\boldsymbol{d}$ in an electric field. The positive and negative charges generate forces in opposite directions, these forces generate a torque as the dipole tries to align itself with the electric field.

The net torque exerted by an applied electric field on an infinitesimal dipole can be found by considering the net force acting about the centre of a small dipole [6]. Each of the charges contributes to the torque:

$$\Gamma = \frac{\boldsymbol{d}}{2} \times q\boldsymbol{E} + \frac{-\boldsymbol{d}}{2} \times \left(-q\boldsymbol{E}\right) = q\boldsymbol{d} \times \boldsymbol{E} \tag{62}$$

From which the torque on a dipole due to an applied electric field can be found:

$$\Gamma_{dipole} = \boldsymbol{p} \times \boldsymbol{E} \tag{63}$$

The above derivation is usually accurate for calculations of the torque on particles in an electric field where the dimensions of the electrode are usually much larger than that of the dielectric particle. From the expression of the torque it can also be seen that the torque does not depend on the gradient of the electric field, so that it is possible to generate a torque as long as the electric field vector and the dipole moment vectors are not parallel.

2.6.2 Time averaged torque

We have shown that the instantaneous torque on a dipole subjected to an applied electric field is given by:

$$\Gamma = \boldsymbol{p} \times \boldsymbol{E}$$

If the torque depends on time as a result of the electric field being time varying (of the form $\boldsymbol{E} = \boldsymbol{E}_0 e^{j\omega t}$, where $\boldsymbol{E}_0$ depends on position only), then the dipole moment will rotate at the same angular velocity as the electric field. But the dipole moment and the electric field will be separated by an angle θ as illustrated in figure 8(b).

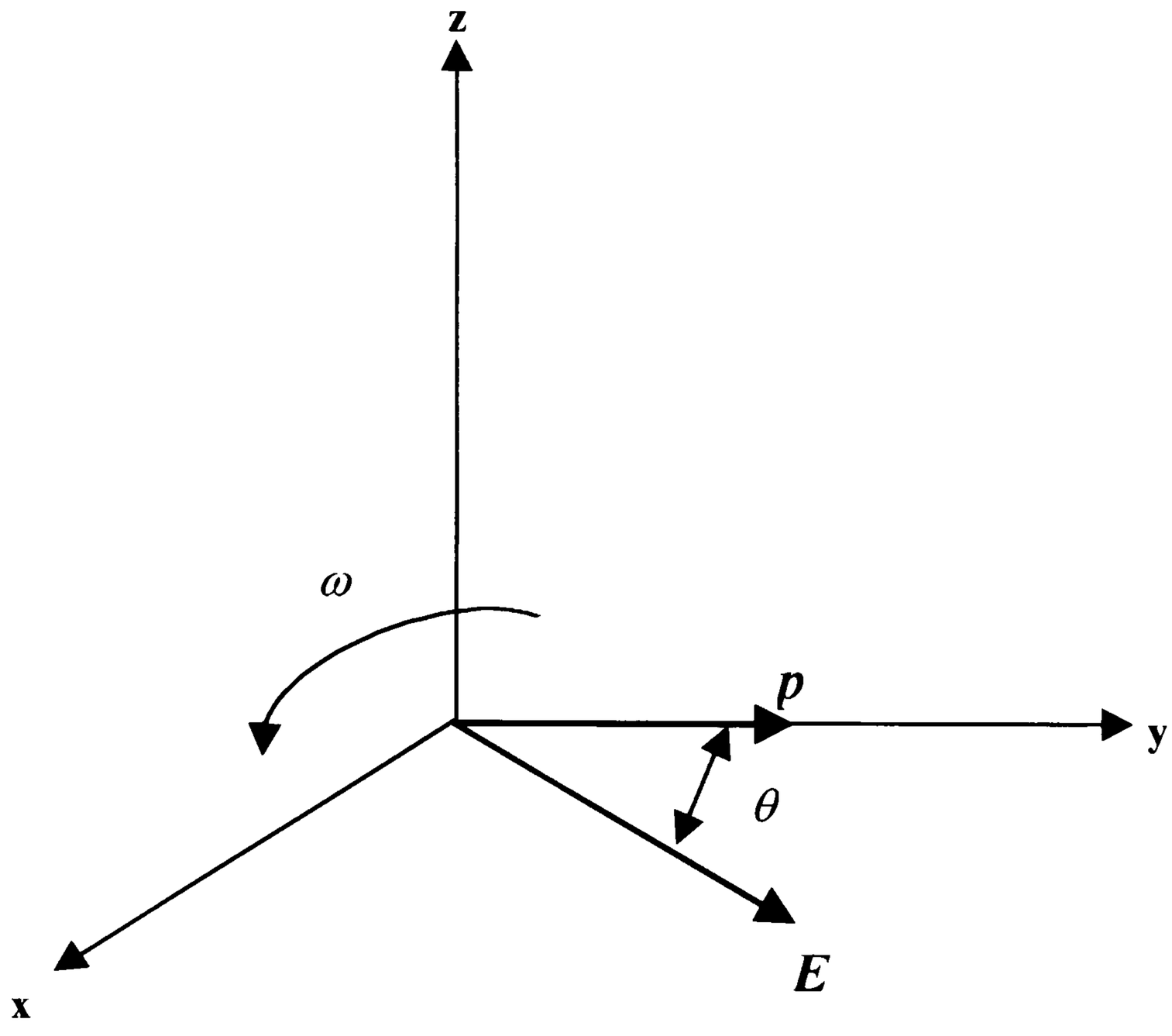

Figure 8(b): Illustration of a dipole moment generated by an externally applied electric field in a Cartesian co-ordinate system. The torque exerted on a dipole $\boldsymbol{p}$ is dependent on the electric field strength $\boldsymbol{E}$ as well as the angle between the two vectors. The direction of rotation depends on phase angle between the electric field and the dipole moment. The angle θ is in the sense of the rotation of $\boldsymbol{p}$ to $\boldsymbol{E}$.

The time-averaged torque can be found using [6]:

$$\langle \Gamma \rangle = \frac{1}{2} \mathrm{Re}\left[\boldsymbol{p} \times \boldsymbol{E}^{*} \right] \tag{64}$$

where $\boldsymbol{E}^{*}$ indicates the complex conjugate of $\boldsymbol{E}$. This then becomes

$$\langle \Gamma \rangle = |\boldsymbol{p}| \boldsymbol{E}_0 \sin\theta \hat{\boldsymbol{z}} \tag{65}$$

Using the expression for the effective polarisibility as given by equation (51) the magnitude of the time averaged torque becomes:

$$\Gamma = 4\pi\varepsilon_m a^3 \left|K(\omega)\right| \boldsymbol{E_0}^2 \sin\theta \tag{66}$$

For which the angle θ is given by:

$$\theta = -\sin^{-1}\left(\frac{\mathrm{Im}\{K(\omega)\}}{\left|K(\omega)\right|}\right) \tag{67a}$$

i.e.:

$$\sin\theta = -\frac{\mathrm{Im}\{K(\omega)\}}{\left|K(\omega)\right|} \tag{67b}$$

It can thus be shown that the time averages torque is as given by [17]:

$$\Gamma = -4\pi\varepsilon_m a^3 \,\mathrm{Im}\{K(\omega)\}\boldsymbol{E_0}^2 \tag{68}$$

Where Im{ } indicates the imaginary part of the Clausius-Mossotti factor. The sign of the imaginary part of the Clausius-Mossotti factor can be either positive or negative, depending on whether the dipole moment vector leads or lags the electric field vector.

2.6.3 Steady state rotation rate

When a particle, suspended in a dielectric medium, rotates it will also experience a drag force. When a spherical particle is rotating in a medium it is subjected to a viscous drag that is characterised by a friction coefficient. This depends on the viscosity of the medium and the geometry and surface properties of the particle. For slow rotation rates (a few $rads^{-1}$) the frictional torque for a spherical stationary body rotating about its own centre can be obtained [19, 20]:

$$F_{drag} = 8\pi a^3 \eta \tag{69}$$

where η is the viscosity of the medium. The viscous drag is proportional the rate of rotation of the sphere $R(\omega)$, i.e.:

$$\Gamma_{drag} = R(\omega)F_{drag} \tag{70}$$

The speed of steady state rotation is limited by the viscous drag, as a result the steady state rotation is then given by:

$$R(\omega) = \frac{\Gamma_{dipole}}{F_{drag}} \tag{71}$$

Solving this expression using the full expression for induced torque gives the steady state rotation rate:

$$R(\omega) = -\frac{\varepsilon_m Im\left(\frac{\varepsilon_p^* - \varepsilon_m^*}{\varepsilon_p^* + 2\varepsilon_m^*}\right)\boldsymbol{E}^2}{2\eta} \tag{72}$$

This is the rotational velocity of a particle exposed to a rotating electric field. The rotation rate is dependent on the frequency of the applied electric field through the Clausius-Mossotti factor. A particle will experience rotation described by equation (72) as long as the approximations invoked in the derivation of the Clausius-Mossotti factor holds.

2.7 Modelling dielectric particles

2.7.1 Spherical dielectric models

A heterogeneous particle can be described by a model that takes into account the makeup of the particle. Biological cells often consist of different compartments that have distinct dielectric properties. Cells might consist of a nucleus, a nuclear membrane, the cytoplasm and a plasma membrane; such a system can be considered to consist of several layers of concentric spherical shells, as illustrated by figure 9. Each of the shells has a distinct complex permittivity given by $\varepsilon_i^* = \varepsilon_i - j\frac{\sigma_i}{\omega}$ and a distinct radius a_i $(i = 1,2,\cdots,N+1)$; with $i = 1$ corresponding to the innermost layer. A smeared out sphere model [15, 21-23] can be used to describe the effective complex permittivity of such a particle.

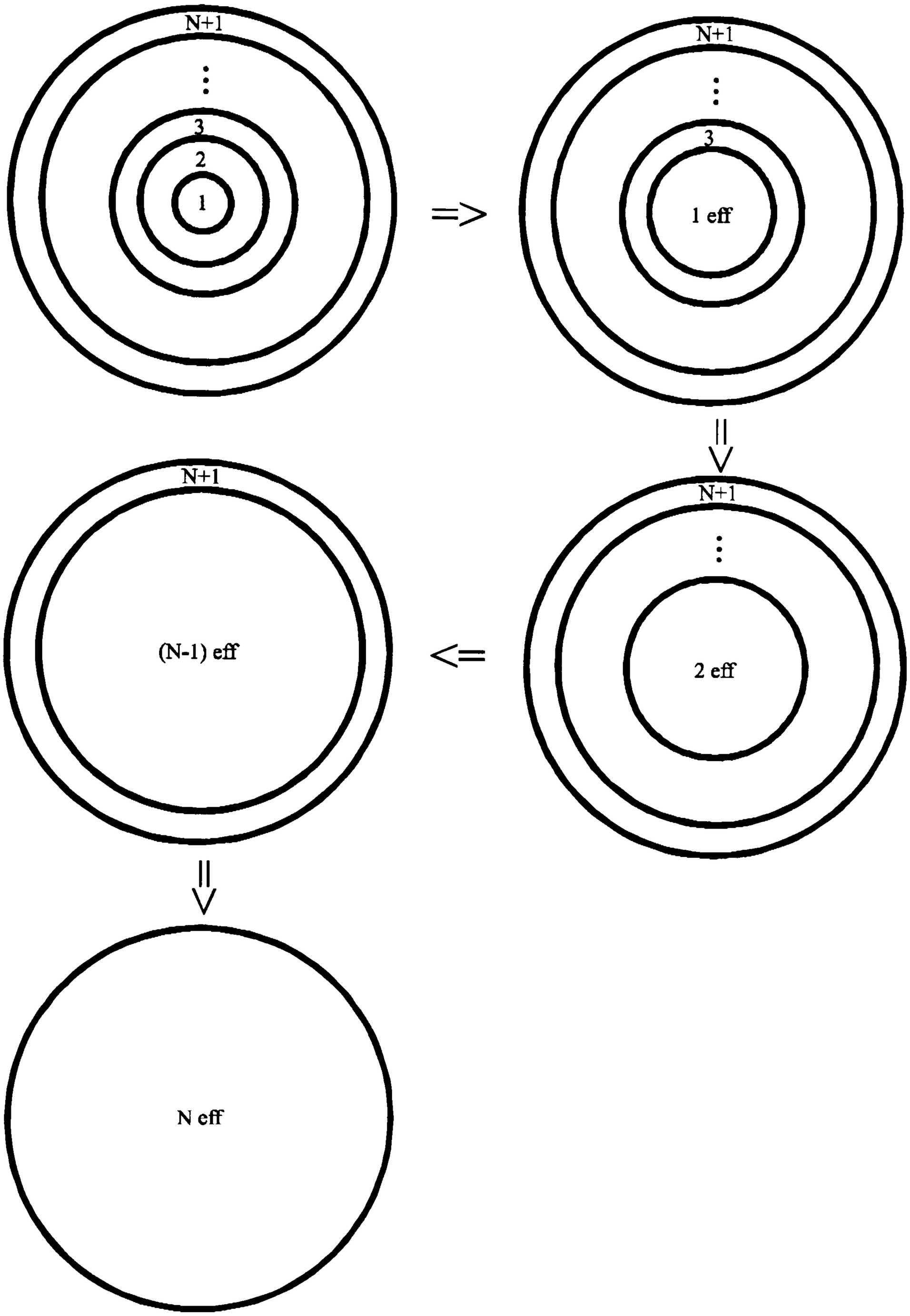

Figure 9: A smeared out spherical shell approach used to determine the effective permittivity of a sphere consisting of *N* shells. The stepwise simplification of an *N* shelled sphere by repeated iterations to a homogeneous sphere with an effective complex permittivity that mimics the dielectric properties of a sphere.

In order to obtain the effective permittivity of a smeared out shell model, the N shelled particle is replaced by a $(N-1)$ shell particle, with the innermost sphere and the first spherical shell being replaced by a sphere with complex permittivity of:

$$\varepsilon_{1eff}^{*} = \varepsilon_{2}^{*}\frac{\left(\frac{a_2}{a_1}\right)^3 + 2\frac{\varepsilon_1^{*}-\varepsilon_2^{*}}{\varepsilon_1^{*}+2\varepsilon_2^{*}}}{\left(\frac{a_2}{a_1}\right)^3 - \frac{\varepsilon_1^{*}-\varepsilon_2^{*}}{\varepsilon_1^{*}+2\varepsilon_2^{*}}} \tag{73}$$

$$= S\left(\varepsilon_1^{*}, \varepsilon_2^{*}, a_1, a_2\right) \tag{74}$$

where the function S is defined as

$$S(a,b,c,d) = b\frac{\left(\frac{d}{c}\right)^3 + 2\frac{a-b}{a+b}}{\left(\frac{d}{c}\right)^3 + 2\frac{a-b}{a+b}} \tag{75}$$

The next step is to replace the $N-1$ particle by a $N-2$ particle, for which the effective complex permittivity would be given by:

$$\varepsilon_{2eff}^{*} = \varepsilon_{3}^{*}\frac{\left(\frac{a_3}{a_2}\right)^3 + 2\frac{\varepsilon_{1eff}^{*}-\varepsilon_3^{*}}{\varepsilon_{1eff}^{*}+2\varepsilon_3^{*}}}{\left(\frac{a_3}{a_2}\right)^3 - \frac{\varepsilon_{1eff}^{*}-\varepsilon_3^{*}}{\varepsilon_{1eff}^{*}+2\varepsilon_3^{*}}} \tag{76}$$

$$= S\left(\varepsilon_{1eff}^{*}, \varepsilon_3^{*}, a_2, a_3\right) \tag{77a}$$

$$= S\left(\left(\varepsilon_1^{*}, \varepsilon_2^{*}, a_1, a_2\right), \varepsilon_3^{*}, a_2, a_3\right) \tag{77b}$$

Repeating this procedure $N-2$ times, allows the particle of N shells to be replaced by an equivalent smeared out shell model with an effective complex permittivity given by:

$$\varepsilon^*_{peff} = \varepsilon^*_{Neff} \frac{\left(\frac{a_{N+1}}{a_N}\right)^3 + 2\frac{\varepsilon^*_{N-1eff} - \varepsilon^*_{N+1}}{\varepsilon^*_{N-1eff} + 2\varepsilon^*_{N+1}}}{\left(\frac{a_{N+1}}{a_N}\right)^3 - \frac{\varepsilon^*_{N-1eff} - \varepsilon^*_{N+1}}{\varepsilon^*_{N-1eff} + 2\varepsilon^*_{N+1}}} \quad (78)$$

For which the function S becomes:

$$= S\left(S\left(S\left(\ldots S\left(\varepsilon^*_1, \varepsilon^*_2, a_1, a_2\right)\ldots\right), \varepsilon^*_N, a_{N-1}, a_N\right), \varepsilon^*_{N+1}, a_N, a_{N+1}\right) \quad (79)$$

This is the general expression for the effective complex permittivity of a particle consisting of an inner sphere surrounded by *N* concentric shells.

The derivation of the Clausius-Mossotti factor and also of the dielectrophoretic force and the electrorotational torque is based on a model of a homogeneous dielectric sphere suspended in a dielectric medium. It has been shown by Huang et al [15] that if a heterogeneous sphere can be described by the smeared out shell model, then the approach for deriving the Clausius-Mossotti factor for a homogeneous sphere can be used for a multi-shelled particle.

2.7.2 Elliptical shell model

The expression for torque exerted on a spherical dielectric particle can be extended to describe the torque induced on a spherical particle with an arbitrary number of shells. In some cases it is not sufficient to consider the case of a spherical particle and more complex models are needed for elliptical particles.

The elliptical particle consists of a multi-shelled ellipse immersed in a dielectric medium as shown in figure 10. The complex permittivity of the medium and the confocal shells are denoted ε^*_{med} and ε^*_i respectively. An elliptical co-ordinate system is introduced by assuming that the outermost surface of the ellipse is a standard ellipsoid with semi-axes a_0. b_0, c_0:

$$\left(\frac{x^2}{a_0^2+\xi}\right)+\left(\frac{y^2}{b_0^2+\xi}\right)+\left(\frac{z^2}{c_0^2+\xi}\right)=1 \qquad (80)$$

where ξ represents a family of surfaces of confocal ellipsoids. When $\xi = 0$ and $\xi = \delta_i$, the above equation represents the outermost and *i*th surfaces respectively.

The semi-axes of the *i*th surface is given by:

$$a_i = (a_0 - \delta_i)^{1/2} \quad b_i = (b_0 - \delta_i)^{1/2} \quad c_i = (c_0 - \delta_i)^{1/2} \qquad (81)$$

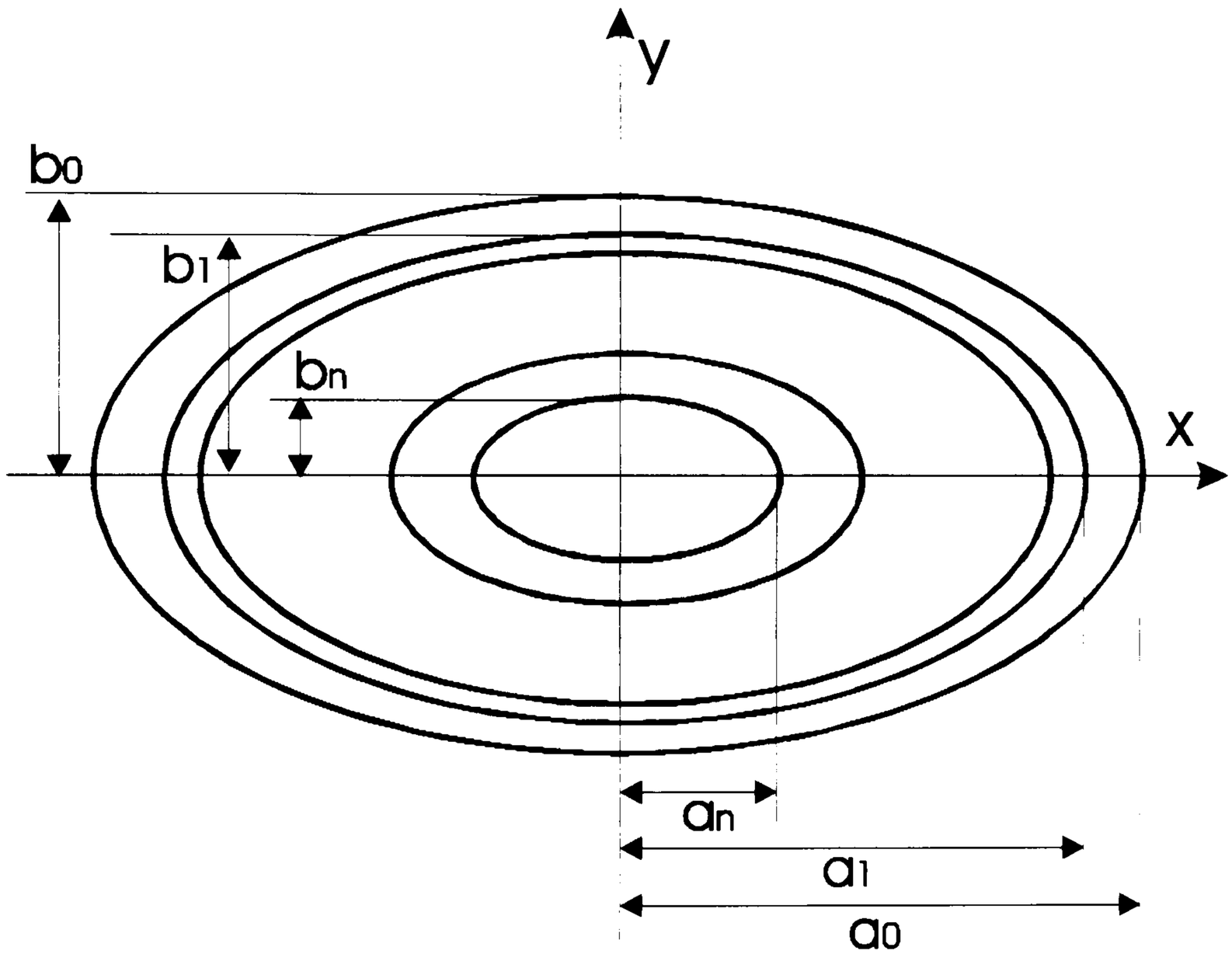

Figure 10: Cross section of a multi shelled ellipse in the x-y plane. The semi-axes for the different shells are given for both the x and the y axes. The innermost shell is given by a_n and b_n, while the outermost shell is described by a_0 and b_0.

It has been shown that [20, 24] for $\alpha = x, y$ the susceptibility of an ellipsoid is given by:

$$\chi_\alpha(\omega) = \frac{\varepsilon^*_{peff} - \varepsilon^*_m}{\left(\varepsilon^*_{peff} - \varepsilon^*_m\right)A_{i\alpha} + \varepsilon^*_m} \tag{82}$$

where $A_{i\alpha}$ is the depolarisation factors along the x and y axes given by:

$$A_{ix} = 0.5 a_i b_i c_i \int_\xi^\infty \frac{d\xi}{(a_i + \xi)R_i} \; A_{oy} \tag{83}$$

$$A_{iy} = 0.5 a_i b_i c_i \int_\xi^\infty \frac{d\xi}{(b_i + \xi)R_i} \tag{84}$$

with

$$R_i = \left\{(a_i^2 + \xi)(b_i^2 + \xi)(c_i^2 + \xi)\right\}^{1/2} \tag{85}$$

These factors can be derived for prolate particles with $a_i > b_i = c_i > 0$ and for oblate particles $a_i = b_i > c_i > 0$ [20]. The term ε^*_{peff} is the effective complex permittivity of a multi-shelled ellipsoid along the $\alpha = x, y$ axes, giving:

$$\varepsilon^*_{peff(\alpha)} = \varepsilon^*_1 \frac{\varepsilon^*_1 + \left(\varepsilon^*_{eff\,2} - \varepsilon^*_1\right)\left[A_{1\alpha} + \nu_1\left(1 - A_{0\alpha}\right)\right]}{\varepsilon^*_1 + \left(\varepsilon^*_{eff\,2} - \varepsilon^*_1\right)\left(A_{1\alpha} + \nu_1 A_{0\alpha}\right)} \tag{86}$$

where $\varepsilon^*_{eff\,2}$ is the resulting effective complex permittivity of the innermost ellipsoids. The effective permittivity of the remaining layers can be obtained using:

$$\varepsilon^*_{eff(i),(\alpha)} = \varepsilon^*_i \frac{\varepsilon^*_i + \left(\varepsilon^*_{eff(i+1)} - \varepsilon^*_i\right)\left[A_{i\alpha} + \nu_i\left(1 - A_{i-1,\alpha}\right)\right]}{\varepsilon^*_i + \left(\varepsilon^*_{eff(i+1)} - \varepsilon^*_i\right)\left(A_{i\alpha} + \nu_1 A_{i-1,\alpha}\right)} \quad i = 2,\ldots,n-2 \tag{87}$$

$$\varepsilon^*_{eff(n-1),(\alpha)} = \varepsilon^*_{n-1} \frac{\varepsilon^*_{n-1} + \left(\varepsilon^*_n - \varepsilon^*_{n-1}\right)\left[A_{n-1,\alpha} + \nu_{n-1}\left(1 - A_{n-2,\alpha}\right)\right]}{\varepsilon^*_{n-1} + \left(\varepsilon^*_n - \varepsilon^*_{n-1}\right)\left(A_{n-1,\alpha} + \nu_{n-1} A_{n-2,\alpha}\right)} \tag{88}$$

In the above

$$\nu_i = \frac{a_i b_i c_i}{a_{i-1} b_{i-1} c_{i-1}} \tag{89}$$

For an elliptical dielectric particle placed in a sinusoidally varying external electric field E, the time-averaged torque is given by [20]:

$$\Gamma_e = 0.5 \mathrm{v}_c \varepsilon_m \, \mathrm{Im}\left(\chi_x(\omega) + \chi_y(\omega)\right) \boldsymbol{E}_0^{\,2} \tag{90}$$

where v_c is the volume of the ellipsoid, ε_m is the permittivity of the medium, and $\chi_x(\omega)$ and $\chi_y(\omega)$ are the x and y components of the susceptibility of the ellipse and $\mathrm{Im}\{\ \}$ indicates the imaginary part of.

The steady state rotation rate of the ellipse can be found by calculating the viscous frictional torque of the particle. It depends on the rotation rate of the ellipsoid, and steady state rotation rate is given by:

$$R(\omega) = \frac{\Gamma_e}{D_f} \tag{91}$$

where D_f is a factor characterising the hydrodynamic resistance to rotation of the particle. The hydrodynamic resistance is found using [20]:

$$D_f = 2V_c \eta \left\{ \frac{\left(a_0^2 + b_0^2\right)}{a_0^2 A_{ox} + b_0^2 A_{0y}} \right\} \tag{92}$$

where η is the viscosity of the medium, a_0 and b_0 are the x and y dimensions of the particle respectively. The terms A_{ox} and A_{oy} are the depolarisation factors of the particle along the x- and y-axis.

2.7.3 *Mixture theory*

The case of a dielectric system consisting of separate dielectric bodies contained within the same volume, is illustrated in figure 11.

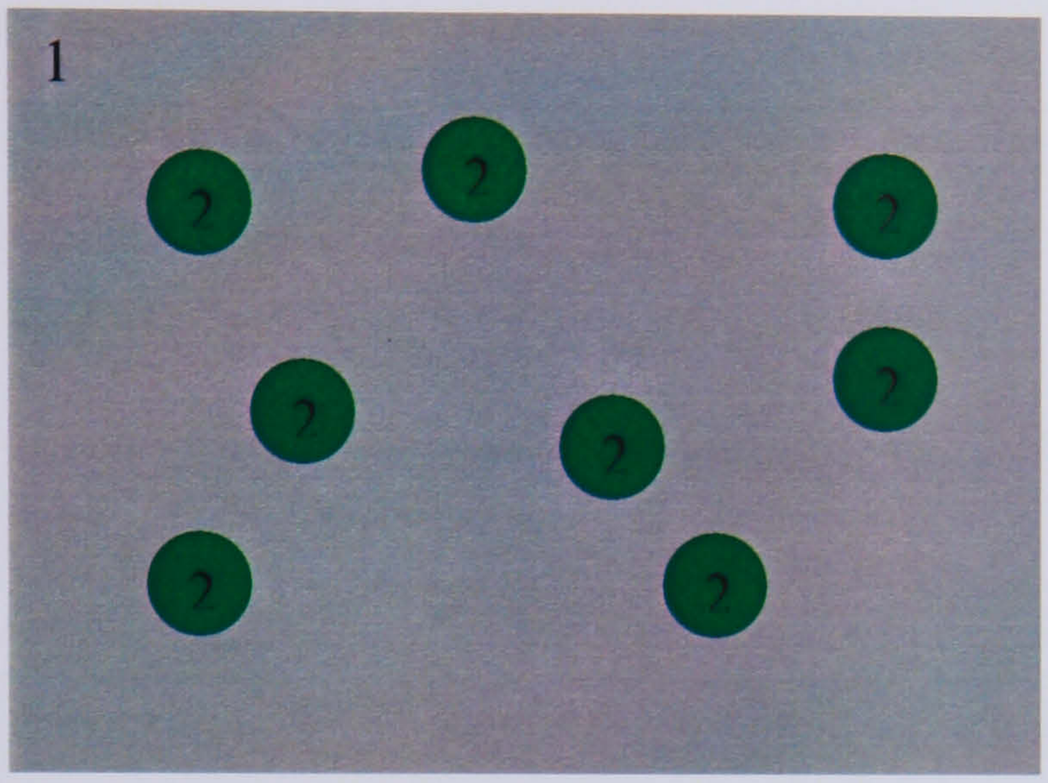

Figure 11: Illustration of a heterogeneous dielectric system in which a number of distinct dielectric bodies ('2') are contained within a homogeneous dielectric ('1').

In such a case standard dielectric mixture theory can be employed to find the complex permittivity of the mixture [25-27]:

$$\varepsilon_{mix}^{*} = \varepsilon_1^{*} \frac{\left(2\varepsilon_1^{*} + \varepsilon_2^{*}\right) - 2\rho\left(\varepsilon_1^{*} - \varepsilon_2^{*}\right)}{\left(2\varepsilon_1^{*} + \varepsilon_2^{*}\right) + \rho\left(\varepsilon_1^{*} - \varepsilon_2^{*}\right)} \tag{93}$$

The subscripts '1' refers to the main dielectric and '2' refers to the dielectric body to the two distinct dielectrics and ρ is the volume fraction of the second dielectric body:

$$\rho = \frac{\upsilon_1}{\upsilon_2} \tag{94}$$

for volumes υ_1, υ_2; υ_1 is the total volume, while υ_2 is the total volume of all the small dielectric bodies. With the use of equation (93), measurements of the

dielectric properties of the mixture can be used to obtain the dielectric properties of the suspended bodies '2'.

2.7.4 Curve fitting

The electrorotational spectrum of a particle is obtained by observing the frequency dependent rotation of a particle subjected to a rotating electric field. The electrorotational spectrum is a complex non-linear function of a particle's dielectric properties and the experimental conditions. In order to obtain the dielectric parameters from an electrorotational spectrum curve fitting procedures have to be employed [28].

The process involves fitting the equation for steady state rotation rate to a model that predicts the dielectric parameters of a particle as given by the smeared out shell model. In the equation for the steady state rotation rate a new factor A is introduced:

$$R(\omega) = -\frac{\varepsilon_m Im\left(\frac{\varepsilon_p^* - \varepsilon_m^*}{\varepsilon_p^* + 2\varepsilon_m^*}\right)\boldsymbol{E}^2}{2\eta} A \tag{96}$$

The factor A is a scaling factor that takes into account that neither the viscosity of the medium (η), nor the electric field strength ($\boldsymbol{E}$) are precisely known. In addition the particle might be in contact with the electrode surface, in which case surface friction also affects the steady state rotation rate.

The curve fitting procedures were carried out using an algorithm that minimises the sum of the deviations between the experimental rotation spectrum ($R_{expt}(\omega_i)$) and the spectrum predicted by the smeared out shell model of a cell with a steady state rotation rate ($R_{est}(\omega_i)$) [28]. For i data points this function can be written as:

$$Min\left\{\sum_i \left(R_{expt}(\omega_i) - R_{est}(\omega_i)\right)^2\right\} \qquad (97)$$

The minimisation was carried out with a routine capable of minimising a function with up to five variables. The routine uses a non-linear Nelder-Mead simplex method [29, 30], part of Matlab® software (Mathworks, Illinois). The Nelder-Mead method minimises a function of n variables. In this case the function is the difference between data points predicted by equation (96) and data points obtained from experiments as expressed by equation (97). The minimisation procedure depends on the comparison of function values at the (n+1) vertices of a general simplex in factor-space, followed by the replacement of the vertex with the highest value by another point. By repeated iterations of this process the simplex adapts itself to the local landscape and contracts to a final minimum. This process in carried out, at each step in the search, by generating a new point in or near the current simplex and, provided it has a smaller value then one of the existing vertices, one of the current vertices is replaced by the new point, giving a new vertex. This step is then repeated until the diameter of the simplex is less than a specified tolerance.

2.7.5 Electric field distribution in electrodes

In both dielectrophoresis and electrorotation experiments, a.c. electric fields are used to manipulate and characterise particles. In order to predict and analyse the movement of a dielectric particle in an electric field it is important to know the electric field configuration. Several authors have simulated the electric fields generated by different types of electrorotation electrodes using numerical techniques. Gimsa *et al* [31] and Holzel [32] used time invariant methods to obtain the electric field generated by polynomial electrodes. However, the most accurate work to date on electrorotational electrodes has been carried out by Hughes *et al* [33], who included the effect of phase distributions in their work. Hughes [34] also simulated the time varying electric fields generated by other electrode configurations such as, amongst others, bone shaped and point electrodes. On the basis of these simulations it was observed that electric fields generated by polynomial electrodes offer the best overall geometry for use in

electrorotational studies. Green *et al* [35] looked at electrodes used for dielectrophoretic manipulation of bioparticles using finite element field simulation software.

(a) Electrorotation

Computer simulations performed by Hughes [34] found that polynomial electrodes have the best overall characteristics for use in electrorotation, and therefore these electrodes were used in electrorotational work undertaken in this thesis.

The polynomial electrodes used were defined in a x-y plane by the expression [36, 37]:

$$\left|x^2 + y^2\right| = k^2 \tag{95}$$

where $2k$ is the distance between the electrode tips as shown in figure 12.

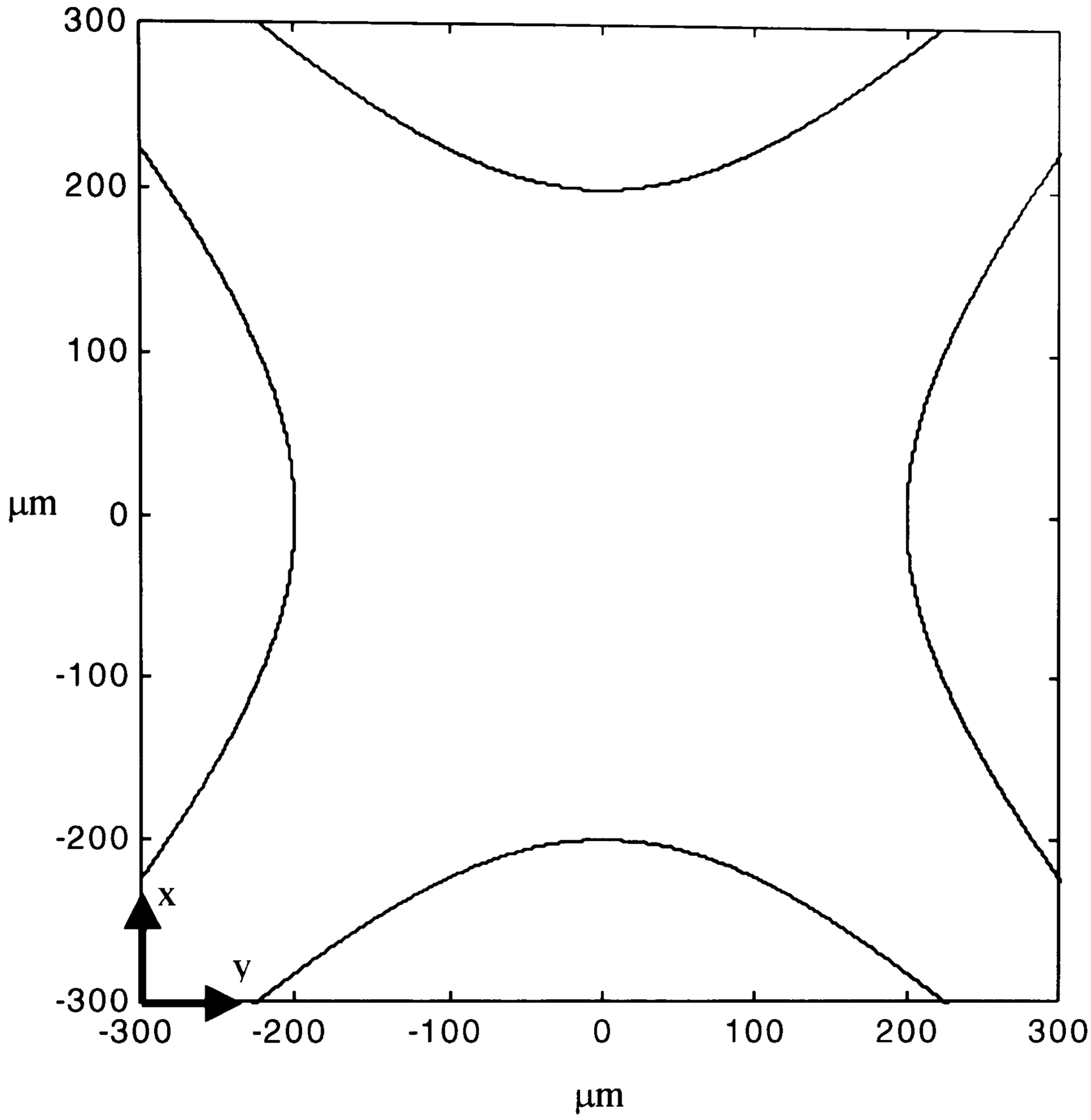

Figure 12: Plot of the central region of a polynomial electrode in an x-y plane where the distance from tip to tip is 400μm. Electrodes used for electrorotation experiments were of this type, electrodes with a gap of 800μm were also used.

From the electric field simulations undertaken by Hughes *et al* [33], it has been shown that polynomial electrodes generate a higher torque (19%) per volt applied to the electrodes compared to circular electrodes. In the central region of the polynomial electrodes there is a smaller area of uniform torque, but outside this area the electric field deviation and hence any dielectrophoretic force is smaller in polynomial electrodes compared to circular electrodes. Polynomial electrodes have a circular region of uniform torque that is about 0.4 times the

distance between the electrode tips in diameter taken from the centre of the electrodes. Outside this area the torque changes rapidly with position [33].

When employing electrorotational spectroscopy the position of a particle within the electrode pattern affects the rotation rate. In order to obtain consistent results a particle should not move when obtaining the rotational spectrum. It is therefore important to be aware that in polynomial electrodes, particles outside an area about 0.6 times the distance between the electrode tips will experience a dielectrophoretic force that can be strong enough to cause particles to move. In this case the movement of particles will cause the rotation rate of particles to change with position.

(b) Dielectrophoresis

Electrodes used for dielectrophoresis experiments generate a large region of strong electric field. Two types of electrode patterns have been employed [37, 38]. They are referred to as castellated and sawtooth electrodes. Of these two types, the sawtooth electrodes give the strongest electric field and also the largest region of high electric fields. Such electrodes are illustrated in figure 13.

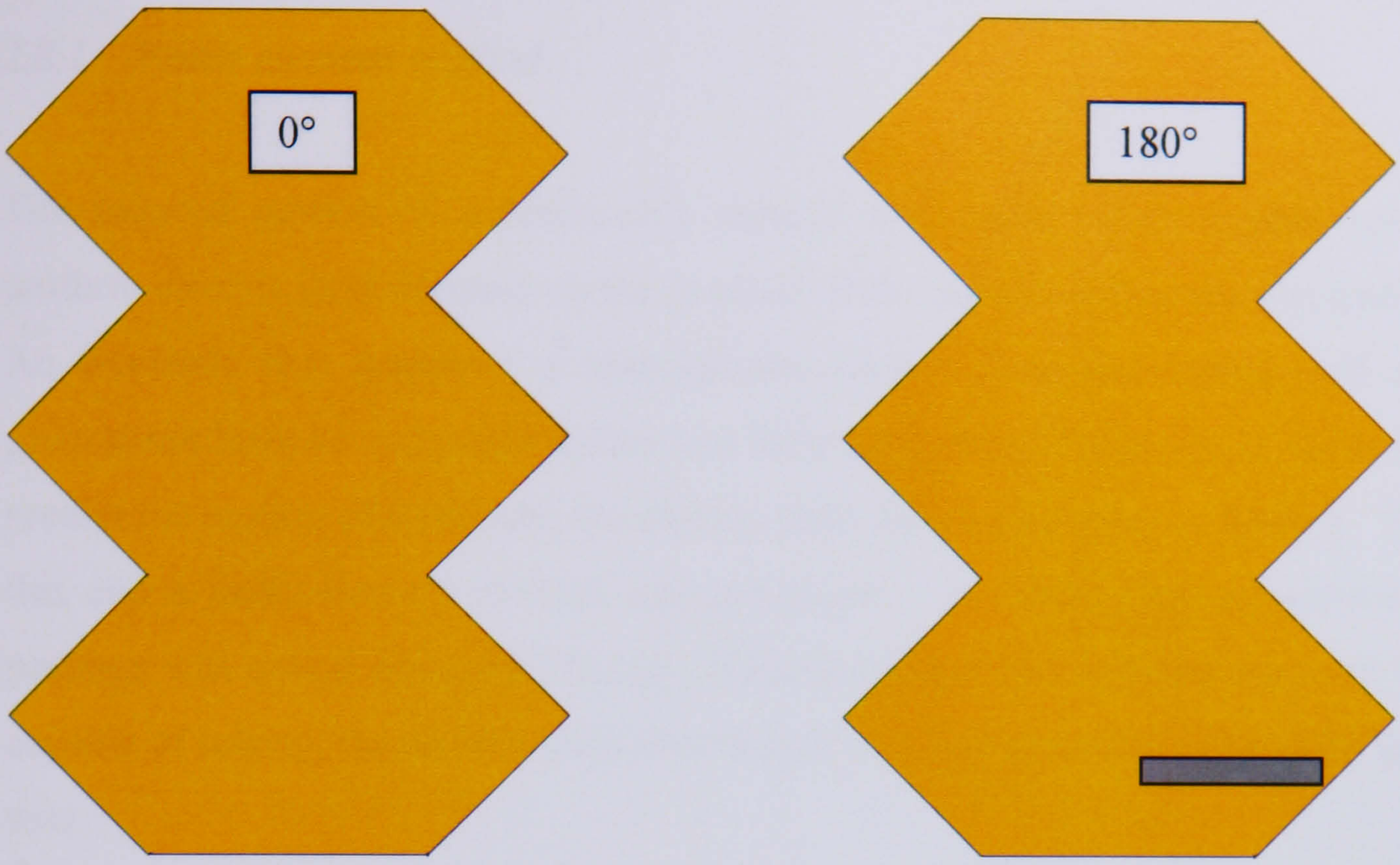

Figure 13: Pattern of a sawtooth electrode, with rectangular features. Scale bar: 100μm. The high field regions are situated between the electrode tips as well as along the electrode edges.

2.8 Electric field simulation

2.8.1 Finite element method

The induced motion of a polarisable particle as a result of an applied non-uniform electric field depends on the position of the particle within the electrode. An electrode that generates a non-uniform electric field distribution will in general not have an analytical solution to the electric field. However, in order to predict the motion of a particle, the electric field distribution must be known. To this end a finite element method was employed. The finite element software package was called Maxwell (Ansoft, Pittsburgh) and this software package is capable of solving the electric field distribution of a 3-D geometry defined by the user.

To solve the electric field distribution, a static field approximation is made. In this case the finite element software is employed to solve Poisson`s equation in its general form:

$$\nabla \cdot \varepsilon \nabla V = -\rho^{v} \tag{98}$$

where V is the potential within the domain which denotes solution space and ρ^{v} is the free volume charge density. Over the surface of the domain two boundary conditions hold:

(a): The Ditrichlet boundary condition in which the electric potential is a constant ($V=V_0$) and the electric field is perpendicular to the surface.

(b): The Neumann boundary condition which the electric field is tangential to the surface:

$$\frac{\partial V}{\partial n} = k \tag{99}$$

k is a constant. The differentiation with respect to n indicates differentiation along the normal of the surface.

It is also possible to have a boundary condition that is a combination of (a) and (b):

$$k_1 V + k_2 \frac{\partial V}{\partial n} = k_3 \tag{100}$$

where k_i are constants. The solution must also take into account variations in ε with position such as at the boundaries between different dielectrics.

The problem space is divided into elements and the electric potential in these elements is approximated to a linear function. Each element has a number of associated nodes, such as end points or midpoints of edges. These elements are used to construct a matrix of the problem space. The matrix is solved to give the potential at each node. This solution is an approximation of the real solution, but by increasing the number of elements it is possible to obtain solutions that are sufficiently accurate.

In Maxwell, a 3-D problem space is divided into a series of tetrahedra. A node is assigned to each of the four corners and the middle of the six edges between the corners giving ten nodes for each element, as illustrated in figure 14. Thus, the equation for the potential at any point inside the tetrahedra can be approximated to the general second order function:

$$\begin{aligned} V(x,y,z) = {} & a_1 + a_2 x + a_3 y + a_4 z + a_5 xy + a_6 yz + a_7 xz \\ & + a_8 x^2 + a_9 y^2 + a_{10} z^2 \end{aligned} \tag{101}$$

the individual constants a_i can be found from the known potential at each node.

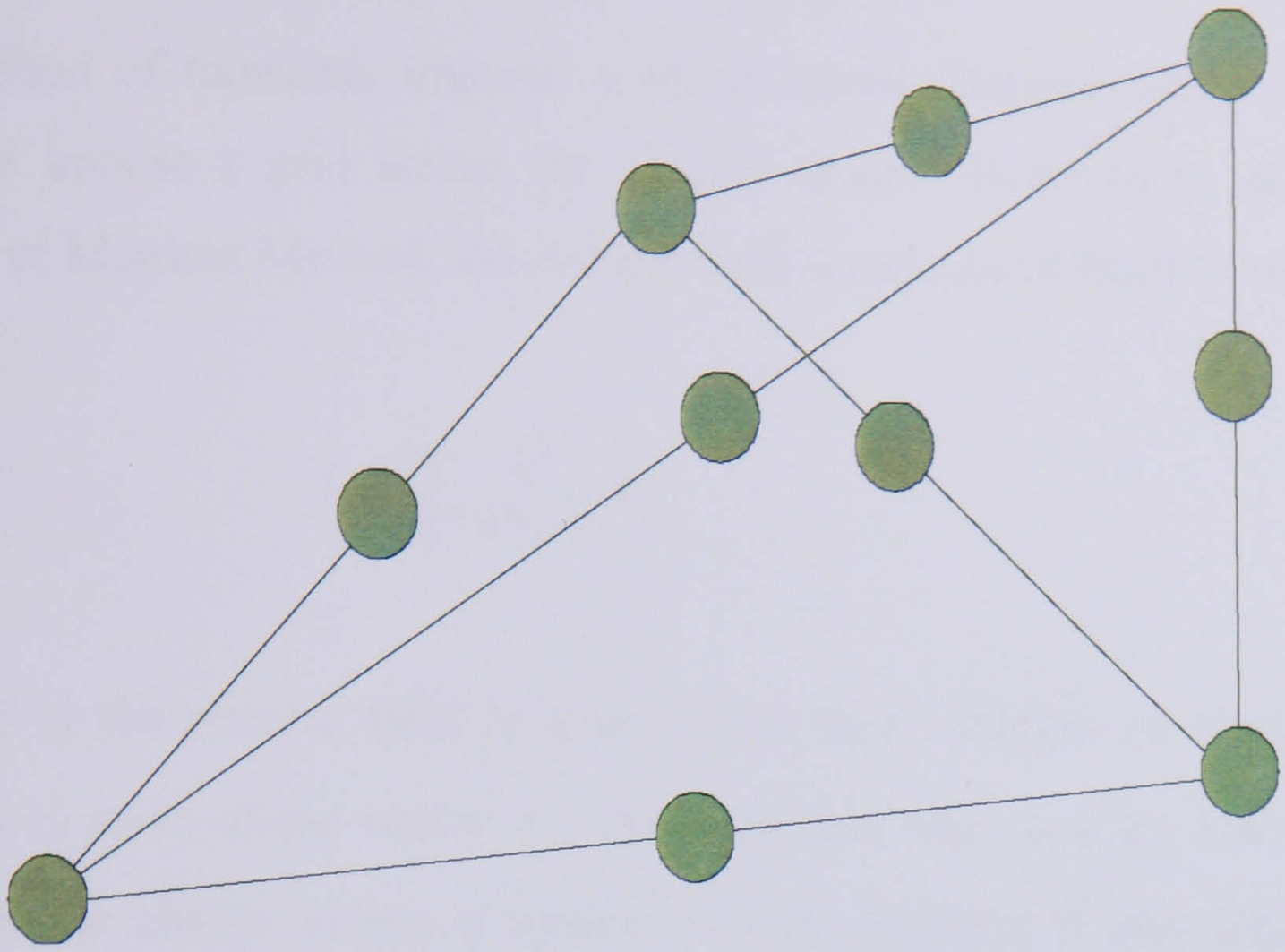

Figure 14: Example of a tetrahedra as used in the Maxwell finite element electric field software package. The tetrahedra consist of one node at each of four corners as well as a node at the midpoint of each six edges between the corners.

The usual procedure for solving a problem is to divide the problem space into a coarse mesh of elements and solve. The resulting solution is not usually accurate and error analysis is performed on the elements. Maxwell then refines the mesh where the error is greatest, adding elements only where an improvement in accuracy is required. The problem is then solved for the new mesh and the error analysis is performed again. This procedure is referred to as adaptive refinement and is repeated until the error over the whole of the problem space reaches a predefined value. Once the process has ended the electric field can be calculated using $\boldsymbol{E} = -\nabla V$.

2.8.2 Method of moments

The induced torque on a polarisable particle depends on the position of the particle within the electrode. An electrode that is used to generate a rotating electric field will in general not have an analytical solution to the electric field distribution. The method of moments was employed to calculate the field distribution in a polynomial electrode.

The method of moments imposes a mesh across charge-bearing electrodes; it does not impose a grid across the sample space. Referred to as the Charge Density or Moment Method, the electric field is calculated from Coulomb's law:

$$E = \sum_i \frac{Q_i}{4\pi\varepsilon r_i^2} \hat{\mathbf{r}}_i \tag{102}$$

where E is the electric field at a point due to i charges of magnitude Q_i a distance r_i away along vector $\hat{\mathbf{r}}_i$. This principle was used by Maxwell [25] to calculate the charge across a square area by dividing it into smaller regions across which the charge was approximately uniform. If the surfaces of the electrodes are divided into sufficiently small subareas, the charge across these subareas can be assumed to be uniformly distributed. The charge on each subarea can be calculated by determining the contribution a unit charge (on a given subarea) makes to the potential at all other subareas. By solving against the known potentials on the electrodes, the charge distribution can be derived. A similar process is subsequently used to calculate the contributions of the charges on the electrodes to the potential at any arbitrary point.

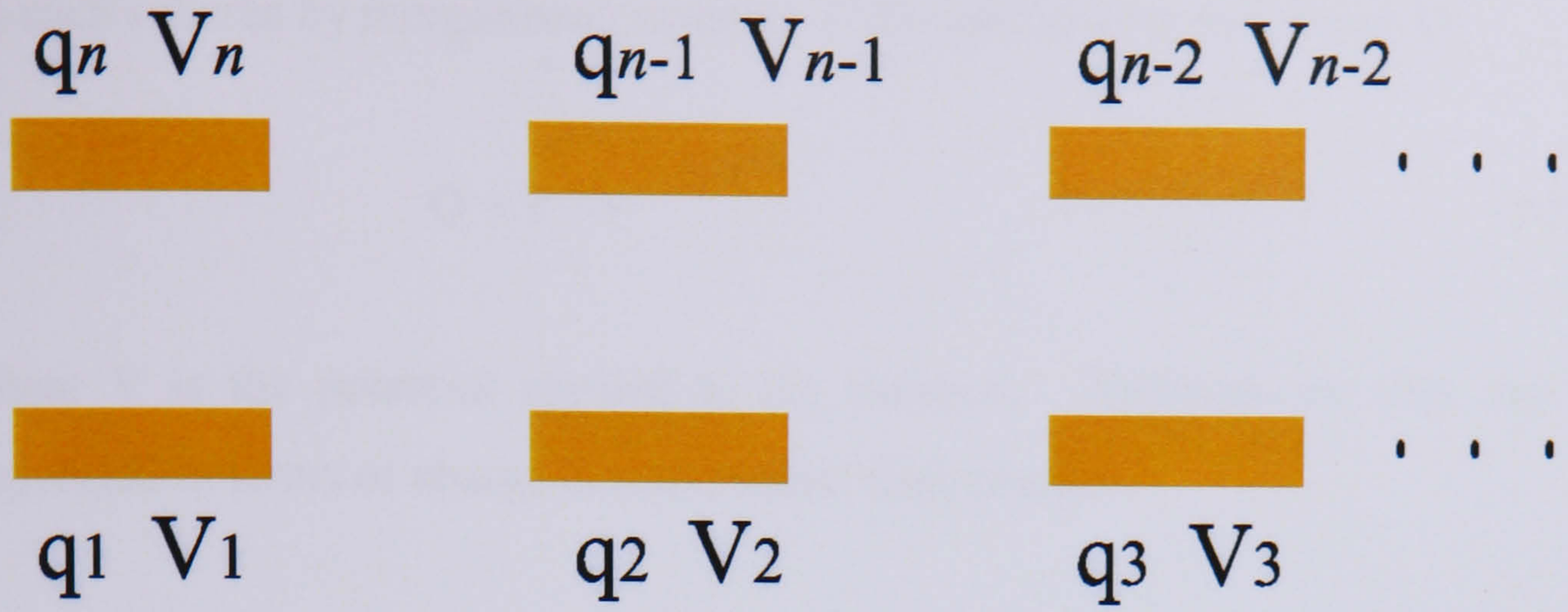

Figure 15: A sequence of n electrodes in space each carrying a charge q_n and a voltage V*n* relative to 0 at infinity.

In a system of *n* conducting electrodes shown in figure 15; the potentials V_n are applied, relative to a potential of 0V at infinity. Each electrode caries a surface charge q_n, the potential at each of the *n* electrodes is related to the charge on the other *n*-1 electrodes. This can be expressed in vector form as:

$$\mathbf{V=PQ} \tag{103}$$

where the elements p_{ij} $(i, j \le n)$ of **P** is a parameter which couples the potential on electrode *i* due to charge *j*, is given by:

$$p_{ij} = \frac{q_j}{4\pi\varepsilon_0\varepsilon_{med}\left|r_{ij}\right|} \tag{104}$$

Element p_{ij} of matrix **P** couples the potential at the midpoint of electrode *i* to a charge on electrode *j* in the absence of any other charges. p_{ij} is obtained from subarea *j*, it is obtained by integrating the charge density in subarea A_j at a distance r_{ij} from such a charge.

Having determined the values of matrix **P** it is possible to calculate the charges on each subarea by reorganising equation (103) and solving for charge **Q**:

$$\mathbf{Q} = \mathbf{P}^{-1}\mathbf{V} \tag{105}$$

where V is the potential applied to the subareas. Alternatively, this can be expressed in terms of charge density, rather than charge:

$$\sigma = \mathbf{P}'^{-1}\mathbf{V} \tag{106}$$

where σ is a charge density vector which is related to **P** by adjusting for the surface area of each element A_j.

Rearranging the above equation, it can be seen that for a given set of points in space, the potential ϕ is dependent on the charge density across the subareas of the electrode, and on a charge-potential relationship matrix:

$$\phi = \sigma\mathbf{P}' \tag{107}$$

The potential at a point due to charge *n* a distance *s* away from the centre of its area is found by integrating over subarea *n* a distance s_n away. If there are a total of *N* subareas then we can derive an expression for the potential ϕ_k at a general point *k* by summing the result of the *N* integrals over subareas *n* a distance s_n away.

The calculation of the potential can be adapted to calculate potentials at points displaced a small, regular distance from the points of study along the axes centered on the sample point. This allows calculation of the electric field at the series of points, by calculating field gradients based on differences between potentials at these points. Having calculated the electric field in vector form in this manner, the data may be saved in the form of matrices $\mathbf{E}x_K$, $\mathbf{E}y_K$ and $\mathbf{E}z_K$. Electrodes modelled using the Method of Moments requires a fixed charge density, thus it is unable to perform true AC analysis. However, an AC cycle can

be divided into a number of static "frames", making it is possible to analyse phase effects across whole a cycle.

2.9 References

1. Lorrain, P., D.R. Corson, and F. Lorrain, *Electromagnetic fields and waves*. 3 ed. 1988, New York: W. H. Freeman and Company.
2. Hippel, A.V., *Dielectrics and Waves*. 1954, New York: John Wiley and Sons.
3. Pethig, R., *Dielectric and Electronic Properties of Biological Materials*. 1979, Chichester: John Wiley and Sons.
4. Debye, P., *Polar Molecules*. 1947, New York: Dover.
5. Berk, L.K.H.V., *Dielectric behaviour of Heterogenous systems*, in *Progress in Dielectrics*, J.B. Birks, Editor. 1960, Heywood: London.
6. Jones, T.B., *Electromechanics of Particles*. 1995, Cambridge: Cambridge University Press.
7. Pohl, H.A., *Dielectrophoresis*. 1978, Cambridge: Cambridge University Press.
8. Pethig, R., *Dielectrophoresis: Using Inhomogeneous AC Electrical Fields to Separate and Manipulate Cells.* Critical Reviews in Biotechnology, 1996. **16**(4): p. 331-348.
9. Wang, X.B., R. Pethig, and T.B. Jones, *Relationship of dielectrophoretic and electrorotational behaviour exhibited by polarized particles.* Journal of Physics D: Applied Physics, 1992. **25**: p. 905-912.
10. Jones, T.B. and M. Washizu, *Multipolar dielectrophoretic and electrorotation theory.* Journal of Electrostatics, 1996. **37**: p. 121-134.
11. Jones, T.B., *Dielectrophoretic force calculation.* Journal of Electrostatics, 1979. **6**: p. 69-82.
12. Denner, V. and H.A. Pohl, *Dielectrophoretic force in electrostatic fields.* Journal of Electrostatics, 1982. **13**: p. 167-174.
13. Fuhr, G., U. Zimmermann, and S.G. Shirley, *Cell motion in time-varying fields: principles and potentials*, in *Electromanipulation of Cells*. 1996.
14. Arnold, W.M. and U. Zimmermann, *Electro-rotation: Development of a technique for dielectric measurements on individual cells and particles.* Journal of Electrostatics. 1988. **21**: p. 151-191.

15. Huang, Y., R. Holzel, R. Pethig, and X.B. Wang, *Differences in the AC electrodynamics of viable and non-viable yeast cells determined through combined dielectrophoresis and electrorotation studies.* Physics in Medicine and Biology, 1992. **37**(7): p. 1499-1517.

16. Gimsa, J., T. Muller, T. Schnelle, and G. Fuhr, *Dielectric Spectroscopy of Single Human Erythrocytes at Physiological Ionic Strength: Dispersion of the Cytoplasm.* Biophysical Journal, 1996. **71**: p. 495-506.

17. Pethig, R., *Biological electrostatics: dielectrophoresis and electrorotation.* Institute of Physics Conference Series, 1991. **118**(1): p. 13-26.

18. Wang, X.B., Y. Huang, R. Holzel, and J.P.H. Burt, *Theoretical and experimental investigations of the interdependence of dielectric, dielectrophoretic and electrorotational behaviour of colloidal particles.* Journal of Physics D: Applied Physics, 1993. **26**: p. 312-322.

19. Edwardes, D., *Motion of a viscous liquid.* Q. J. Pure Appl. Phys, 1893. **26**: p. 71-78.

20. Kakutani, T., S. Shibatani, and M. Sugai, *Electrorotation of non-spherical cells: theory for ellipsoidal cells with an arbitrary number of shells.* Bioelectrochemistry and Bioenergetics, 1993. **31**: p. 131-145.

21. Fricke, H., *A mathematical treatment of the electric conductivity and capacity of disperse systems.* Phys. Rev., 1924. **24**: p. 575-587.

22. Hanai, T., *Theory of the dielectric dispersion due the interfacial polarization and its application to emulsion.* Kolloid Z., 1960. **171**: p. 23-31.

23. Irimajiri, A., T. Hanai, and A. Inouye, *A dielectric theory of 'multi-stratified shell' model with its application to a lymphoma cell.* Journal of Theoretical Biology, 1979.

24. Stratton, J.A., *Electromagnetic Theory*. 1941, New York: McGraw-Hill.

25. Maxwell, J., *A Treatise on Electricity and Magnetism*. 3 ed. Vol. 1. 1892. Oxford: Oxford University Press.

26. Wagner, K.W., ed. *Die Isolierstoffe der Elektrotechnik*. , ed. H. Scering. 1924, Springer: Berlin.

27. Zhou, X.F., G.H. Markx, R. Pethig, and I.M. Eastwood, *Differentiation of viable and non-viable bacterial biofilms using electrorotation.* Biochimica et Biophysica Acta, 1995. **1245**: p. 85-93.

28. Gascoyne, P.R.C., F.F. Becker, and X.B. Wang, *Numerical analysis of the influence of experimental conditions on the accuracy of dielectric parameters derived from electrorotational measurements.* Bioelectrochemistry and Bioenergetics, 1995. **36**: p. 115-125.

29. Nelder, J.A. and R. Mead, *A simplex method for function minimization.* The Computer Journal, 1964. 7: p. 308-313.

30. Zeidler, E., *Applied Functional Analysis. Applications to Mathematical Physics*. Applied Mathematical Siences 108. 1995: Springer-Verlag.

31. Gimsa, J., R. Glaser, and G. Fuhr, *Remarks on the field distribution in four electrode chambers for electrorotational methods.* Studia Biophysica, 1988. **125**: p. 71-76.

32. Holzel, R., *Electric field calculation for electro-rotation electrodes.* Journal of Physics D: Applied Physics, 1993. **26**: p. 2112-2116.

33. Hughes, M.P., X.B. Wang, F.F. Becker, P.R.C. Gascoyne, and R. Pethig, *Computer-aided analysis of electric fields used in electrorotation studies.* Journal of Physics D: Applied Physics, 1994. **27**: p. 1564-1570.

34. Hughes, M.P., *Electrokinetic manipulation of Particles*, PhD Thesis University of Wales, 1995.

35. Green, N.G., H. Morgan, and J.J. Milner, *Manipulation and trapping of sub-micron bioparticles using dielectrophoresis.* Journal of Biochemical and Biophysical Methods, 1997. **35**: p. 89-102.

36. Huang, Y. and R. Pethig, *Electrode design for negative dielectrophoresis.* Measurement Science and Technology, 1991. **2**: p. 1142-1146.

37. Green, N.G., *Dielectrophoresis of sub-micrometer particles*, PhD Thesis University of Glasgow, 1998.

38. Pethig, R., Y. Huang, X.B. Wang, and J.P.H. Burt, *Positive and negative dielectrophoretic collection of colloidal particles using interdigitated castellated microelectrodes.* Journal of Physics D: Applied Physics. 1992. **24**: p. 881-888.

Chapter 3: Electrorotation measurements of the virus life cycle of Herpes Simplex Virus Type 1 infected Baby Hamster Kidney Fibroblasts. *I. Background and Methods.*

3.1 Summary

The dielectric properties of baby hamster kidney fibroblasts (BHK C-13) cells were measured using electrorotation before and after infection with Herpes Simplex Virus, type 1 (HSV-1). The dielectric properties and morphology of the cells were investigated as a function of time after infection. The mean specific capacitance of the uninfected cells was 2.0μF/cm^2, reducing to a value of 1.5μF/cm^2 at 12 hours post-infection. This change was interpreted as arising from changes in the cell membrane morphology coupled with alterations in the composition of the cell membrane as infection progressed. The measured changes in the cell capacitance were correlated with alterations in cellular morphology determined from Scanning Electron Microscope (SEM) images. Between 9 and 12 hours post-infection the internal permittivity of the cell exhibited a rapid change, reducing in value from $75\,\varepsilon_o$ to $58\,\varepsilon_o$ and this was correlated with the generation of large numbers of golgi derived membrane vesicles and enveloped viral capsids.

The data is discussed in relation to the known life cycle of HSV-1 and indicates that electrorotation can be used to observe dynamic changes in both the dielectric and morphological properties of virus infected cells. Calculations of the dielectrophoretic spectrum of uninfected and infected cells have been performed and the results show that cells in the two states could be separated using appropriate frequencies and electrode arrays.

3.2 Introduction

The technique of electrorotation has been used to study the dielectric properties of a number of biological particles [1-16]. A detailed theoretical treatment of electrorotation is given in the theory chapter.

Early electrorotation measurements of liposomes found different characteristic frequencies for the dielectric relaxations of different types of liposomes and reactions to changes in pH of the suspension medium were also observed [3]. Electrorotation has also been used to study the effect of the biocide polyhexamide on the properties of yeast cells [11] where the cytoplasmic membrane conductivity was observed to increase gradually with increasing biocide concentration. A drop in the internal conductivity of the cells was also reported, attributed to an increase in ion leakage across the membrane as a result of the biocide concentration being high enough to affect ion transport across the cytoplasmic membrane. Differences in the membrane capacity and conductivity of fertilised and unfertilised rabbit oocytes have been observed [12]. The change in the capacitance was thought to have been caused by alterations in the membrane structure following fertilisation. The increase in the membrane conductivity was attributed to an increase in metabolic activity as a result of fertilisation, leading to a higher number of transport channels in the membrane.

Early electrorotation measurements were also carried out to study the time-dependent interaction of erythrocytes with influenza virus [8]. The experiments showed that changes in ion-permeability of the membrane resulted in a drop in the cytoplasmic conductivity and this effect could be followed using electrorotion. The effects of antibiotics on the membranes of human erythrocytes [13] have also been followed. In this case the effect of the antibiotic nystatin, was to induce a rapid increase in transmembrane permeability coupled with shrinkage of the cells, both of which could be determined through their influence on electrorotation properties. The use of electrorotation to study the effect of treating erythrocytes with the lipophilic anion dipicrylamine [17] gave convincing evidence that inserting such artificial charge carriers into plasma membranes contributed significantly to the rotational spectra of erythrocytes

suspended in low conductivity media. The authors were able to extract quantitative data on the partition and the transmembrane translocation rate of the anion dipicrylamine, and values were in good agreement with corresponding literature values. Recent work has shown that infection of erythrocytes with the malaria parasite *Plasmodium falciparum*, causes a time dependent change in the rotation spectrum which is indicative of an outflux of ions via the plasma membrane [14] consistent with the production of parasite-associated membrane pores.

The interaction of lipophilic ions (in the form of negatively charged tungsten carbonyl complexes) with mammalian cells was studied by electrorotation [18]. From the electrorotational spectra it was possible to deduce that the negatively charged tungsten carbonyl complexes were, for the most part, able to introduce mobile charges into membranes. As a result it was found that the tungsten derivatives could be considered to act as lipophilic anions. The authors found that the partition coefficients and translocation rate constants derived from electrorotational spectra were found to be in agreement with values obtained from charge pulse experiments on artificial membranes.

Changes in the dielectric properties of lymphocytes following stimulation with mitotic agents were studied by Arnold *et al* [15]. Both B and T lymphocytes were challenged with mitotic agents and the changes in the conductivity, permittivity and morphology of the cells followed as a function of time. The response was shown to parallel increases in transmembrane transport following mitogenic stimulation. Observations of the electrorotation properties of normal and malignant cells [16] have shown that significant changes occur in the morphology and dielectric properties of cells during and after transformation. The internal properties of the cells were shown to remain unchanged, while significant changes were observed in the properties of the membrane. These alterations were shown to closely follow changes in the structure of the membrane.

Electrorotation was used in conjunction with flow cytometry to study the incorporation of DNA, protein and extra plasma membrane by three mammalian

cell lines arrested by the drug aphidicolin or doxorubicin [19]. Using these techniques the authors were able to show that drugs used to arrest the cells had not affected the fundamental bilayer, but that an increase in the number and size of microvilli must have occurred. It was also observed that drug-mediated arrest of the G1-S or the G2/M boundaries did not arrest synthesis of protein or total membrane area. Hypo-osmotic stress was found to be tolerated better by arrested cells than untreated cells, indicating that excess plasma membrane allows cells to better tolerate rapid cell expansion.

Most of the experimental work on cells has used excitation frequencies up to 20MHz, which limits the observations to changes associated with the plasma membrane and to a lesser extent the cytoplasm. Recent advances in circuit design have enabled measurements to be made at frequencies up to 1.6GHz [10, 20], allowing detailed dielectric data on the interior of cells to be obtained. For example, Holzel has demonstrated [20] that data over the frequency window from 100MHz to 1GHz was required to extract the dielectric properties of the innermost parts of yeast cells from the electrorotational spectrum. In particular, Gimsa *et al* [10] have been able to measure the dielectric relaxation of haemoglobin inside erythrocytes, and hence determine the dielectric properties of haemoglobin using high-frequency electrorotation techniques.

The technique of electrorotation allows measurements to be made of single cells within a mixture so that the dielectric properties of different sub-populations can be measured. This data can then be used to optimise conditions for cell sorting by dielectrophoretic methods [5, 21]. There have been numerous reports on successful separation of cell population using dielectrophoretic methods. For example, Gascoyne *et al* [22] used data obtained from electrorotation to model the dielectric characteristics of MDA-231 human breast cancer cells and resting T-lymphocytes in order to design a dielectrophoretic affinity column. This device was shown to be capable of separating cancer cells from the resting T-lymphocytes. Talary *et al* [23] used a similar method to obtain a six-fold enrichment of stem cells expressing the CD34+ antigen from bone marrow samples and peripheral blood. In a similar vein, cells that have been infected with virus could also potentially be separated from uninfected cells using

dielectrophoretic methods tailored to the differences in the dielectric properties of the cells before and after infection.

In order to probe the effects of viral infection of fibroblast cells, electrorotational spectroscopy of individual cells was used. The electrorotation spectra of BHK(C-13) cells were measured for frequencies up to 20MHz. Using this frequency range means that the dielectric parameters of the membrane and the cytoplasm can be probed. The dielectric parameters are reflected in the shape of the electrorotational spectra; and curve fitting procedures were used to obtain the individual dielectric properties of the membrane and cytoplasm. Cells were modelled using a single shell model that neglects the influence of the nucleus [24]. Electrorotational spectra were taken at different times during the viral infection-cycle, allowing time dependent changes in the dielectric parameters of BHK(C-13) fibroblasts following infection with HSV-1 to be obtained.

3.3 Virus life-cycle

The infectivity cycle of the virus is illustrated in figure 1 and can be summarised as follows: upon infection, the virus binds to membrane surface receptors followed by glycoprotein-meditated fusion of the viral envelope with the cell's plasma membrane, releasing the capsid into the cytoplasm. The capsid is rapidly transported along the microtubule network [25] to the vicinity of a nuclear pore, to which the capsid binds, whereupon viral DNA is released and enters the nucleus.

This causes reprogramming of protein synthesis and gene expression, resulting in viral gene expression and DNA replication. Viral DNA begins to appear in the nucleus 3 hours after infection, with replication being completed 12-14 hours post-infection. Preceding DNA replication is transcription of viral immediate-early genes, relying on host cell RNA interacting with certain viral tegument proteins. The protein products of the immediate-early genes are themselves regulatory proteins required to turn on or modulate the expression of other viral genes including early, delayed-early and late genes in temporal sequence. Early genes encode most of the enzymes and factors required for viral DNA replication, the delayed-early and the late genes encode most of the structural proteins of the virion. The transcription of viral genes, replication of the viral genome and assembly of nucleocapsids take place entirely in the cell nucleus. The nucleus is also where progeny viral genomes are packaged into newly assembled capsids.

The DNA-containing capsids leave the nucleus by budding through the inner nuclear membrane into the perinuclear space where the virion acquires an envelope. Two theories exist about how the viruses leave the perinuclear space. One states that the envelope obtained at the inner nuclear membrane is retained. while viral tegument and envelope proteins are modified as the virus exits the cell via the exocytic pathway. The other states that the envelope acquired at the inner nuclear membrane is lost by fusion of the enveloped particle with a cytoplasmic membrane, and that a new envelope is acquired by envelopment of cytoplasmic nucleocapsids at other cytoplasmic membranes, most probably those

of the Golgi apparatus. Whatever model is correct mature enveloped virions ultimately appear in cytoplasmic transport vesicles in the form of Golgi derived transport vesicles, in which virions are transported to the plasma membrane and released onto the cell surface by exocytosis without cell lysis [26-29]. This process is summarised in figure 1.

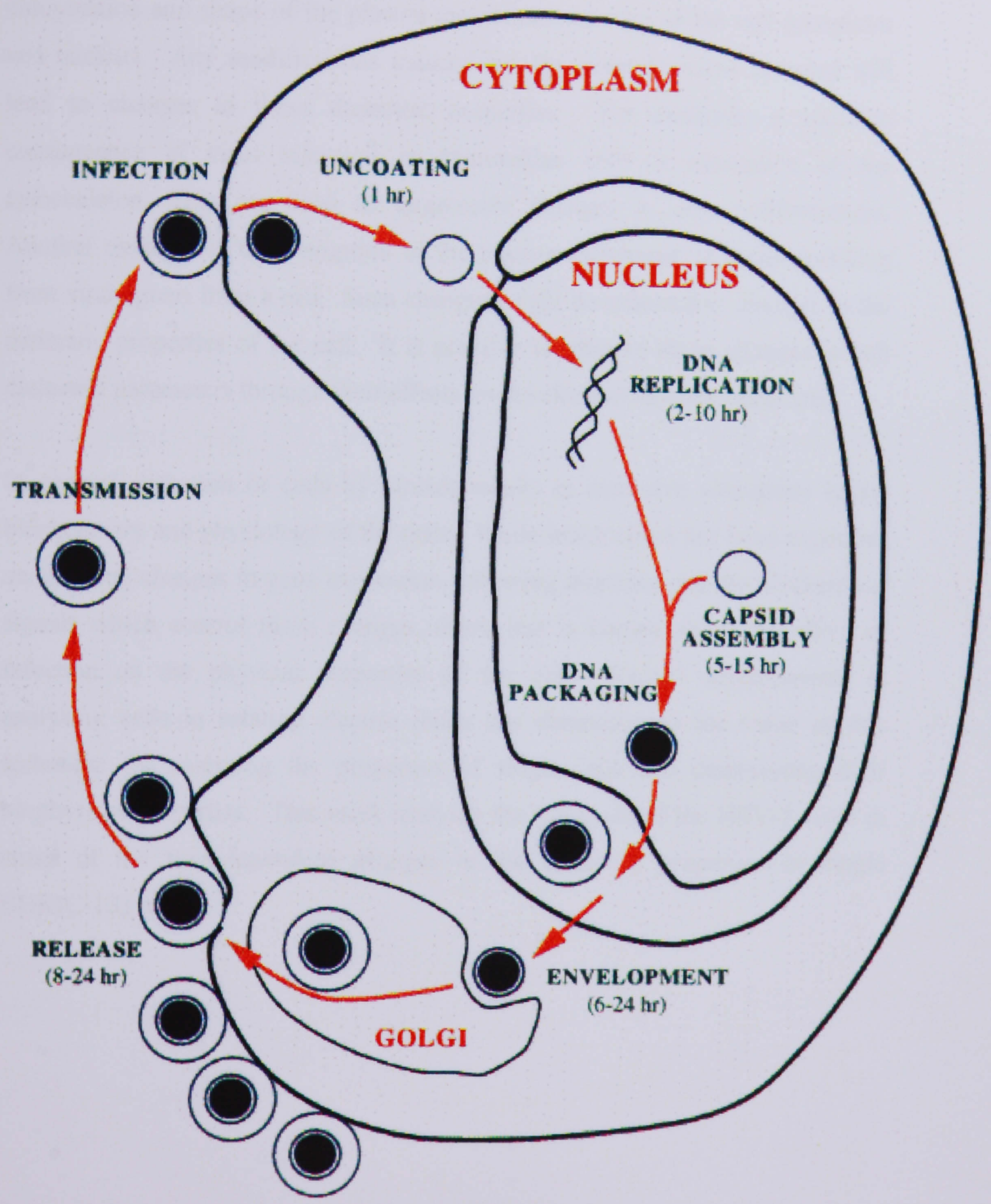

Figure 1: Schematic representation of the life cycle of Herpes Simplex Virus, type 1. It shows the different stages of the life cycle, including virus entry, uncoating, replication and assembly, envelopment and release.

3.4 Importance of dielectric parameters

The dielectric properties of a cell (capacitance and conductance) reflect the composition and shape of the plasma membrane and also of the cell cytoplasm and nucleus. Any modifications induced by, for example, virus invasion will lead to changes in these dielectric properties. For example, a common consequence of virus infection in mammalian cells is disruption of the cytoskeleton. This can lead to large-scale changes in cell conformations. Another example is the disruption of the plasma membrane of a cell resulting from viral egress from a cell. Such changes might be reflected in changes in the dielectric properties of the cell. It is possible to observe these changes in cell dielectric parameters through their effects on the electrorotational behaviour.

In general, infection of cells by viruses results in extensive alterations in the biochemistry and physiology of the cells. While much effort has been expended on studying changes in gene expression following infection and the biochemical signals which control these changes, much less is known about the effect of infection on the physical properties of the cell. Recent developments in analysing cells in rotating electric fields has demonstrated the value of this technique for analysing the properties of single cells and determining their biophysical properties. This work analyses the life cycle of the HSV-1 virus in terms of the time-dependent changes in the dielectric properties of single BHK(C-13) cells.

3.5 Materials and Methods

3.5.1 Cell culture and virus infection.

Cells from a tissue culture adapted Baby Hamster Fibroblast (BHK21 C13) cell line were maintained in Glasgow-modified Eagle's medium (Gibco/BRL) supplemented with 10% tryptose phosphate broth and 10% newborn calf serum. Cells were grown on 60mm tissue culture plates (Corning), to a density of $5x10^6$ cells/plate. Cells are normally adherent, and in order to obtain electrorotation spectra cells were carefully removed from the culture dishes using mechanical methods.

To ensure simultaneous infection of all cells, 10 plaque forming units (p.f.u.) per cell of Ficol gradient purified HSV-1 strain 17 [30] were used. The purified virus was stored at -70°C in aliquots of 50μl. For each experiment a fresh aliquot was used. At appropriate times after infection the cells were harvested by scraping into the tissue culture medium, pelleted by centrifugation at 400g and resuspended in the suspension medium used for electrorotation measurements which consisted of 320mM Sucrose, 0.2mM EDTA, 0.1mM PBS and 0.3mM PEG.

3.5.2 Electrorotation measurements

The rotating electric field was generated from a four phase direct digital synthesised frequency generator, designed and constructed in-house. Four-electrode polynomial arrays were used for the measurements [31, 32], with a distance between opposing tips of 800μm. The electrodes were fabricated by evaporating a layered structure of gold/palladium/titanium onto glass microscope slides using standard photolithographic techniques [33].

Electrorotational measurements were obtained from cells that had been harvested and resuspended at a concentration of approximately 10^4 cells per ml in a suspending medium with a conductivity of 17.5mSm^{-1}, at a temperature of 20°C.

The conductivity of the medium was measured using a Hewlett-Packard 4192A-impedance analyser with a Sentek conductivity cell at a frequency of 100kHz. For the electrorotation measurements, a chamber was constructed around the electrode array with a volume of approximately 1ml and sealed with a cover slip. The entire electrode-chamber assembly was placed on an inverted microscope and cell rotation imaged with a CCD camera and recorded using S-VHS video. The frequency dependent rotation rate was measured using a stopwatch. The spectrum of single isolated cells, which were located within the central area of the electrode array [34], were measured at four points per decade over the frequency range 3 kHz to 20 MHz at a voltage of 2V (rms) connected to the 4-electrodes in phase quadrature. The experimental set-up is illustrated in figure 2.

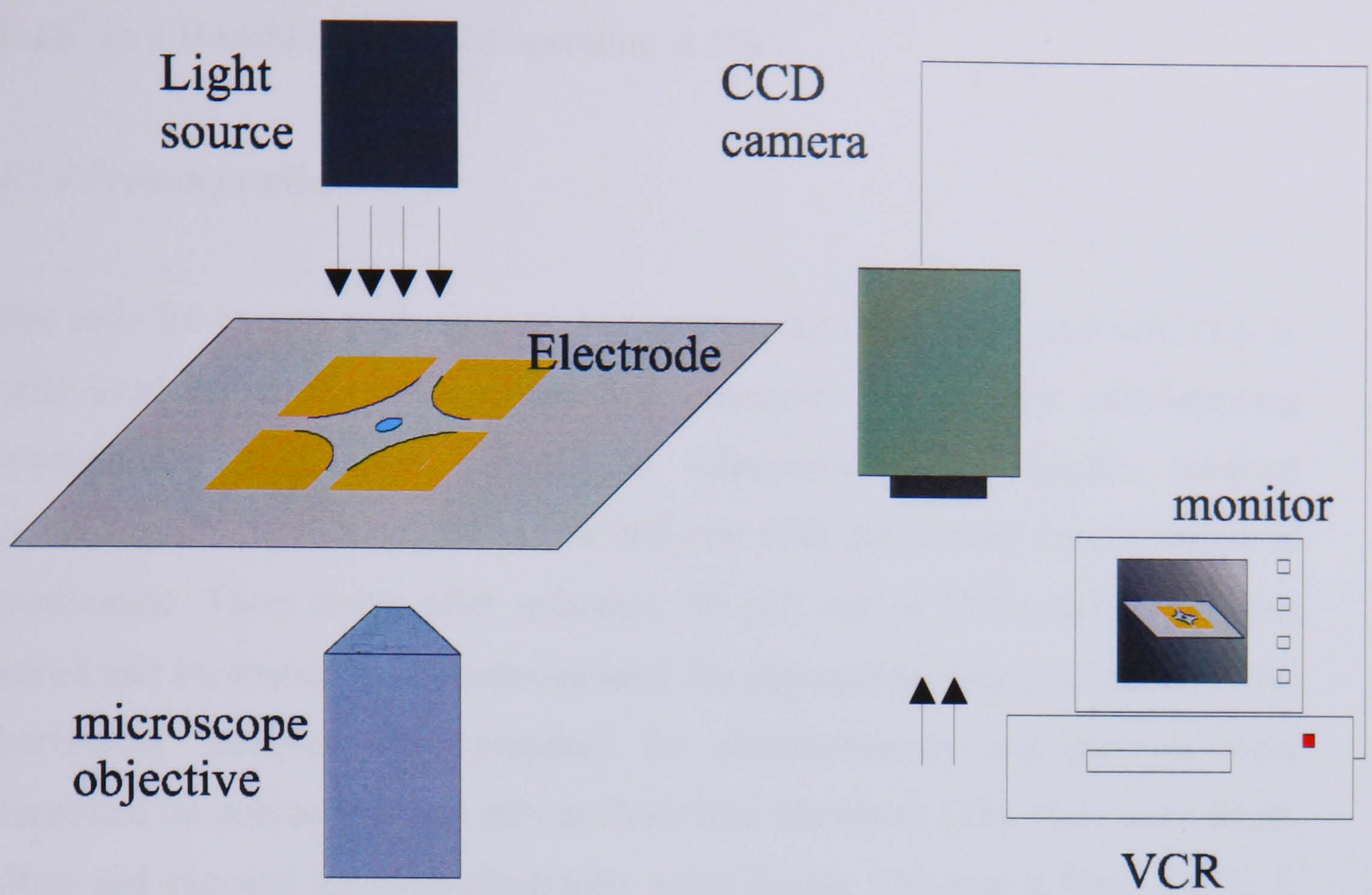

Figure 2: Experimental setup used to obtain the electrorotational spectra of fibroblast cells prior to and following infection with HSV-1. The electrodes were energised using a DDS signal generator.

3.5.3 Scanning Electron Microscope (SEM) images

At appropriate times after infection the culture medium was removed from the culture dish and the cell monolayer was carefully washed with phosphate buffered saline (PBS). The cells were then scraped into fresh PBS and allowed to settle onto glass cover slips coated with poly-l-lysine. After 5 minutes unattached cells were removed by rinsing in fresh PBS. Adsorbed cells were fixed with a 2.5% solution of glutaraldehyde in PBS for 1h, rinsed in PBS and exposed to 1% osmium tetroxide for a further hour. The cells were dehydrated by sequential immersion in 30, 50, 70, 90 and 2x100% ethanol followed by a 50:50 ethanol:acetone solution and then 100% acetone. Cells were then critical point

dried and sputter coated with gold. Images were taken at a magnification of 5×10^3 on a Hitachi S-800 SEM operating at 30kV.

3.5.4 Protein profiles

The cells for protein analysis were harvested at the same times post-infection as cells used for electrorotation and SEM analysis. For protein radiolabelling experiments, cells were infected in Glasgow-modified Eagle's medium containing 2% new-born calf serum and one fifth the normal concentration of methionine. Three hours after infection, 50 μCi /ml of [35S]-methionine was added and incubation was continued until the appropriate time post-infection for harvesting. Samples were prepared for electrophoresis and proteins were separated on polyacrylamide gels as described elsewhere [35]. Gels were fixed, dried and exposed for autoradiography using Kodak X-O-mat S film. Dr. F. J. Rixon (MRC Virology Unit, Glasgow) performed this work.

3.5.5 Data analysis and Theory

When in suspension, BHK cells are spherical in shape so they can be approximated to a series of concentric spheres, consisting of the plasma membrane, the cytoplasm, nuclear membrane and the nucleus. Owing to the limited frequency bandwidth of our experimental apparatus, it was not possible to obtain data at sufficiently high frequencies to probe the nucleus and the nuclear membrane. Thus the cells were modelled using a single shell model, which only considers the membrane and the cytoplasm; the nucleus being considered as part of the cytoplasm.

The spherical single-shell model treats the cell as a solid particle (the cytoplasm plus nucleus) surrounded by a thin insulating membrane. At low frequencies the electric field does not penetrate the cell membrane so that the measured electrical parameters are a function only of the membrane capacitance and conductance. At higher frequencies the electric field penetrates the cell so that the electrical properties of the cytoplasm can be probed. Analysis of the data in terms of this

simple model has been found to be remarkably effective and gives reproducible values for the conductivity and permittivity of the membrane and of the interior of the cell [36, 37]. The specific membrane capacitance is calculated in terms of the membrane permittivity according to: $C_{spec} = \varepsilon_{mem}/d$, were d is the membrane thickness and ε_{mem} is the permittivity of the membrane.

The steady state rotation rate, $\mathbf{R}(\omega)$ imparted upon a dielectric particle depends upon the electric field and the suspension medium surrounding the particle [9] according to the expression given by equation (96) in the theory chapter:

$$\mathbf{R}(\omega) = -\frac{\varepsilon_m Im\left(\dfrac{\varepsilon_p^* - \varepsilon_m^*}{\varepsilon_p^* + 2\varepsilon_m^*}\right)\boldsymbol{E}^2}{2\eta} A \qquad (1)$$

The particle was modelled using the smeared out shell model, according to which the complex permittivity of the particle can be written as the sum of the membrane and internal complex permittivities [37] as given by equation (73) in the theory chapter:

$$\varepsilon_p^* = \frac{\left[\dfrac{a}{a-d}\right]^3 + 2\left[\dfrac{\varepsilon_{int}^* - \varepsilon_{mem}^*}{\varepsilon_{int}^* + 2\varepsilon_{mem}^*}\right]}{\left[\dfrac{a}{a-d}\right]^3 - \left[\dfrac{\varepsilon_{int}^* - \varepsilon_{mem}^*}{\varepsilon_{int}^* + 2\varepsilon_{mem}^*}\right]} \qquad (2)$$

where a is the radius of the cell and ε_{int}^* and ε_{mem}^* are the complex permittivities of the cell interior and membrane respectively. Using curve-fitting procedures the dielectric parameters of the cells can thus be obtained.

An algorithm that minimises the sum of the difference between the experimental rotation spectrum and the spectrum predicted by the single shell model of a cell with a steady state rotation rate [36] using from equations (96) and (73) is described by equation (97) in the theory chapter:

$$Min\left[\sum_i \left(\mathbf{R}_{expt}(\omega_i) - \mathbf{R}_{est}(\omega_i)\right)^2\right] \quad (3)$$

Using this procedure the specific membrane capacitance (C_{spec}), the internal permittivity (ε_{int}) and the internal conductivity (σ_{int}) of the cell were obtained. The membrane conductivity of the cells was extremely low and impossible to accurately predict from the electrorotation or dielectrophoretic cross over data. Also since this value has little effect on the other dielectric parameters the conductivity of the membrane was set to a fixed value of $\sigma_{mem} = 5 \times 10^{-7}$ Sm^{-1} during curve fitting [36].

To quantify the accuracy of curve fitting a regression coefficient (ρ) was calculated according to:

$$\rho = 1 - \left[\frac{\sum_i \left(\mathbf{R}_{expt}(\omega_i) - \mathbf{R}_{est}(\omega_i)\right)^2}{\sum_i \left(\mathbf{R}_{expt}(\omega_i)\right)^2}\right] \quad (4)$$

A value close to unity for the regression coefficient implies that the model used to fit the electrorotational data was successful. Only data in which the regression coefficient was greater than 0.985 was used. Data sets that produced a regression coefficient less than this value were rejected.

3.5.6 Verification of Membrane conductivity using Dielectrophoretic Crossover Frequency Measurements

Electrorotation provides a useful tool for analysing the dielectric properties of individual cells. From electrorotational data it is possible to extract information about the permittivity of the membrane as well as the permittivity and conductivity of the interior. However the conductivity of a plasma membrane is often very low and as a result it is often not possible to ascertain its value from electrorotation spectra [36]. Such low conductivity values do not to affect the shape of electrorotational spectra and as a result it is usual to assume that the membrane conductivity is low when performing curve-fitting procedures on

electrorotational data. However, if the membrane conductivity reaches a sufficiently high value it will start to affect the shape of electrorotation spectra. It is therefore important to obtain an independent value for the membrane conductivity of the cells. This can be done using dielectrophoretic crossover frequency measurements.

The technique of measuring the dielectrophoretic crossover frequency for a range of medium conductivities makes it possible to find the membrane conductivity of a population of cells. When a cell is exposed to an externally applied non-uniform electric field it experiences a dielectrophoretic force as given by equation (61) from the theory chapter:

$$\boldsymbol{F} = 2\pi\varepsilon_m a^3 \,\mathrm{Re}\{K(\omega)\}\nabla \boldsymbol{E}^2 \tag{5}$$

For a suitable combination of frequency, medium conductivity and cell size this force becomes equal to zero. The frequency at which this occurs is referred to as the dielectrophoretic cross over frequency. The dielectric cross over frequency is the frequency at which the real part of $K(\omega)$ is equal to zero, so that the dielectrophoretic force becomes zero. For a cell modelled with the single shell model, the dielectrophoretic crossover frequency is given by [16]:

$$f_{cross} = \frac{\sqrt{2}}{8\pi a C_{spec}} \sqrt{(4\sigma_m - aG_{mem})^2 - 9G_{mem}^2 a^2} \tag{6}$$

Were σ_m is the conductivity of the suspending medium, a is the radius of the cell, C_{spec} is the specific membrane capacitance of the cell and $G_{mem} = (\sigma_{mem}/d)$ is the conductivity per unit area of the membrane (d is the membrane thickness).

Dielectrophoretic crossover frequency measurements were carried out on two sets of cells. The first sets were mock-infected cells, while the second set of cells were infected at 10 pfu, the same as for the electrorotational studies. Cross over data was measured for infected cells 18 hours post infection. The membrane

conductivity of these time points could be obtained and compared Also the specific membrane capacitance obtained from the two types of experiments could be compared.

Measurements of the dielectrophoretic crossover frequency of BHK(C-13) cells was performed using a polynomial electrode with a gap of 400μm between electrode tips, at an applied potential of up to $5V_{pk-pk}$. For each experiment 200μl of cells at a concentration of 10^7 cells per ml were spun down and resuspended in 400μl of 320mM Sucrose, 0.2mM EDTA and 0.3mM PEG, with the amount of PBS being varied to adjust the medium conductivity. The dielectrophoretic crossover frequency of at least five cells per medium conductivity was measured at suspension medium conductivities of $2.8mSm^{-1}$, $9.2\ mSm^{-1}$, $15.7mSm^{-1}$, $22.1mSm^{-1}$ and $32.4mSm^{-1}$. Cells in suspension were confined to the electrodes using a chamber that was constructed around the electrode array using clear nail varnish and a 13mm diameter coverslip giving an enclosed volume of approximately 25μl.

The results of dielectrophoretic crossover frequency measurements were analysed using an algorithm that minimised the difference between experimentally obtained crossover frequencies and those predicted using equation (6):

$$Min\sum_{i}\left(f_{cross(theory),i}-f_{cross(\mathrm{exp}eriment),i}\right)^2 \qquad (7)$$

were i is the number of data points. The algorithm employs a Nelder-Mead method [38] to calculate average values for the specific membrane capacitance and the area specific membrane conductivity of the cells measured.

3.5.7 Determination of virus surface coverage

When a virus infects a cell, changes occur in the structure of the cell. One change is the appearance of virions on the cell surface as a result of exocytosis. These first appear after about 6 hours post infection, they then appear in

increasing amounts up to approximately 12 hours post-infection. Beyond this time the number of virions on the surface of the plasma membrane starts to decline [26, 39]. It is possible that the presence of large amounts of virions on the surface of a cell might affect the dielectric properties of the cell. If viruses are present on the surface of a BHK(C-13) cell then their presence can be modelled by adding an outer layer to the single shell model. The outer shell was modelled as a monolayer of virus particles of variable volume fraction with suspending medium taking up the spaces between viruses, as shown in figure 3.

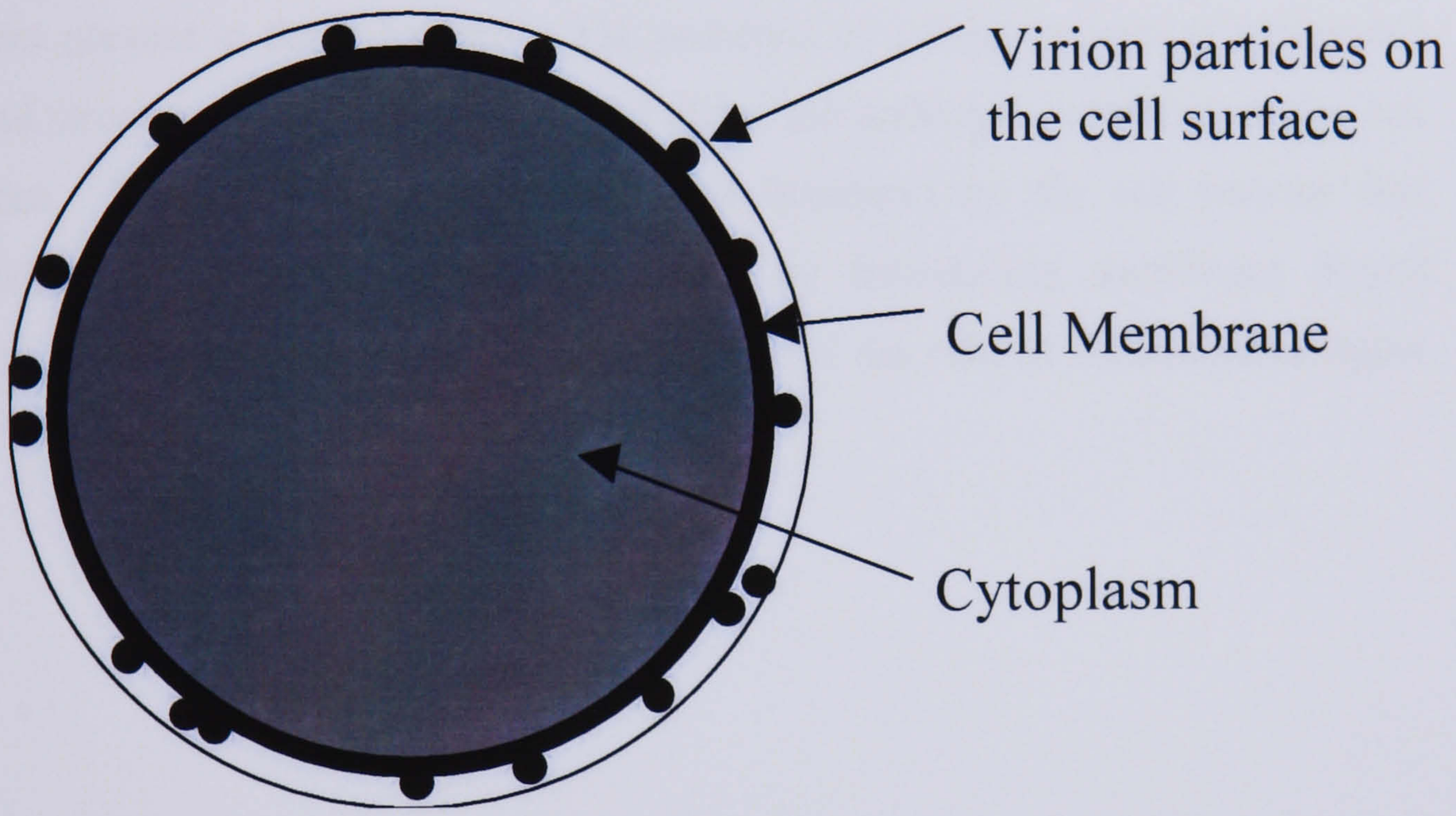

Figure 3: Schematic of multi shell model of BHK(C-13) cell covered with HSV-1. The outer layer consists of a mixture of HSV-1 and suspension medium.

Dielectric mixture theory can be used to calculate the effective permittivity of a mixture of two different dielectric bodies according to equation (93) from the theory chapter.

$$\varepsilon_{mix}^{*} = \varepsilon_{v}^{*} \frac{\left(2\varepsilon_{v}^{*} + \varepsilon_{p}^{*}\right) - 2\rho\left(\varepsilon_{v}^{*} - \varepsilon_{p}^{*}\right)}{\left(2\varepsilon_{v}^{*} + \varepsilon_{p}^{*}\right) + \rho\left(\varepsilon_{v}^{*} - \varepsilon_{p}^{*}\right)} \tag{8}$$

where the particles of permittivity ε_p^* is suspended within a dielectric with permittivity ε_v^* and ρ is the volume fraction taken up by the particles.

3.5.8 Determination of the bound structures within the cytoplasm

Another change that occurs in virus infected cells is the presence of increasing amounts of membrane bound structures within the cell. The presence of these structures results in a larger fraction of the cytoplasm being taken up by membrane bound structures. The membrane bound structures can be vacuoles derived from the golgi apparatus which often contain viruses, or enveloped viruses present in the cytoplasm. The presence of a large amount of membrane bound structures would be expected to affect the dielectric properties of the cell interior. The effect of membrane bound structures on the cell interior was modelled using dielectric mixture theory by introducing membrane bound structures into the previously uniform interior of the cell, as illustrated in figure 4.

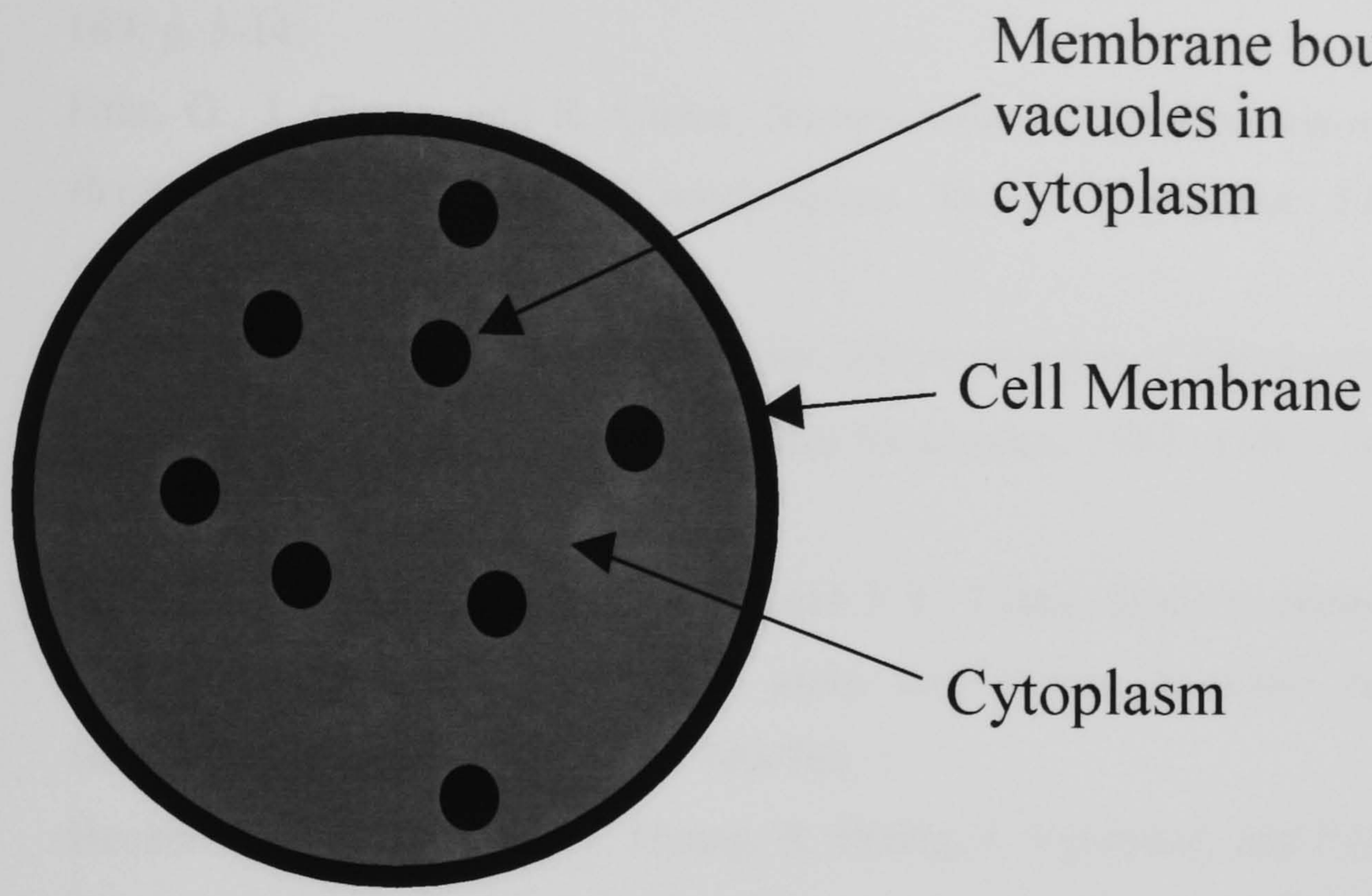

Figure 4: Membrane bound structures in the previously uniform cytoplasm of a BHK(C-13) modelled using the single shell model. The vacuoles are present in increasing amounts following infection.

3.6 References

1. Fuhr, G., J. Gimsa, and R. Glaser, *Interpretation of Electrorotation of Protoplasts II. Interpretation of Experiments.* Studia Biophysica, 1985. **109**: p. 5-14.
2. Fuhr, G., J. Gimsa, and R. Glaser, *Interpretation of Electrorotation of Protoplasts I. Theoretical Considerations.* Studia Biophysica, 1985. **108**(3): p. 149-164.
3. Wicher, D., J. Gundel, and H. Matthies, *Electrorotation of Liposomes in the α- and β- Dispersion range.* Studia Biophysica, 1987. **119**(1-3): p. 103-104.
4. Gimsa, J., P. Marszalek, U. Loewe, and T.Y. Tsong, *Dielectrophoresis and electrorotation of neurospora slime and murine myeloma cells.* Biophysical Journal, 1991. **60**: p. 749-760.
5. Becker, F.F., X.B. Wang, Y. Huang, R. Pethig, J. Vykoukal, and P.R.C. Gascoyne, *Separation of human breast cancer cells by differential dielectric affinity.* Proceedings of the National Academy of Science, 1995. **92**: p. 860-864.
6. Huang, Y., X.B. Wang, R. Holzel, F.F. Becker, and P.R.C. Gascoyne, *Electrorotational studies of the cytoplasmic dielectric properties of Friend murine erythroleukaemia cells.* Physics in Medicine and Biology, 1995. **40**: p. 1789-1806.
7. Wang, J., V.L. Sukhorukov, C.S. Djuzenova, U. Zimmermann, T. Muller, and G. Fuhr, *Electrorotational spectra of protoplasts generated from giant marine alga Valonia utricularis.* Protoplasma, 1997. **196**: p. 123-134.
8. Gimsa, J., C. Pritzen, and E. Donath, *Characterisation of Virus-Red-Cell interaction by electrorotation.* Studia Biophysica, 1989. **130**(1-3): p. 123-131.
9. Arnold, W.M. and U. Zimmermann, *Electro-rotation: Development of a technique for dielectric measurements on individual cells and particles.* Journal of Electrostatics, 1988. **21**: p. 151-191.

10. Gimsa, J., T. Muller, T. Schnelle, and G. Fuhr. *Dielectric Spectroscopy of Single Human Erythrocytes at Physiological Ionic Strength: Dispersion of the Cytoplasm.* Biophysical Journal, 1996. **71**: p. 495-506.
11. Zhou, X.F., G.H. Markx, and R. Pethig, *Effect of biocide concentration on electrorotation spectra of yeast cell.* Biochimica et Biophysica Acta, 1996. **1281**: p. 60-64.
12. Arnold, W.M., R.K. Schmutzler, S. Al-Hasani, D. Krebs, and U. Zimmermann, *Differences in membrane properties between unfertilised and fertilised single rabbit oocytes demonstrated by electro-rotation - Comparison with cells from early embryos.* Biochimica et Biophysica Acta, 1989. **979**: p. 142-146.
13. Gimsa, J., T. Schnelle, G. Zechel, and R. Glaser, *Dielectric Spectroscopy of Human Erythrocytes: Investigations under the influence of Nystatin.* Biophysical Journal, 1994. **66**: p. 1244-1253.
14. Gascoyne, P., R. Pethig, J. Satayavivad, F.F. Becker, and M. Ruchirawat, *Dielectrophoretic detection of changes in erythrocyte membranes following malarial infection.* Biochimica et Biophysica Acta, 1997. **1323**: p. 240-252.
15. Hu, X., W.M. Arnold, and U. Zimmermann, *Alterations in the electrical properties of T and B lymphocyte membrane induced by mitogenic stimulation. Activation monitored by electro-rotation of single cells.* Biochimica et Biophysica Acta, 1990. **1021**: p. 191-200.
16. Huang, Y., X.B. Wang, F.F. Becker, and P.R.C. Gascoyne, *Membrane changes associated with the temperature-sensitive P85$^{gag-mos}$ - dependent transformation of rat kidney cells as determined by dielectrophoresis and electrorotation.* Biochimica et Biophysica Acta, 1996. **1282**: p. 76-84.
17. Sukhorukov, V.L. and U. Zimmermann, *Electrorotation of erythocytes treated with dipicrylamine: Mobile charges within the membrane show their "signature" in rotational spectra.* Journal of Membrane Biology, 1996. **153**(2): p. 161-169.
18. Kurschner, M., K. Nilsen, C. Andersen, V.L. Sukhorukov, *et al.*, *Interactions of lipophilic ions with the plasma membrane of mammalian*

cells studied by electrorotation. Biophysical Journal, 1998. **74**(6): p. 3031-3043.

19. Sukhorukov, V.L., C.S. Djuzenova, W.M. Arnold, and U. Zimmermann, *DNA, Protein and Plasma Membrane Incorporation by Arrested Mammalian-Cells.* Journal of Membrane Biology, 1994. **142**(1): p. 77-92.
20. Holzel, R., *Electrorotation of single yeast cells at frequencies between 100 Hz and 1.6 GHz.* Biophysical Journal, 1997. **73**: p. 1103-1109.
21. Stephens, M., M.S. Talary, R. Pethig, A.K. Burnett, and K.I. Mills, *The dielectrophoresis enrichment of CD34$^-$ cells from peripheral blood stem cell harvests.* Bone Marrow Transplantation, 1996. **18**: p. 777-782.
22. Gascoyne, P.R.C., X.-B. Wang, Y. Huang, and F.F. Becker, *Dielectrophoretic Separation of Cancer Cells from Blood.* IEEE Transactions on Industry Applications, 1997. **33**: p. 670-678.
23. Talary, M.S., K.I. Mills, T. Hoy, A.K. Burnett, and R. Pethig, *Dielectrophoretic separation and enrichment of CD34+ cell subpopulation from bone marrow and peripheral blood stem cells.* Medical and Biological Engineering and Computing, 1995: p. 235-237.
24. Huang, Y., R. Holzel, R. Pethig, and X.B. Wang, *Differences in the AC electrodynamics of viable and non-viable yeast cells determined through combined dielectrophoresis and electrorotation studies.* Physics in Medicine and Biology, 1992. **37**(7): p. 1499-1517.
25. Sodeik, B., M.W. Ebersold, and A. Helenius, *Microtube-mediated Transport of Incoming Herpes Simplex Virus 1 Capsids to the Nucleus.* The Journal of Cell Biology, 1997. **136**(5): p. 1007-1021.
26. Steven, A.C. and P.G. Spear, *Herpesvirus Capsid Assembly and Envelopment*, in *Structural Biology of Viruses*, W. Chiu, R.M. Burnett, and R.L. Garcea, Editors. 1997, Oxford University Press: Oxford. p. 312-351.
27. Smith, J.D. and E.d. Harven, *Herpes Simplex Virus and Human Cytomegalovirus Replication in WI-38 Cells I. Sequence of Viral Replication.* Journal of Virology, 1973. **12**(4): p. 919-930.

28. Morgan, C., H.M. Rose, M. Holden, and E. Jones, *Electron Microscopic observations on the Development of Herpes Simplex Virus.* Journal of Experimental Medicine, 1959. **110**: p. 643-656.

29. Johnson, D.C. and P.G. Spear, *Monensin Inhibits the Processing of Herpes Simples Virus Glycoproteins, Their Transport to the Cell Surface, and the Egress of Virions from Infected Cells.* Journal of Virology, 1982. **43**(3): p. 1102-1112.

30. Szilagyi, J.F. and C. Cunningham, *Identification and characterisation of a novel non-infectious herpes simplex virus-related particle.* Journal of General Virology, 1991. **72**: p. 661-668.

31. Holzel, R., *A simple Wide-Band sine wave quadrature oscillator.* IEEE Transactions on Instrumentation and Measurement, 1993. **42**(3): p. 758-760.

32. Huang, Y. and R. Pethig, *Electrode design for negative dielectrophoresis.* Measurement Science and Technology, 1991. **2**: p. 1142-1146.

33. Green, N.G., *Dielectrophoresis of sub-micrometer particles*, PhD Thesis University of Glasgow, 1998.

34. Hughes, M.P., X.B. Wang, F.F. Becker, P.R.C. Gascoyne, and R. Pethig, *Computer-aided analysis of electric fields used in electrorotation studies.* Journal of Physics D: Applied Physics, 1994. **27**: p. 1564-1570.

35. Leslie, J., F.J. Rixon, and J. Mclalauchilan, *Overexpression of Herpes Simplex Virus Type 1 tegument protein VP22 increases its incorporation into virus particles.* Virology, 1996. **220**: p. 60-68.

36. Gascoyne, P.R.C., F.F. Becker, and X.B. Wang, *Numerical analysis of the influence of experimental conditions on the accuracy of dielectric parameters derived from electrorotational measurements.* Bioelectrochemistry and Bioenergetics, 1995. **36**: p. 115-125.

37. Wang, X.B., Y. Huang, P.R.C. Gascoyne, F.F. Becker, R. Holzel, and R. Pethig, *Changes in Friend murine erytroleukaemia cell membranes during induced differentiation determined by electrorotation.* Biochimica et Biophysica Acta, 1994. **1193**: p. 330-344.

38. Nelder, J.A. and R. Mead, *A simplex method for function minimization.* The Computer Journal, 1964. **7**: p. 308-313.

39. Rixon, F.J., C. Addison, and J. McLauchlan, *Assembly of enveloped tegument structures (L particles) can occur independently of virion maturation in herpes simplex virus type 1-infected cells.* Journal of General Virology, 1992. **73**: p. 277-284.

Chapter 4: Electrorotation measurements of the virus life cycle of Herpes Simplex Virus Type 1 infected Baby Hamster Kidney Fibroblasts. *II Results.*

4.1 Electrorotation

4.1.1 Electrorotational data

Electrorotational spectra for HSV-1 infected BHK(C-13) cells were obtained at discrete times throughout a single cycle of virus replication. The time points chosen were at 0, 6, 9, 12, 18 and 26 hours after infection. At each time point electrorotational spectra were obtained for 8 to 10 individual cells. To ensure the reproducibility of the results, the time courses were performed in two ways.

Method 1: Discontinuous time course.

In this approach, each time point (5 data sets in total) was treated as a separate experiment. Thus, five culture dishes were infected simultaneously with 10pfu/cell of virus. They were incubated at 37°C and at the appropriate time after infection (e.g. 6 hours) all the cells were harvested. The cells were stored in growth medium at 4°C in order to reduce metabolic processes and cell deterioration, the electrorotation spectra were taken as soon as possible. Since each spectrum took approximately 30 minutes, to accumulate up to 10 spectra (sequentially) took several hours. Typically two to three spectra (each representing a single cell) were obtained from one plate of cells. Therefore, using this method up to 10 electrorotational spectra were obtained for each time point.

Method 2: Continuous time course.

In method 1, above, each batch of cells being examined were harvested at the same time and stored at 4°C until used for measurement. Although metabolic processes are greatly delayed at low temperatures, we felt it necessary to confirm

that the behaviour of the cells was not affected by this treatment. As an alternative approach, therefore, five replicate plates of cells were infected simultaneously with virus. The plates were incubated at 37°C and at each of the desired times (e.g. 6 hours) one was removed, the cells harvested and electrorotation spectra determined immediately. Incubation of the remaining plates was continued until the next time point when the process was repeated. At each time point 2-4 spectra were collected. In order to obtain the required number of electrorotational spectra needed to determine average values for the cell properties at each time point, this entire procedure was repeated three times.

A rotation spectrum for an uninfected BHK(C-13) cell is shown in figure 1a. This cell had been cultured to confluence before being physically removed from the culture dish surface and its spectrum recorded. At a medium conductivity of 17.5mSm^{-1} the cell exhibits an anti-field rotation peak at approximately 30kHz. The best fit to the data obtained using a single shell model is shown by the solid line, and for this particular cell the parameter set used to obtain this fit is given by: $C_{spec} = 2.30\mu F/cm^2$, $\sigma_{int} = 0.23 Sm^{-1}$ and $\varepsilon_{int} = 61\,\varepsilon_o$ with $a = 6.7\mu m$.

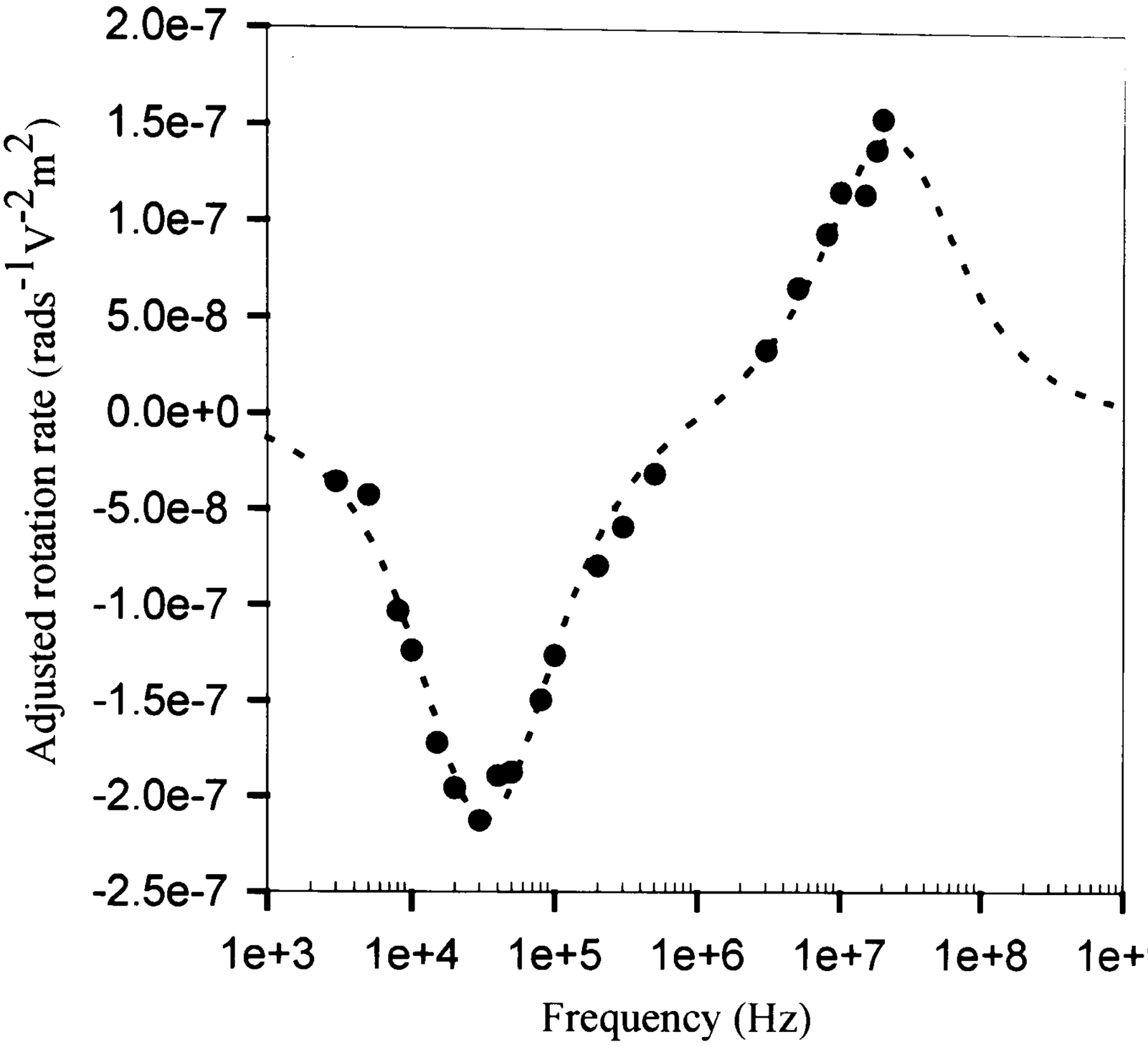

Figure 1a. A typical electrorotation spectra for an uninfected BHK(C-13) cell. The solid line represents the best fit to the experimental data. The best fit dielectric parameters for this particular cell were: $Cspec$ = 2.30 μF/cm^2, $\varepsilon_{int} = 61\varepsilon_0$ and σ_{int} = 0.23 Sm^{-1}. The regression coefficient was $\rho = 0.994$.

A typical electrorotation spectrum for a BHK cell 18 hours post-infection is shown in figure 1b, and in this case a best to a single shell model fit was obtained with: $C_{spec} = 1.52\mu F/cm^2$, $\sigma_{int} = 0.45 Sm^{-1}$ and $\varepsilon_{int} = 46\,\varepsilon_o$ with a = 6.8μm. This data shows that (for the same medium conductivity) the infected cell exhibits an anti-field rotation peak at approximately 50kHz.

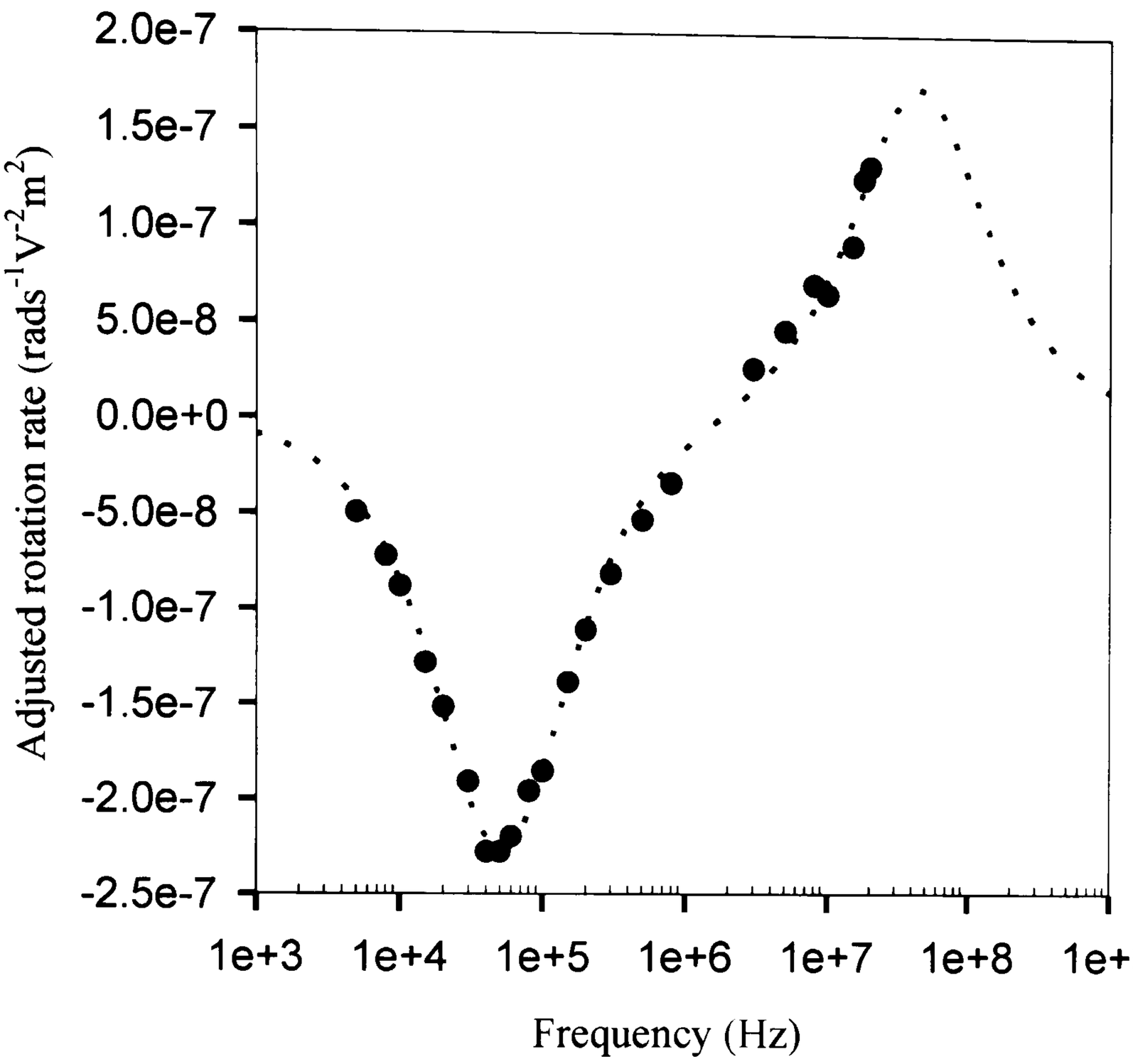

Figure 1b. A typical electrorotational spectrum for a BHK(C-13) cell, 18 hours after infection with HSV-1 at 10pfu. Solid line represents the best fit to the experimental data. The best fit dielectric parameters derived for this particular cell were: *Cspec* = 1.52 μF/cm^2, ε_{int} = 46ε_0 and σ_{int} = 0.45Sm^{-1}. The regression coefficient was ρ = 0.996.

4.1.2 Verification of cell model

Experimental data was fitted to theory using the spherical single-shell model that treats the cell as a solid particle (the cytoplasm plus nucleus) surrounded by a thin insulating membrane. A spherical double shell model of a cell consists of the concentric spheres starting with the nucleus, followed by the nuclear membrane, the cytoplasm and the plasma membrane. In this model a total of

eight dielectric parameters is needed to describe a cell, compared to the four parameters needed to define a single shell model.

The nucleus of a BHK(C-13) cell has a diameter 0.5 times that of the whole cell. The nuclear membrane would be expected to have dielectric parameters that are similar to that of the plasma membrane, while the interior of the nucleus would be expected to have dielectric parameters similar to those of the cytoplasm. Assigning these values, as well as those of the cytoplasm and the plasma membrane to a double shell model, as well as generating a single shell model of the cell that ignores the nucleus allows a comparison of the Clausius-Mossotti factor generated by a single shell and a double shell model to be performed. The effect of using the double shell model as compared with single shell model is shown in figure 2. From the figure it is clear that a nucleus has little effect on the Clausius-Mossotti factor.

A further complication in determining the dielectric parameters of the nucleus is that a double shell model contains eight independent dielectric parameters, but from a curve with two peaks it is only possible to obtain four independent parameters [1]. *Holzel* [2] overcame this problem by building a signal generator capable of sweeping the frequency window from 100Hz to 1.6GHz and an electrode chamber in which it was possible to adjust the conductivity of the suspending medium while retaining the same cell in the electrode array. This enabled the author to take electrorotational data at four different medium conductivities and thus obtained enough data to derive the eight independent dielectric parameters of a double shell model. However, the extra complications involved in obtaining the data needed to derive all the dielectric parameters make it unpractical to use the double shell model.

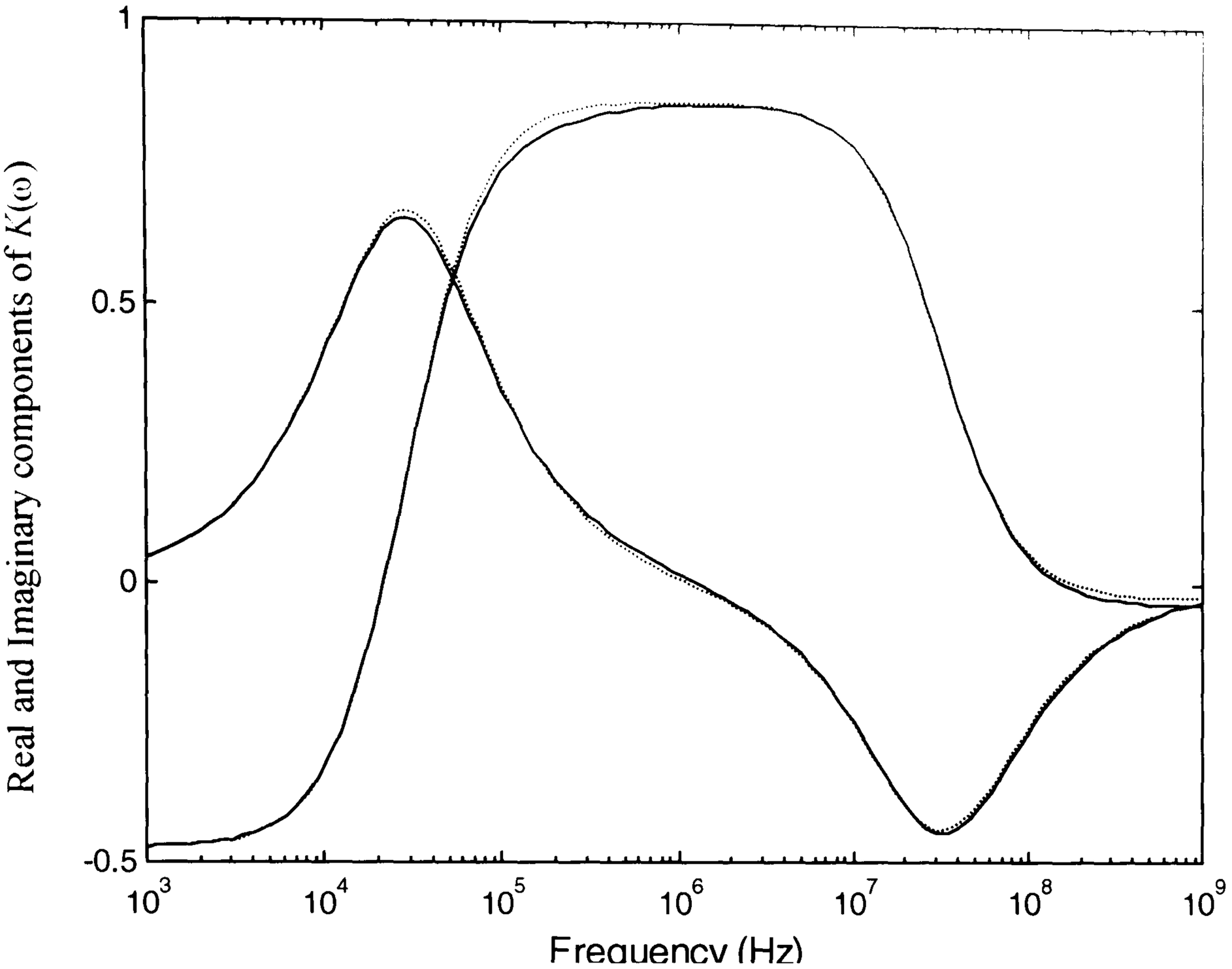

Figure 2: Comparison of the Clausius-Mossotti factor generated using a single shell model (dashed line) and a double shell model (solid line) of a BHK(C-13) cell.

4.2 Protein profiles

To confirm that the cells being analysed in the electrorotation studies were properly infected, protein synthesis was analysed by labelling the cells with [^{35}S]methionine. The protein profiles at times 0, 6, 9, 12, 18, and 26 hours post-infection are shown in figure 3, with several of the more prominent virus specific proteins labelled (this work was performed by Dr F.J. Rixon). As expected, viral proteins, including structural components of the capsid (VP5), tegument (VP16 and VP22), and envelope (gB), are present in increasing amounts from 6 hours post-infection. The time course of protein synthesis is typical for HSV-1 infected BHK cells [3] and demonstrates that the infection is progressing normally under these experimental conditions.

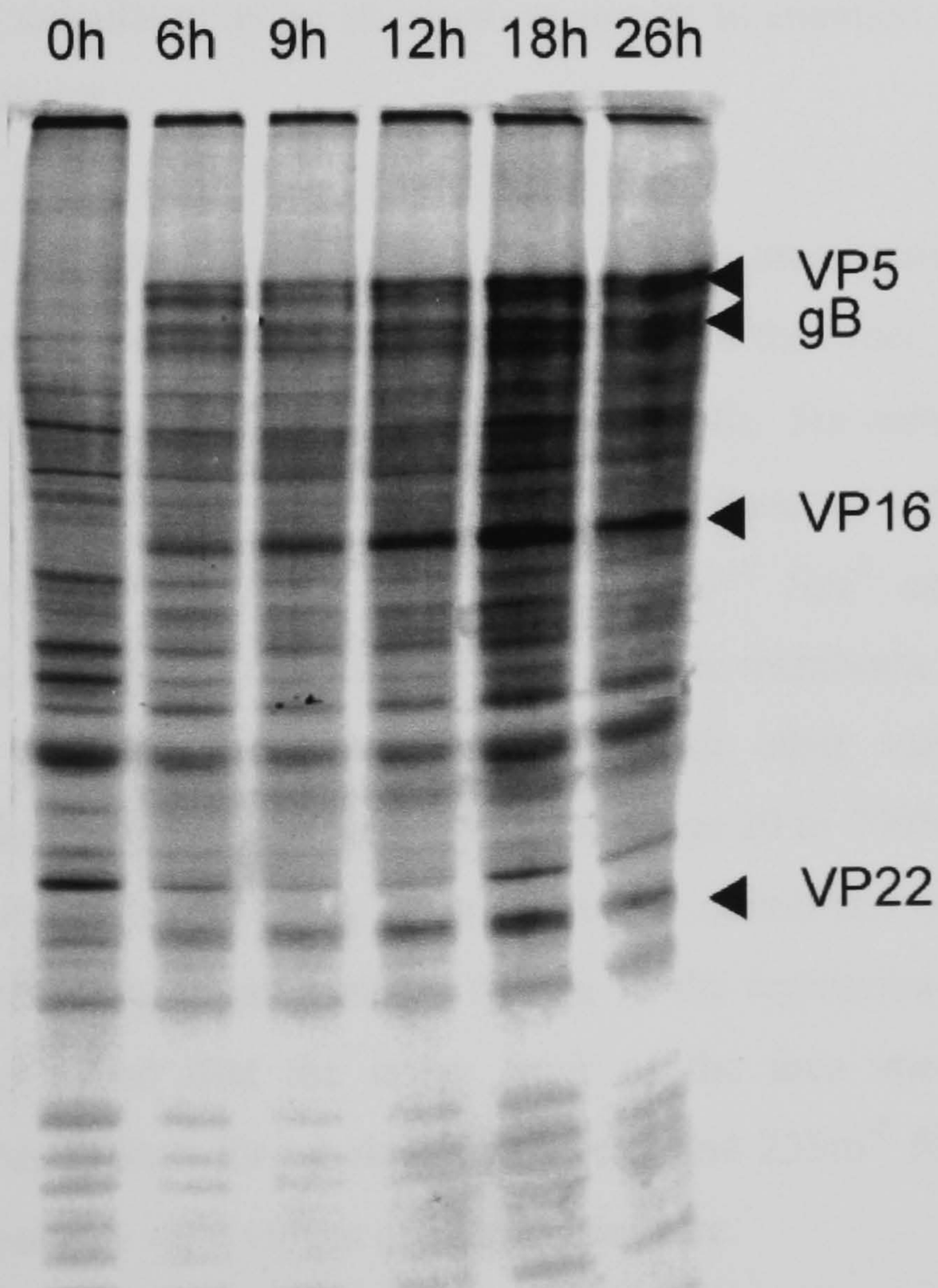

Figure 3. Protein profiles of HSV-1 infected BHK(C-13) cells. The figure shows the protein profiles for the cells at time 0, 6, 9, 12, 18, and 26 hours post-infection and structural components of the capsid (VP5), tegument (VP16 and VP22), and envelope (gB), are present in increasing amounts from 6 hours post-infection.

4.3 Membrane conductivity

The crossover frequencies of individual mock infected BHK(C-13) cells are given in figure 4a, while the crossover frequencies of BHK(C-13) cells infected with HSV-1 for 18 hours are given by figure 4b. In both figures the fitted data points are also shown along with a plane that gives the best fit of crossover frequency with respect to cell radius and medium conductivity. It can be seen that in both cases the crossover frequency increases, as the medium conductivity increases, as expected from equation (7), background and methods chapter. Analysis of the dependence of the crossover frequency on the suspension medium conductivity, cell size and cell dielectric parameters using a minimisation algorithm as used to obtain the cell dielectric parameters. In order to quantify the accuracy of the best fit to the experimental data, a regression coefficient was calculated using an equation similar to equation (4), background and methods chapter

The best fit to the data was obtained with a specific membrane capacitance of $1.75\mu Fm^{-2}$, an area specific membrane conductivity of the order 10^{-10} Sm^{-2} and a regression coefficient of 0.9025 for mock infected cells. For cells infected for 18 hours the algorithm gave a specific membrane capacitance of $1.49\mu Fm^{-2}$, an area specific membrane conductivity of the order 10^{-10} Sm^{-2} and a regression coefficient of 0.9642. A value for the area specific membrane conductivity of the order of 10^{-10} Sm^{-2} does not compare with other values quoted for mammalian cells [4-6], where values are in the range 20 to $700Sm^{-2}$. In order to check the sensitivity of the fit to the area specific membrane conductivity, this factor was increased gradually until a change in the regression coefficient was noted. It was found that the upper limit of the area specific membrane conductivity was $11Sm^{-2}$ for mock infected cells and $23Sm^{-2}$ for infected cells, comparing favourably with values quoted in literature.

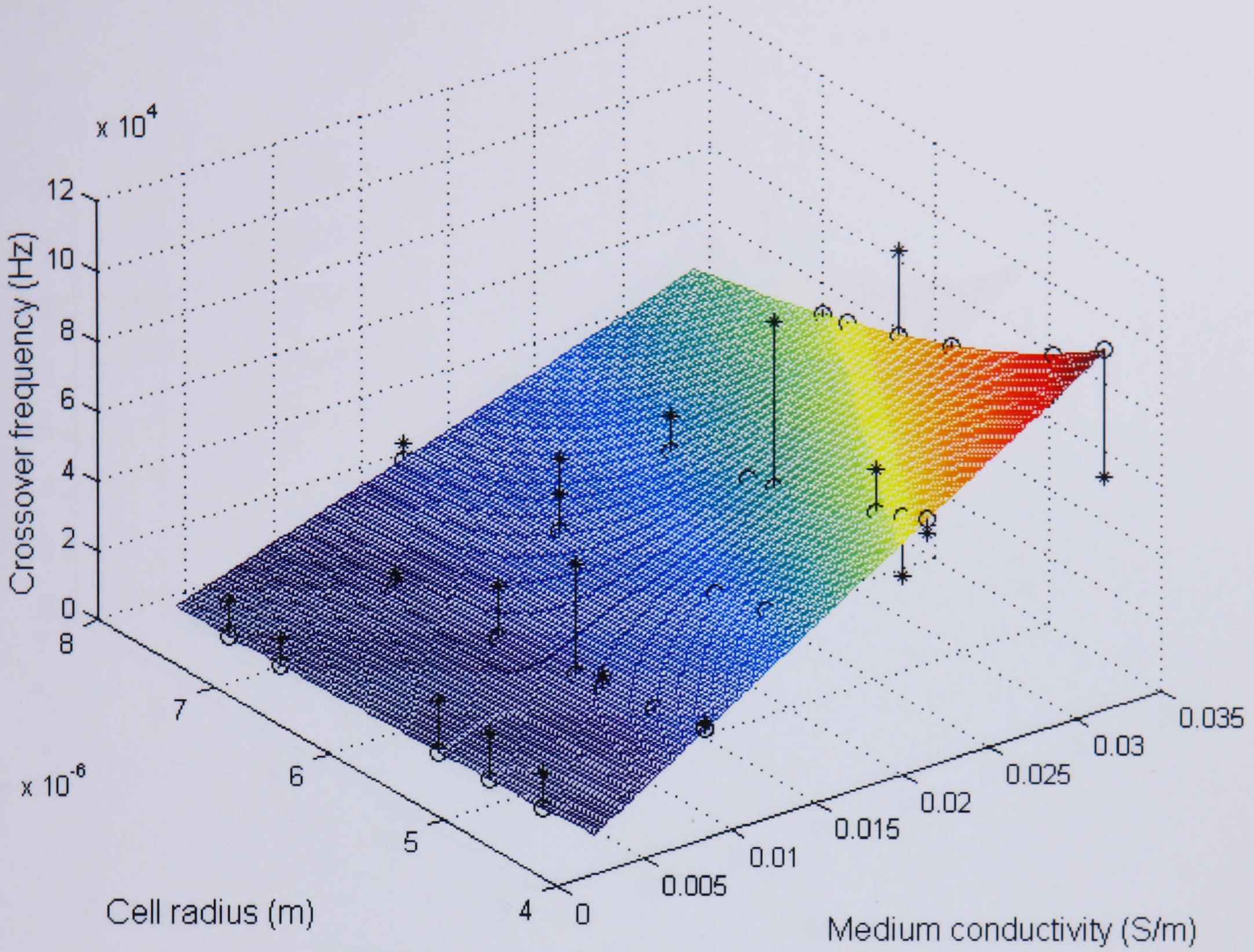

Figure 4(a). The dependence of the dielectrophoretic crossover frequency of mock infected BHK(C-13) cells on medium conductivity and cell size. The data points are represented by '*', the fitted points by 'o'. The cell dielectric parameters obtained were specific membrane capacitance of 17.5mFm^{-2} and the area specific membrane conductivity for mock-infected cells was <11Sm^{2}, for a regression coefficient of 0.9025

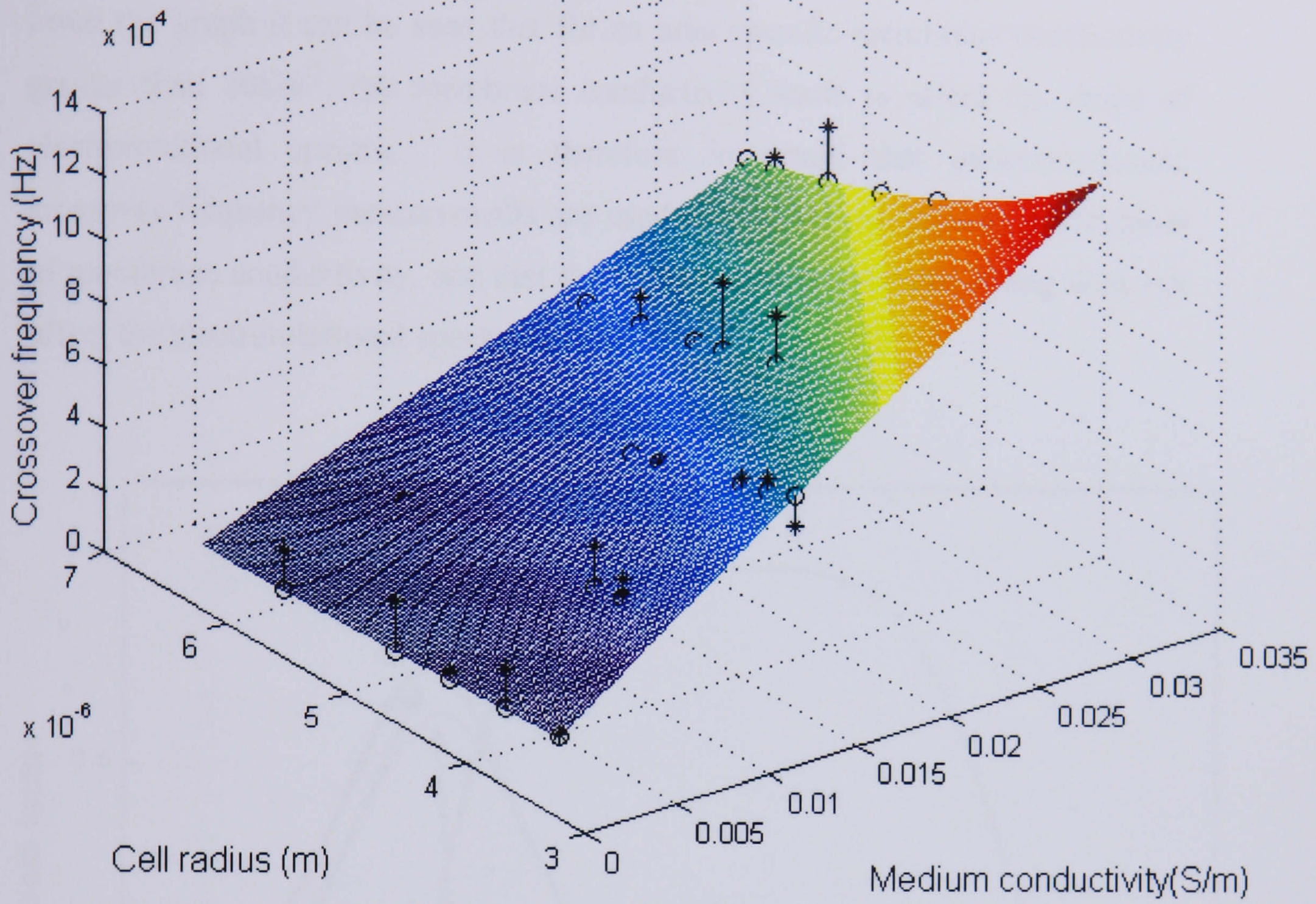

Figure 4(b). The dependence of the dielectrophoretic crossover frequency of BHK(C-13) cells infected for 18 hours on medium conductivity and cell size. The data points are represented by '*', the fitted points by 'o'. The cell dielectric parameters obtained were specific membrane capacitance of 14.9mFm^{-2} and the area specific membrane conductivity for mock-infected cells was <23Sm^{2}, for a regression coefficient of 0.9642

Applying curve fitting techniques to the data for the dielectrophoretic crossover frequency of BHK(C-13) cells (both prior to infection with HSV-1 and 18 hours post infection) showed that the membrane conductivity was very low. The specific membrane capacitance obtained was within the range of the values obtained for the corresponding time points using electrorotation measurements (see figure 6). During curve fitting of the electrorotational data the membrane conductivity was fixed at $\sigma = 5 \times 10^{-7}$ Sm^{-1}, corresponding to an area specific conductivity of 70Sm^{-2}. However, as can be seen from figure 5, values for the area specific membrane conductivity of less than 70Sm^{-2} do not significantly

affect the electrorotational spectrum of a cell when suspended in a medium with a conductivity of $17.5mSm^{-1}$.

From the graph it can be seen that for an area specific membrane conductivity greater than $70Sm^{-2}$, the membrane conductivity starts to affect the shape of electrorotational spectra. It is therefore important that dielectrophoretic crossover frequency measurements are used to give an independent verification of membrane conductivity, and that the value used during curve fitting does not affect the electrorotational spectrum.

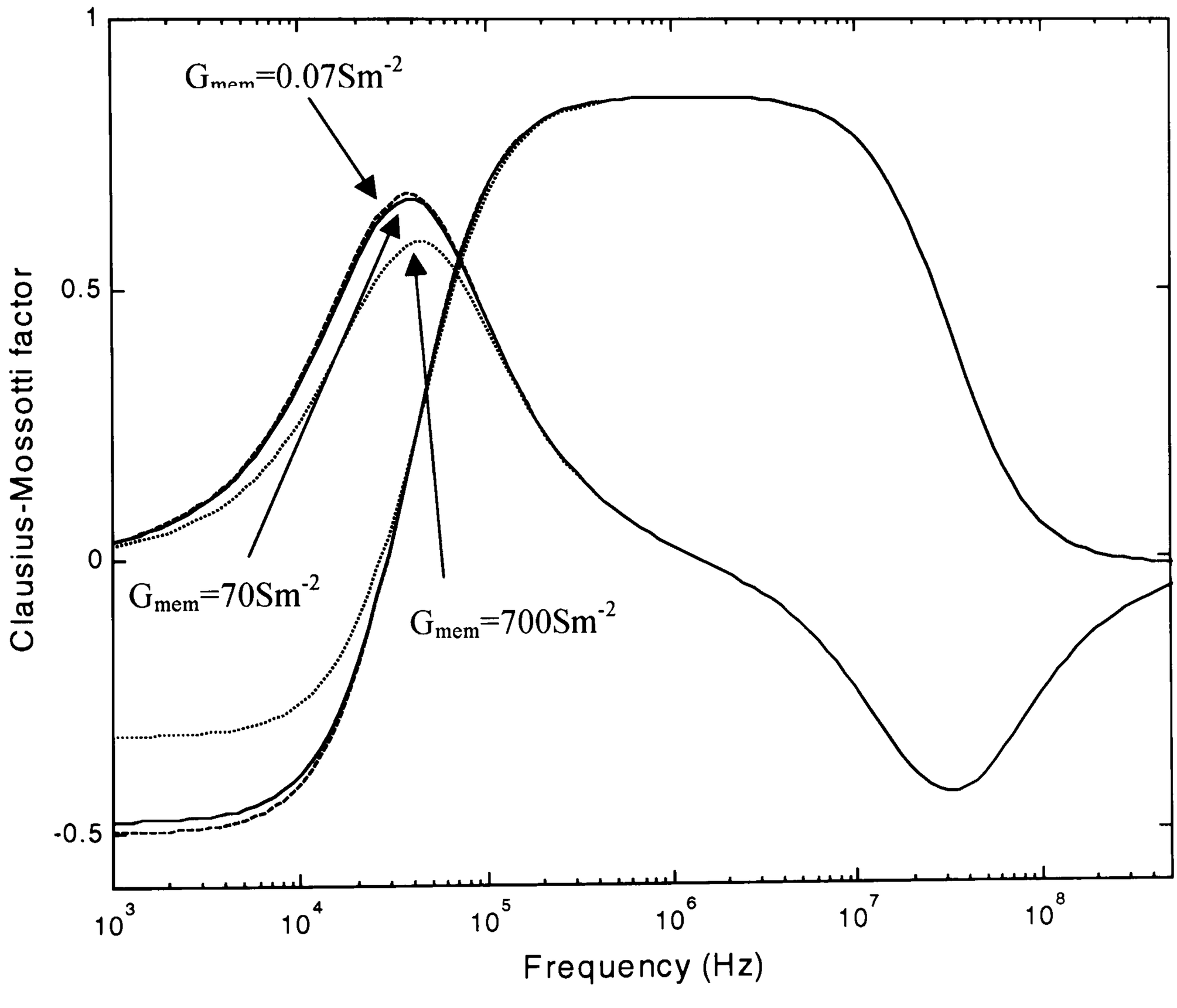

Figure 5: Variations in the Clausius-Mossotti factor for a mock infected BHK(C-13) cell with variations in the membrane conductivity. The membrane conductivity was set at $G_{mem}=0.07Sm^{-2}$, $70Sm^{-2}$ and $700Sm^{-2}$. It can be seen it is only for G_{mem} greater than $70Sm^{-2}$ that the membrane conductivity has a significant effect on the Clausius-Mossotti factor.

4.4 Specific membrane capacitance

The time dependent changes in the specific membrane capacitance of BHK(C-13) cells following infection for both the interrupted and the continuous time courses are plotted in figure 6. The data plotted in this figure represents the mean of the specific membrane capacitances with standard errors shown. The membrane thickness, *d*, was set at 7nm to obtain this data.

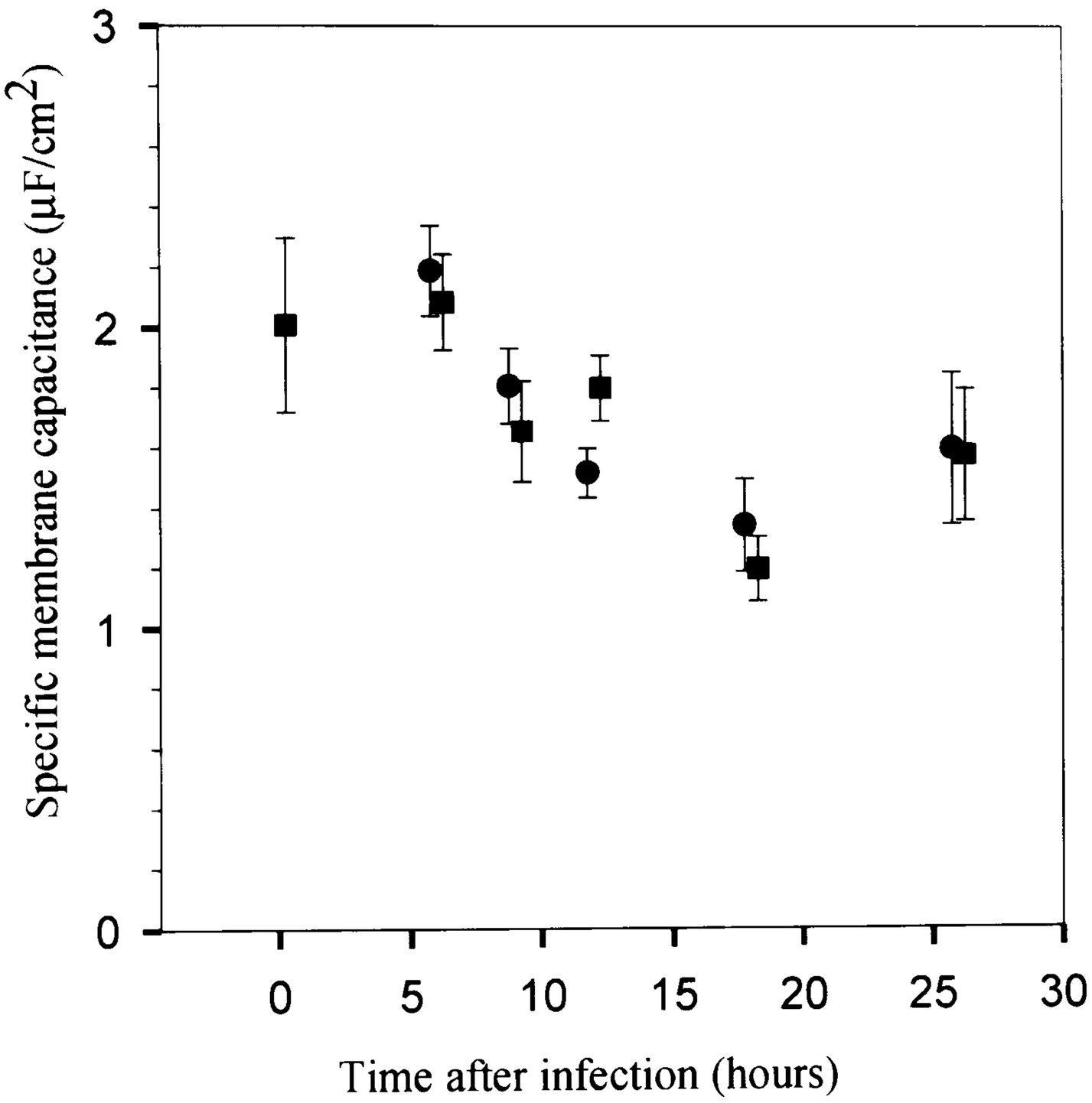

Figure 6. Plot of the change in the specific membrane capacitance of BHK(C-13) cells following infection with HSV-1. The symbol (•) denotes the continuous while (▪) denotes the discontinuous time course experiments. For clarity the points have been offset on the time axis by +0.25h for the discontinuous and -0.25h for the continuous time course. Vertical bars show the standard error.

It can be seen from figure 6 that a gradual decrease in the specific membrane capacitance of the cells occurs with time after infection with HSV-1. The same decrease is observed for both the interrupted and the continuous time course experiments. The capacitance of the uninfected cells is 2.0μF/cm^2, and this decreases to 1.6-1.8μF/cm^2 at 9 hours post-infection. There was a steady decrease with time up to 18 hours after infection, when the capacitance reached 1.25μF/cm^2. The specific membrane capacitance then increased again to a final value of 1.5μF/cm^2, 26 hours post-infection.

4.5 Surface morphology and membrane composition

Implicit in the single shell model is the assumption that the surface is smooth. However, as can be seen from the SEM of a cell surface in figure 7, the surface of a real cell differs considerably from the ideal.

Figure 7: A SEM image of a BHK cell. It clearly shows that the membrane of a cell is not smooth, rather it consists of a large number of invaginations and irregularities.

The cell membrane is composed of a lipid bilayer, with a number of biomolecules such as cholesterol and ion channels spanning part of or the whole thickness of the membrane. In electrical terms these different regions can be modelled as a number of separate electrical components in parallel so that the specific membrane capacitance can be described by the following simple expression [7]:

$$C_{spec} = \alpha C_{lip} + (1-\alpha) C_{other} \qquad (1)$$

where α is the fraction of the cell surface composed of lipid bilayer, and the subscripts "lip" and "other" refer to the lipid bilayer and other components (biomolecules) respectively. A schematic representation of the changes in a plasma membrane as a result of various biomolecules spanning the whole or part of the lipid bilayer is given in figure 8.

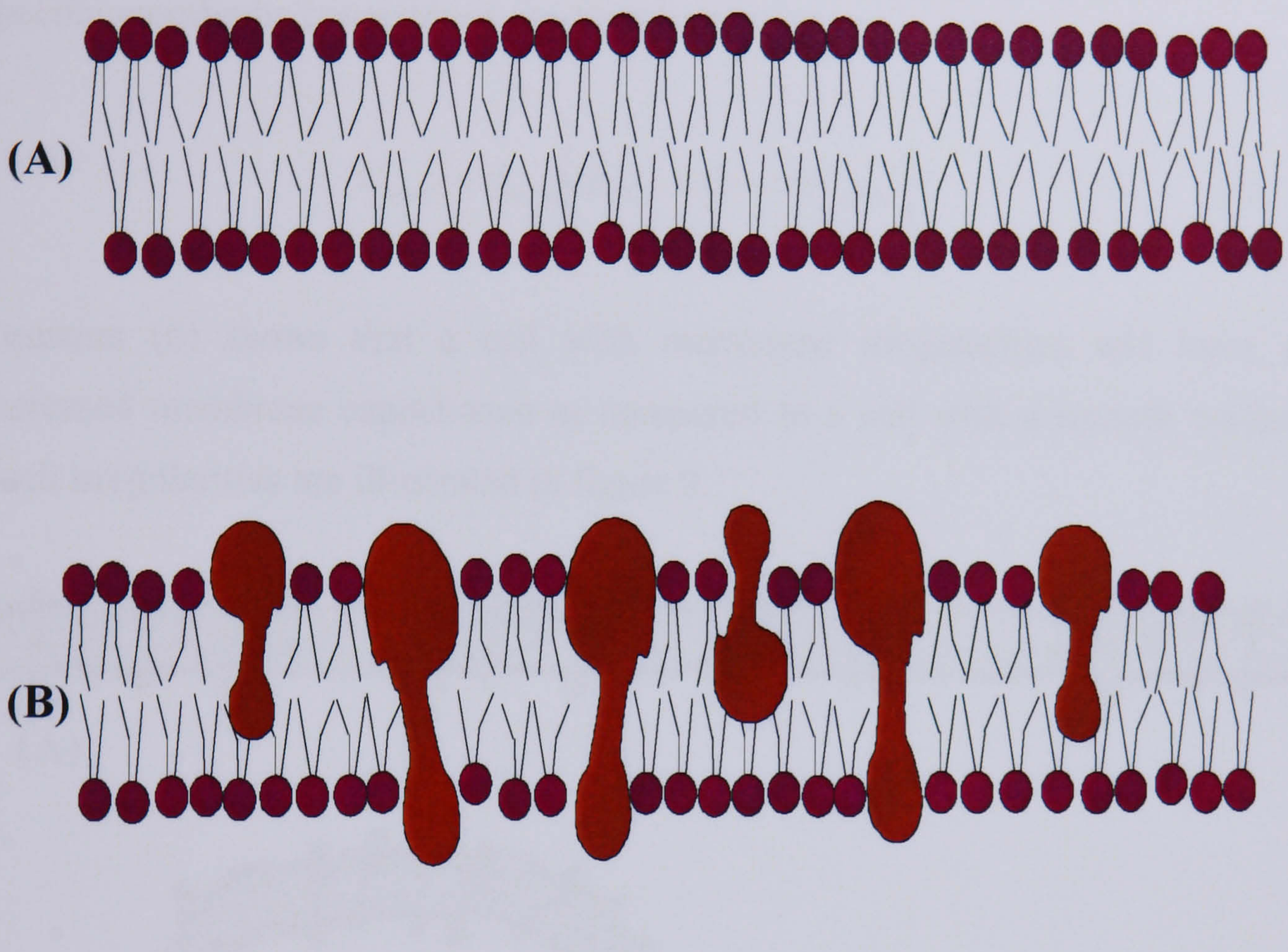

Figure 8: A schematic representation of the lipid bilayer of a cell. Figure 8(A) shows a membrane consisting solely of a lipid bilayer, corresponding to $\alpha = 1$. Figure 8(B) shows a membrane that is composed to a mixture of biomolecules and the lipid bilayer. This corresponds to $\alpha < 1$.

It has been estimated for mammalian cells [7] that values for these membrane parameters are $C_{lip} = 0.78\mu F/cm^2$ and $C_{other} = 1.04\mu F/cm^2$. Assuming that typically 60% of the membrane surface consists of biomolecules other than the lipid bilayer (i.e. α=0.4), then the value of $C_{spec} = 0.94\ \mu F/cm^2$, which is too low to account for the measured values for BHK(C-13) cells. The maximum C_{spec} allowed by the model is with α=0, i.e. $C_{spec} = 1.04\mu F/cm^2$, compared to values of $C_{spec} = 2.01\mu F/cm^2$ obtained for BHK cells. Thus, in general, this approach is

inadequate to explain the observed magnitude of specific membrane capacitance measured for the BHK(C-13) cells.

In order to account for such discrepancies, the concept of a folding factor ϕ_{mem} was proposed [8] to take into account that, due to features such as microvilli, folds, ruffles and blebs, a cell surface is highly irregular and invaginated. The specific membrane capacitance can then be written as:

$$C_{spec} = \phi_{mem}\left[\alpha C_{lip} + (1-\alpha)C_{other}\right] \qquad (2)$$

Equation (6) shows that a cell with membrane irregularities will have an increased membrane capacitance as compared to a cell with a smooth surface. Such irregularities are illustrated in figure 9.

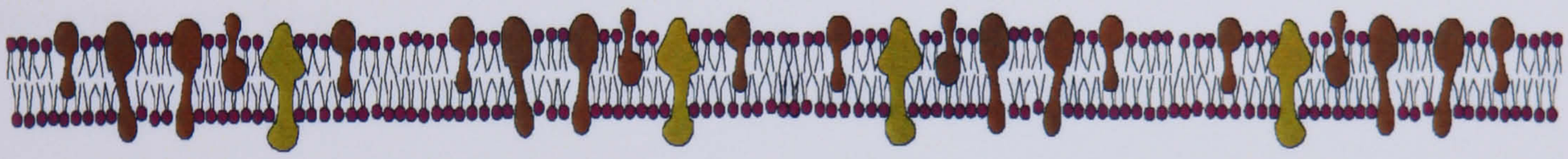

(A)

(B)

Figure 9: Schematic representation of the plasma membrane of a cell. It shows the differences in the membrane folding factor for a smooth cell (figure 9(A)), with $\phi_{mem} = 1$ and for a cell with a surface containing invaginations and irregularities (figure 9(B)), where $\phi_{mem} > 1$.

The membrane of a BHK cell contains a number of different proteins. which span part of or the whole thickness of the membrane. Such a membrane would be expected to have a high membrane capacitance (since α would be low). The herpes virus particle contains 12 or more integral envelope proteins. As infection proceeds, these proteins are synthesised in increasing amounts and most are inserted into cellular membranes including the plasma membrane [9]. In parallel with this process, synthesis of many host cell proteins is inhibited. Consequently, as infection progresses the composition of the cell membrane tends to approach that of the viral envelope. Viral glycoproteins are known to span the viral envelope but, however, as the virus is non-metabolising, there are no ion channels in its envelope. Thus it is possible that the viral membrane may have a lower membrane capacitance than the BHK(C-13) cell membrane. The reduction in the specific membrane capacitance of the plasma membrane throughout infection may therefore reflect the convergence of its properties towards those of the virus envelope.

4.6 Scanning Electron Microscopy

The time dependent changes in the membrane folding factor following virus infection were observed by SEM. Examples of mock-infected cells and infected cells at times 9, 18 and 26 hours post-infection are shown in figure 10.

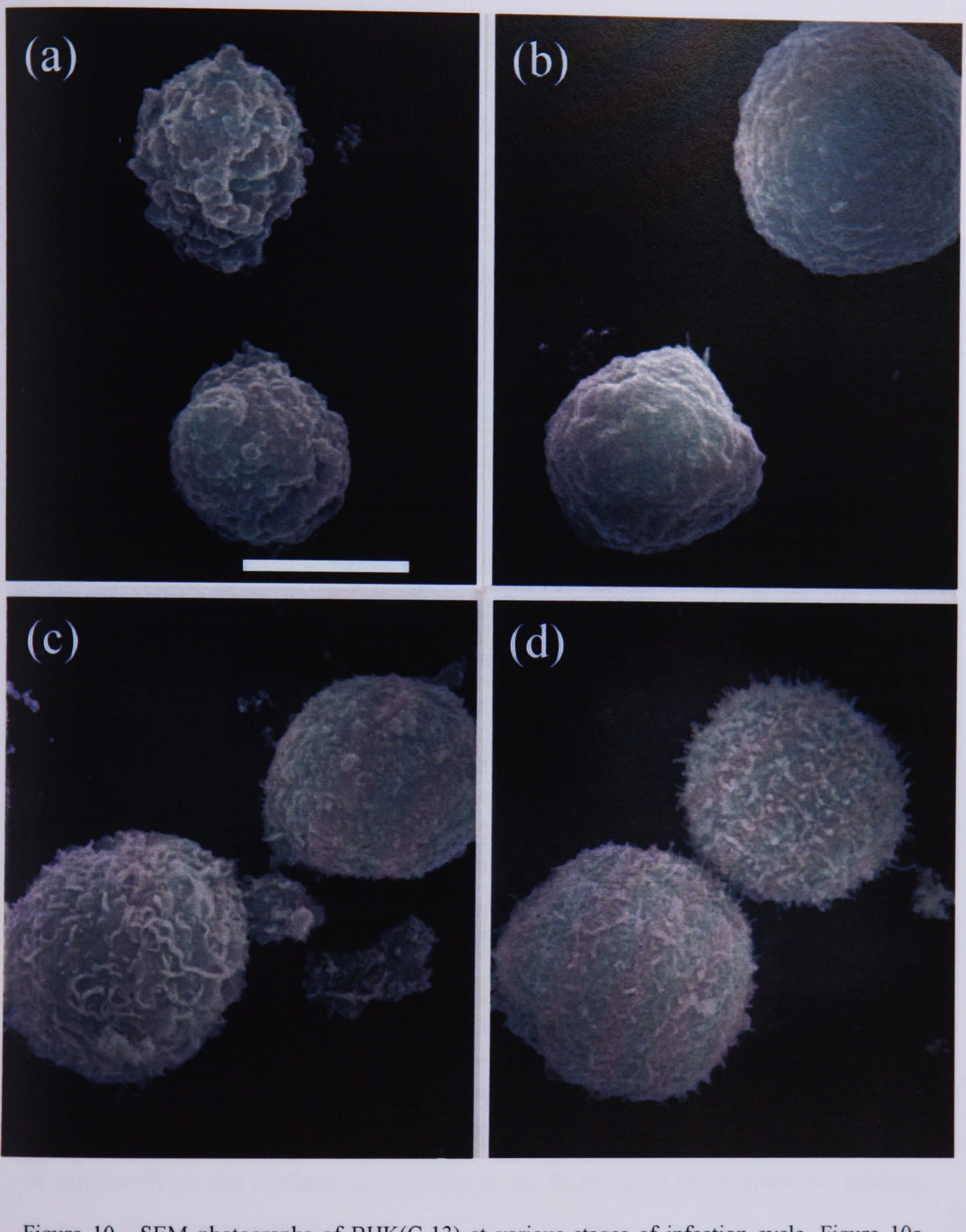

Figure 10. SEM photographs of BHK(C-13) at various stages of infection cycle. Figure 10a shows an uninfected BHK(C-13) cell, whilst the remaining BHK(C-13) cells were infected with 10pfu/cell for HSV-1 for 9h (figure 10b), 18h (figure 10c) and 26h (figure 10d). All cells were harvested and prepared for microscopy as described in Methods. The scale bar represents 6μm.

These images reveal that there are no dramatic changes in the overall appearance of the cells following infection. However, differences in their surface morphologies can be seen at the different times. Thus, in comparison with infected cells, uninfected cells (figure 10a) are less uniformly spherical and have a surface membrane that has few microvilli but shows evidence of large scale irregularities, such as folds and ruffles. Cells that have been infected for 9 hours (figure 10b) are rounder and have membranes that exhibit greater roughness, on a small scale, than uninfected cells. There is an increase in the number of microvilli, and there seems to be a reduction in the large scale features apparent in the uninfected cells. These changes are even more pronounced at 18 and 26 hours post-infection (figure 10c and d), where the cell surface is uniformly rounded with a further increase in the number of microvilli, as time progresses.

From the images shown in figure 10 there appear to be two factors that affect the cell folding factor throughout the life cycle of the virus. Mock-infected cells have a surface with large-scale irregularities but relatively little small-scale roughness due to microvilli. After infection the shape of the cells becomes more uniform; the large-scale is lost and microvilli become increasingly evident. The reduction in the large-scale irregularities with time would be expected to reduce the membrane folding factor, while an increase in the appearance of microvilli would cause a small increase. Another possible reason for the drop in the membrane capacitance is that the composition of the cell membrane changes during the infection cycle, tending towards the properties of the viral envelope.

A small increase in the specific membrane capacitance of the cells occurs at the end of the virus life cycle. This could be due to a further increase in the number of microvilli on the surface; giving rise to an increase in the membrane folding factor at 26 hours post-infection.

4.7 Mixture theory applied to progeny virions

When viruses reach the surface of a cell thorough exocytosis, large amounts of progeny virions can be found on the cell surface. Assuming they are closely packed as many as 10^4 virions would be needed to cover the surface of a cell. Changes in the dielectrophoretic and electrorotational spectra of BHK(C-13) cells (in a suspending medium of conductivity 17.5mSm^{-1}) with virions on the cell surface modelled using the method outlined in section 5.7 (background and methods chapter). The result of the modelling is shown in figure 11. Curves (a) shows the case for zero viruses, whilst curves (b) and (c) are for 5,000 and 10,000 viruses on the cell surface respectively. It can be seen from the figure that there is a 9% reduction in the dielectrophoretic force on the cell when 5,000 virions are present on the surface. This number is representative of the number of virions which would be expected to be made by the host cell and might be found on the surface of a cell following exocytosis. With 10,000 virions on the cell surface, there is a marked change in both the dielectrophoretic and electrorotational spectra. This change is not seen in our electrorotation data and indicates that the presence of such large numbers of virus particles, although theoretically possible, is unlikely to occur in practice.

The data in figure 11 indicates it should be possible to separate virus-infected cells undergoing exocytosis according to the amount of virions present on the cell using techniques such as field flow fractionation [10] which can discriminate small changes in the Clausius-Mossotti factor.

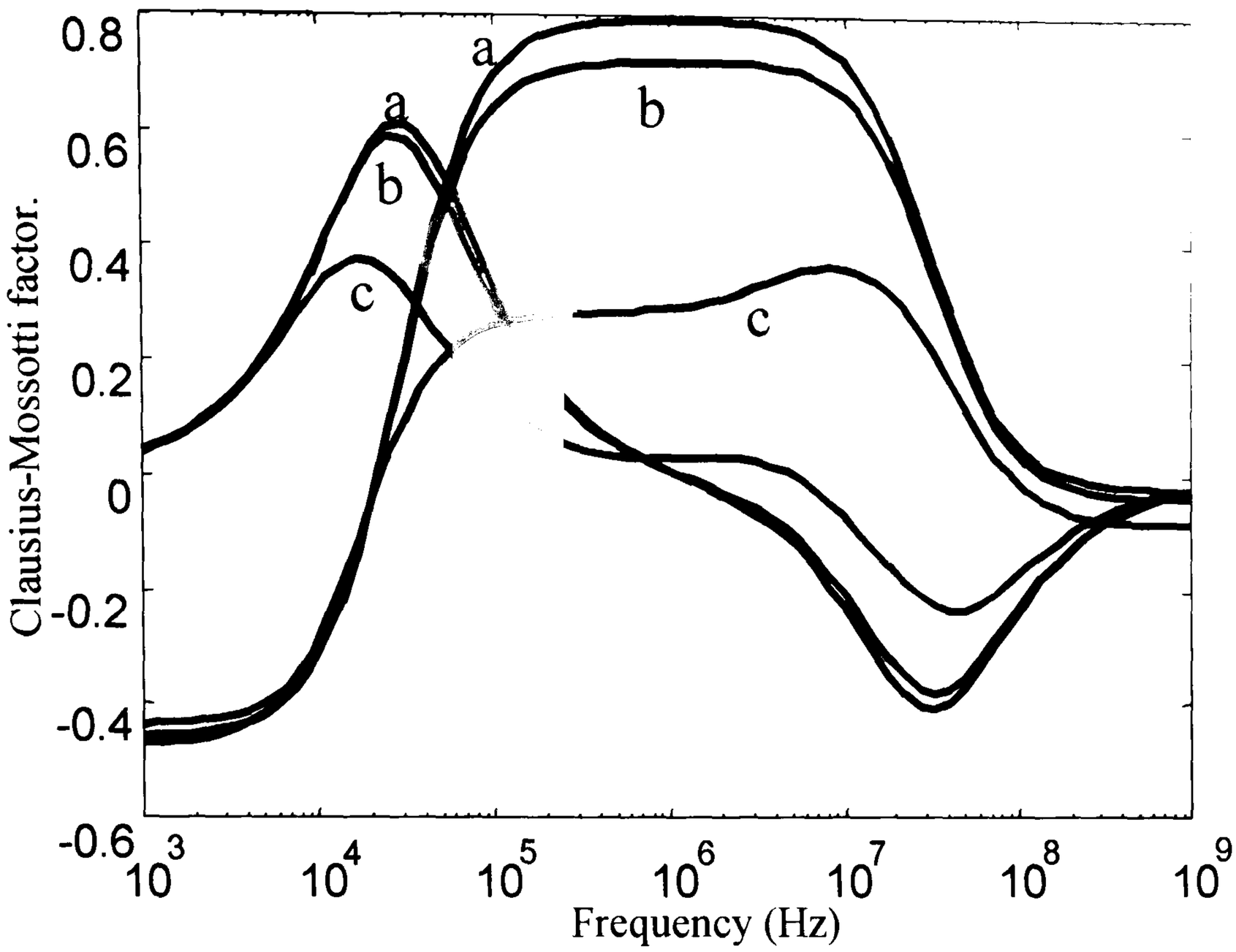

Figure: 11. The effect of HSV-1 on the surface of a BHK(C-13) cell, variations in the real and imaginary components of $K(\omega)$ with number of virions. Curves (a) shows the case for zero viruses, whilst curves (b) and (c) are for 5,000 and 10,000 viruses on the cell surface respectively.

4.8 Internal permittivity

The time dependent changes in the internal permittivity of BHK cells following infection are shown in figure 12 for both the interrupted and the continuous time course experiments. The graph represents the mean of the internal permittivities with the standard errors shown.

Owing to the limitations in the data at high frequencies, the spread in the range of values is greater than for the specific capacitance. However, the trend in the data is clear and the average internal permittivity of cells taken from both the discontinuous and the continuous time course experiments are in good agreement with each other. It can be seen that the internal permittivity of BHK cells changes with time following infection. For uninfected cells the permittivity is $\varepsilon_{\text{int}} = 75 \pm 12\,\varepsilon_o$, which is in general agreement with other literature values obtained for mammalian cells [4]. Following infection with HSV-1 the internal permittivity drops by nearly $20\,\varepsilon_o$ to a lower value of $\varepsilon_{\text{int}} = 58 \pm 10\,\varepsilon_o$ at 10 hours post-infection, thereafter remaining constant.

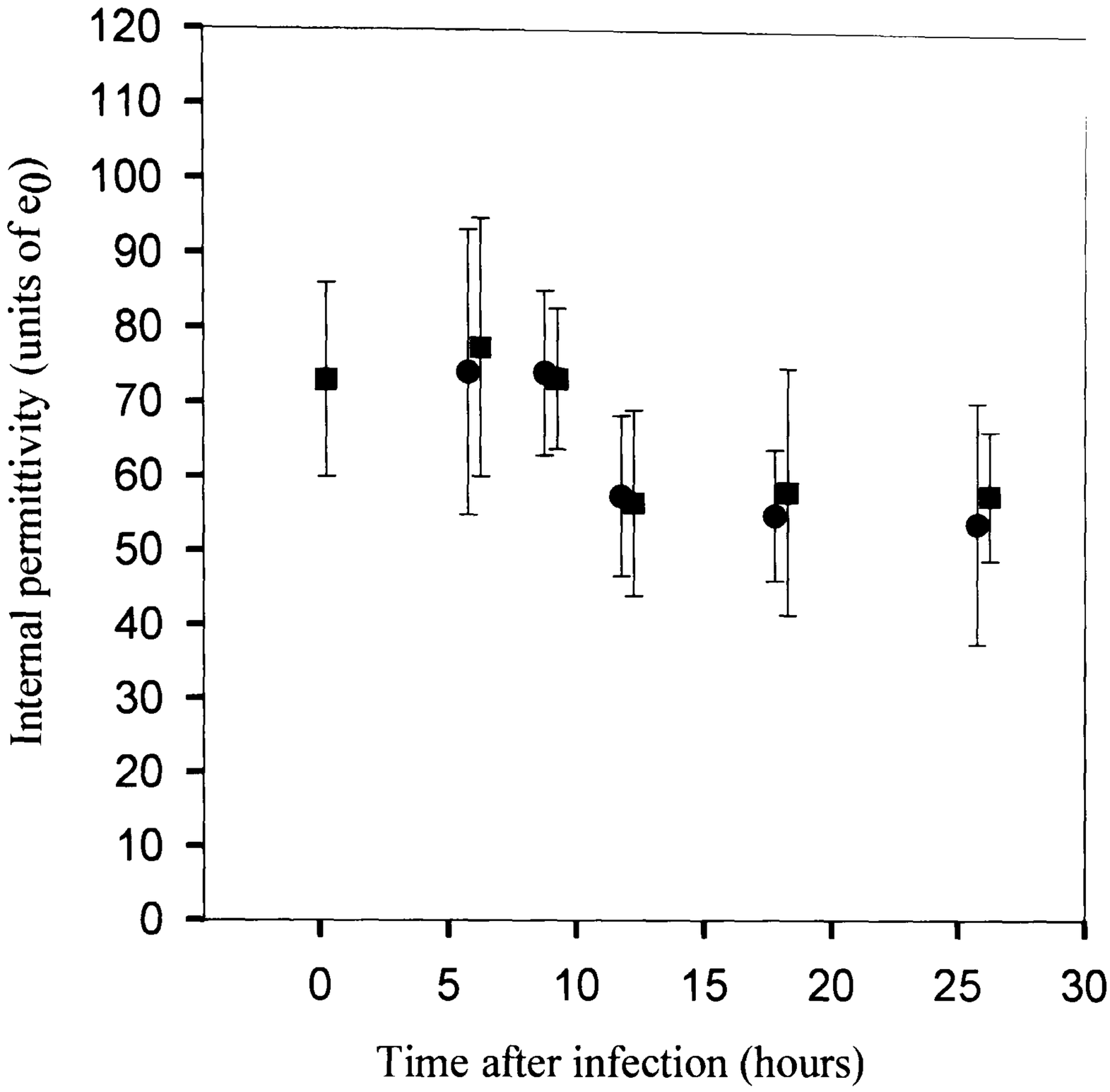

Figure 12. A plot of the time dependent change in the internal permittivity of BHK(C-13) cells following infection with HSV-1. The symbol (•) denotes the continuous while (▪) denotes the discontinuous time course experiments. For clarity the points have been offset on the time axis by +0.25h for the interrupted and -0.25h for the continuous time course. Vertical bars show the standard error.

4.9 Internal conductivity

The time dependent changes in the internal conductivity of BHK(C-13) cells following infection are shown figure 13 for both the discontinuous and the continuous time courses. The graph represents the mean of the internal conductivities with the standard errors shown. The average value for the internal conductivity remains within the range 0.3 and 0.42 Sm^{-1} throughout the infectious cycle. This value can be compared with a growth medium conductivity of $1.4Sm^{-1}$ and a suspending medium conductivity of $0.0175Sm^{-1}$.

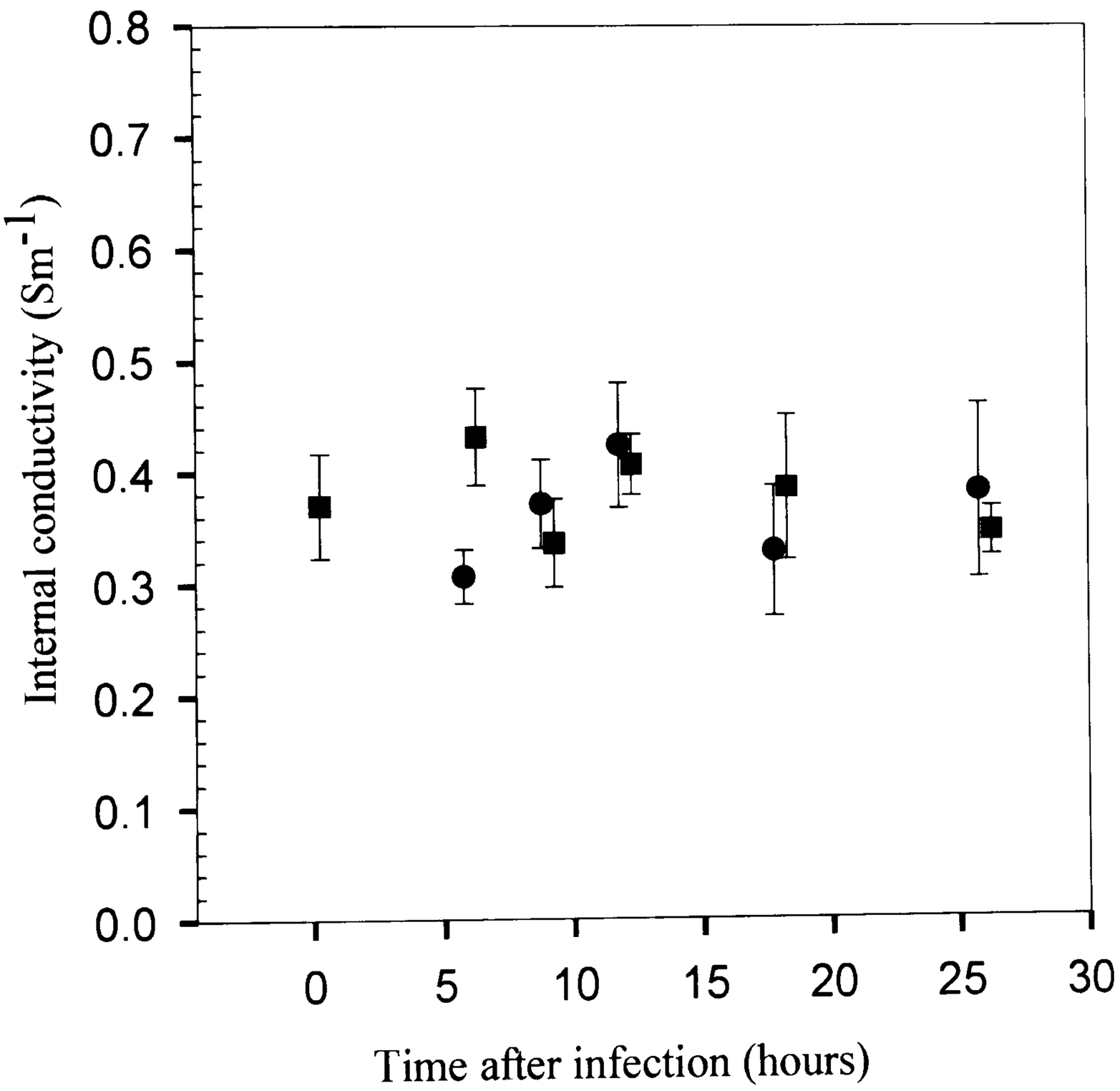

Figure 13. A plot of the time dependent change in the internal conductivity of BHK(C-13) cells following infection with HSV-1. The symbol (•) denotes the continuous while (▪) denotes the interrupted time courses. For clarity the points have been offset on the time axis by +0.25h for the interrupted and -0.25h for the continuous time course. Vertical bars show the standard error.

4.10 Mixture theory applied to cell interior

As infection progresses, increased amounts of golgi apparatus derived membrane bound structures and virions are present in the cytoplasm of cells. In order to determine the effect of these membrane bound structures on the dielectric properties of the cytoplasm, dielectric mixture theory was used. When applying dielectric mixture theory to the cytoplasm (as outlined in section 5.8, background and method chapter), the vacuoles were modelled as membrane bound spheres 1μm in diameter of identical capacitance and conductivity as an infected cell. The vacuole interior was assumed to consist of a medium (with dielectric parameters identical to the cytoplasm of an uninfected cell) and a volume fraction equal to 0.4 of virions. The exact value of this volume fraction does not affect the final outcome of the modelling and is therefor an arbitrary choice. The dielectric parameters of the enclosed virions were obtained from Hughes *et al* [11]. Dielectric mixture theory was used to model the dielectric parameters of the cytoplasm with increasing amounts of membrane bound structures in the form of vacuoles. The results were compared with the dielectric parameters obtained from the electrorotational spectra using a single shell model.

The results can be seen in figure 14, which shows that as the volume fraction of the membrane bound structures (in the form of vacuoles) increases, the value of the permittivity of the interior drops (for frequencies greater than approximately 10^4Hz). Also the conductivity of the interior decreases. The permittivity is lowered because the membrane bound structures have a lower permittivity than the remainder of the cytoplasm. The conductivity is lowered because the membranes have a very low conductivity, which causes the overall conductivity of the interior to drop. The values for the cytoplasm calculated from dielectric mixture theory (solid lines) can be compared with the dielectric parameters obtained from curve-fitting procedures (dotted line). Another dispersion due to the presence of these structures occurs at frequencies greater than approximately 10GHz, this dispersion falls outside the frequency range of figures 14 and 15.

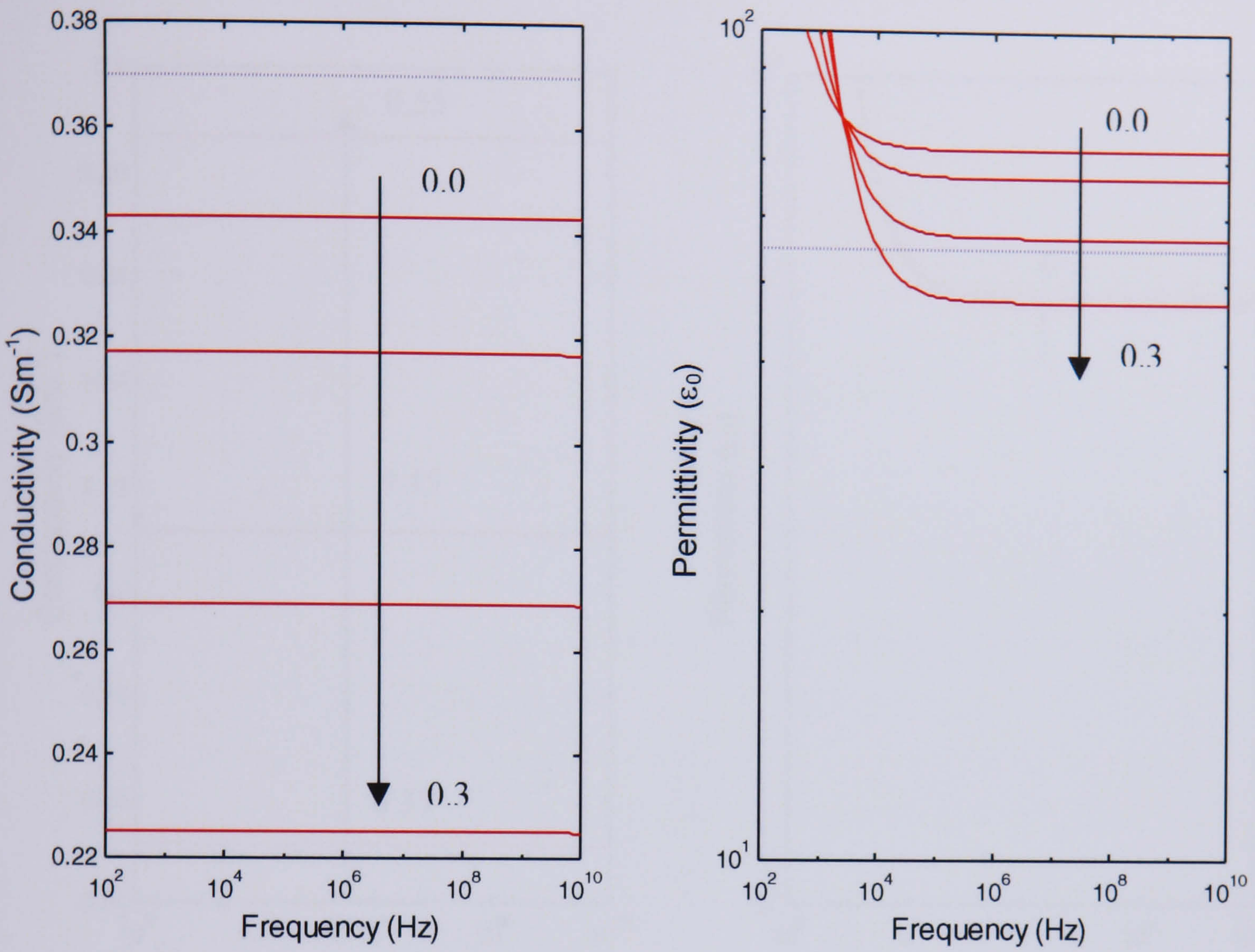

Figure 14: The changes in the permittivity and the conductivity of the interior of a BHK(C-13) cell with increasing volume fraction of membrane bound structures. The arrows indicates how the permittivity and conductivity changes as the volume fraction increases. The volume fractions used were 0.05. 0.1, 0.2 and 0.3. The dotted lines indicate the values obtained for infected cells from electrorotational data.

From figure 14 it can be seen that the conductivity of the cell interior (modelled using dielectric mixture theory) is lower than the value obtained from electrorotational spectra. This drop in the overall conductivity was compensated for by increasing the conductivity of the remaining part of the cytoplasm (the volume not occupied by the vacuoles). The results are shown in figure 15, where it can be seen that increasing this component of the cytoplasm causes the overall conductivity of the cell interior to increase, but only causes a slight increase in the permittivity of the interior.

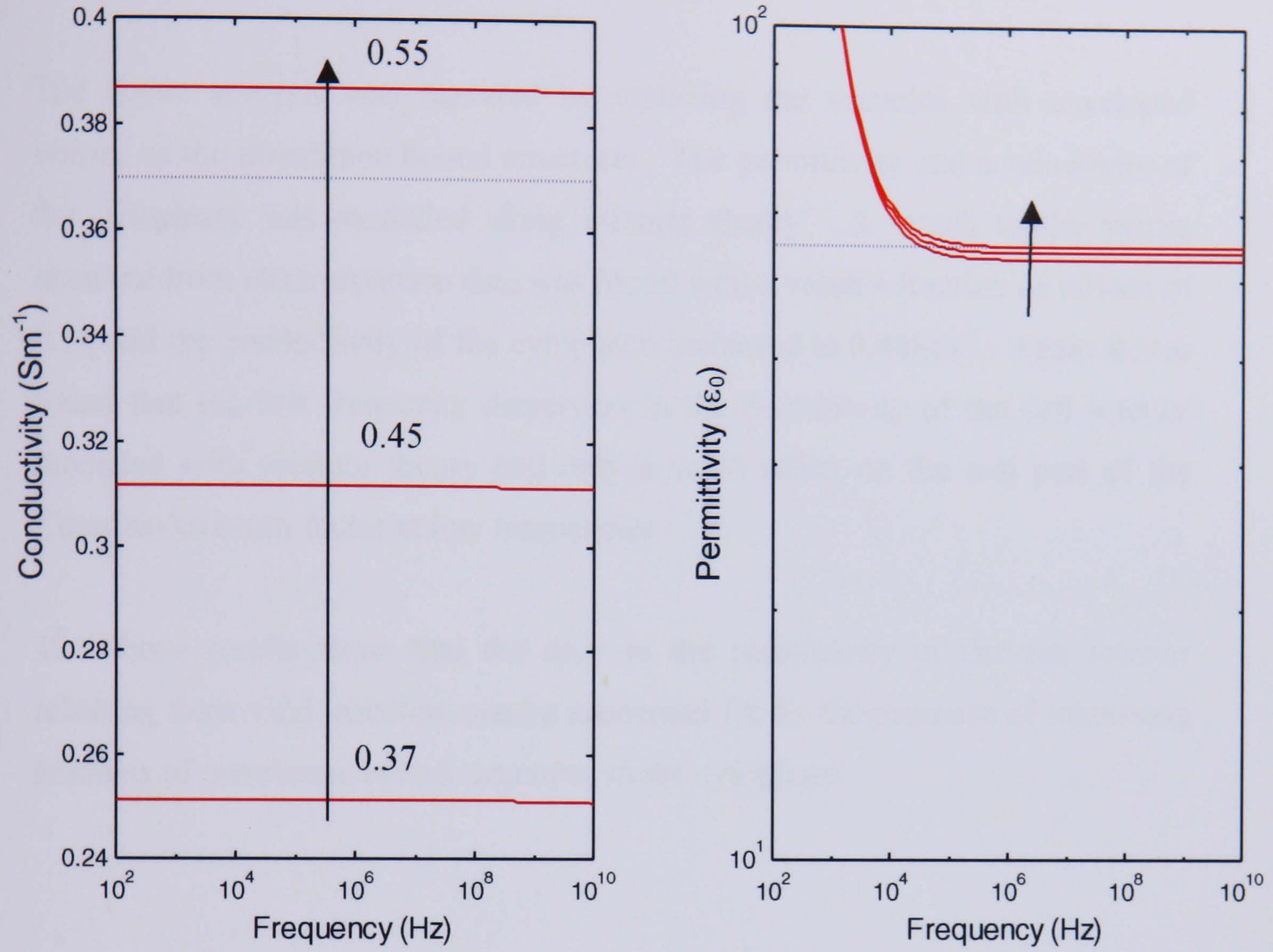

Figure 15: The changes in the permittivity and the conductivity of the interior of a BHK(C-13) cell plotted for increasing conductivity of the the cytoplasm outside the membrane bound structures. The arrows indicate how the permittivity and conductivity changes as the conductivity of the cytoplasm outside the membrane bound structures is increased. The conductivities used were 0.37, 0.45 and 0.55Sm^{-1}, while the volume fraction of vacuoles was 0.24. The dotted lines indicate the values obtained for infected cells from electrorotational data.

The best match to the dielectric parameters of the cytoplasm was obtained for a volume fraction of 0.24 for the membrane bound structures, and a conductivity of 0.53Sm^{-1} for the part of the cytoplasm outside the membrane bound structures.

The dielectric properties of the cells were measured over a frequency range from 1kHz to 20MHz. In this frequency range the low frequency dispersion in the permittivity of the cell interior that (seen in figures 14 and 15) was found to

cause only a slight increase in the magnitude of the real part of the Clausius-Mossotti factor for frequencies less than 10^4 Hz. The imaginary part of the Clausius-Mossotti factor was not affected.

The above analysis was repeated by replacing the vacuoles with enveloped virions as the membrane bound structures. The permittivity and conductivity of the cytoplasm was modelled using mixture theory. A match to the values obtained from electrorotation data was found with a volume fraction of virions of 0.18 and the conductivity of the cytoplasm increased to $0.48 Sm^{-1}$. Again it was found that the low frequency dispersion in the permittivity of the cell interior modelled with mixture theory had only a small effect on the real part of the Clausius-Mossotti factor at low frequencies.

The above results show that the drop in the permittivity of the cell interior resulting from viral infection can be accounted for by the presence of increasing amounts of membrane bound structures in the cytoplasm.

4.11 References

1. Gascoyne, P.R.C., F.F. Becker, and X.B. Wang, *Numerical analysis of the influence of experimental conditions on the accuracy of dielectric parameters derived from electrorotational measurements.* Bioelectrochemistry and Bioenergetics, 1995. **36**: p. 115-125.
2. Holzel, R., *Electrorotation of single yeast cells at frequencies between 100 Hz and 1.6 GHz.* Biophysical Journal, 1997. **73**: p. 1103-1109.
3. Leslie, J., F.J. Rixon, and J. Mclauchlan, *Overexpression of Herpes Simplex Virus Type 1 tegument protein VP22 increases its incorporation into virus particles.* Virology, 1996. **220**: p. 60-68.
4. Huang, Y., X.B. Wang, F.F. Becker, and P.R.C. Gascoyne, *Membrane changes associated with the temperature-sensitive P85$^{gag-mos}$- dependent transformation of rat kidney cells as determined by dielectrophoresis and electrorotation.* Biochimica et Biophysica Acta, 1996. **1282**: p. 76-84.
5. Gimsa, J., P. Marszalek, U. Loewe, and T.Y. Tsong, *Dielectrophoresis and electrorotation of neurospora slime and murine myeloma cells.* Biophysical Journal, 1991. **60**: p. 749-760.
6. Gascoyne, P., R. Pethig, J. Satayavivad, F.F. Becker, and M. Ruchirawat, *Dielectrophoretic detection of changes in erythrocyte membranes following malarial infection.* Biochimica et Biophysica Acta, 1997. **1323**: p. 240-252.
7. Wang, X.B., Y. Huang, P.R.C. Gascoyne, F.F. Becker, R. Holzel, and R. Pethig, *Changes in Friend murine erythroleukaemia cell membranes during induced differentiation determined by electrorotation.* Biochimica et Biophysica Acta, 1994. **1193**: p. 330-344.
8. Hu, X., W.M. Arnold, and U. Zimmermann, *Alterations in the electrical properties of T and B lymphocyte membrane induced by mitognic stimulation. Activation monitored by electro-rotation of single cells.* Biochimica et Biophysica Acta, 1990. **1021**: p. 191-200.
9. Hutchinson, L., C. Roop-Beaucamp, and D.C. Johnson, *Herpes Simplex Virus glycoprotein K is known to influence fusion of infected cells, yet is not on the cell surface.* Journal of Virology. 1995. **69**(7).

10. Becker, F.F., X.B. Wang, Y. Huang, R. Pethig, J. Vykoukal, and P.R.C. Gascoyne, *Separation of human breast cancer cells by differential dielectric affinity.* Proceedings of the National Academy of Science, 1995. **92**: p. 860-864.

11. Hughes, M.P., H. Morgan, and F.J. Rixon. *Characterisation of Herpes Simplex virus particles by dielectrophoretic crossover methods.* in *20th Annual International Conference of the IEEE in Medicine and Biology society*. 1998. Hong Kong.

Chapter 5: Electrorotation measurements of the virus life cycle of Herpes Simplex Virus Type 1 infected Baby Hamster Kidney Fibroblasts. *III Discussion and Conclusions.*

5.1 Discussion

5.1.1 Virus life-cycle and cell ultrastructure

During infection of cells with HSV-1, the initial step is the binding of virions to cellular receptors, followed by fusion of the virion and cell membranes, leading to internalisation of the virion components. In this work, the cells were infected with 10p.f.u. per cell of highly purified virus. With such a low number of virions binding to the cells, it is unlikely that they will have any directly measurable effect on the dielectric properties of a cell, particularly since it is a transient event. After membrane fusion there is a rapid cascade of processes that result in a switch in gene expression from cellular to viral genes. However, the gross morphology of the cell was not detectably altered until several hours after infection when cells grown as monolayer cultures began to round up and lose their normal, extended conformation. This rounding proceeded until the cells were predominantly spherical by which stage they usually had detached from the tissue culture vessel. (In the experiments presented in this thesis, all the cells are spherical because they have been physically detached from the support for rotation measurements). The cause of the rounding appears to be the depolymerisation of microtubules and of actin containing microfilaments that are important for maintenance of the cellular ultrastructure. The cytoskeletal network is known to be important for transport of incoming viral DNA-containing capsids to the nucleus [1] but this is a very early event, which takes place before its disruption. It is not clear whether the disruption of the cytoskeleton is a functional feature of virus infection or simply a side effect of the drastic changes in macromolecular synthesis and organisation that are consequent upon infection.

5.1.2 Membrane capacitance

Changes also occur in the cell membrane as infection progresses, although the physical nature of these changes has not been well studied. Both increases [2. 3] and decreases [4] in the numbers of microvilli have been reported following HSV infection of mammalian cells, as well as the formation of larger structures (folds and blebs). One consistent feature is the appearance of progeny virions on the cell surface. In BHK(C-13) cells, these start to appear about 6 hours after infection and their numbers increase markedly until approximately 12 hours, after which they decline again [5]. The changes in the membrane ultrastructure are apparent in both the dielectric data and the SEM images (figure 10 in the results chapter) of the cells. As these images show, there was an obvious change in the morphology of the membrane as infection progressed, but they do not indicate that there were major changes in the shape of the cells. All the cells were spherical owing to detachment from the culture vessel. However, there was a tendency towards more uniform rounding as infection progressed, as evidenced by a reduction in the size and number of irregular surface folds and creases, which was accompanied by an increase in the numbers of microvilli (figure 10 in the results chapter).

It appears that the membrane of the detached uninfected cell has large-scale irregularities including folds and creases and that this changes to a more uniform conformation following infection, probably as a result the disruption of the cytoskeleton. This effect is apparent in the time dependency of the specific membrane capacitance where, between 6 and 9 hours post-infection, there was a rapid decrease of approximately 25%, compared with an uninfected cell. At this time exocytosis is well under way. The decrease in capacitance continues with time, both as the surface of the cell becomes smoother and the overall surface area reduces, together with the fact that the cell membrane takes on the composition of the viral envelope.

5.1.3 Membrane permeability and internal conductivity

Although the virus leaves the cell by exocytosis, this is not accompanied by cell lysis. The plasma membrane therefore retains its integrity throughout the productive phases of infectious cycle. It is not known whether membrane permeability is affected, although decreases in membrane fragility following HSV infection have been reported for a number of mammalian cell types [6]. We did not distinguish changes in permeability in our electrorotational and dielectrophoretic data. Figure 13 in the results chapter shows that the internal conductivity of the cell remained unchanged throughout the life cycle of the virus at between 0.30 and 0.42Sm^{-1} during the entire time course of the experiments for all the cells measured. This can be compared with the growth medium conductivity of 1.4Sm^{-1} and a suspension medium conductivity of 0.0175Sm^{-1}.

Dielectrophoretic crossover frequency measurements on mock infected cells and cells infected for 18 hours showed that the membrane conductivity of BHK(C-13) cells remained low through the infection cycle of the virus. The membrane capacitances obtained from these measurements were within the error of those obtained from electrorotational spectra. Together these results confirmed that the membrane did not become appreciably permeable as a result of viral infection and the resulting exocytosis.

5.1.4 Internal permittivity

By 6 hours post-infection, virus particles are beginning to be made and the process of virus release begins. Virus capsids are synthesised in the nucleus and transported across the nuclear membrane. The capsids are surrounded by the tegument proteins and pass through the golgi apparatus, where they probably acquire the viral envelope [7, 8], before exiting the cell. The fraction of the cytoplasmic volume occupied by membrane bound vacuoles increases as a result of infection, since infection of cells with HSV-1 is known to cause proliferation of golgi derived membranes, generating large numbers of vacuoles (many containing virus particles) of different sizes [9]. The synthesis of large number of vacuoles and enveloped virions could lead to a marked reduction in the

permittivity of the cytoplasm. A step change in internal permittivity occurred sometime between 9 and 12 hours post-infection, when large quantities of virions are being produced. This suggests that processes which give rise to the production of large numbers of vacuoles are switched on at around 9-12 hours and thereafter their rate of loss, by fusion with the plasma membrane, is probably equal to the rate of production. Thus the reduction in internal permittivity could be attributed to an increase in the number of membrane containing structures (vacuoles, virions) within the cell cytoplasm during viral replication.

This observation is supported by the results of applying dielectric mixture theory to model the cytoplasm. When the membrane bound structures were modelled as golgi derived transport vesicles, the model indicated that they occupied a volume fraction of 0.24 of the cell interior. However, if the membrane bound structures were modelled as virions, they occupied a volume fraction of 0.18 of the cell interior. These volume fractions are equivalent to a cell containing up to $2x10^4$ virus particles; an amount that is within the limits of the number of virions a cell produces.

Thin section images by *Rixon et al* [5], showed viruses enclosed in cytoplasmic vacuoles being transported to the cell surface, while images by Smith and De Harven [9] showed the presence of long stretches of nuclear membrane reduplication as well as membrane bound cisternae in the cytoplasm. Morgan *et al* [10] observed a large number of partially formed virus particles within cells. These images show that the membrane bound structures were not fully filled with virions. It is therefore likely that the number of virus particles in the cell interior is lower than $2x10^4$.

From the modelling it was found that the presence of a large amount of membrane bound structures reduced the overall conductivity of the cytoplasm. For the overall internal conductivity of cells to have remained constant, the conductivity of the cytoplasm outside the membrane bound structures would have to have increased to 0.48-0.53Sm^{-1} depending on the type of membrane bound structures within the cytoplasm. This indicates that the total ion concentration within the cell remains unchanged.

5.1.5 Prospects

Dielectrophoresis can be used as a method for separating cells of different dielectric properties. For example, human breast cancer cells (MDA231) have been separated from normal human erythrocytes using a dielectrophoretic affinity column [11]. The electrorotation spectrum for a particular cell type can be analysed to give the frequency dependent dielectric properties of the cells and thus develop optimal cell separation conditions or protocols. For the particular case of the BHK(C-13) cells, pre- and post-infection, the corresponding dielectrophoretic spectrum was calculated from the electrorotation data and the results are shown in Figure 11. This figure shows the real and imaginary components of the factor $\left(\frac{\varepsilon_p^* - \varepsilon_{med}^*}{\varepsilon_p^* + 2\varepsilon_{med}^*}\right)$ (the Clausius-Mossotti factor) which gives an indication of the force and torque on a particle respectively plotted for a medium conductivity of 17.5mSm^{-1}. The curves are computed from the mean values of the dielectric parameter set, for mock infected cells, curve (a) and for cells 18 hours post-infection, curve (b). The error bars represent the maximum deviation that occurs in the data, computed from the maximum range in the measured dielectric parameters for all the cells.

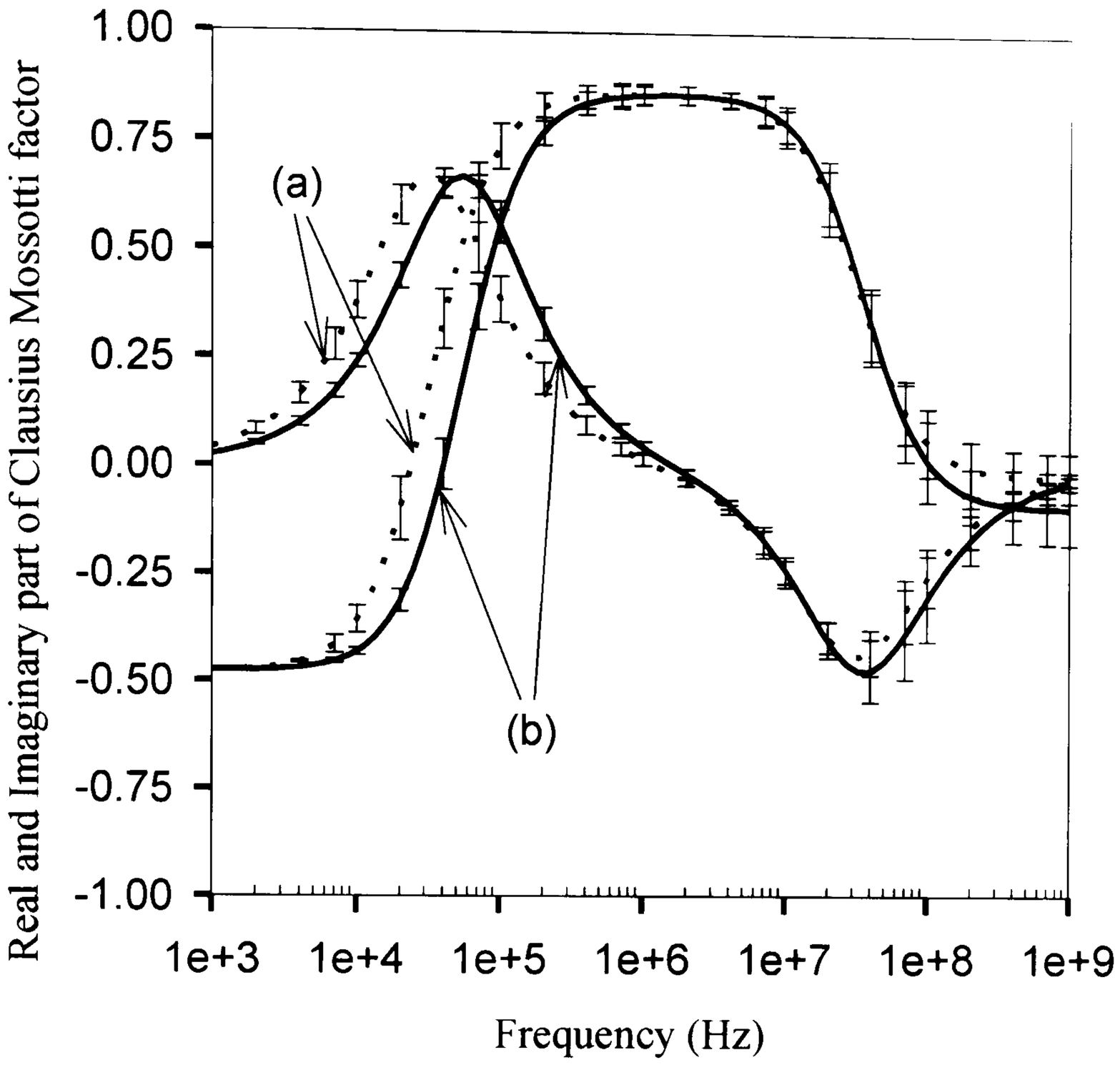

Figure 1. The frequency dependence of the real and imaginary components of the Clausius-Mossotti factor for uninfected BHK cells. Curve (a) gives the Clausius-Mossotti factor for uninfected cells, whilst curve (b) is the Clausius-Mossotti factor for cells infected for 18 hours. Both curves are for a suspending medium conductivity of 17.5mSm^{-1}. The error bars represent the range of possible values of the Clausius-Mossotti factor as derived from the range of the various dielectric parameters. The plot shows that at this conductivity and in a frequency window from 20kHz to 40kHz the two types of cells could be separated using dielectrophoretic methods.

It can be seen from figure 1 that over a frequency window from 20kHz to 40kHz, the uninfected cells experience a positive dielectrophoretic force whilst the 18 hours post-infected cells experience negative dielectrophoresis, implying that the two cell types could be successfully separated in an appropriate electrode chamber.

5.2 Conclusions

It was shown that electrorotation can be used as a technique to probe the time-dependent biophysical changes which take place as a cell undergoes viral invasion, replication and release. It has been shown that the membrane capacitance of the cells changes markedly between 6 and 9 hours post-infection, presumably as a result of changes in the morphology of the cell membrane. Scanning electron microscope images of cells, taken at discrete times post-infection, indicate that the membrane morphology varied with the virus life-cycle causing a reduction in the effective surface area of the cells. Using dielectrophoretic crossover frequency measurements it was confirmed that there was no increase in the conductivity of the membrane as a result of exocytosis. This was further confirmed by the fact that the internal conductivity of the cells remained constant throughout the virus replication cycle at 0.30 to 0.42 Sm^{-1}, which can be compared with a growth medium conductivity of $1.4Sm^{-1}$. A step change in internal permittivity was recorded between 9 and 12 hours post-infection, this reduction was found to correlate with increased generation of membrane bound structures in the form of golgi apparatus derived membranes which envelopes the virions within the cytoplasm. Other structures enveloped by membranes could also contribute to a reduction in the internal permittivity, they are present inside cells in the form of enveloped virions as well as partially formed virus particles.

This work points to the potential application of electrorotation techniques as a method for the non-invasive analysis of virus-host interactions. Further refinements to the technique, such as confinement of cells in electrical or optical traps, would allow measurements to be made on a single cell and for data to be collected over the entire 24 hour life cycle of virus infectivity. The work also suggests further biomedical applications and highlights the potential of dielectrophoretic separation techniques for the retrieval and separation of infected cells from uninfected cells.

5.3 References

1. Sodeik, B., M.W. Ebersold, and A. Helenius, *Microtube-mediated Transport of Incoming Herpes Simplex Virus 1 Capsids to the Nucleus.* The Journal of Cell Biology, 1997. **136**(5): p. 1007-1021.
2. Krempein, U., B.M. Jockisch, and C. Jungwirth, *Herpes Simplex Virus-induced cell surface protrusions.* Intervirology, 1984. **22**: p. 156-163.
3. Katsumoto, T., A. Hirano, T. Kurimura, and A.Takagi, *In Situ Electron microscopical observations of cells infected with Herpes Simplex Virus.* Journal of General Virology, 1981. **52**: p. 267-278.
4. Schlehofer, J.R., H. Hampl, and K.-O. Habermehl, *Differences in the morphology of Herpes Simplex Virus Infected cells: I. Comparative scanning and transmission electron microscopic studies on HSV-1infected HEp-2 and Chick Embryo Fibroblast cells.* Journal of General Virology, 1979. **44**: p. 133-442.
5. Rixon, F.J., C. Addison, and J. McLauchlan, *Assembly of enveloped tegument structures (L particles) can occur independently of virion maturation in herpes simplex virus type 1-infected cells.* Journal of General Virology, 1992. **73**: p. 277-284.
6. Schlehofer, J.R., K.-O. Habermehl, W. Diefenthal, and H. Hampl, *Reduction of ^{51}Cr-permeability of tissue culture cells by infection with Herpes simplex Virus Type 1.* Intervirology, 1979. **11**: p. 158-166.
7. Genderen, I.L.V., R. Brandumarti, M.R. Torrisi, G. Campadelli, and G.V. Meer, *The phospholipid composition of extracellular Herpes Simplex virions differ from that of the host cell nuclei.* Virology, 1994. **200**: p. 831-836.
8. Browne, H., S. Bell, T. Minson, and D.W. Wilson, *An endopasmic reticulum-retained Herpes Simplex Virus glycoprotein H is absent from secreted virons: Evidence for reenvelopement during egress.* Journal of Virology, 1996. **70**(7): p. 4311-4316.
9. Smith, J.D. and E.d. Harven, *Herpes Simplex Virus and Human Cytomegalovirus Replication in WI-38 Cells I. Sequence of Viral Replication.* Journal of Virology, 1973. **12**(4): p. 919-930.

10. Morgan, C., H.M. Rose, M. Holden, and E. Jones, *Electron Microscopic observations on the Development of Herpes Simplex Virus.* Journal of Experimental Medicine, 1959. **110**: p. 643-656.

11. Becker, F.F., *et al.*, *Separation of human breast cancer cells by differential dielectric affinity.* Proceedings of the National Academy of Science, 1995. **92**: p. 860-864.

Chapter 6: Determination of the dielectric properties of polystyrene beads complexed with herpes simplex virus

6.1 Summary

The effect of complexing polystyrene beads with virions was probed by electrorotational methods. Antibodies to HSV-1 were complexed with beads coated with secondary antibodies. Electrorotation measurements were performed on beads with and without HSV-1 particles complexed to the surface. Neither type of bead responded to rotating electric fields, making differentiation of the beads by electrorotation impractical. Dielectric modelling of beads of different sizes showed that the relative difference in the real part of the Clausius-Mossotti factor increases as the bead size decreases. This suggests that it could be possible to detect the presence of virus on appropriately sized beads using dielectrophoretic methods rather than electrorotational methods.

6.2 Introduction

The electrorotation of polystyrene beads has been used as an assay for the parasites *Criptosporidium* and *Giardia* [1] in water supplies. The assay was based on using latex beads with a binding agent specific to the parasites. When a bead is exposed to a rotating electric field, the rotation rate dependends on the surface conductance of the bead. Treating the bead so as to attach a binding agent specific to a parasite has the effect of altering the surface conductance of the bead, thus changing the rotation rate of the bead. When parasites attached to the binding agent, the surface conductance of the bead was further affected, giving rise to changes in the rotation rate of the bead. By observing the rotation rate of the bead it was possible to detect the presence or absence of parasites in raw water supplies. The authors also outlined how the method could be developed further for DNA analysis [1].

The separation of different beads has also been demonstrated using a system based on dielectrophoretic gravitational field flow fractionation. It was demonstrated that polystyrene beads with different surface functionalisations and of different sizes could be separated from a mixture into separate batches [2]. The continuous separation of different types of latex particles was also demonstrated, raising the possibility that large amounts of such beads could be separated.

A biosensor for the herpes virus has been demonstrated [3]. In this case, specific antibodies have been used to develop a method of detection capable of distinguishing between different strains of herpesvirus. The authors coated a pizoelectric crystal with a protein onto which an antibody specific for a particular type of virion was attached. Virions then attached to the antibody and the effect of the virions on the resonant frequency of the crystal could be monitored. Using this method it was possible to selectively detect relatively small amounts of herpes particles.

Electrorotation has been used to complex viable and non-viable *Escherichia coli* to the surface of latex beads [4]. It was demonstrated that electrorotation can be

used to differentiate between beads with one of individual viable or on non-viable *E. coli* on the surface and hence determine the viability individual micro-organisms.

For electrorotational measurements, beads were first coated with anti-mouse IgG, then with monoclonal mouse anti-HSV-1 IgG to which HSV-1 virions were attached. At each stage the electrorotational spectra of the beads was obtained. The results of each stage were analysed with a view to ascertaining the possibility of developing a method for detecting HSV-1. This process is illustrated in figure 1.

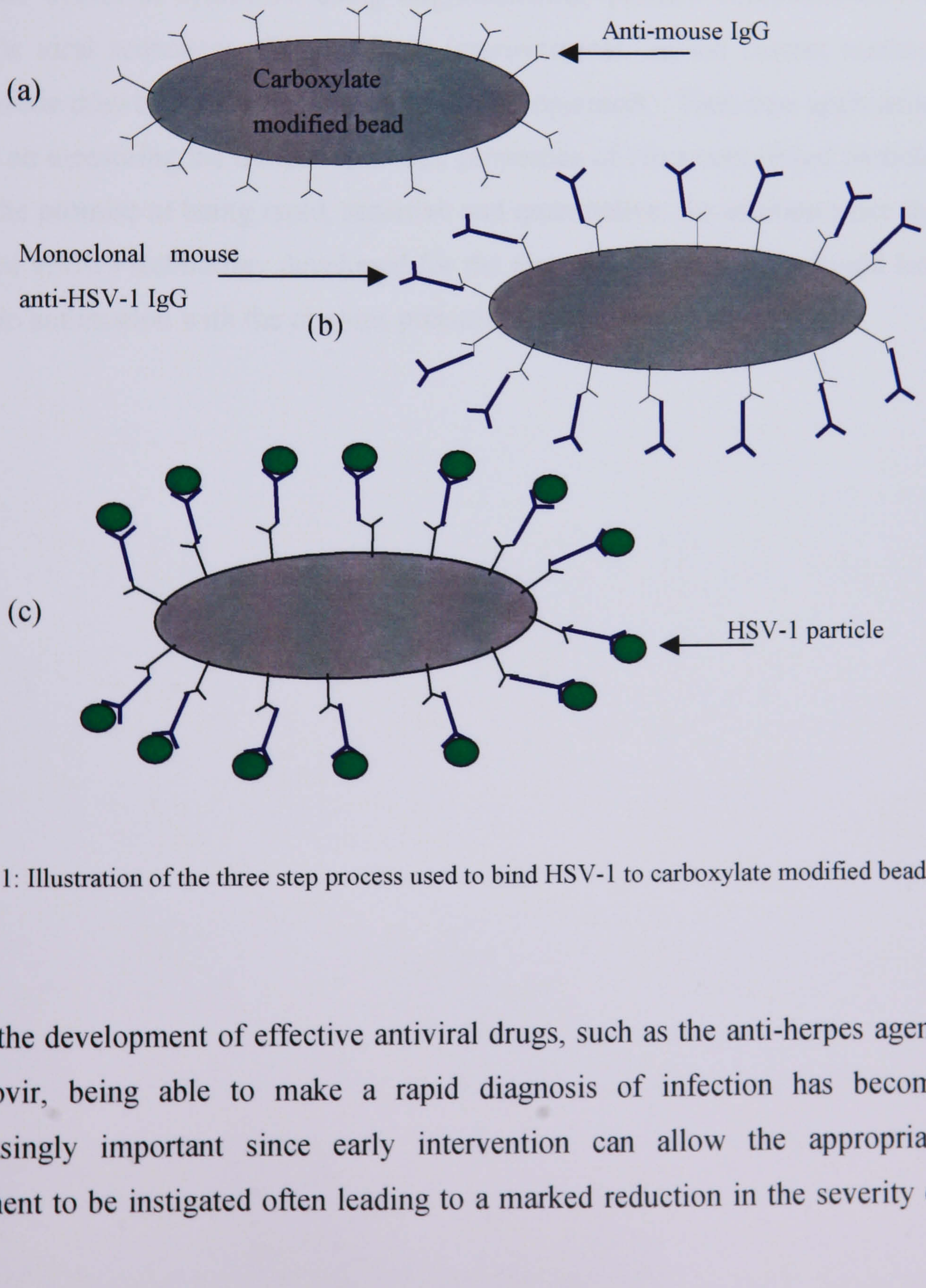

Figure 1: Illustration of the three step process used to bind HSV-1 to carboxylate modified beads.

With the development of effective antiviral drugs, such as the anti-herpes agent, acyclovir, being able to make a rapid diagnosis of infection has become increasingly important since early intervention can allow the appropriate treatment to be instigated often leading to a marked reduction in the severity or

spread of disease. Accurate and rapid diagnosis is also important to ensure that unnecessary and possibly inappropriate treatment is not carried out. Classical diagnostic procedures usually require long and uncertain procedures. Newer immunological methods are now used, in particular nucleic acid based techniques, although direct visualisation of virus particles by electron microscopy is still an important tool for some viruses. Immunology approaches can either take the form of direct detection of virus proteins using specific antibodies, or, more commonly, measurement of the host's immune response to the virus. The most powerful of the newer techniques is the polymerase chain reaction (PCR), in which viral nucleic acid (DNA or RNA) is amplified through multiple cycles of synthesis, using oligonucleotide primers complementary to specific viral sequences. Despite these improvements, all the current methods have some drawbacks and most require skilled operators. Thus new approaches based on measuring the dielectrophoretic properties of virus complexed particles hold the promise of being rapid, sensitive and quantitative. In addition since this method utilises technology developed for the electronics industry, it should lend itself to automation with the obvious potential for lowering costs.

6.3 Theory

For an elliptical particle suspended in a dielectric medium with viscosity η and exposed to an electric field $\boldsymbol{E}$ the steady state rotation rate is:

$$\boldsymbol{R}(\omega) = -\varepsilon_m \frac{\mathrm{Im}\left(\chi_x(\omega) + \chi_y(\omega)\right)\boldsymbol{E}^2}{4\eta\left\{\dfrac{\left(a_0^2 + b_0^2\right)}{a_0^2 A_{0x} + b_0^2 A_{0y}}\right\}} \tag{1}$$

Where the minus sign indicates that the dipole moment lags the electric field, ε_{m} is the permittivity of the suspending medium and Im{} indicates the imaginary component of, while A_{0x} and A_{0y} are the depolarisation factors of the x and y components (described in the theory chapter), which for a prolate particle is given by [5]:

$$A_{ox} = \frac{\left[\dfrac{q_0}{\left(q_0^2 - 1\right)^{1/2}}\right]\ln\left[\left(q_0 + \sqrt{q_0^2 - 1}\right) - 1\right]}{q_0^2 - 1} \tag{2a}$$

$$A_{oy} = \frac{(1 - A_{0x})}{2} \tag{2b}$$

for $\alpha = x, y$, and q_0 is calculated from the major axis a_0 and the minor axis b_0 of the polystyrene bead by $q_0 = \dfrac{a_0}{b_0}$.

The terms χ_x and χ_y are the x and y components of the susceptibility of the dielectric particle given by:

$$\chi_\alpha(\omega) = \frac{\varepsilon_p^* - \varepsilon_m^*}{\left(\varepsilon_p^* - \varepsilon_m^*\right)A_\alpha + \varepsilon_m^*} \tag{3}$$

for $\alpha = x, y$, ε_m^* and ε_p^* are the complex permittivities of the suspending medium and the particle respectively.

An expression which describes the measured conductivity of a polystyrene bead is given by [6, 7]:

$$\sigma_p = \sigma_b + \frac{2\kappa_s}{a} + \frac{A}{(1+j\omega T)^\alpha} \qquad (4)$$

where σ_p is the bulk conductivity, κ_s is the surface conductance. The factrors A, T and α define the low frequency conductivity dispersion that gives rise to the low frequency rotation peak. This dispersion is considered to be associated with the electrical double layer and Zhou *et al* [7] proposed that at low frequencies polarisation effects due to counterions and co-ions in the electrical double layer gives rise to a time-varying conductance that gives rise to the low frequency conductivity dispersion. To date insufficient experimental data exists for this proposition to be confirmed.

The permittivity and bulk conductivity of the polystyrene beads is known, so that it is possible to obtain the surface conductance from the electrorotational spectra. This is done by comparing an experimental electrorotational spectrum with a spectrum predicted by equation (1) (using equations 2-4 for suitable substitutions) using curve fitting procedures which minimises the difference between experimental and predicted spectra. This procedure has been described in more detail in the theory chapter.

The effect of attaching virions to the surface of a polystyrene bead was modelled using dielectric mixture theory. This was done by treating the HSV-1 on the surface of the beads as an extra layer that consisted of a mixture of HSV-1 virions and suspension medium, described in more detail in the theory chapter.

6.4 Materials and Methods

6.4.1 Electrodes and Electrorotational Measurements

Beads were suspended in 280mM mannitol and contained within a chamber made up by clear nail varnish with a coverslip used as a lid, the volume was approximately 20μl. Electrorotational measurements were carried out using polynomial electrodes that were 400μm from tip to tip as described earlier.

In order to visualise particles as small as virions a Nikon Microphot microscope with fluorescent objectives was used. A green fluorescent probe was used to mark virus particles, while the TRITC conjugated anti-mouse IgG was fluorescent red. The probes were excited by a UV-light source and visualised using a fluorescent microscope objective. A colour filter was used to restrict the light to the desired wavelength range. The presence of polystyrene beads in a sample solution was confirmed using a white-light source to illuminate the sample from underneath.

6.4.2 Binding protocol of carboxylate modified beads

In order to attach proteins to the surface of the polystyrene beads the following procedure was used:

1) Prepare 100ml of phosphate buffers (PBS), pH 7.4 and pH 6.5.
2) Prepare 100ml of 10mM MES (2-[Morpholino]ethanesufonic acid)buffer.
3) Prepare 100ml 1M Glycine
4) Dissolve protein (mouse IgG (whole molecule)) at 10mg/ml in 50mM PBS, pH 6.5.
5) Mix 100μl of IgG solution (10mg/ml) with 400μl 10mM MES (solution 1). Mix 100μl of 2% w/v solids COOH modified microspheres and 400μl 10mM MES (solution 2). Mix solutions 1 and 2 together in a glass centrifuge tube.

5) Add 1-2mg of EDAC (1-Ethyl-3-(3-Dimethylamino-propyl)carbodiimide). Mix by vortexing.
6) Incubate the reaction mixture on a rocker or orbital shaker for 2h at room temperature.
7) Add Glycine to a final concentration of 100mM to quench the reaction (this was obtained by adding 100µl of 1.1M Glycine to 1ml). Incubate at room temperature for 30 minutes.
8) Centrifuge to separate protein labelled microsphere particles from unreacted protein. Use 8000 rpm on a micro-centrifuge for 20 minutes.
9) Resuspend the pellet in 1ml of 50mM PBS, pH 7.4, by gentle vortexing or by use of a bath sonicator. Centrifuge as in step 8). Repeat twice more.
10) This gives a final solution with approximately $1x10^8$ beads per ml.

6.4.3 Virus cultivation and preparation

HSV-1 virions were purified using protocols established by Szilagyi and Cunningham [8]. The virus particles were pelleted from tissue culture medium (TCM) by centrifugation at 23,000 g for 2 hours at 4°C. They were resuspended in TCM and centrifuged through a 35 ml gradient of 5-15% w/w Ficoll 400 in TCM at 12,000 rpm in a Sorvall AH629 rotor. The virion band was collected, diluted in TCM, pelleted at 20,000 rpm in AH629 tubes, resuspended in an appropriate volume of TCM and frozen at -70°C for future use.

The viruses were fluorescently labelled with NBD-dihexadecylamine (Molecular Probes Inc). The dye was dissolved in DMF at a concentration of 2 mg/ml and then added to the virus solution (in TCM) at a 1:100 dilution. Particles were incubated for 20mins at room temperature, pelleted at 20,000 rpm for 10 minutes in a Sorvall TLA 100.2 rotor and resuspended in iso-osmotic (280mM) mannitol.

6.4.4 Complexing of HSV-1 with antibody coated polystyrene beads

In order to attach virus to beads, the beads were first coated with anti-mouse IgG using the binding protocols described above, followed by the attachment of monoclonal mouse anti-HSV-1. This was done by adding 5μl of the protein to 400μl of anti-mouse IgG conjugated beads suspended in 280mM mannitol at a concentration of $1x10^7$ beads per ml. The mixture was left at room temperature on an orbital shaker set to 400rpm for 1 hour. The beads were then spun down at 8000rpm in a microcentrifuge for 20 minutes and resuspended in 400μl of 280mM mannitol. 2μl of HSV-1 at a concentration of 10^{12} virions per ml was added to the solution before it was placed on an orbital shaker at 400rpm for 30 minutes.

It was found necessary to perform additional experiments to confirm that the correct binding had taken place at each step. These experiments were performed with TRITC conjugated anti-mouse IgG.

The TRITC label emits red light when excited by UV-light; the red TRITC label was chosen as it is easy to differentiate from the green fluorescent dye that was used to label the virions. It was used to test if the monoclonal anti-HSV-1 IgG protein had attached to beads coated with anti-mouse IgG. The testing was performed in several stages:

(i) To test for non-specific binding of TRITC conjugated anti-mouse IgG to beads coated with anti-mouse IgG; 2μl of TRITC conjugated anti-mouse IgG was added to a 400 μl a solution of 280mM mannitol containing secondary antibody coated beads at a concentration of $1x10^7$ beads per ml. The final solution was then placed on an orbital shaker set to 400rpm for 30 minutes. The extent of non-specific binding could be observed with a fluorescent microscope.

(ii) The next step in the process was to bind monoclonal mouse anti-HSV-1 IgG to the anti-mouse IgG coated beads. This was performed by observing the extent of specific binding of TRITC conjugated anti-mouse IgG to beads coated with monoclonal mouse anti-HSV-1 IgG. To this

end, 2µl of TRITC conjugated anti-mouse IgG was added to a 400µl solution of 280mM mannitol containing monoclonal mouse anti-HSV-1 IgG coated beads at a concentration of $1x10^7$ beads per ml. The final solution was placed on an orbital shaker set to 400rpm for 30 minutes. The extent of specific binding could be observed with a fluorescent microscope.

By observing the difference in the amount of TRITC conjugated mouse IgG that attached to the beads in the two control experiments it was possible to ascertain if monoclonal mouse anti-HSV-1 IgG attached to beads coated with mouse IgG.

6.5 Results

6.5.1 Electrorotation of untreated carboxylate modified beads

Electrorotation spectra was collected for 5 COOH modified beads suspended in a medium with a conductivity of $3.5mSm^{-1}$, and the average value of each data point for the 5 spectra was calculated, as was the standard deviation of the rotation rate at each data point. Curve fitting procedures was applied to this average spectrum and the result is shown in figure 2. The fitted curve gave $\kappa_s = 1.80nS$, A= 0.002, T= 0.0006 and $\alpha = 0.70$.

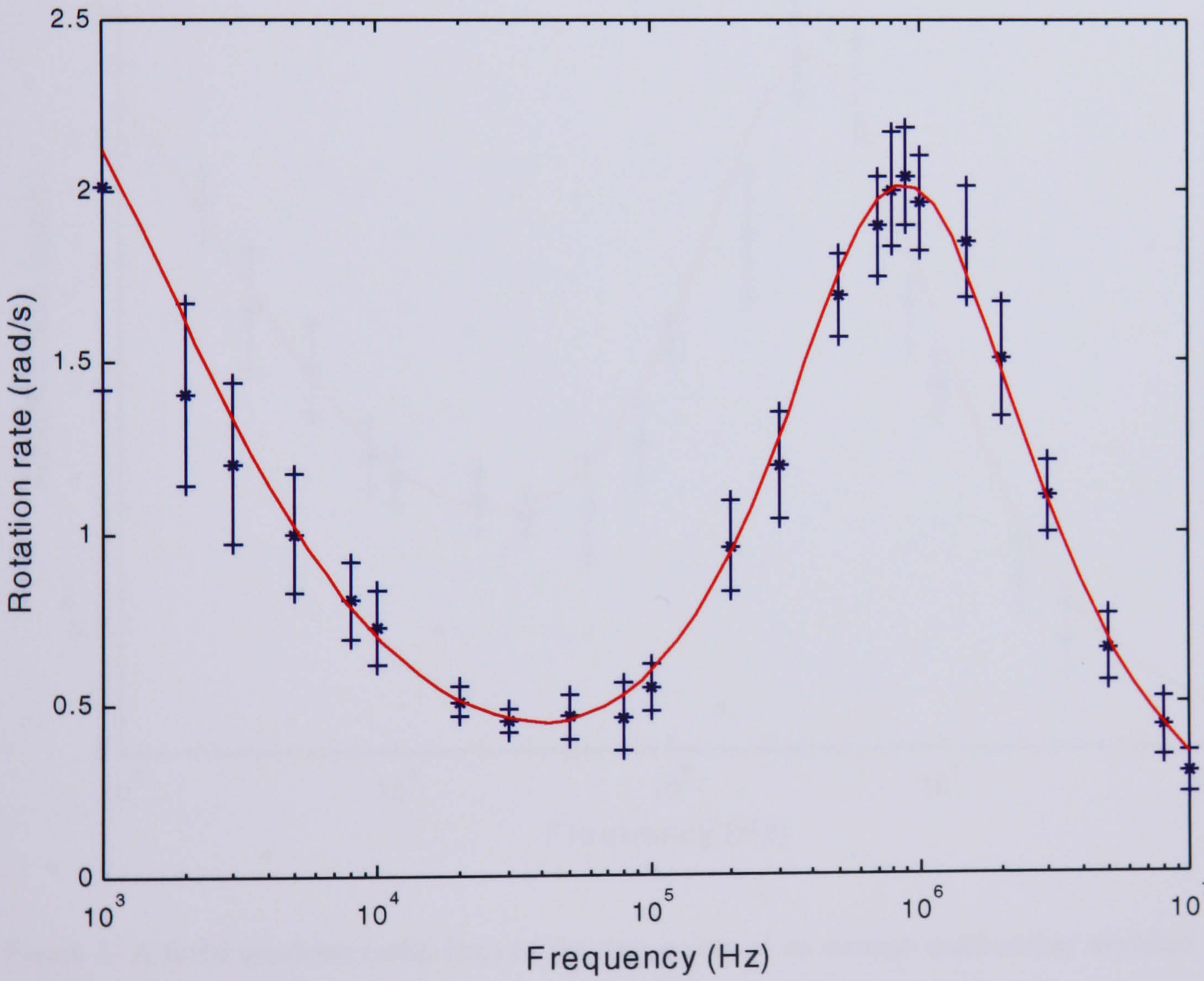

Figure 2: A fitted spectrum (solid line) fitted to the data points of an average untreated coarboxilate modified polystyrene bead. The dielectric parameters used were $\kappa_s = 1.80nS$, A= 0.002, T= 0.0006 and $\alpha = 0.70$. The error bars represent the standard deviation of the rotation rate at each data point.

6.5.2 Electrorotation of EDAC treated carboxylate modified beads

Electrorotation was performed on 5 separate EDAC functionalised polystyrene beads suspended in a medium with a conductivity of 1.5mSm^{-1}. As before, curve fitting procedures were applied to an average spectra obtained by taking the average value of each data point of the spectra. The results are shown in figure 3, were $\kappa_s = 0.65nS$, A= 0.00056, T= 0.0004and $\alpha = 0.67$, with the error bars representing the standard deviation of the rotation rate at each data point.

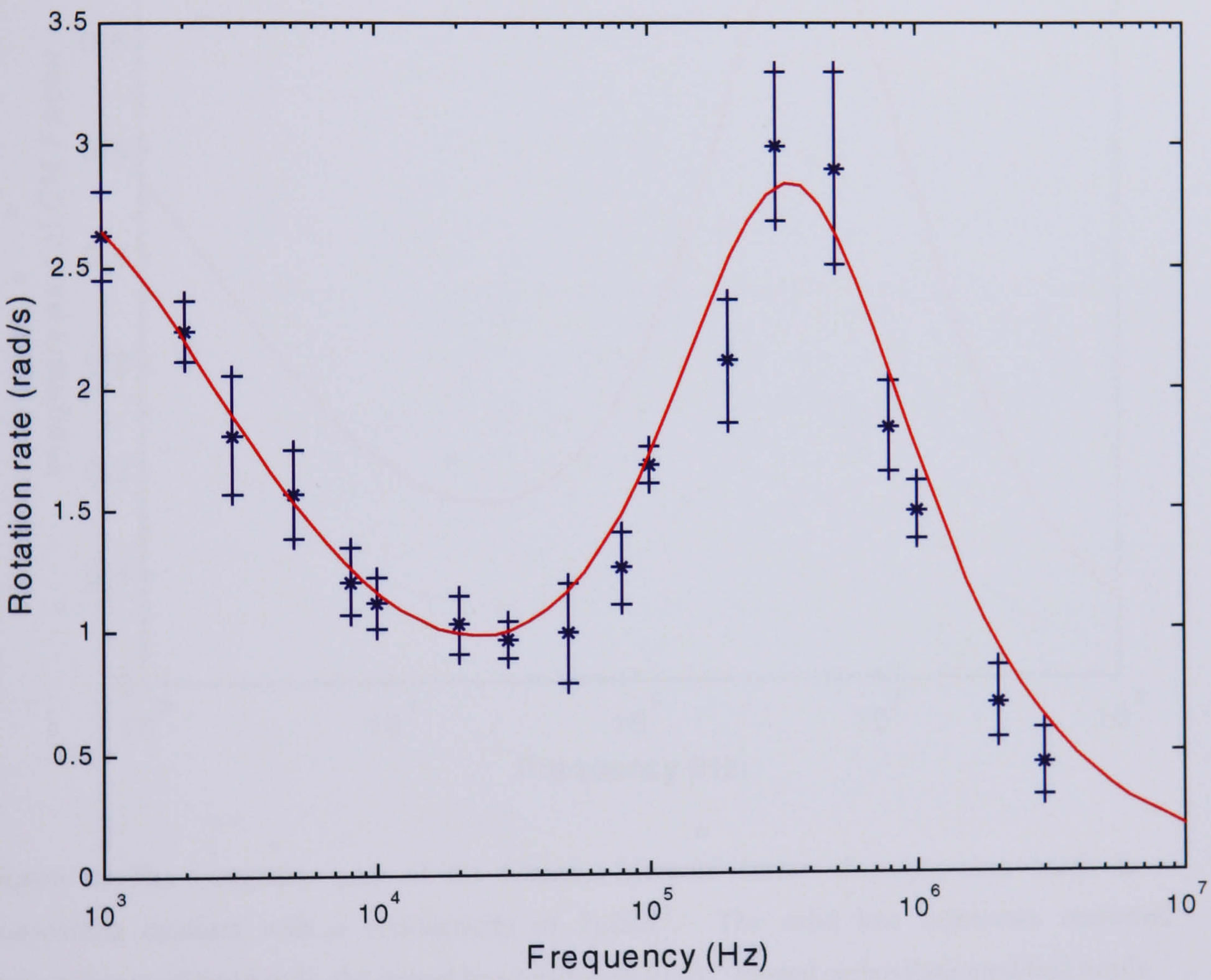

Figure 3: A fitted spectrum (solid line) of the data points of an average coarboxilate modified polystyrene bead treated with EDAC only. The dielectric parameters used in obtaining this were $\kappa_s = 0.73nS$, A= 0.0005, T= 0.0003 and $\alpha = 0.75$. The error bars represent the standard deviation of the rotation rate at each data point.

In order to compare the Clausius-Mossotti factor of the two types of beads, the imaginary components were plotted for a medium conductivity of $2mSm^{-1}$, the results are shown in figure 4. From this figure it can be seen that the rotation rate of an EDAC modified bead is slower than the rotation rate of an untreated bead under identical experimental conditions.

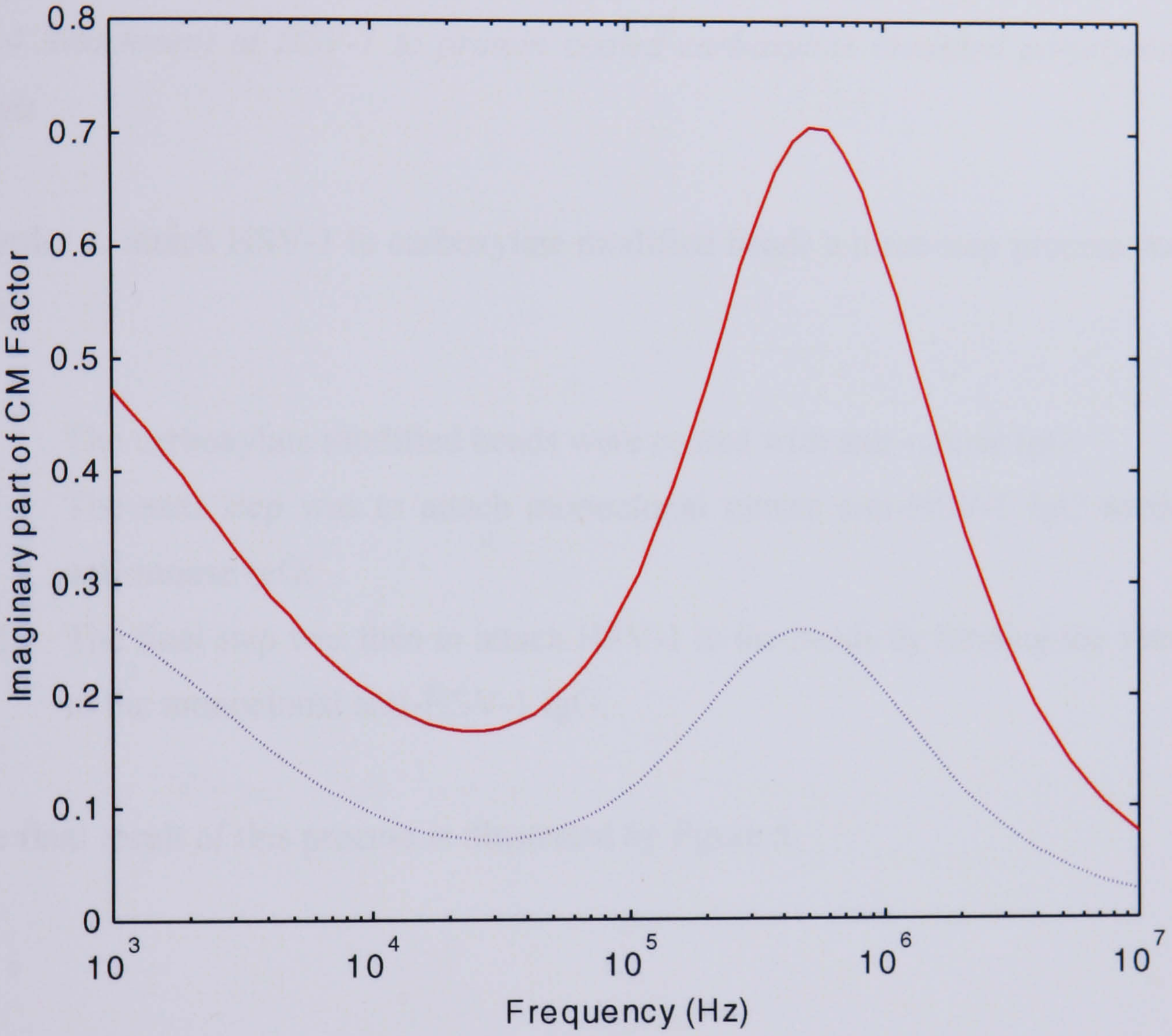

Figure 4: The imaginary part of the Clausius-Mossotti factor of polystyrene beads in a suspending medium with a conductivity of $2mSm^{-1}$. The solid line represents untreated carboxilate modified beads, the dotted line represents EDAC treated carboxilate modified beads.

6.5.3 Electrorotation of protein coated carboxylate modified beads

Polystyrene beads were coated with anti-mouse IgG and electrorotation measurements performed on these beads. All of the beads (more than 50) failed to rotate under the influence of the applied electric field, at voltages in the range 1 to 12V(peak-peak) and frequencies in the range 100Hz to 20MHz.

6.5.4 Attachment of HSV-1 to protein coated carboxylate modified polystyrene beads

In order to attach HSV-1 to carboxylate modified beads a three-step process was used:

(i) The carboxylate modified beads were coated with anti-mouse IgG.

(ii) The next step was to attach monoclonal mouse anti-HSV-1 IgG to the anti-mouse IgG;

(iii) The final step was then to attach HSV-1 to the beads by binding the virus to the monoclonal anti-HSV-1 IgG.

The final result of this process is illustrated by figure 5.

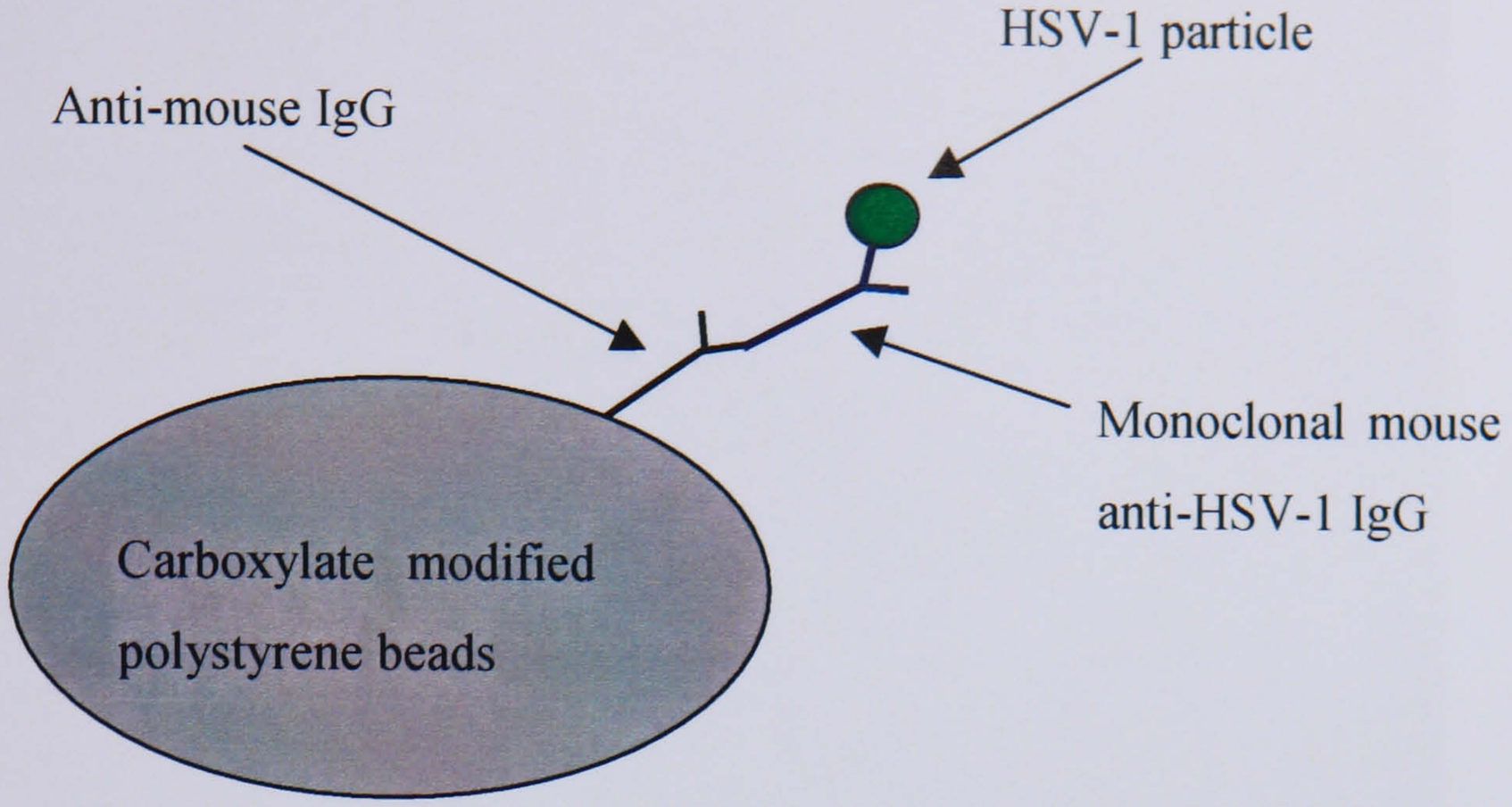

Figure 5: Attachment of HSV-1 particles to beads by the use of a primary antibody to couple the virus particle to a secondary antibody attached to the surface of the polystyrene bead. Drawing is not to scale.

After beads had been coated with anti-mouse IgG and resuspended in 280mM mannitol, a small amount (2μl) of TRITC conjugated anti-mouse IgG was added to the solution to measure non-specific binding. The results can be seen in figure 6.

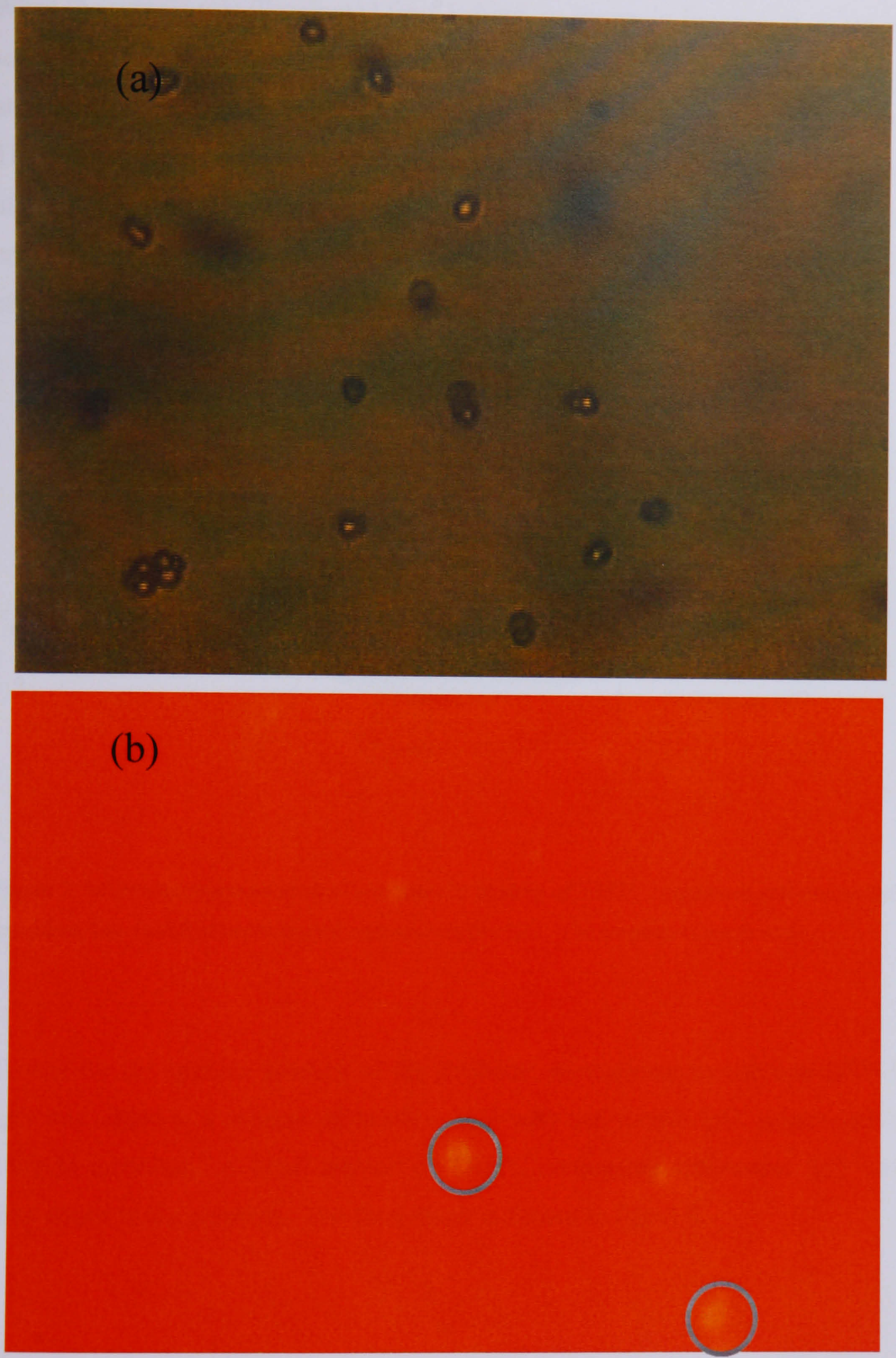

Figure 6: Non-specific binding of TRITC conjugated anti-mouse IgG to anti-mouse IgG coated beads. Figure 6(a) shows the beads present in the solution. While figure 6(b) shows that a small amount of non-specific binding of TRITC conjugated mouse IgG to anti-mouse IgG coated beads occurs, as illustrated by the circles. Figure 6(a) and 6(b) are not the same fields.

When the sample was illuminated from behind, as shown in figure 6(a), it can be seen that beads were present in the solution. Once this illumination is removed and the beads are illuminated by UV-light only, as shown in figure 6(b), the TRITC conjugated anti-mouse IgG can be seen to make the solution red. It can also be seen that a small amount of non-specific binding of TRITC conjugated anti-mouse IgG to polystyrene beads coated with anti-mouse IgG occurred. This effect is illustrated in figure 7.

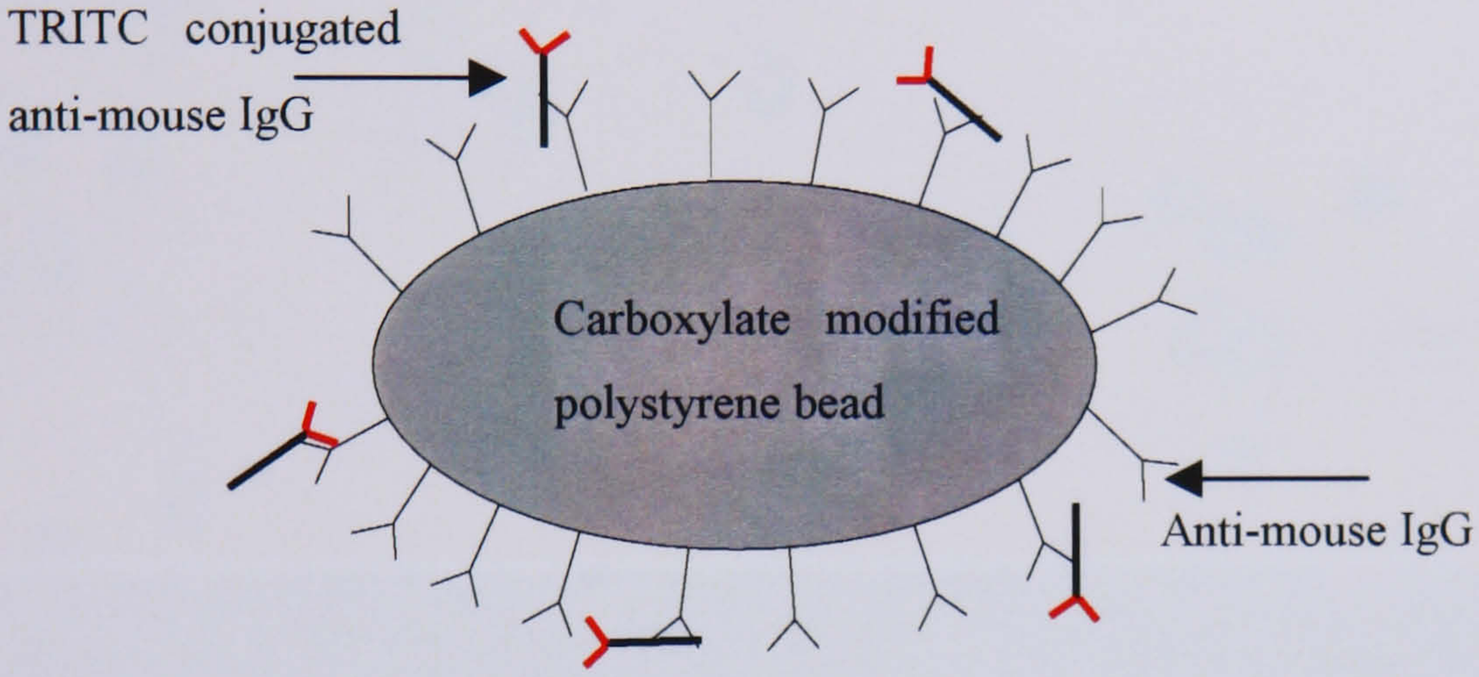

Figure 7: Schematic representation of non specific binding of TRITC conjugated anti-mouse IgG to carboxylate modified beads coated with anti-mouse IgG. The diagram is not to scale.

To test for the specific binding of the antibody, monoclonal mouse anti-HSV-1 IgG was added to a solution of beads coated with anti-mouse IgG, suspended in 280mM mannitol. A small amount of TRITC conjugated anti-mouse IgG was then added to the solution. The final result is shown in figure 8.

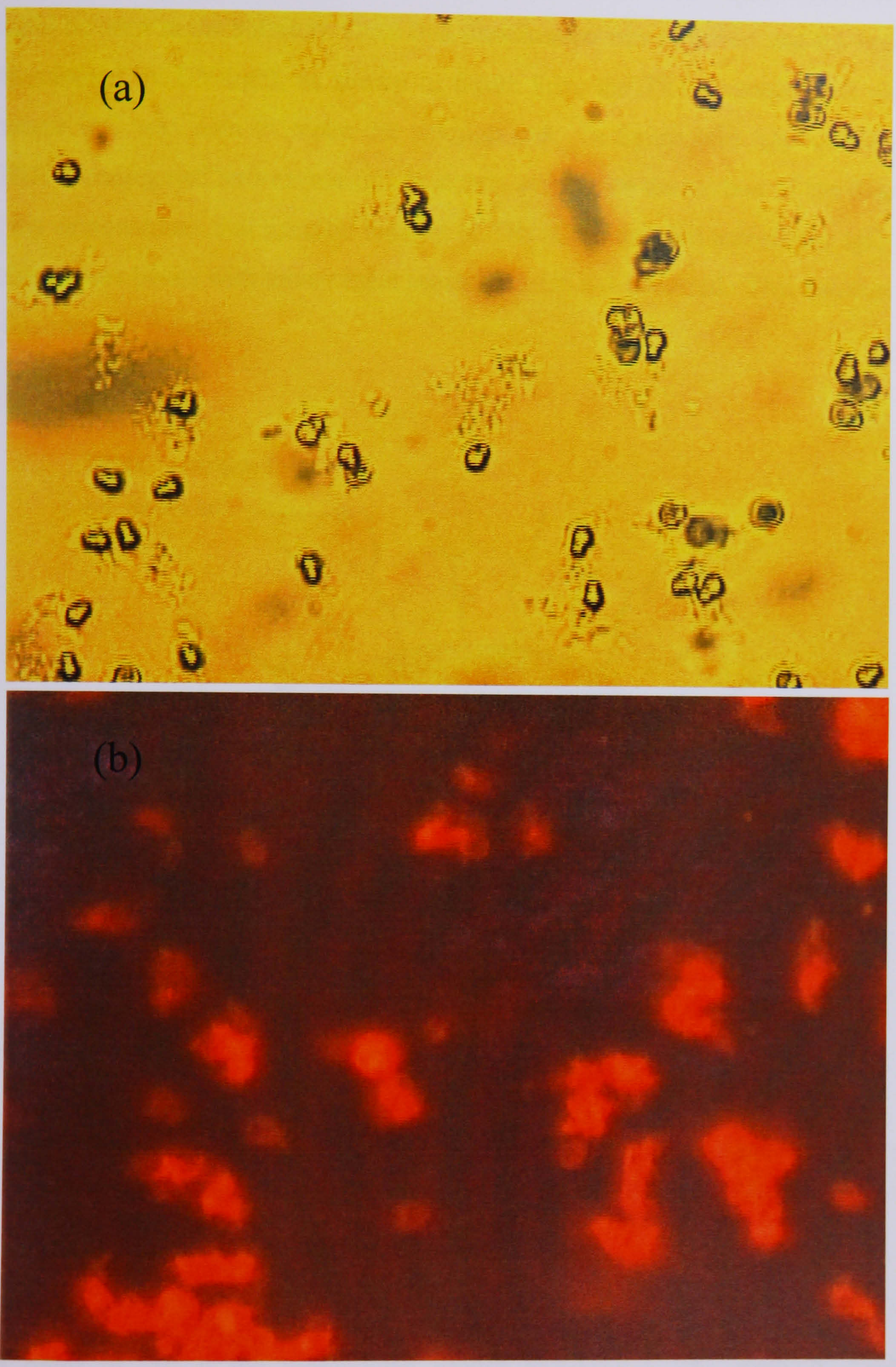

Figure 8: Beads present in the solution are shown in figure 8(a), while the specific binding of TRITC conjugated mouse IgG to anti-mouse IgG coated beads with monoclonal mouse anti-HSV-1 IgG is clearly evident in figure 8(b). Figure 8(a) and 8(b) are not the same fields.

When the sample was illuminated from behind, as shown in figure 8(a), beads could be seen in the solution. Once this illumination was removed and the beads illuminated by UV-light, as shown in figure 8(b), the TRITC conjugated anti-mouse IgG was seen to make the solution red. In figure 8(b) aggregation of TRITC conjugated anti-mouse IgG is clearly evident on the surface of the beads. This demonstrates that specific binding of TRITC conjugated anti-mouse IgG to polystyrene beads with monoclonal mouse anti-HSV-1 occurred. This reaction is illustrated in figure 9.

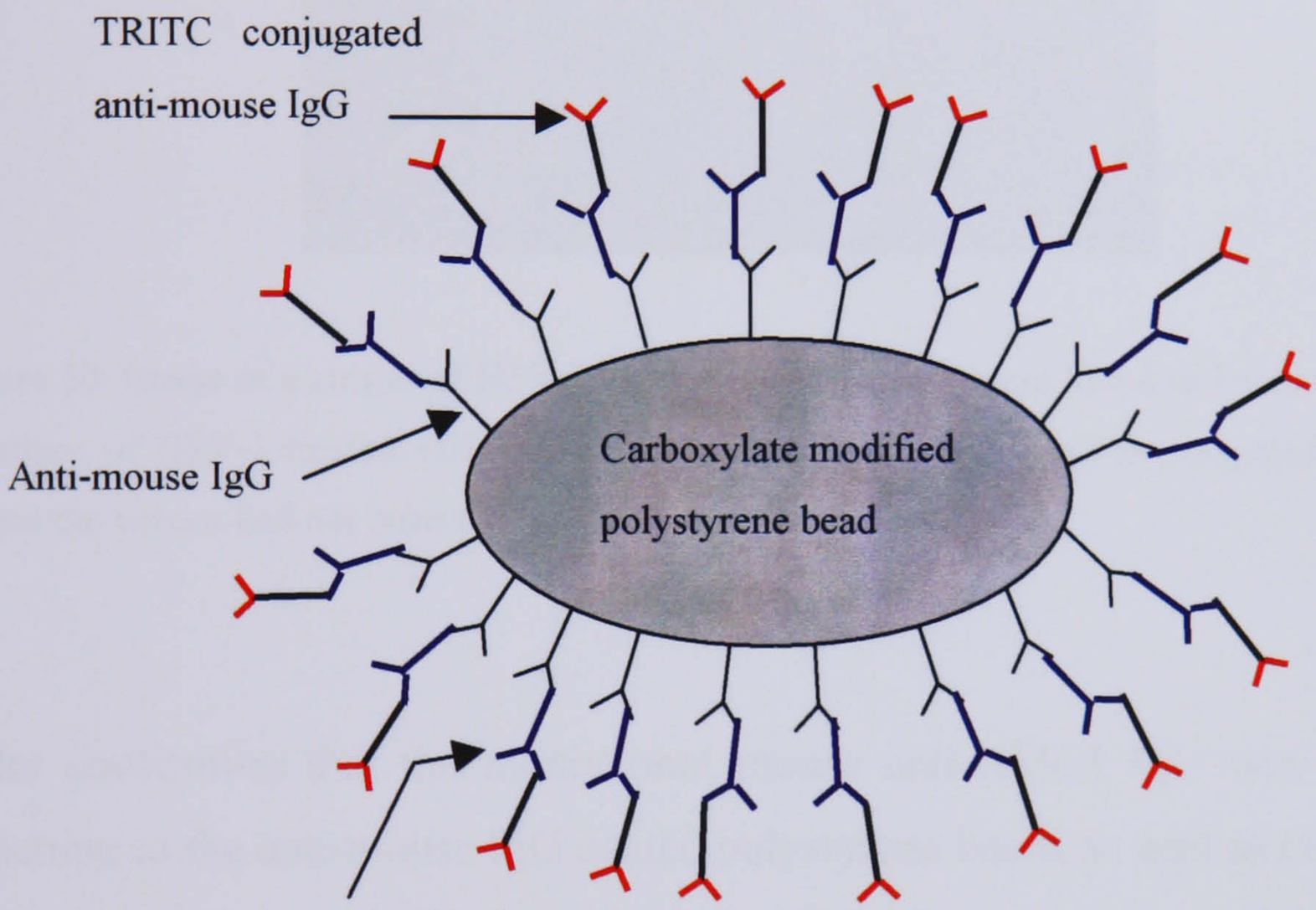

Figure 9: Schematic representation of specific binding of TRITC conjugated anti-mouse IgG to carboxylate modified beads coated with monoclonal mouse anti-HSV-1. The diagram is not to scale.

In order to test if the monoclonal mouse anti-HSV-1 IgG antibody could complex with virions, two solutions containing virions were compared. In one solution no antibody was added, while in the other solution the antibody was added. Both solutions were from the same stock of virions. The solutions were left on an orbital shaker for 30 minutes at 600rpm. In the solution containing

monoclonal mouse anti-HSV-1 IgG, clusters of HSV-1 were formed as shown in figure 10. This Indicated that the monoclonal mouse anti-HSV-1 IgG was binding to the HSV-1 virions, causing the virions to clump together.

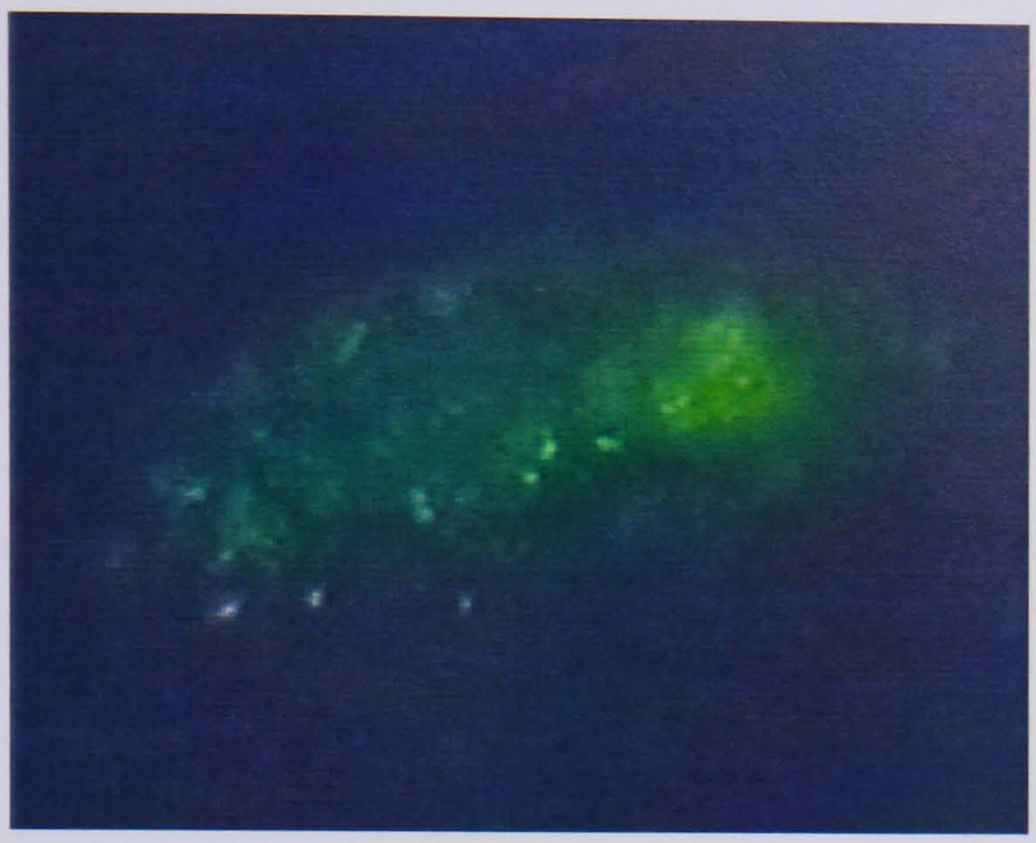

Figure 10: Image of a cluster of HSV-1 virions. Such clusters were found to be more frequent in solutions of HSV-1 treated with monoclonal mouse anti-HSV-1 IgG as compared to solutions where the virions had not been treated with the antibody.

After confirming that the monoclonal mouse anti-HSV-1 IgG was capable of attaching to the anti-mouse IgG coated polystyrene beads as well as being able to bind to the virions, HSV-1 was complexed with antibody coated beads. The result of binding virions to the beads can be seen in figure 11.

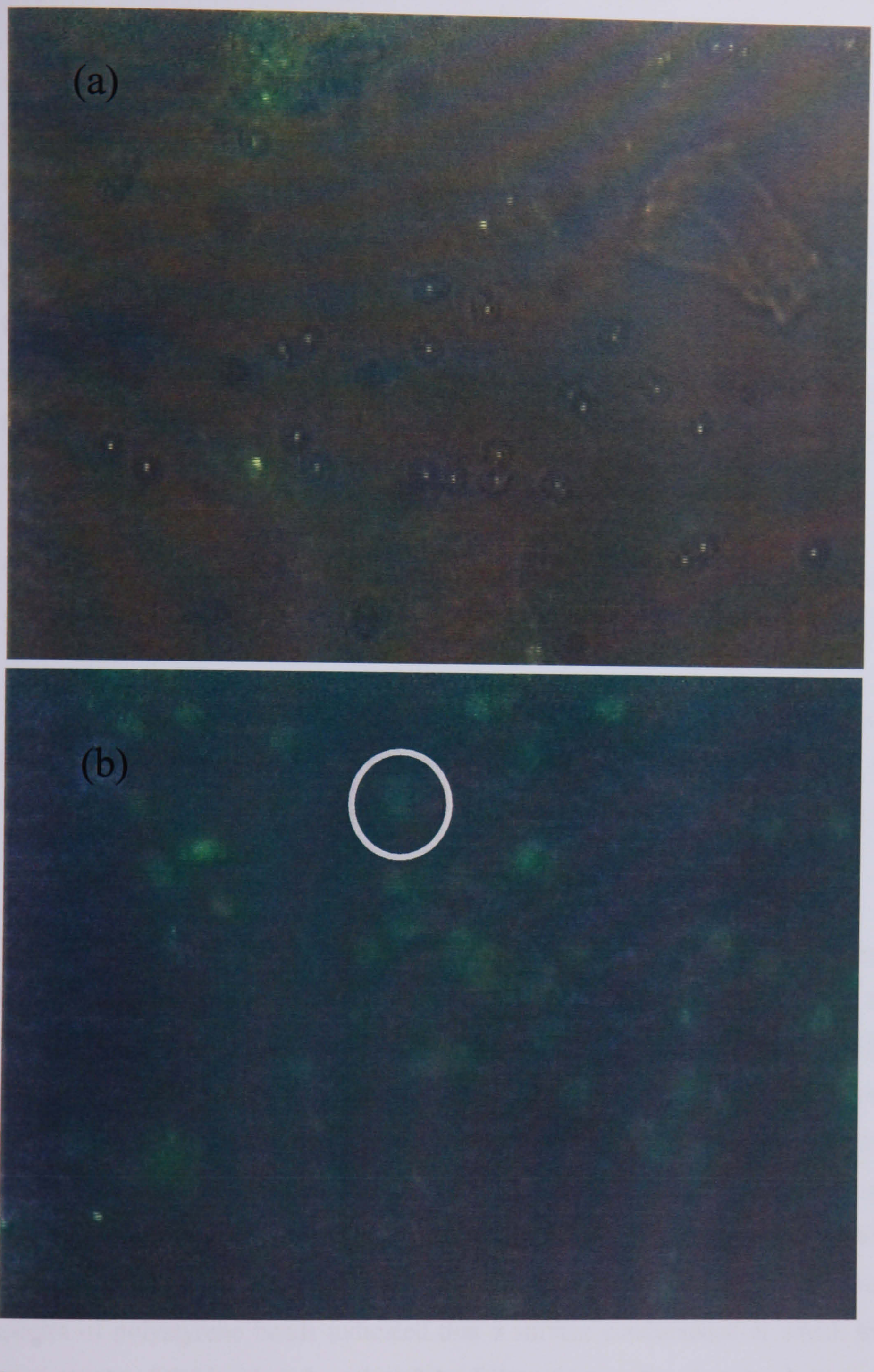

Figure 11: The result of coating beads with HSV-1. The beads in the sample can be seen in figure 11(a), while the beads coated by the green HSV-1 virions are shown in figure 11(b). Encircled is an example of a HSV-1 coated bead. Figure 11(a) and (b) are not the same frame.

Figure 11(a) shows the solution illuminated with white light and it can be seen that there are beads present in the solution. When the solution was exposed to UV-light, beads coated with HSV-1 virions could be seen. The virions were labelled with a green fluorprobe, and were seen as green dots. Therefore presence of a green particle of the same size and shape as the beads implies that the virions had attached to the bead. The circle in figure 11(b) highlights such a bead covered with HSV-1 particles. Beads treated in the same manner but without HSV-1 attached to the surface cannot be seen in UV-light, The images therefore show that the attachment of virions to the polystyrene beads was successful.

6.5.5 Electrorotation of protein coated carboxylate modified beads complexed with HSV-1

Electrorotation of beads coated with HSV-1 was attempted. However, it was not possible to obtain rotational motion of the polystyrene beads over a range of voltages up to 12V(peak to peak) and medium conductivities in the range 0.6-10mSm^{-1} for frequencies between 100Hz and 20MHz.

The slowest rotation rate that has been recorded with the experimental apparatus employed in the course of these experiments is 0.1 rads^{-1}, this value can be compared with the rotation rates from 0.25 up to 3 rads^{-1} in figures 2 and 3. The rotation rate of a bead is directly related to the imaginary part of the Clausius-Mossotti factor, which in turn is dependent on the surface conductance of the bead. Calculation of the rotation rate for a range of surface conductances can give an indication of the required surface conductance for the magnitude of the rotation rate to be less than 0.1 rads^{-1}. Such calculations of the electrorotational spectra of polystyrene beads indicated that a surface conductance at which the rotation rate of the beads is less than 0.1rads^{-1}, and hence too slow to observe. is in the range κ_s=0.2nS to κ_s=0.1nS. According to these assumptions and calculations, outside this range the magnitude of the rotation rate was observable.

6.6 Discussion

6.6.1 Data analysis

The attachment of a secondary antibody to polystyrene beads followed by the attachment of a primary antibody specific to HSV-1 was shown to be a successful approach to binding virions to beads. Simple control experiments were used to confirm the specificity of binding by the different antibodies, confirming that HSV-1 did bind to the monoclonal mouse anti-HSV-1 IgG, which in turn had bound to the anti-mouse IgG coupled to the surface of the beads.

Electrorotational measurements were performed on the beads at each stage in the process. It was found that untreated carboxylate-modified beads had a surface conductance of 1.85nS (this compares with a surface conductance of 0.73nS reported for carboxylate and amino-functionalised beads obtained from Polysciences by Zhou *et al* [7]), while beads treated with EDAC had a reduced surface conductance of 0.73nS.

Once an antibody was attached to the surface of the beads it was not possible to induce rotation of the beads. The lowest measured rotation rate in figures 2 and 3 is 0.25 $rads^{-1}$, but experimentally values as low as 0.1 $rads^{-1}$ were measured. At lower rotation rates beads would did not complete a full rotation or rotated in a jagged manner as if they were subject to movement generated by joule heating of the suspension medium. Under these conditions it was not possible to obtain meaningful rotation data. There were also cases were the beads would not rotate at all, but move slightly as if subjected to Brownian motion. Such behaviour in the beads could occur as a result of the imaginary part of the Clausius-Mossotti factor of the bead being too small to cause the beads to rotate.

Modelling of the electrorotational spectra of polystyrene beads showed that this is behaviour is likely to be caused by the beads having a rotation rate less than 0.1 $rads^{-1}$ and therefore a surface conductance in the range κ_s=0.1-0.2nS.

Attachment of HSV-1 failed to induce rotation of the beads, indicating that attaching virions does not significantly alter the surface conductance of the protein coated beads. As a result it was not possible to differentiate beads with or without HSV on the surface using electrorotation.

6.6.2 Dielectric mixture theory applied to virions on the surface of polystyrene beads

Further analysis of the effect of attaching a layer of HSV-1 to the surface of a protein coated polystyrene bead was performed by employing models that used dielectric mixture theory. The surface of the beads was modelled as a layer consisting of suspension medium and virions. For this model the surface conductance of the beads was set to κ_s=0.2nS, i.e. the value obtained for protein coated beads. This value also corresponds to values that were obtained for 216nm protein coated beads using dielectrophoretic cross-over frequency measurements (Data to be published, Hughes *et al*). As shown in figure 12, it can be seen that the imaginary component of the Clausius-Mossotti factor only changes slightly with increasing amounts of virions on the surface of the bead. The rotation rate that would result from the calculated Clausius-Mossotti factor would be 0.08rads^{-1}, which is less than the lowest rotation rate observed in the course of the electrorotational experiments. This correlates with our observations where it was not possible to observe rotation on beads coated with antibodies or when HSV-1 was attached to the anti-body.

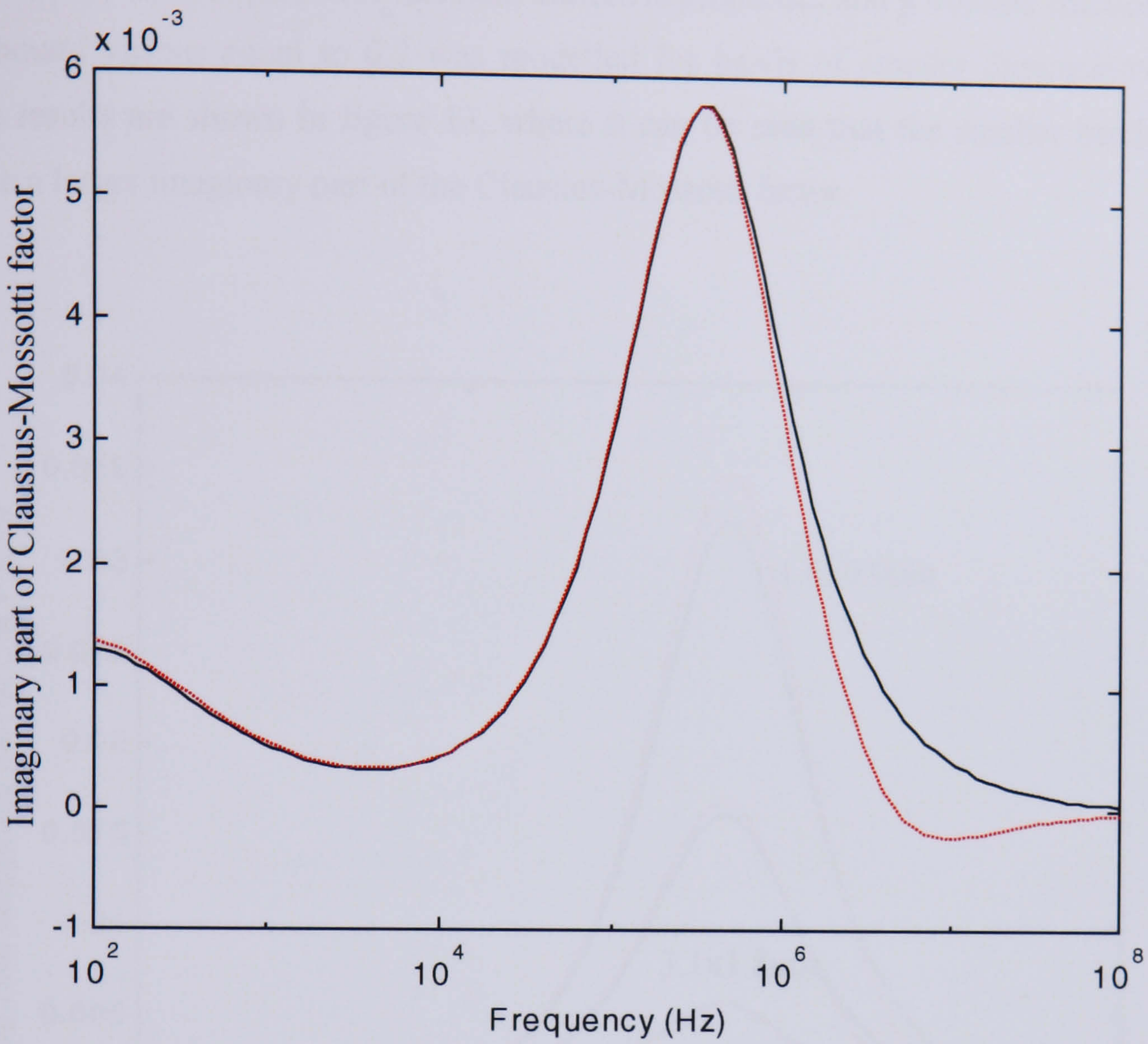

Figure 12: Simulation of the effect of varying the volume fraction of HSV-1 on the surface of a polystyrene bead. The volume fraction of virus on the surface of the beads were 0 (black line) and 0.3 (red line).

The similarity in the two spectra can be explained if the surface conductance of the virus being approximately κ_s=0.2nS (for viruses that are 1-10 days old, data to be published, Hughes *et al*). The surface conductance of the virus is very similar to that of the bead, meaning that complexing virions to the surface of a bead will not change the overall conductance of the bead surface, resulting in the spectrum remaining unchanged. If the surface conductance of the beads is raised by an order of magnitude a reduction in the imaginary part of the Clausius-Mossotti factor occurs.

The beads used were 5.2x3.1μm in size. The effect of attaching HSV-1 virions to protein coated beads, with identical dielectric properties and a volume fraction of bound virions equal to 0.2 was modelled for beads of smaller dimensions. The results are shown in figure 13, where it can be seen that the smaller beads have a larger imaginary part of the Clausius-Mossotti factor.

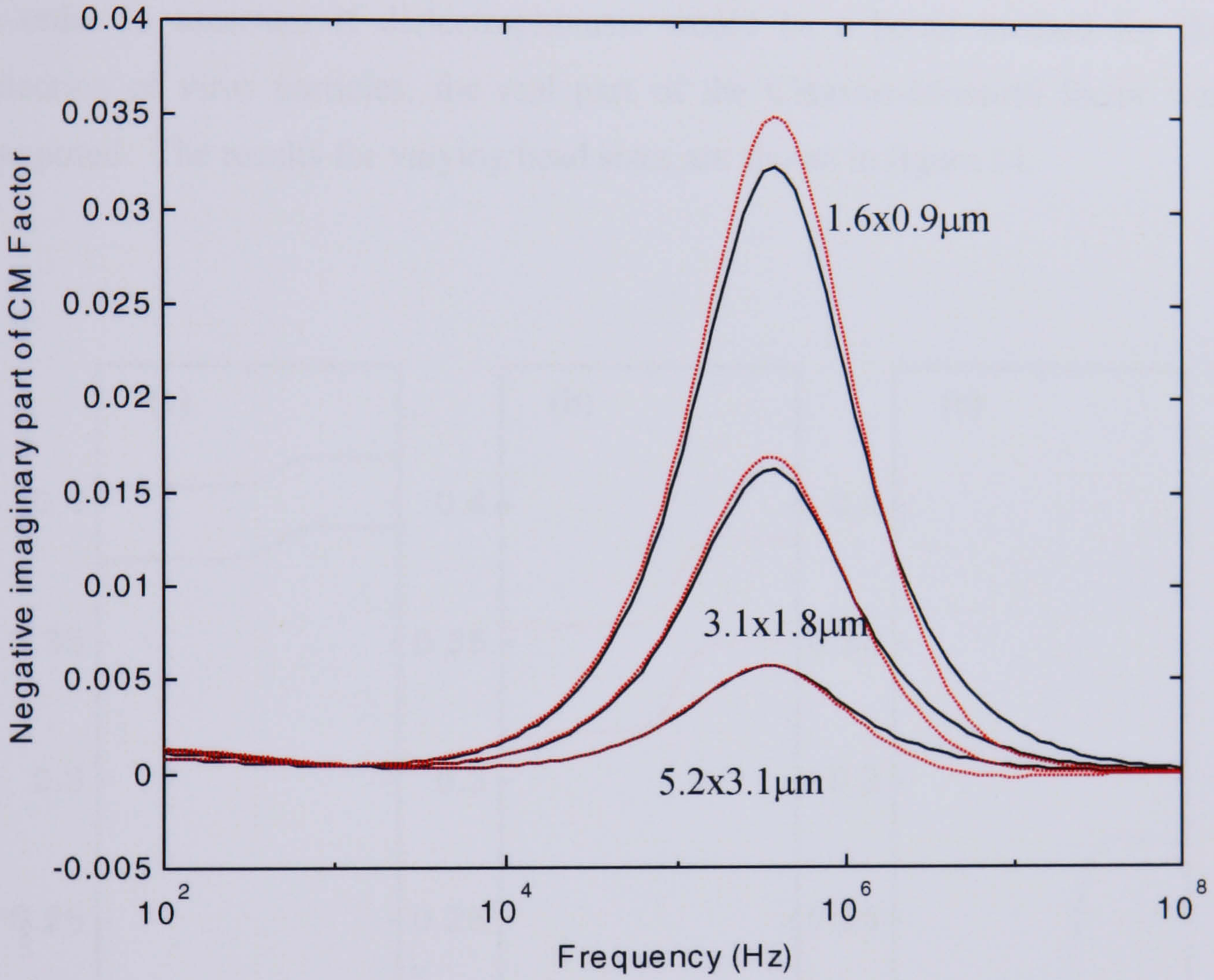

Figure 13: Variation in the imaginary part of the Clausius-Mossotti factor with bead size. With (red line) and without (black line) HSV-1 (volume fraction = 0.2) complexed to the bead. The size variations of the beads were 5.2x3.1μm, 3.1x1.8μm and 1.6x0.9μm.

The imaginary part of the Clausius-Mossotti factor for all the bead sizes is quite small. The rotation rate of the smallest (1.6x0.9μm) beads would peak at $0.4 rads^{-1}$, a value experimentally difficult to detect accurately. As a result it would be difficult to obtain spectra sufficiently accurate to detect the small difference between beads with or without complexed HSV-1 using electrorotation. However, Burt *et al* [1] have demonstrated that using suitable

experimental apparatus it is possible to obtain accurate rotation spectra for beads 0.8μm in diameter, with a maximum rotation rate of 0.25rads^{-1}. The authors also demonstrated that it was possible to differentiate between beads coated with different types of antibodies. These results indicate that improvement of the experimental apparatus could lead to the detection of HSV-1 complexed to small polystyrene beads with electrorotation.

In order to ascertain if dielectrophoresis would be a better method for the detection of virus particles, the real part of the Clausius-Mossotti factor was computed. The results for varying bead sizes are shown in figure 14.

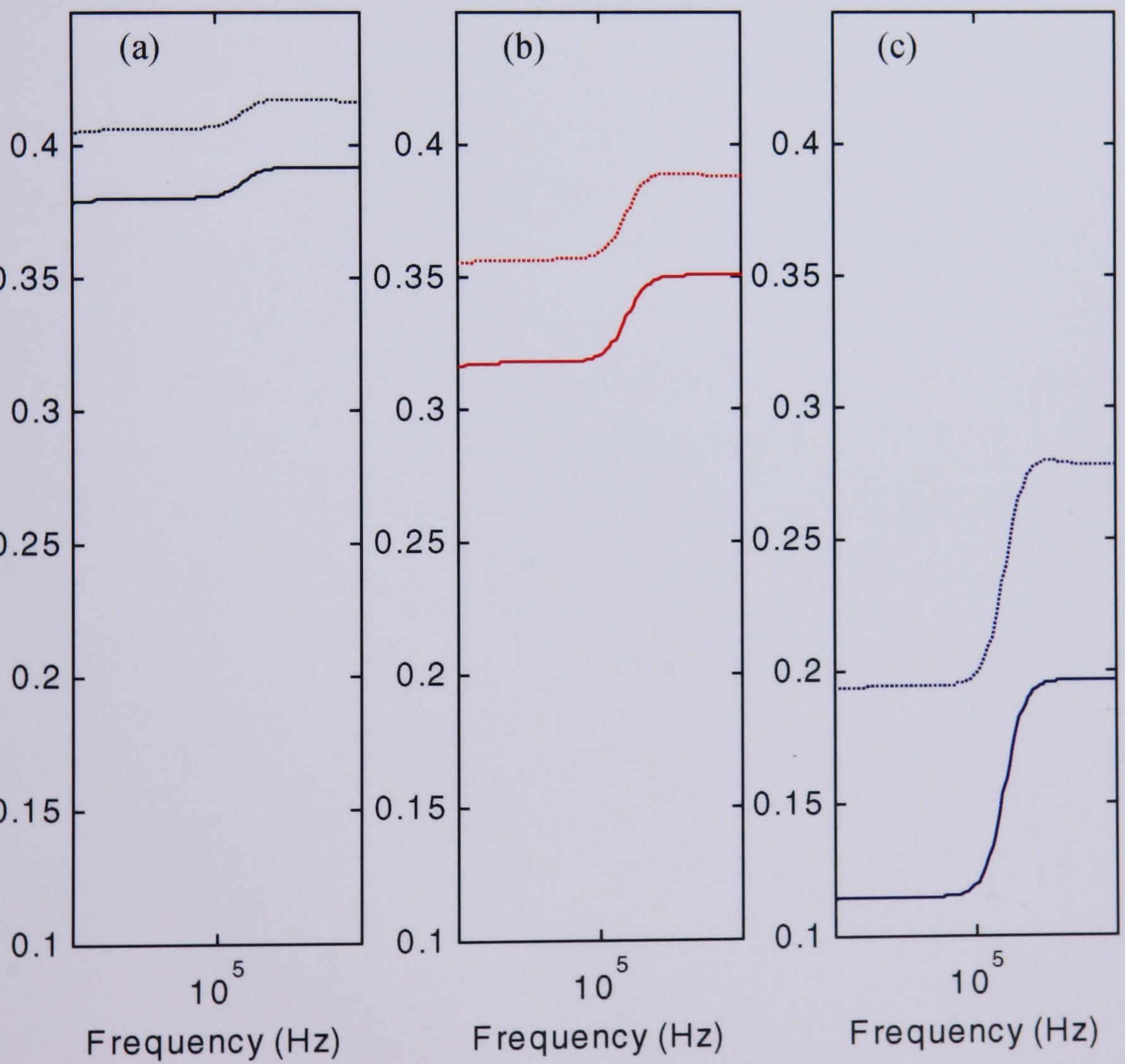

Figure 14: The effect of attaching HSV-1 (volume fraction = 0.2) to the surface of polystyrene beads. The solid lines represents beads without HSV-1, while the dotted lines are beads with virions on their surfaces. Figure 14(a) is for beads with dimensions:of 5.2x3.1μm (black), 14(b) is for beads of: 3.1x1.8μm (red); figure 14(c) is for beads of: 1.6x0.9μm (blue).

The force on a particle experiencing dielectrophoresis is proportional to the volume of the particle as well as to the Clausius-Mossotti factor. It can be seen from figure 14 that while the force decreases with a reduction in the bead size and Clausius-Mossotti factor, the relative difference in the force between beads with and without HSV-1 increases. This indicates that using a suitable bead size it may be possible to detect the difference between beads with and without HSV-1.

6.7 Conclusions

Primary antibodies specific to HSV-1 were successfully used to complex HSV-1 to the surface of polystyrene beads coated with a secondary antibody. The attached virions could be clearly seen using a fluorescent objective. Using electrorotation it was not possible to differentiate between beads with the virus specific antibody attached from beads with HSV-1 attached as both types of beads failed to respond to rotating electric fields. However results presented by Burt *et al* [1] indicate that with care it is possible to obtain accurate rotation spectra of protein coated bead less than 1mm in diameter. This suggests that it might be possible to detect HSV-1 complexed to small beads.

Modelling beads of different sizes suggest that as the bead size decreases, the relative difference in the real part of the Clausius-Mossotti factor increases, perhaps making it possible to detect the presence of virus on beads by dielectrophoresis. The modelling suggests that, using beads of appropriate size, dielectrophoresis might be an appropriate method for the detection of beads with virions attached to the surface. Thus, if a sufficient number of virions is attached to a particular bead they could alter its dielectric properties in a detectable manner [9-13]. Further developments of such a method could lead to real time separation of beads with and without virions using Field-Flow-Fractionation [2], or continuous separation as described by Markx *et al* [14].

6.8 References

1. Burt, J.P.H., K.L. Chan, D. Dawson, A. Parton, and R. Pethig, *Assays for microbial contamination and DNA analysis based on electrorotation.* Annales De Biologie Clinique, 1996. **54**: p. 253-257.
2. Wang, X.B., J. Vykoukal, F.F. Becker, and P.R.C. Gascoyne, *Separation of polystyrene microbeads using dielectrophoretic/gravitational field-flow-fractionation.* Biophysical Journal, 1998. **74**: p. 2689-2701.
3. Konig, B. and M. Gratzel, *A novel immunosensor for Herpes Virus.* Analytical Chemistry, 1994. **66**: p. 341-344.
4. Hodgson, C.E. and R. Pethig, *Determination of the viability of Escherichia coli at the single organism level by electrorotation.* Clinical Chemistry, 1998. **44**(9): p. 2049-2051.
5. Kakutani, T., S. Shiatani, and M. Sugai, *Electrorotation of non-spherical cells: theory for ellipsoidal cells with an arbitrary number of shells.* Bioelectrochemistry and Bioenergetics, 1993. **31**: p. 131-145.
6. Arnold, W.M., H.P. Schwan, and U. Zimmermann, *Surface conductance and other properties of latex particles measured by electrorotation.* Journal of Physical Chemistry, 1987. **91**: p. 5093-5098.
7. Zhou, X.F., G.H. Markx, R. Pethig, and I.M. Eastwood, *Differentiation of viable and non-viable bacterial biofilms using electrorotation.* Biochimica et Biophysica Acta, 1995. **1245**: p. 85-93.
8. Szilagyi, J.F. and C. Cunningham, *Identification and characterisation of a novel non-infectious herpes simplex virus-related particle.* Journal of General Virology, 1991. **72**: p. 661-668.
9. Docoslis, A., N. Kalogerakis, L.A. Behie, and K.V.I.S. Kaler, *A novel dielectrophoresis device for the selective isolation of viable cells in cell culture media.* Biotechnology and Bioengineering, 1997. **34**: p. 239-250.
10. Green, N.G., H. Morgan, and J.J. Milner, *Manipulation and trapping of sub-micron bioparticles using dielectrophoresis.* Journal of Biochemical and Biophysical Methods, 1997. **35**: p. 89-102.
11. Hughes, M.P., H. Morgan, F.J. Rixon, J.P.H. Burt, and R. Pethig, *Manipulation of herpes simplex virus type 1 by dielectrophoresis.* Biochimica et Biophysica Acta, 1998. **1425**: p. 119-126.

12. Pethig, R., *Dielectrophoresis: Using Inhomogeneous AC Electrical Fields to Separate and Manipulate Cells.* Critical Reviews in Biotechnology, 1996. **16**(4): p. 331-348.

13. Pethig, R., Y. Huang, X.B. Wang, and J.P.H. Burt, *Positive and negative dielectrophoretic collection of colloidal particles using interdigitated castellated microelectrodes.* Journal of Physics D: Applied Physics. 1992. **24**: p. 881-888.

14. Markx, G.H. and R. Pethig, *Dielectrophoretic separation of cells: continuous separation.* Biotechnology and Bioengineering, 1995. **45**: p. 337-343.

Chapter 7: Mapping the Electrorotational Torque in Planar Microelectrodes

7.1 Summary

The dielectric properties of a polarisable particle can be characterised by measuring the frequency dependence of the torque in a rotating electric field. Measurements performed using planar electrodes indicate a spatial variation in the torque across the dimensions of the array. In order to map this variation, the variation in rotation rate of elliptical latex beads was measured in 203 discrete positions in a 400x400μm polynomial electrode array. It was shown that torque variations across the electrode array can exceed 50% of the mean value at the centre. Data averaging and smoothing was performed to reveal trends that match theoretical predictions made using numerical models. The results indicate that the torque depends on variations in both the magnitude and phase of the electric field.

7.2 Introduction

The rotation rate of a particle depends on the electric field strength (as described in the theory chapter). However, experiments have shown that particles exhibit a spatially dependent rotation rate within an electrode area, caused by non-uniformities in the electric field. In order to minimise the experimental error measurements are usually made within the central region of the electrode array where the electric field is considered constant [1-3]. For example Burt *et al* [4] imposed an arbitrary restriction on electrorotation measurements so that only particles within a circle of radius defined by 1/3 of the distance from chamber centre to electrode tip were studied.

Field-mapping in large electrodes (cm scale) has been used in order to determine the variation in electric field as a function of particle position within an electrode chamber [5, 6]. Numerical methods have also been used to calculate the electric field distribution [5-7]. Both Gimsa *et al* [5] and Hölzel [6] assumed that the torque varies only as a function of the square of the electric field. Hughes *et al* [7] showed that the torque is also related to the phase difference between the x and y components of the electric field within the rotation area, but this model has not been demonstrated practically.

A previous attempt to produce a "rotation map" was undertaken by Fuhr *et al* [8] who measured the spatial variation in rotation rate of oat protoplasts suspended in an electrode chamber formed by inserting four metal pins into an electrolyte solution. The rotation rate was measured at only 17 discrete points within the central area of the electrode chamber and a ±10% deviation in rotation rate was measured. Such a small variation was probably due to the fact that the electrodes were circular pins producing a uniform field in the centre. This data can not be used to verify the results predicted by Hughes *et al* [7], as the electrodes simulated were planar microelectrodes, which would not be expected to generate the same field distribution as the "pin electrodes" employed by Fuhr *et al*.

In order to verify the simulation performed by Hughes *et al* [7], measurements of the spatial variation of electrorotational torque within a polynomial electrode [9] was performed. The rotation rate of elliptical latex beads was measured at 203 different discrete positions within the electrode array. The spatial variation in rotation rate was analysed and the results point to trends which are similar to the predictions made in [7], implying that differences in phase as well as the magnitude of the electric field determine the torque exerted on a particle.

7.3 Theory

In this work slightly ellipsoidal beads were used so that the polarisation depends on the orientation of the bead to the field [10]. However, all the beads lie with the long axis parallel to the surface and in plotting the rotation rate the polarisability of all the beads was assumed to be identical.

Simulations of the time-invariant electric field in polynomial electrodes have been performed previously [5, 6]. However, simulations of rotating field vectors suggests that both the *magnitude* and *phase* of the rotating electric field varies across the electrode [7] so that an effective electric field factor $\boldsymbol{E}_{eff}^2$ can be introduced to compensate for this:

$$\boldsymbol{E}_{eff}^2 = \boldsymbol{E}_x \boldsymbol{E}_y \sin(\phi_x - \phi_y) \qquad (4)$$

where the subscripts x and y indicate the x and y components of the electric field and the phase ϕ. Both the magnitude and phase in the x and y directions are spatially dependent implying that the torque exerted on particles rotating in the electrode chamber varies as a function of position by as much as a factor 2.

7.4 Materials and methods

7.4.1 Electrodes

The electrodes were of a polynomial design [9], with a 400μm gap between opposing electrode tips, as illustrated by figure 1. They were fabricated on glass slides by conventional photolithographic processes, and consisted of 100nm Au deposited over a 10nm Ti/10nm Pa underlayer. A chamber was constructed around the electrode array using clear nail varnish and a 13mm diameter coverslip giving an enclosed volume of approximately 10μl.

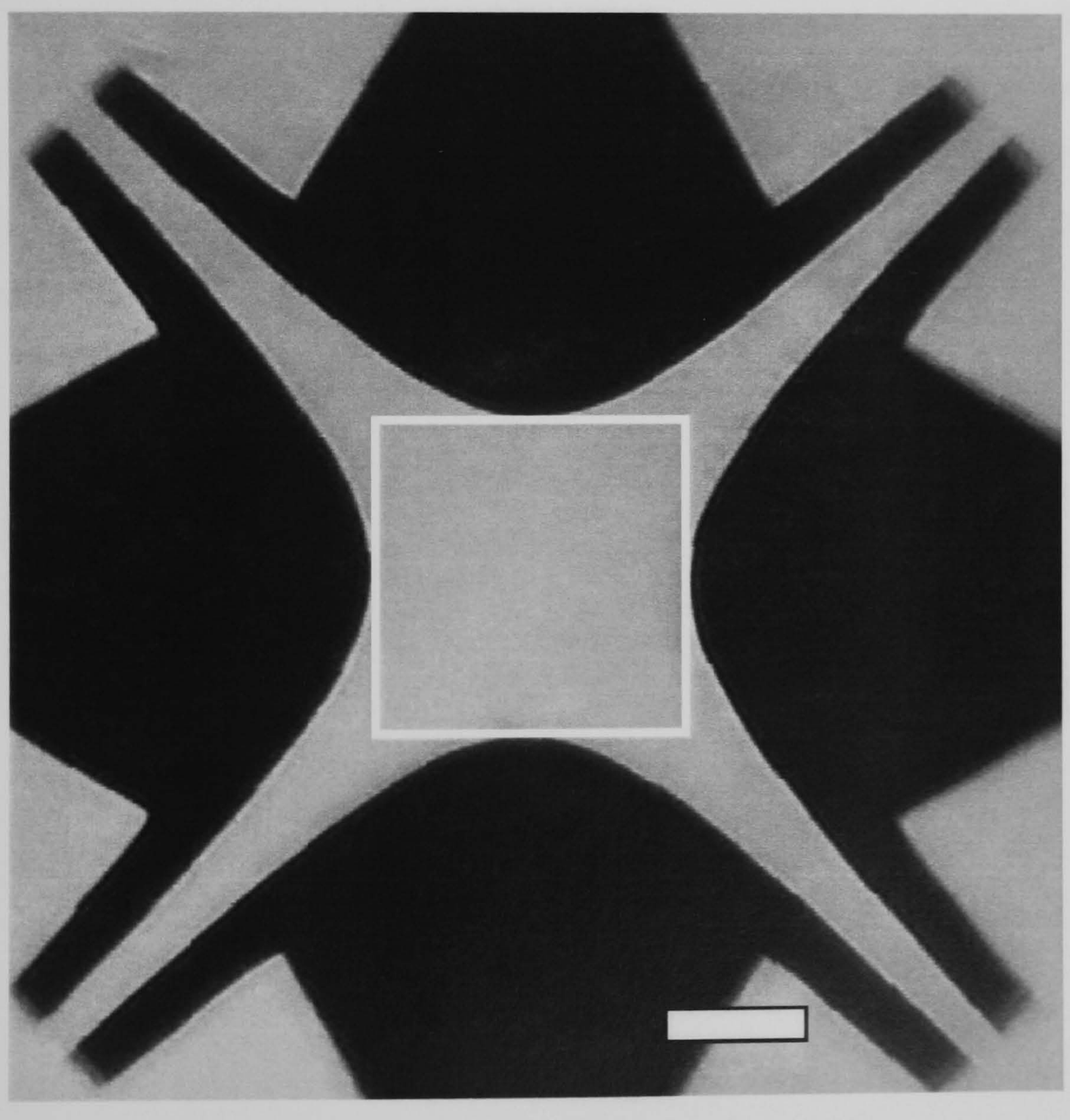

Figure 1: A photograph of the electrodes used in this work, fabricated from a 100nm thick gold layer over 10nm Ti/10nm Pd seed layer onto glass slides. Scale bar: 200μm. The box indicates the region of the electrode within which measurements were made.

7.4.2 Experimental

Experiments were performed using carboxylate modified elliptical latex beads (Bangs Laboratories, Illinois) which were 3x5μm in size. They were washed and resuspended in 280mM mannitol solution to a final concentration of approximately $2x10^7$ beads/ml. A 4-phase Direct Digital Synthesiser (DDS) was used to give a signal at a frequency of 1MHz, at 12 Volts peak to peak. The beads were imaged using a Nikon inverted microscope, a Panasonic digital camera and JVC S-VHS video recorder. Only beads further than 15μm apart from each other were measured and typically 60 beads occupied the electrode area at any one time. Rotation rates were obtained by examining the images on a large television monitor with a precision in measurement to ±1μm. Rotation rates were measured using a stopwatch over 5 complete revolutions per bead. Several experiments were made so that the rotation rate in a total of 203 positions across the whole array was measured. The data was processed using Matlab® software.

7.5 Results

Figure 2 shows an image of the beads in the electrode array. On application of the electric field, negative dielectrophoresis pushed the beads away from the electrode edges by up to 50μm. Although particles were observed to rotate in this region, the dielectrophoreticaly induced motion was too rapid to allow measurement of the rotation rate at a single point. Particles which rotated near the electrode edges, or in the inter-electrode gaps did so in a non-uniform manner where the bead alternated between rapid semicircular rotation and pauses where no motion was observed. Outside this region beads rotated smoothly about a stationary axis.

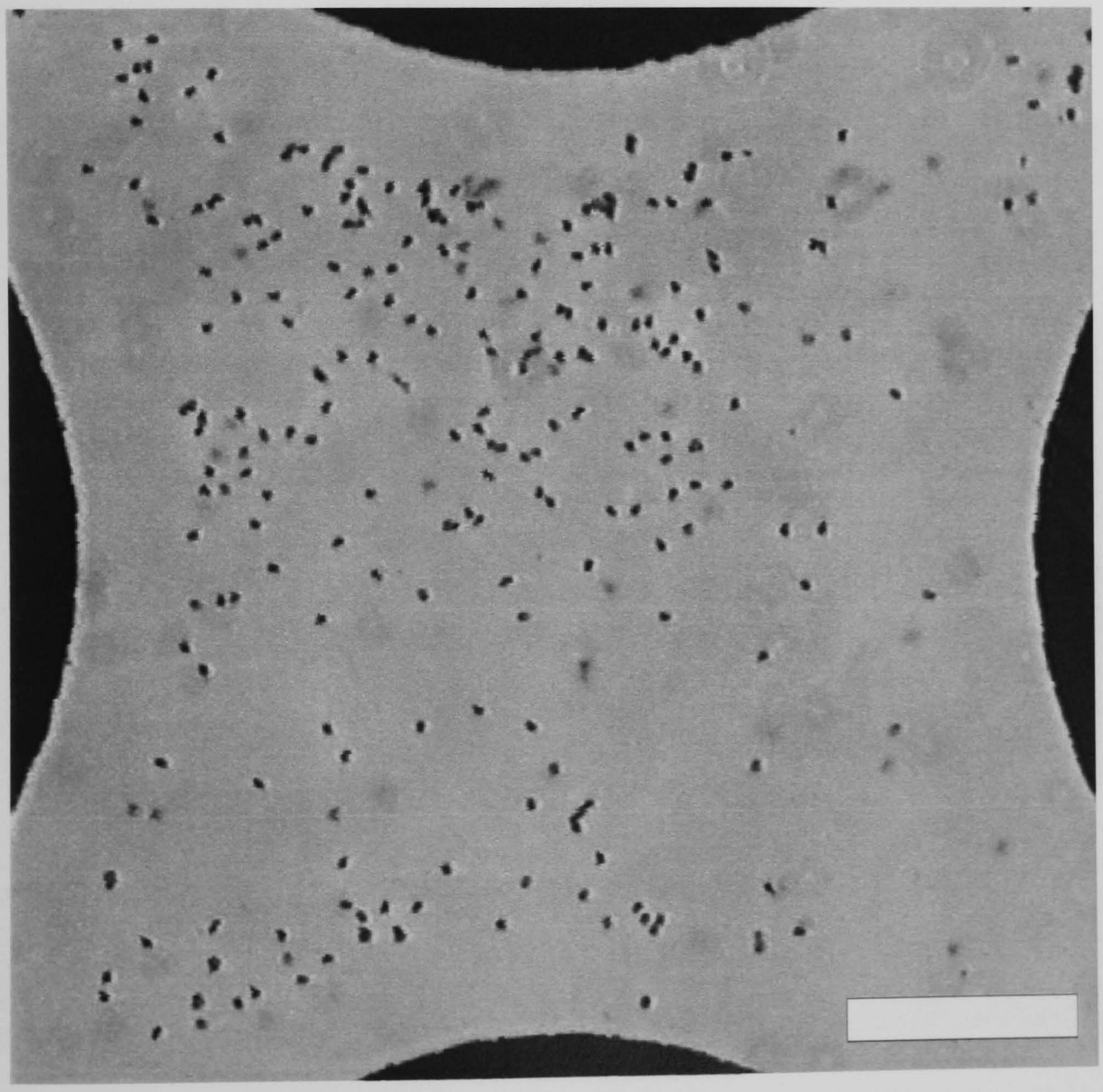

Figure 2: A captured video image of the elliptical beads rotating in an electric field. This image shows that the beads are repelled from the electrode edges by dielectrophoresis. A 50μm wide band, free of beads is apparent at the electrode edges, so rotation measurements could not be made in this region. Only beads more than 15μm from adjacent beads were measured. Scale bar: 100μm

The normalised rotation rate for 203 random points across this region is plotted in figure 3(a). The position of each measurement point is indicated in figure 3(b) with the co-ordinate point (0,0) at the centre of the electrode array. The data plotted in figure 3(a) shows the normalised rotation rate, with a value of 1 assigned to the mean value of the rate of rotation for the particles closest to (0,0). The graph has been drawn using the Delaunay triangulation function to interpolate between the data points, such that any point on the chart takes the value of the *nearest* recorded point to it. This figure shows that the rotation rate of beads nearest to the electrode tips (but 50μm away from the edges) is approximately 1.5x greater than the mean rotation at the centre of the electrodes. The lowest rotation rates are found towards the inter-electrode gaps (±200, ±200), where values were typically 0.8x that at the electrode centre.

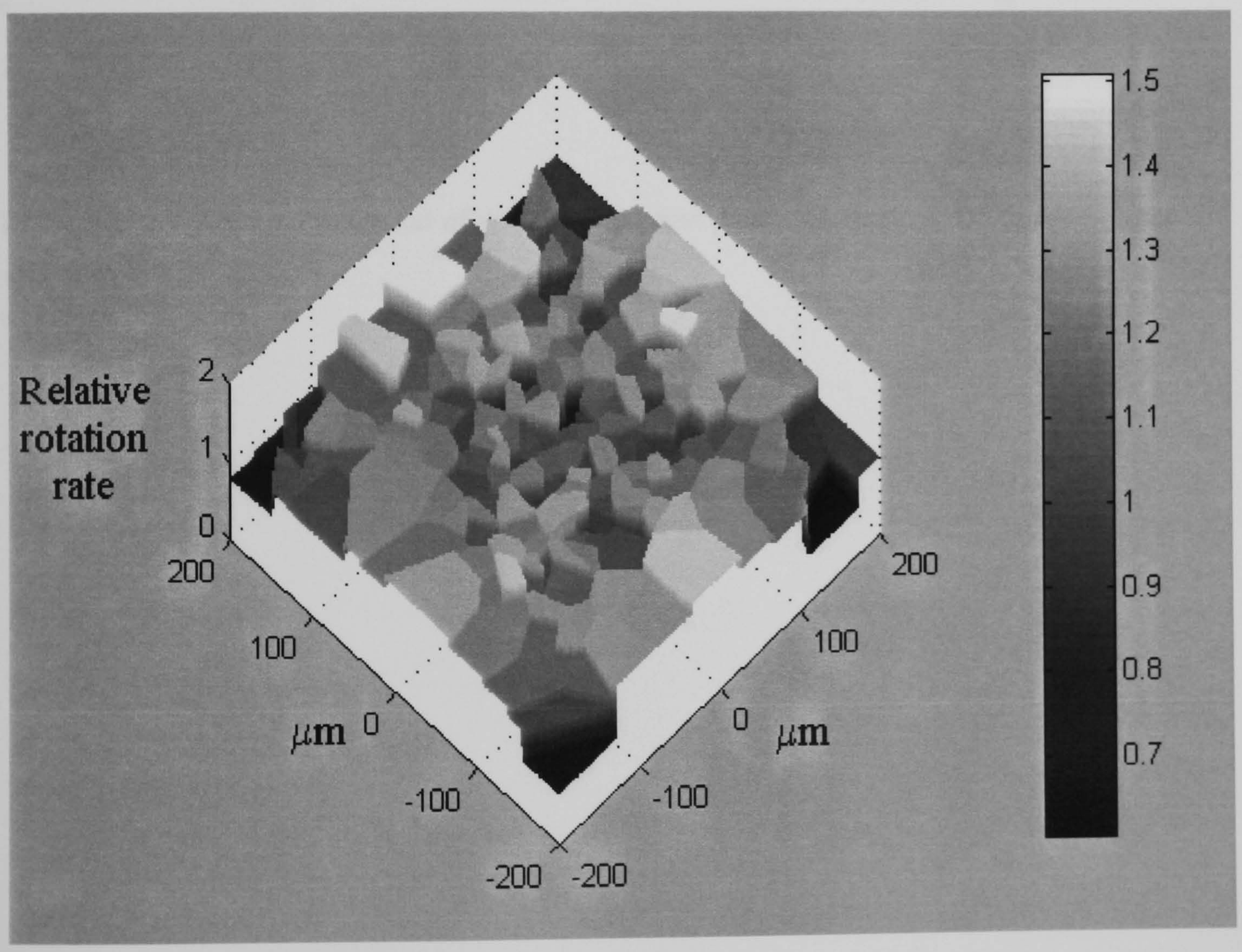

Figure 3(a): Plot showing the rotation rate measured across the electrode area, defined by the box in figure 1. The figure shows how the normalised measured rotation rate varies relative to the value at the centre of the electrodes.

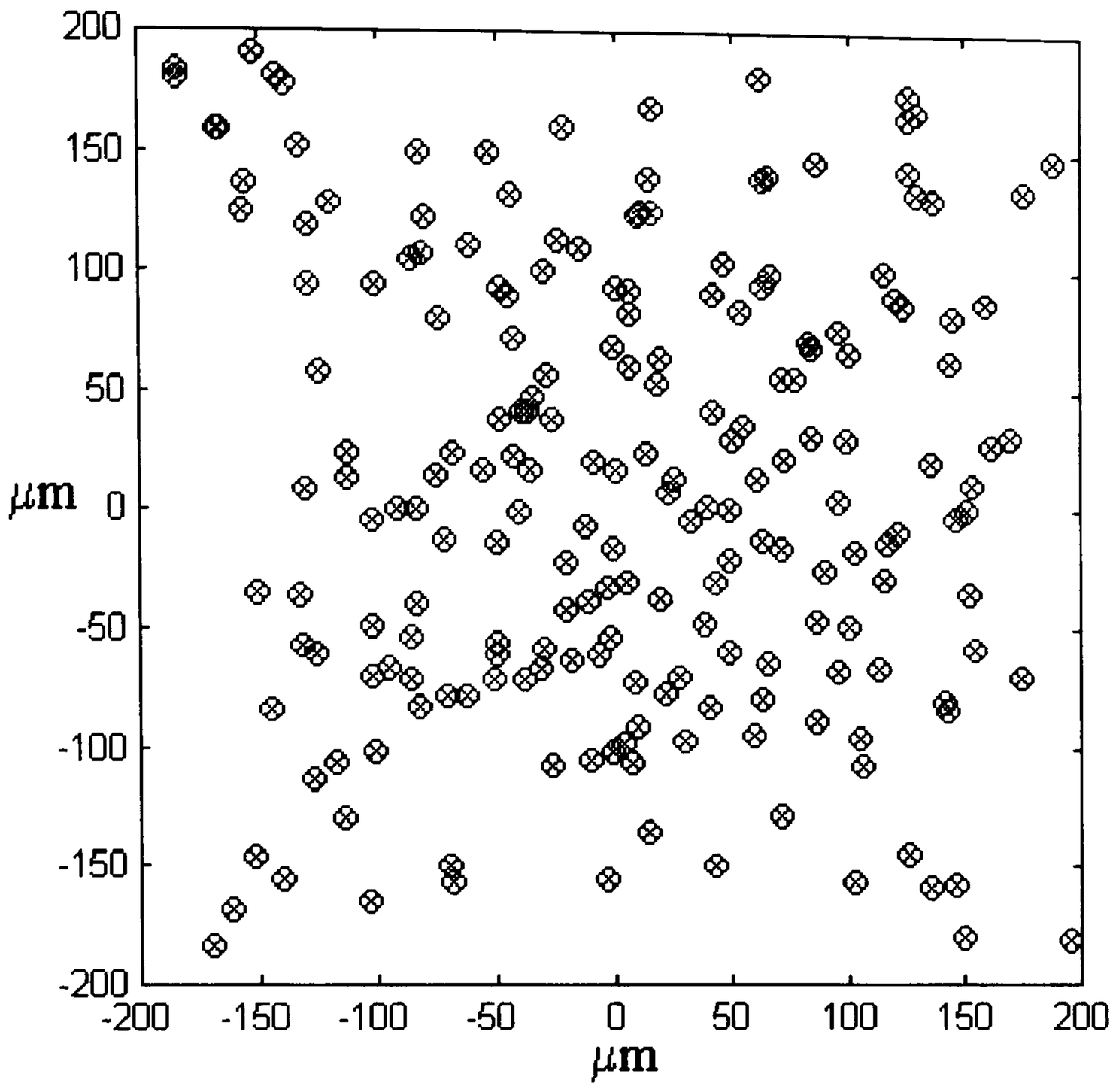

Figure 3(b): A plot of the location of the measured data points. A total of 203 discrete points were measured.

7.6 Discussion

7.6.1 Data analysis

As can be seen from figure 2, beads were pushed away from the electrode edges during the course of electrorotational measurements. The force experienced by the beads was the result of electric field non-uniformities giving rise to a negative dielectrophoretic force. Hughes [11] used the method of moment to conduct simulations of the dielectrophoretic force generated during electrorotation by polynomial electrodes, the results of which are shown in figure 4 (corresponding to the region defined by the box in figure 1). The arrows show the direction and relative magnitude of the dielectrophoretic force. It can be seen that the distribution of the beads in figure 2 which result from the dielectrophoretic force the beads experience during electrorotation correlate well with the magnitude and direction of the dielectrophoretic force vectors.

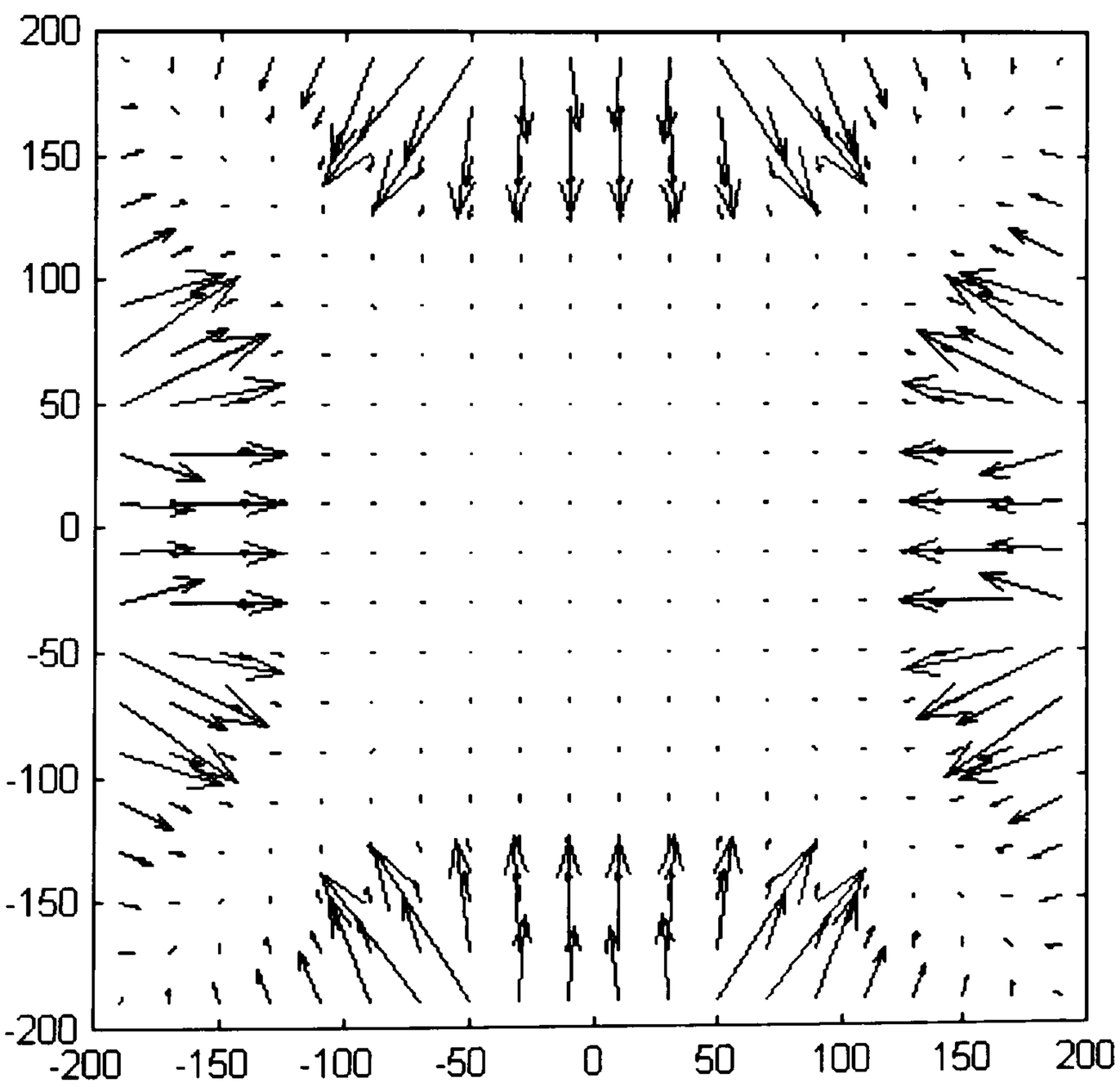

Figure 4: Method of moments simulation of the dielectrophoretic force distribution in the central region of polynomial electrodes used for electrorotation measurements.

It can be seen from figure 3(a) that the rotation rate is not uniform across the electrode and in general the rate near the electrode tips is higher than at the centre, or the electrode corners. The experimental error in obtaining the rotation data for single beads was estimated to be within ±5%. In addition, local variations in rotation rate were observed, probably caused by a combination of factors such as differences in bead properties, variations in the height of the bead above the electrode plane, or interactions between the bead and glass. Independent measurements of the variation in the characteristic rotation spectra for a selection of beads, all measured in the central region of the electrode array, indicated a maximum variation of ±5%. In order to more accurately determine the torque distribution further data analysis was performed.

Since the polynomial electrode array is symmetrical about 4 axes, the experimental data points can be mirrored 8 times which effectively increases the number of data points in any octant by a factor or 8. The results of this operation are shown in figure 5, where the torque distribution is now easier to visualise. It shows that the rotation rate is uniform across the central region of the electrode array, and rises towards the edges with a peak value of 1.5x the central average at the boundary of measurement, approximately 50μm from the electrode tips.

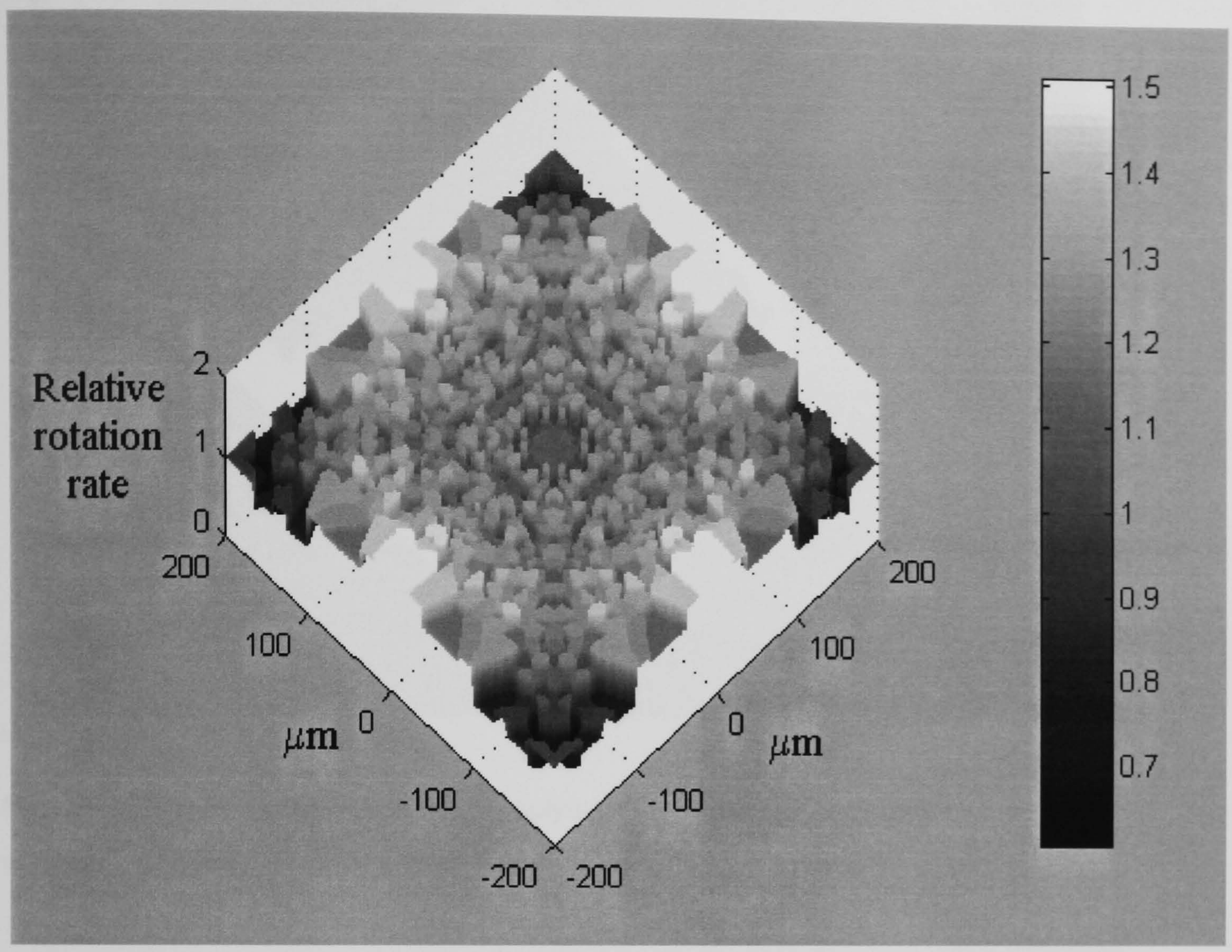

Figure 5: A plot showing the rotation rate determined by mirroring each data point 8 times around the 4 axes of symmetry.

Figures 6(a)-6(c) show the results of pixel by pixel averaging figure 5 using 10μmx10μm, 20μmx20μm and 40μmx40μm windows respectively. As the averaging window size is increased, local variations are removed and an underlying variation across the electrode array is seen. As the window size increases a slight local maxima can be seen in the direction of inter-electrode gaps. In order to test for errors, the original data (figure 3(a)) was subtracted from the averaged data (figure 6(c)). Maximum variations were ±0.15x the average central torque value and randomly distributed across the array.

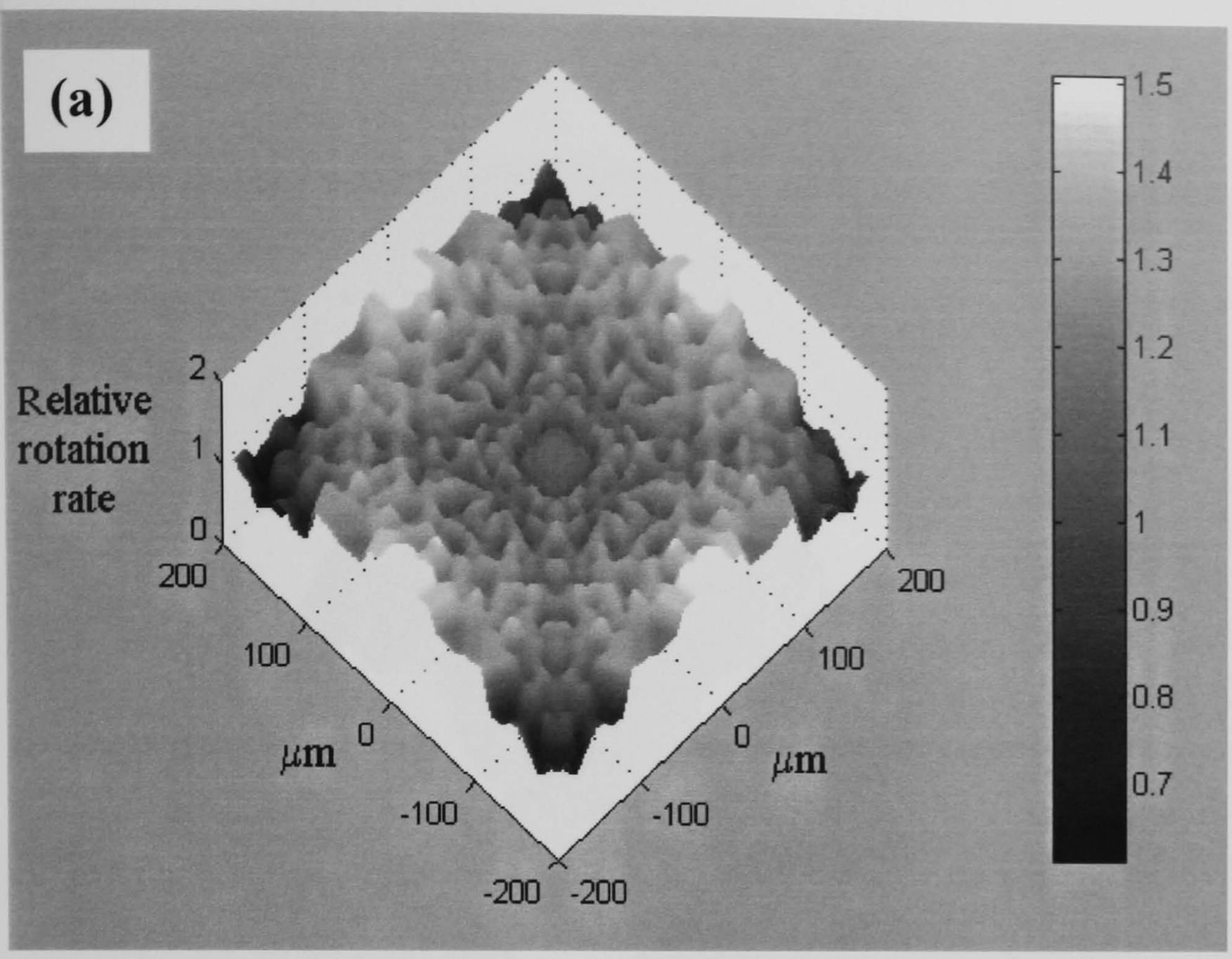

Figure 6(a): The figure show the result of applying a rolling average across the data set described in figure 5. The size of the window was: 10μmx10μm.

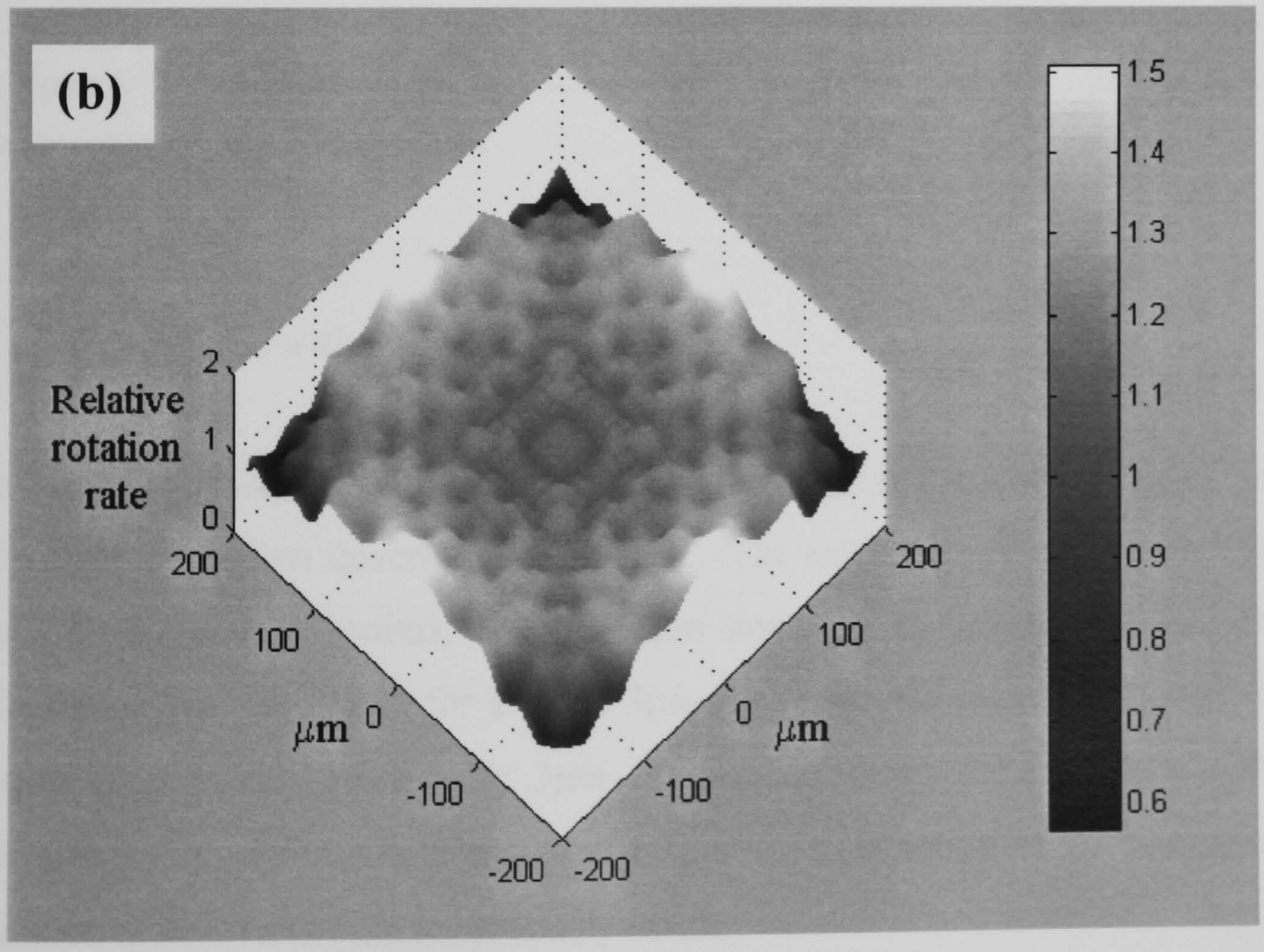

Figure 6(b): The figure show the result of applying a rolling average across the data set described in figure 5. The size of the window was: 20μmx20μm.

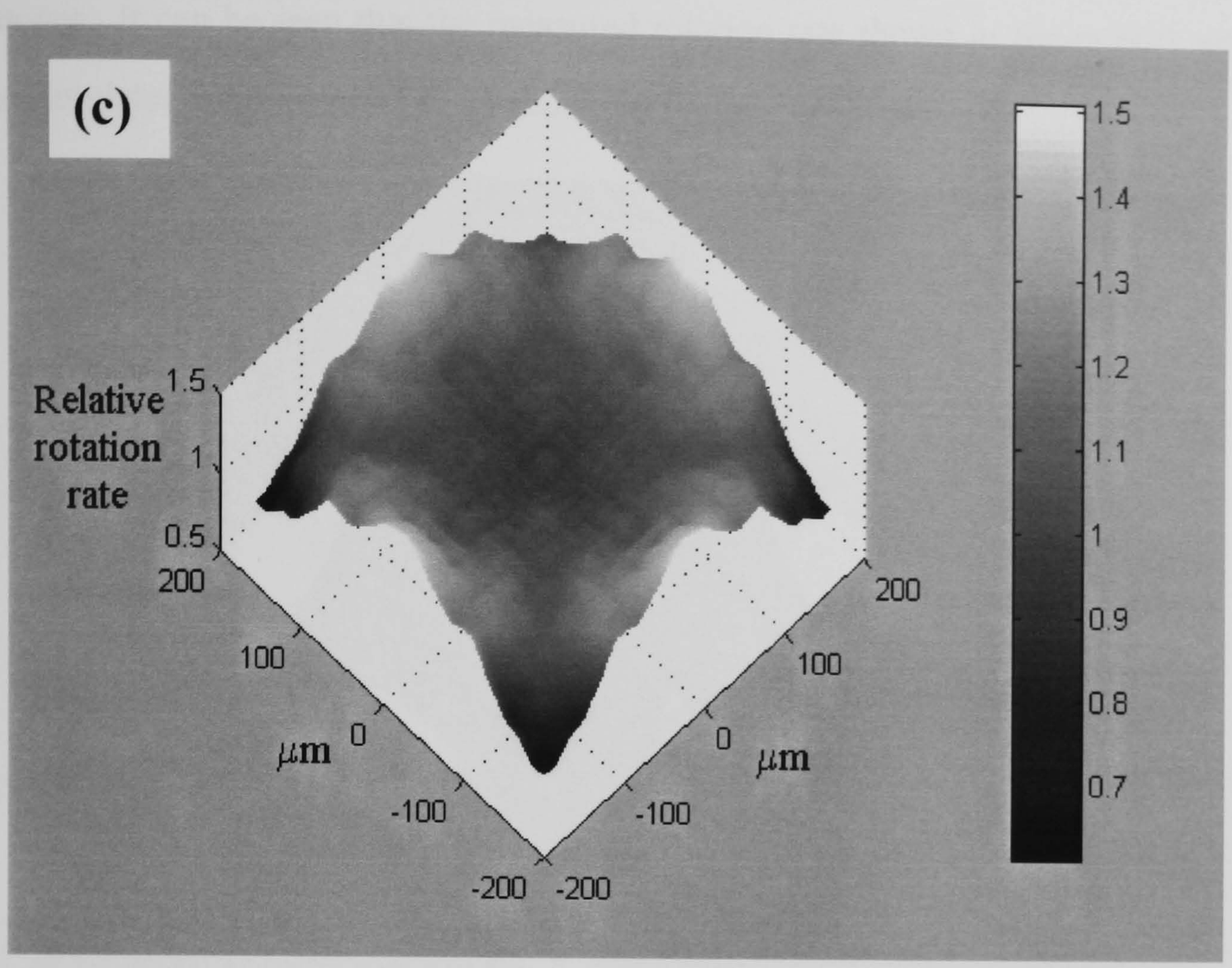

Figure 6(c): The figure show the result of applying a rolling average across the data set described in figure 5. The size of the window was 40μmx10μm. The general trends in torque distribution can be seen more clearly in this figure.

7.6.2 Comparison with theoretical model

In previous work [7], the electric field was analysed for a 400x400μm gap electrode in a plane covering 800x800μm. The simulation space was divided into 80x80 discrete points, spaced 10μm apart on a regular grid and the simulation was calculated for a plane 3μm above the electrodes. Although the beads used in this work were 3μm in diameter along the minor axis, the differences in electric field between 1.5μm (corresponding to the centre of rotation of bead) and 3μm are probably minor.

Figure 7 shows a simulation of $\boldsymbol{E}_{eff}^{2}$, confined by the box in figure 1, in the plane 3μm above the electrode calculated using the method of moments as outlined in

[7], these simulations were performed by Dr. M.P. Hughes at the University of Bangor. It can be seen that the measured rotation rate shown in figure 6(c), and the simulated rotation rate (E_{eff}^2) shown in figure 7 are similar in shape.

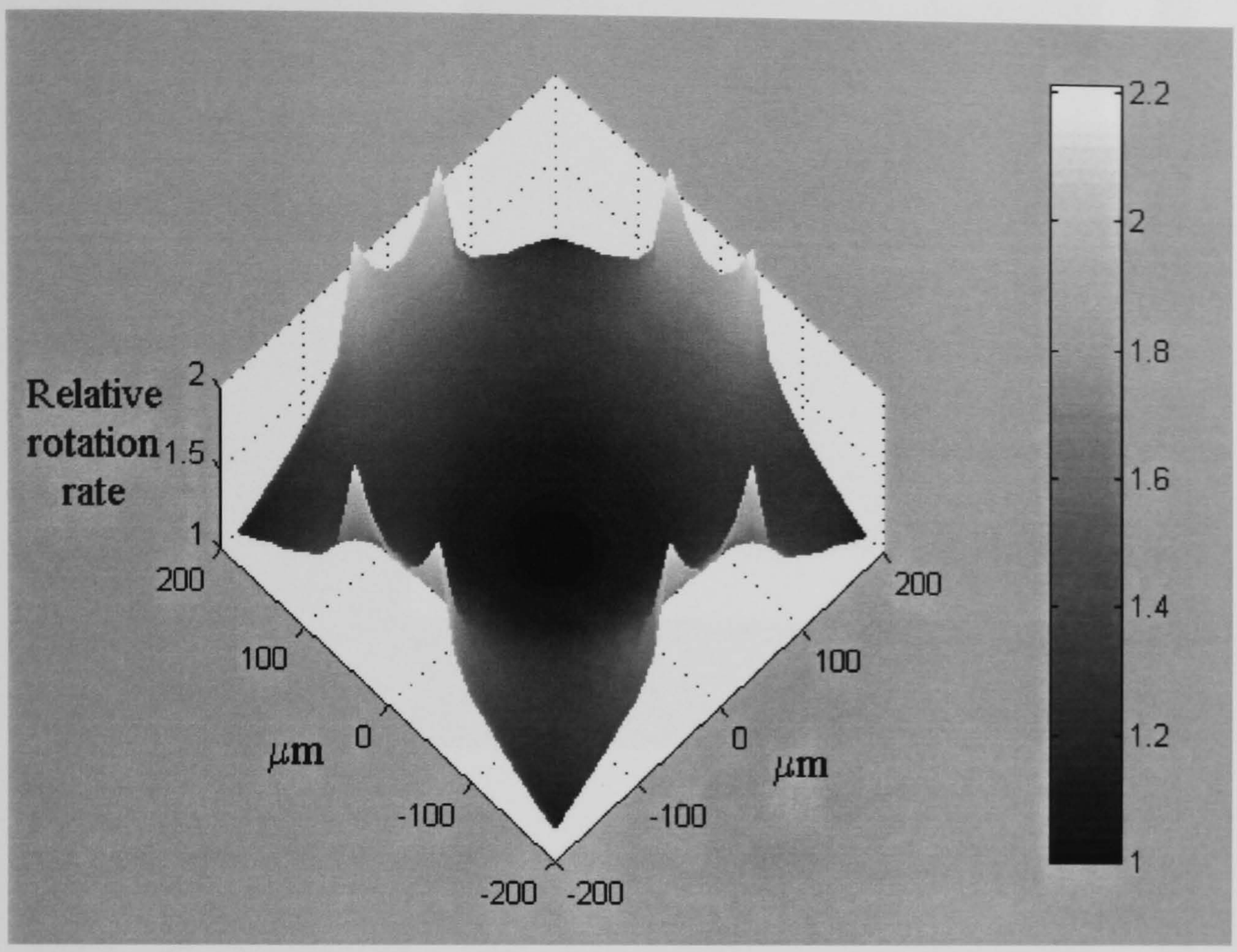

Figure 7: A simulation of the torque distribution relative to the value at the centre (0,0) calculated in a plane 3μm above the electrode surface in an area defined by the box in figure 1. The simulated rotation rate compares favourably with the experimentally determined torque distribution shown in figure 6(c).

A grey scale representation of the theoretical and experimental data is shown in figure 8 (a) and (b) respectively. A good correlation can be seen between the simulated rotation rate (normalised E_{eff}^2), figure 8(a) and the experimental data, figure 8(b). The correlation can be seen in the regions of low rotation rate at the central areas that are of the same magnitude in both cases. Also the increasing rotation rate in the direction of the electrode tips is the same in both cases, as is the reduction in rotation rate on approaching the inter-electrode gaps. The latter effect gives rise to a shallow maximum at approximately (±100,±100).

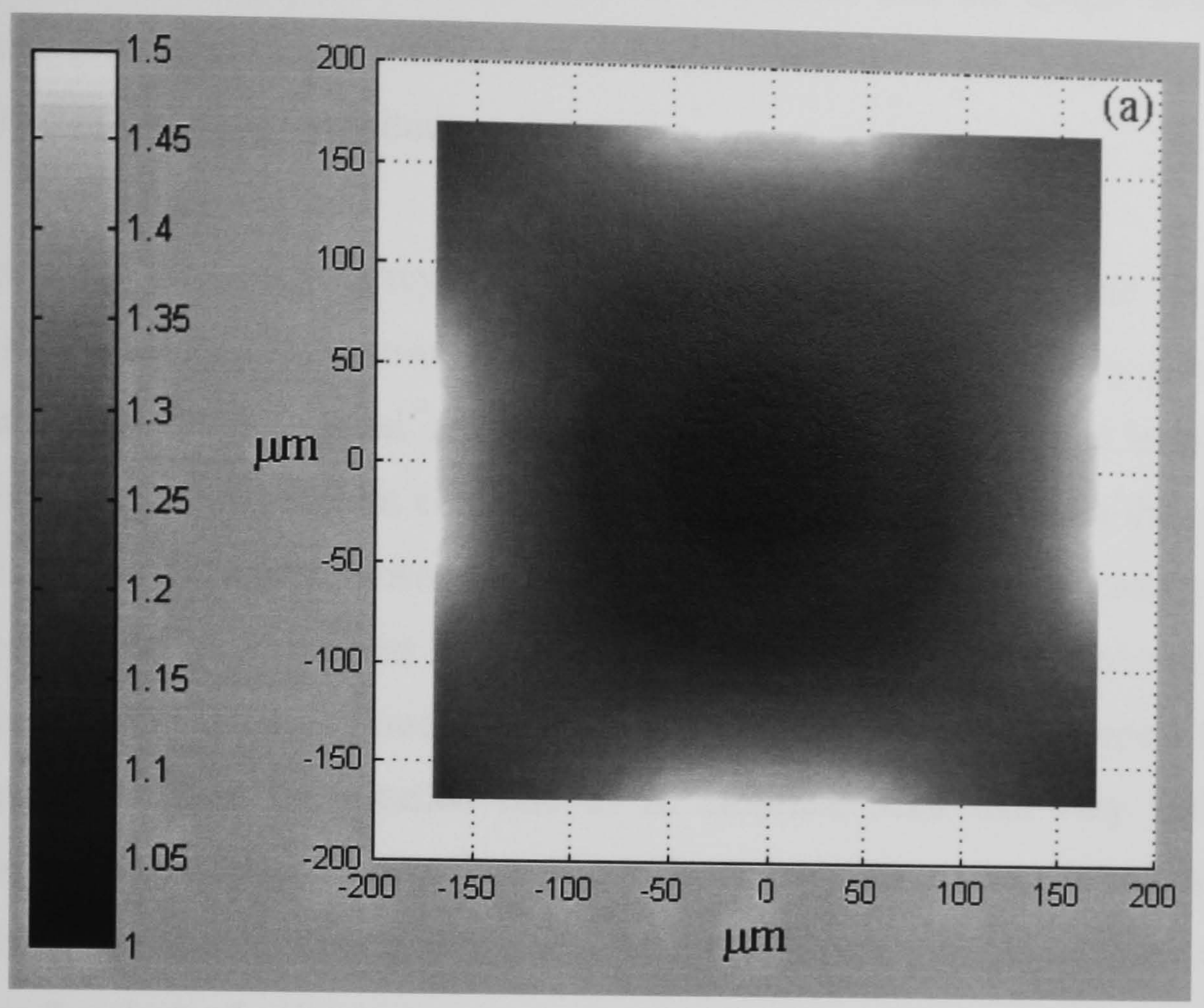

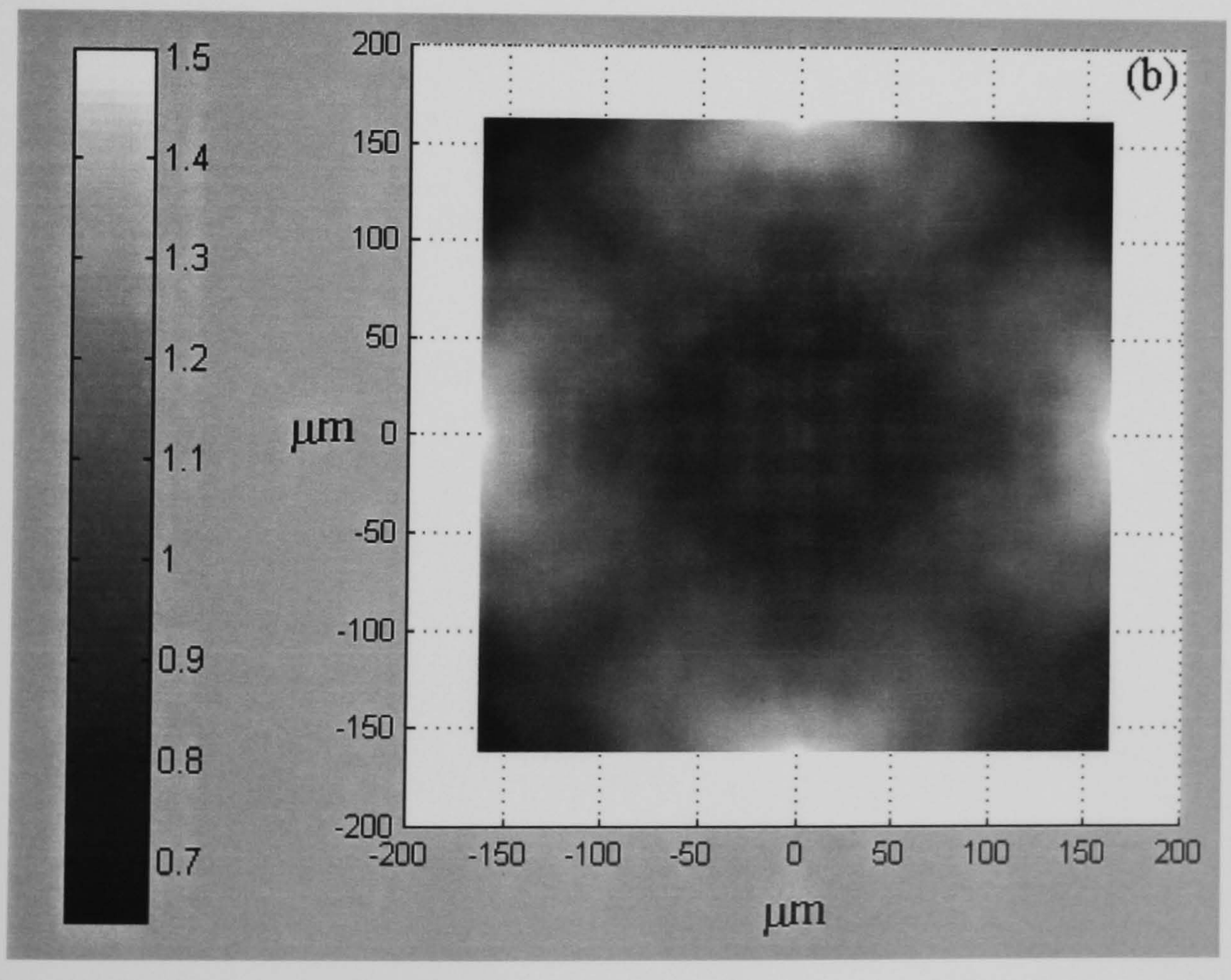

Figure 8:A grey scale plot of the simulated rotation rate (a) and the experimentally measured rotation rate (b) taken from figures 7 and 6(c) respectively. Adjacent scales indicate the relative rotation rates. The similarity between the experimental and predicted rotation rates is evident.

The principal discrepancy is that experiments indicate that the torque near the inter-electrode gaps (±150, ±150) falls to 0.7, whereas the model predicts that it should be of the same magnitude as the centre.

A reason for this discrepancy may be due to the magnitudes of the rotating vectors $\boldsymbol{E}_x$ and $\boldsymbol{E}_y$. The non-uniform rotation rate could be caused by a vector combination of a rotational and an alignment torque. The time averaged alignment torque will remain constant, so that the bead will align with the major axis along $\boldsymbol{E}_{max}$. Superimposed on this is the rotating torque, which acts either with or against the alignment torque. The overall effect is that the torque will vary depending on the alignment of the bead so that its motion will appear to be non-uniform. Thus the rotation rate of an elliptical bead will vary with its orientation to the field. Finally, near the electrode edge the electric field contains a significant z-direction component, which may cause the particle to rotate at an angle to the electrode plane.

7.7 Conclusions

In order to justify the use of electrorotation data for particles distributed across an electrode chamber, it is important to determine the effect that the non-uniformity of electric field magnitude and phase has on those particles. In order to assess this, the electrorotation rates of over 200 latex spheres have been measured across an electrode array to determine the variation in induced torque as a function of position within the array. This study demonstrated that the torque varies by in excess of 50% depending on the position within the array.

Comparison of the variation in torque as mapped across the inter-electrode space indicates a defined shape to the torque variation, which may be used to validate existing theories of electrorotation. The variation closely matches the torque distribution predicted by numerical models which take into account variations in local phase, and shows that both variations in the magnitude and phase of the electric field cause variations in the induced rotation of particles.

Recent work by De Gasperis *et al* [12] and Zhou *et al* [13] have led to the development of automated systems for the determination of rotation rates. Such a system could be adapted to automatically adjust the measured rotation rate of a particle depending on the position of the particle in the electrode chamber. This would increase the number of cells available for study by compensating for wide variations in position-related local torque variations away from the central region.

7.8 References

1. Arnold, W.M. and U. Zimmermann, *Rotating-field-induced rotation and measurement of the membrane capacitance of single mesophyll cells of Avena sativa.* Z. Naturforsch., 1982. **37c**: p. 908-915.
2. Zhou, X.F., G.H. Markx, and R. Pethig, *Effect of biocide concentration on electrorotation spectra of yeast cell.* Biochimica et Biophysica Acta, 1996. **1281**: p. 60-64.
3. Chan, K.L., P.R.C. Gascoyne, F. Becker, and R. Pethig, *Electrorotation of liposomes; verification of dielectric multi-shell model for cells.* Biochimica et Biophysica Acta, 1997. **1349**: p. 182-196.
4. Burt, J.P.H., K.L. Chan, D. Dawson, A. Parton, and R. Pethig, *Assays for microbial contamination and DNA analysis based on electrorotation.* Annales De Biologie Clinique, 1996. **54**: p. 253-257.
5. Gimsa, J., R. Glaser, and G. Fuhr, *Remarks on the field distribution in four electrode chambers for electrorotational methods.* Studia Biophysica, 1988. **125**: p. 71-76.
6. Holzel, R., *Electric field calculation for electro-rotation electrodes.* Journal of Physics D: Applied Physics, 1993. **26**: p. 2112-2116.
7. Hughes, M.P., X.B. Wang, F.F. Becker, P.R.C. Gascoyne, and R. Pethig, *Computer-aided analysis of electric fields used in electrorotation studies.* Journal of Physics D: Applied Physics, 1994. **27**: p. 1564-1570.
8. Fuhr, G., T. Muller, A. Wagner, and E. Donath, *Electrorotation of oat protoplasts before and after fusion.* Plant Cell Physiology, 1987. **28**: p. 549-555.
9. Huang, Y. and R. Pethig, *Electrode design for negative dielectrophoresis.* Measurement Science and Technology, 1991. **2**: p. 1142-1146.
10. Kakutani, T., S. Shiatani, and M. Sugai, *Electrorotation of non-spherical cells: theory for ellipsoidal cells with an arbitrary number of shells.* Bioelectrochemistry and Bioenergetics, 1993. **31**: p. 131-145.
11. Hughes, M.P., *Electrokinetic manipulation of Particles*, PhD Thesis University of Wales, 1995.
12. Gasperis, G.D., X.B. Wang, J. Wang, F.F. Becker, and P.R.C. Gascoyne, *Automated electrorotation: dielectric characterization of living cells by*

real time motion estimation. Measurement Science and Technology. 1998.

13. Zhou, X.F., J.P.H. Burt, and R. Pethig, *Automatic cell electrorotation measurements: studies of the biological effect of low frequency electromagnetic fields and of heat shock.* Physics in Medicine and Biology, 1998.

Chapter 8: Cell reactions to dielectrophoretic manipulation.

8.1 Summary

The phenomenon of dielectrophoretic particle manipulation holds promise for many biotechnology applications, including new methods for cell sorting. Cell manipulation typically involves transient exposure for 15 minutes to radio-frequency AC electric fields generated using planar microelectrodes. The aim of this work was to investigate a range of acute effects of dielectrophoretic manipulation on the normal physiology of isolated cells. Cells were suspended in isoosmotic Mannitol and exposed to a 5MHz, 21V(peak to peak) electric field using electrodes with 100μm feature sizes. The cells were assigned to three experimental groups; non-exposed controls, exposed cells processed immediately after cessation of the field, and exposed cells processed after a time delay.

The results can be summarised as follows: SEM observations of spread cells cultured on the devices showed no apparent acute effects of field exposure on cell morphology, cell-doubling rates in exposed cells subsequent to field-exposure or transient incubation in mannitol were no different from control cells. While an MTT 'mitochondrial stress' assay indicated no alteration in the rate of oxidative respiration in exposed cells 0.5 hours after exposure to the field, and Western blot analysis indicated upregulation of fos protein in cells 0.5 hours after field-exposure, which was confirmed using densitometry. Finally, reverse transcription of cellular mRNA followed by PCR amplification, polyacrylamide gel electrophoresis and autoradiography of cDNA banding revealed differential gene expression between controls and exposed cells processed immediately after cessation of the field. Differential gene expression persisted in exposed cells at least 0.5 hours after removal from the field. Other observations indicated that temperature fluctuation in the mannitol solution was minimal, suggesting that upregulated mRNA may not have been related to thermally-induced heat shock protein.

The results indicated that exposure to AC fields during dielectrophoretic cell manipulation is associated with upregulation of the intermediate-early gene cfos and also transcription of other as yet unidentified genes. These transcriptional events were not manifest as gross changes in cell morphology or cell-cycle dynamics.

8.2 Introduction

8.2.1 Cellular responses to dielectrophoresis

If dielectrophoresis is to be used to manipulate cells that are later used for clinical proposes it is important to investigate the nature and extent of any cellular responses to dielectrophoretic manipulation, as identifying such effects is clearly relevant to the development of dielectrophoretic cell sorting technologies. Cells are known to be capable of exhibiting very rapid and quantifiable responses to a variety of stimuli. As there are not any appropriate precedents that suggest an obvious subcellular system as a potential target for the dielectrophoretic field. it was deemed necessary to screen a spectrum of possible resultant effects using a range of different biological investigations.

These include scanning electron microscopy, which was applied to investigate the gross alignment responses of cells to externally applied electric field gradients, modulation of filopodia and lamellipodia initiation and also ultrastructural alterations in membrane integrity. Other biological investigations include possible alterations in cell-cycle control system dynamics that were measured by standard assessment of doubling rates in a fibroblast-like cell line. As well as the use of an MTT ((3-[4,5-Dimethylthiazol-2-yl]-2,5-diphenylterazolium bromide; Thiazolyl blue, Sigma, UK) mitochondrial stress assay in order to determine whether any field-activation effect was dependent upon an increase in oxidative respiration. Finally, alterations in gene expression was tested at two levels. Firstly, expression of the intermediate-early gene c-fos was investigated indirectly using an immunochemical localisation of fos protein on a Western blot of pooled cell lysate. Secondly, mRNA fingerprinting was carried out using sets of random primers as an assessment of non-specific gene transcription in a wider context.

8.3 Experimental methods

8.3.1 Fabrication and electrode design.

In order to probe the effect of dielectrophoresis on cells, a non-uniform electric field was generated using a microfabricated electrode of a sawtooth pattern. A photograph of the electrodes is shown in figure 1 with a feature size between tips of 100μm. This sawtooth pattern was chosen in order to generate regions of high electric field at the electrode tips [1], and thus trap cells with positive dielectrophoretic forces. The electrodes were fabricated using standard photolithographic techniques, and consisted of layers of 10nm Titanium, 10nm Palladium and 100nm of Gold deposited onto a glass slide. The electrode array was 8 mm by 11 mm and the cells were confined by a perspex cloning ring to give a chamber height of 6 mm.

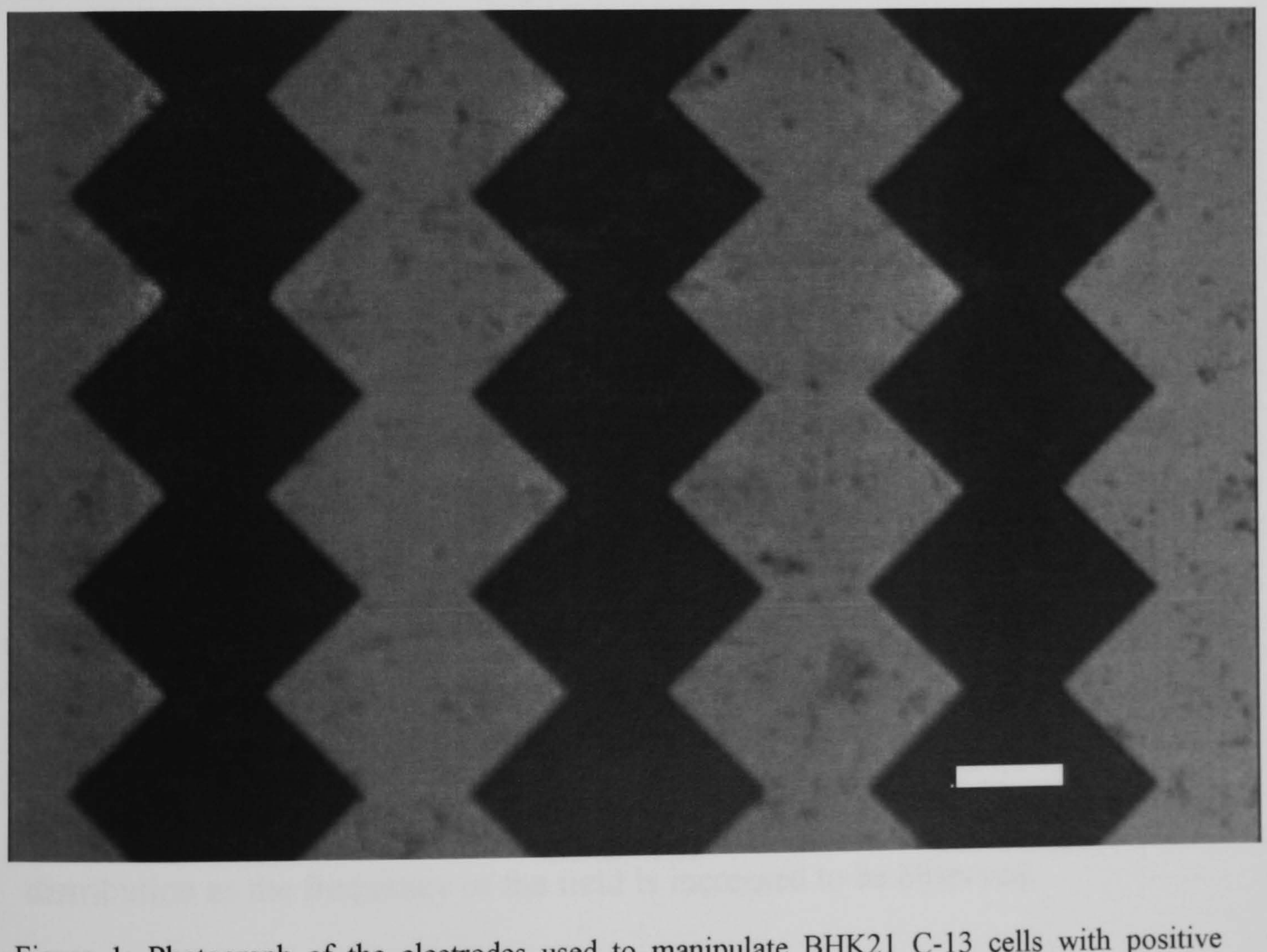

Figure 1: Photograph of the electrodes used to manipulate BHK21 C-13 cells with positive dielectrophoresis. The scale bar represents 100μm.

8.3.2 Cell handling during dielectrophoresis.

For dielectrophoretic experiments, cells were removed from the culture plates, resuspended and washed once in a medium consisting of 280mM mannitol and 0.1mg/ml BSA, with a conductivity of $10mSm^{-1}$, measured using a HP 4292A impedance analyser and a Sentex conductivity cell. The cells were introduced onto the electrode array at a density of $1.5x10^5$ cells/ml and allowed to settle for 5 minutes prior to the application of a signal of 21 $V_{pk\text{-}pk}$ and a frequency of 5MHz for 15 minutes. At this voltage and frequency the cells experienced positive dielectrophoresis.

8.3.3 Electric field mapping and membrane potential calculations

The sawtooth electrode generates a highly non-uniform electric field. In order to calculate the electric field strength at different points on the electrode, finite element simulation software was used (Ansoft®, Maxwell 3-D) to obtain electrostatic plots of the field distribution. The software employed does not take into account free charge and is therefore not able to solve Poisson's equation. As such the software can not solve time dependent changes in the electric field, so the simulations undertaken are steady state approximations of an alternating electric field. Electric field plots were also calculated with a cell located near the electrode edge. The cell was modelled as a solid dielectric sphere, and the electric field plots were performed for two different cell permittivities. In the first case the permittivity of the cell was set to be equal to the permittivity of a cell membrane, in the second case the permittivity of the cell was set to be equal to the permittivity of the cell interior. When the frequency of an applied electric field increases, it starts to penetrate into the cell interior. Plotting the electric field for a low and high cell permittivity allows the changes in the electric field distribution as the frequency of the field is increased to be observed.

The cell was also modelled as a heterogeneous dielectric system, approximated to a solid dielectric sphere surrounded by a thin membrane. Using this model, an

expression for the electric potential ΔU dropped across the cell membrane as a function of the applied electric field and frequency can be obtained [2]:

$$\Delta U = \frac{{}^{3}\!/_{2} Ea\cos\theta}{1 + a(G_{mem} + j\omega C_{mem})\left(\rho_i + {}^{\rho_s}\!/_{2}\right)} \qquad (1)$$

In this expression C_{mem} is the specific membrane capacitance, G_{mem} is the membrane conductance per unit area, a=7μm is the radius of the cell, ρ is a general resistivity and the subscripts i and s refer to the cell interior and the suspending medium respectively. The polar angle with respect to the field is given by θ.

8.3.4 *Cell culture.*

Fibroblast-like BHK 21 C13 cells from Glasgow University stock were maintained using standard cell culture methods. The basic culture medium was the Glasgow modification of Eagle's minimal essential medium (Gibco, Scotland) supplemented with 3mM glutamate, 100 units/ml penicillin, 100 μg/ml streptomycin, 2.5μg/ml ampherotericin B, 10%v/v calf serum, 10% tryptose phosphate broth and 20mmol Hepes saline. Cell suspensions were obtained by detachment of confluent monolayers using 0.05% trypsin in 0.2mg/ml EDTA after rinsing in $Ca^{2+}Mg^{2+}$ - free 20mM Hepes-buffered Hank's balanced salt solution. Trypsinisation was stopped by addition of serum containing medium, prior to centrifugation, resuspension, trituration and counting of cell density. 0.4 ml of cells suspension was plated onto the devices at a density of $1.5x10^5$ cells per ml.

8.3.5 Analysis of cell division parameters.

Cells were assigned to exposed and non-exposed control groups of equal volume fraction in medium as assessed using a haemocytometer. The electric field was applied to one group of cells using the parameters described above. Immediately after exposure the average cell numbers in each group were counted using a haemocytometer and the cells subsequently plated into 6 x 25ml TC flasks at equal cell densities. This was assigned time zero. Subsequent counts of cells per field of view were obtained using phase-contrast optics for 5 fields of view, selected by systematic random sampling for all 12 flasks at 21, 31, 44, 55, 69 and 97 hours after plating. Cell counts over the observation period were compared using a Kolmogorov-Smirnov two-sample test.

8.3.6 Examination of cell morphology.

Cells were plated onto the devices at a density of $5x10^4$ cells/ml and placed at a temperature of 37°C for 24 hours to adhere and spread both over and between the electrodes. The cells were then exposed to the field using the same parameters as before and then immediately washed once in HBSS and then fixed for 15 minutes using 1% v/w glutaraldehyde in 0.1M PBS at room temp. After fixation and preparation for SEM, examination proceeded with removal of the fixation solution followed by 3 x 5 min rinses in fresh 0.1M PBS and post-fixation in 1% v/v osmium tetroxide in RO water for 10 minutes. After a further 3 rinses x5 minutes in RO water the cells were dehydrated through increasing concentrations of alcohol in RO water to 100% alcohol within 1 hour. The cells were then placed in 1:1 solutions of alcohol in hexamethyldisilazane (HMDS) for 2 x 5 minutes and then in HMDS alone for 2 x 5mins. After the second immersion the cells on the devices were allowed to air dry. The devices were then mounted on SEM stubs, sputter coated with gold palladium, earth-strapped using silver dag and examined using a Hitachi SEM 800 operated at 10kV. This process was repeated for a control sample that was not exposed to electric fields but otherwise given identical treatment.

8.3.7 Mitochondrial stress (MTT) assay.

Alterations in mitochondrial stress were probed using an MTT assay for both cells exposed to the electric field and the control cells. One 0.5ml sample of cells at $1x10^6$ cells/ml were exposed to the electric field. A control sample was maintained under the same conditions but without the field. After pelleting at 2000rpm for 5mins the cells were resuspended in Hank's balanced salt solution (Sigma, UK) containing 0.5mg/ml MTT ((3-[4,5-Dimethylthiazol-2-yl]-2,5-diphenylterazolium bromide; Thiazolyl blue, Sigma, UK) and incubated at 37°C for 3 hours. Active mitochondrial dehydrogenases in living cells reduce the yellow dye to the insoluble purple formazan, while dead cells do not affect the dye. After repelleting at 2000rpm for 5mins the converted dye was solubilised by triturating vigorously in 0.2ml isopropanol. Finally the absorbance of the dye was scanned between 400 and 700nm using a spectrophotometer. A spectrophotometric reading was taken at 570nm. This work was performed in collaboration with Dr S. Britland (School of Pharmacy, University of Bradford).

8.3.8 fos-protein Western blotting and immunodetection.

One hour after field-exposure two sets of control and exposed cells were tested for expression of fos-protein. From each experiment 0.2ml aliquots of cell suspension were mixed with an equal volume of gel sample buffer (50 mM Tris - HCl pH 6.8; 0.5 % sodium dodecyl sulphate; 10 % glycerol; 0.5 % 2 - mercaptoethanol; 0.01 % bromophenol blue) and boiled for five minutes. The cooled samples were then centrifuged at 14,000g for five minutes. 15 ml aliquots were subjected to polyacrylamide - SDS electrophoresis using a discontinuous system (4% stacking; 10% resolving; 1.5mm thickness) in a minigel format (Hoefer Mighty Small). Running conditions were typically 50 mA continuous current for 1 hour. After electrophoresis was complete, the proteins were transferred to PVDF membrane (NEN DuPont) using a semi - dry transfer system (Hoefer) (100mA constant current for one hour). Membranes were agitated in 0.1 M phosphate buffered saline plus 0.05% tween - 20 (PBST) containing 5 % fat free milk powder (Marvel) for one hour to block protein binding sites. The membranes were then washed in PBST and probed with anti c-fos antibody

(rabbit polyclonal antisera Ab-5, Calbiochem) (1:500 titre) in 1% bovine serum albumin/PBST for one hour. After washing off excess, bound antibody was detected by incubation with a goat anti rabbit antisera conjugated to horseradish peroxidase (1: 80,000 titre) followed by enhanced chemiluminescent detection of enzyme activity (Renaissance, NEN DuPont) on Reflection film (NEN DuPont). Replicate blots were also incubated with anti c -fos antisera in the presence of amino acids 4-17 c fos peptide fragment (Oncogene Research Products) to assess the specificity of the reaction. This work was performed in collaboration with Dr S. Britland and Dr A.T. Evans (School of Pharmacy, University of Bradford).

8.3.9 mRNA fingerprinting - Experimental Design.

An onset control group was processed at the start of the experiment. A second group of cells were exposed to the electric field for 0.25 hours and then processed immediately after being removed from the field. A third group of cells was exposed to a field with same intensity and duration as before. However, on removal from the field these cells were replaced in the incubation chamber for a further 0.5 hours prior to processing. The purpose of the 0.5hour delay prior to processing was to determine whether gene expression in this group of cells was altered in comparison with acutely processed cells and onset controls.

8.3.10 mRNA fingerprinting - isolation of mRNA.

Fingerprinting RNA populations was done using a randomly selected primer for first strand cDNA synthesis. PCR amplification was then used to amplify the products. Cells were collected from the devices immediately after completion of the experiments and thoroughly homogenised in 0.8 ml of RNA zolTM B solution (Biogenesis Ltd, Poole, UK) to expose the contents of the cytosol for separation. Approx. 1ml of 'cytosol'/RNA zolTM B solution was then transferred to an Eppendorf tube and 80 µl of chloroform added. The samples were then vortexed for 15 seconds and stored on ice for 5 minutes. After centrifuging at 12,000g at 4°C for 15 minutes the aqueous phase was collected and the RNA precipitated by the addition of an equal volume of the aqueous phase (approx. 400µl) of isopropanol for at least 45 minutes at 4°C. The RNA

precipitates were centrifuged for 15 minutes and then washed once with 0.8ml of 75% ethanol. Quantities of RNA were assessed by spectrophotometry at 260nm and up to 5ug RNA was used for cDNA synthesis. This work was performed by T.T. Li (Centre for Cell Engineering, University of Glasgow).

8.3.11 mRNA fingerprinting - first-strand cDNA synthesis.

Up to 5μg of the RNA sample was combined with 1μl cDNA synthesis oligo $(dT)_{12-18}$ primer and 2μl sterile H_2O and made up to 5μl. cDNA was made directly from the total RNA since only mRNA has a poly A tail corresponding to the oligo DT primer. The Ependorf tubes were then incubated at 70°C for 3 minutes. 5μl of the cDNA master mix , made up from 2μl of 5x first-strand buffer, 2μl of dNTP mix, 5μM each of dATP, dCTP, dTTP and dGTP and 1μl of MMLV (Moloney murine leukaemia virus) reverse transcriptase (Clonetech Inc., USA), was added to each reaction tube and incubated at 42°C for 1 hour. The reactions were then terminated by incubation at 75°C for 10 minutes. All the cDNA samples were then stored at -20°C. This work was performed by T.T. Li (Centre for Cell Engineering, University of Glasgow).

8.3.12 PCR for mRNA fingerprinting - cDNA amplification.

Each cDNA sample was thawed slowly and then combined with the polymerase reaction mixture containing 10X PCR buffer, sterile H_2O, 1.5mM $MgCl_2$, 0.2mM dNTP mix, 3.3μM ^{32P}dATP (3000Ci/mmole), and 1unit Taq polymerase (Boehringer Mannheim), 0.1μM ofthe P1;T1 OR P2;T2 primers (P1:5'-ATTAACCCTCACTAAATGCTGGTGG-3' and T1: 5'-CATTATGCTGAGTGATATATCTTTTTTTAG-3' ; P2: 5'-ATTAACCCTCACTAAAGATCTGACTG-3' and T2:5' CATTATGCTGAGTGATATCTTTTTTTTTAC-3') /20μl reaction mixture, and cycled first through 94°C for 5 minutes, 40°C for 5 minutes, and 72°C for 5 minutes. This was followed by 2 cycles of 94°C for 2 minutes, 40°C for 5 minutes and 68°C for 5 minutes, followed by 22 cycles of 94°C for = 1minute, 60°C for 1 minute and 68°C for 2 minutes. The PCR amplified fragments were separated on a denaturing polyacrylamide gel run for 2-3 hours at 85W. The gel was dried and exposed to X-ray film for 1-3 days. This work was performed by T.T. Li (Centre for Cell Engineering, University of Glasgow).

8.4 Results.

8.4.1 Dielectrophoresis

Prior to the application of the electric field, cells were suspended in the isoosmotic mannitol solution at a conductivity of $10mSm^{-1}$, placed over the electrodes and allowed to settle. They were observed to be randomly distributed as shown in the photograph of figure 2(a). A potential of 21V peak to peak at a frequency of 5MHz was then applied and after 10 seconds the cells moved towards the high field regions at the electrode tips and along the electrode edges, as shown in figure 2(b). Once the cells had moved into the high field regions they remained there for the duration of the experiments (15 minutes).

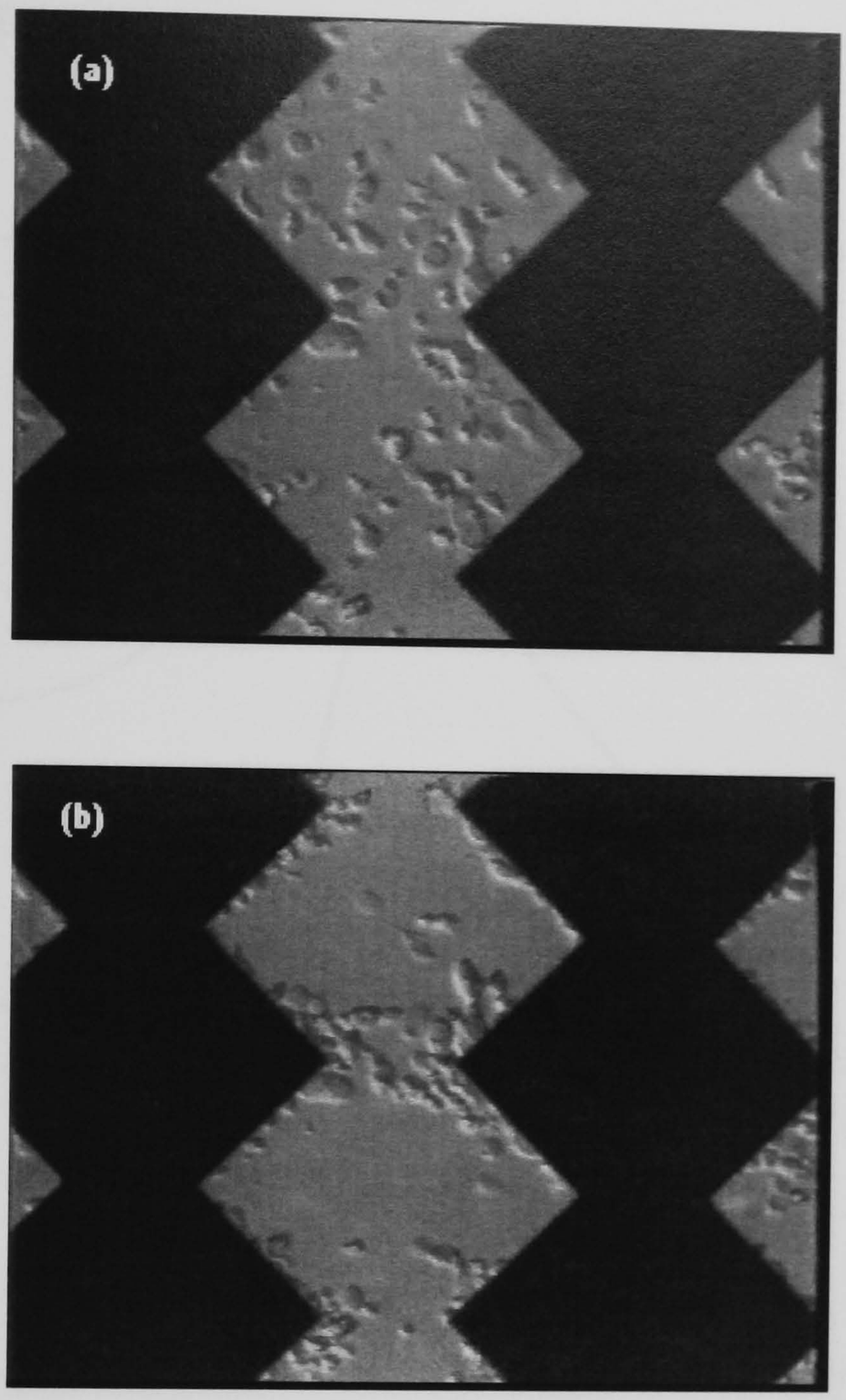

Figure 2: BHK cells suspended in 280mM mannitol and 0.1mg/ml BSA, sealed by a cloning ring on a sawtooth electrode pattern as seen through an inverting microscope before the electric field was applied (figure 2(a)) and 10 seconds after the field was applied (figure 2(b)).

Measurements of the dielectric properties of BHK(C-13) cells had been made using electrorotation methods (as described in the chapters detailing the time dependent changes in BHK(C-13) cells following infection with HSV-1). This indicated that the plasma membrane had a specific capacitance of $2\mu Fcm^{-2}$ and a conductivity of $5x10^{-7}Sm^{-1}$ and the cell interior a permittivity of $75\varepsilon_0$ and a conductivity of $0.32Sm^{-1}$. These dielectric parameters were used to calculate the frequency variation of the Clausius-Mossotti factor. For a medium conductivity of $10mSm^{-1}$ the results are shown in figure 3, where it can be seen that at a

frequency of 5MHz the cells experience positive DEP as observed experimentally figure 2(b).

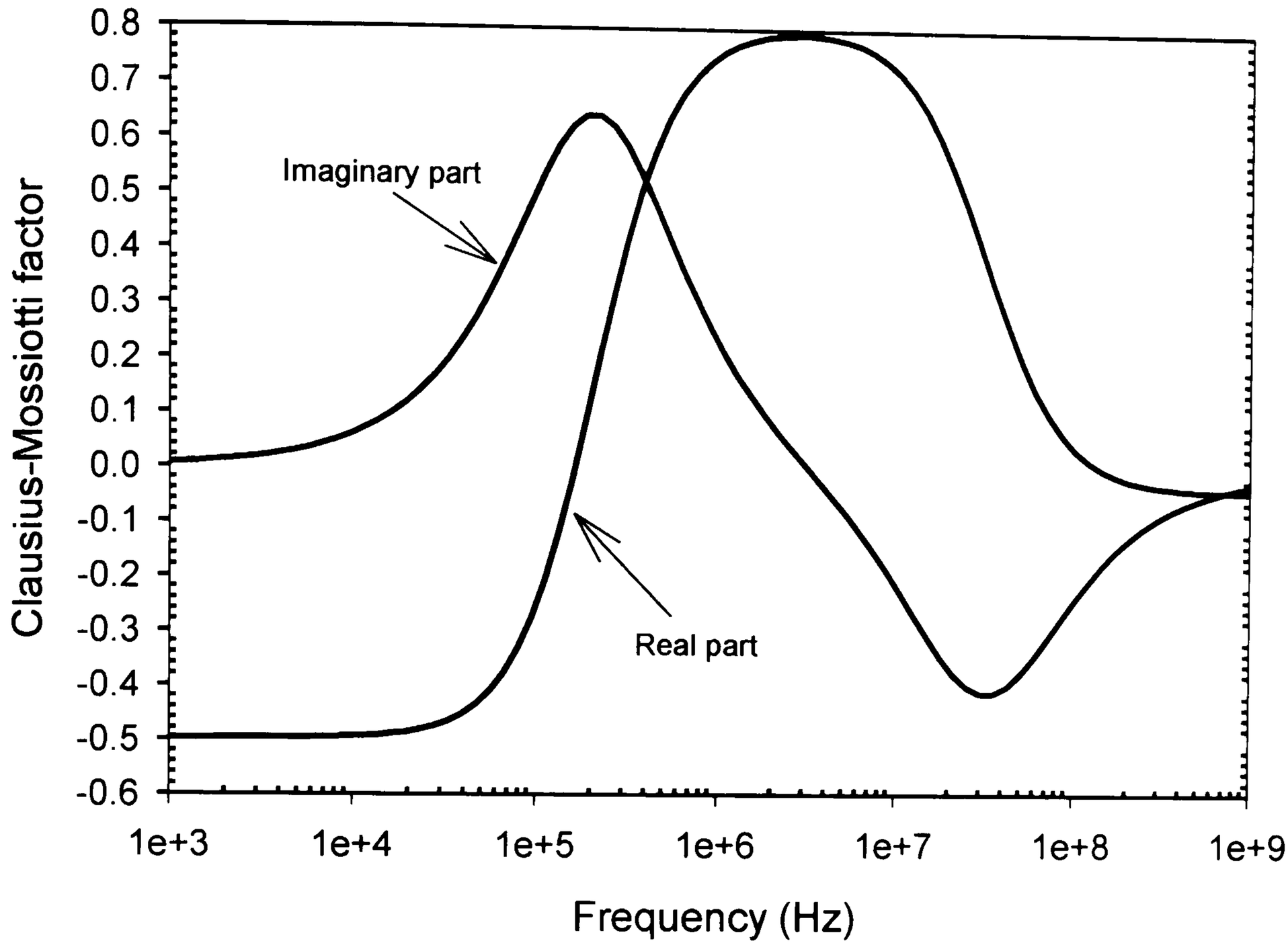

Figure 3: The real and the imaginary components of the Clausius-Mossotti factor of a BHK21 C-13 cell suspended in $10mSm^{-1}$.

8.4.2 Electric field and power dissipation simulation.

Electric field simulation software (Ansoft, UK), was used to calculate the electric field distribution for the sawtooth electrode array both with and without a cell. At an applied potential of 21V peak to peak, the calculated electric field distribution in a plane 6μm above the electrode surface is as shown in figure 4(a). The highest electric field occurs at the electrode tips, reaching a maximum of $3.7x10^5 V_{pk-pk}m^{-1}$. During experiments, cells experiencing positive dielectrophoresis would be attracted to these regions of high electric field.

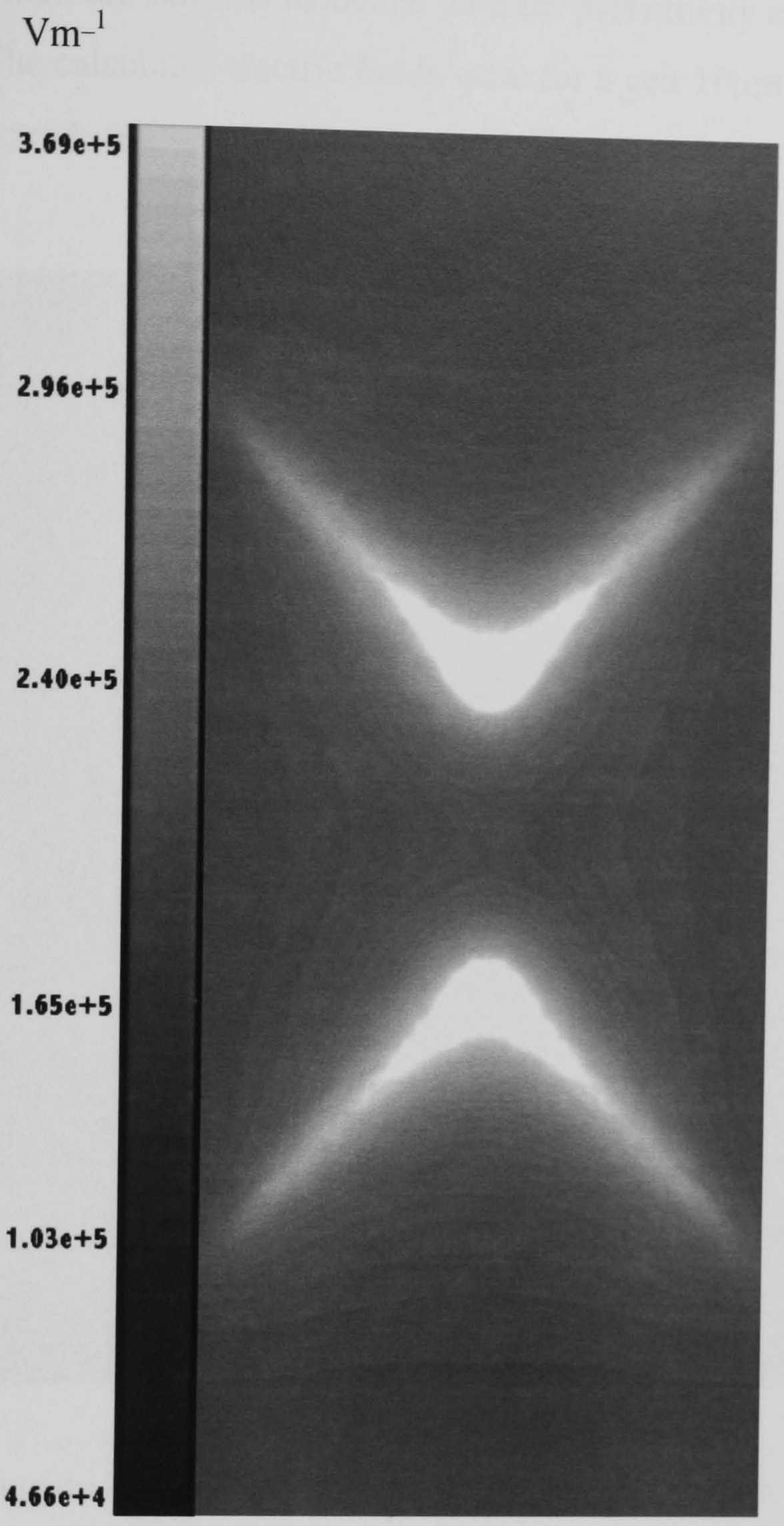

Figure 4(a): Simulation of the electric field strength in sawtooth electrodes, 5mm above the electrode surface. A voltage of $21V_{pk\text{-}pk}$ was applied to the electrodes. From the plot it can be seen that the regions of high electric field strength is at the electrode tips.

In order to estimate the localised power distribution around a cell, the distribution of E^2 was calculated for the cell with two different permittivities. Figure 4(b) shows the distribution of E^2 when the cell was modelled with the permittivity equal to a plasma membrane (ε_r=15.8), while Figure 4(c) shows the

distribution of E^2 when the cell was modelled with the permittivity equal to a cell interior (ε_r=55). The calculated electric fields were for a cell 10μm in diameter, 20μm from the electrode tip.

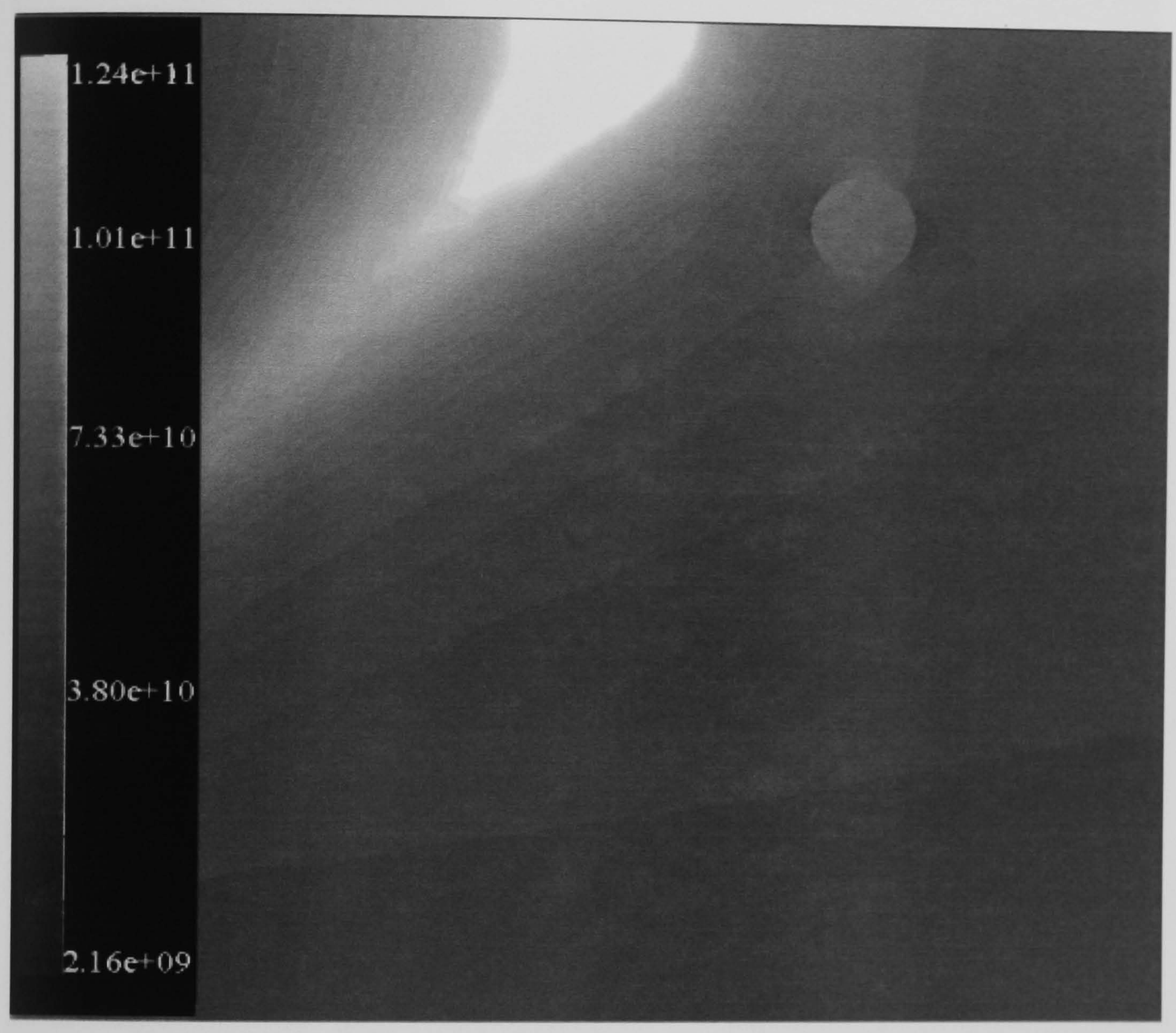

Figure 4(b): Simulation of the square of the electric field strength in the presence of a cell with the permittivity set equal to a plasma membrane near the electrode edge in a sawtooth electrode, 6μm above the electrode surface. A voltage of $21V_{pk\text{-}pk}$ was applied to the electrodes. From the plot it can be seen that the electric field is consistent with the cell experiencing a net dipole moment.

Figure 4(b) shows E^2 within the cell and that it was approximately $5x10^{10}$ $V^2_{pk\text{-}pk}m^{-2}$ in magnitude, from this it can be calculated that according to the simulation the potential drop across the cell is $2.8V_{pk\text{-}pk}$.

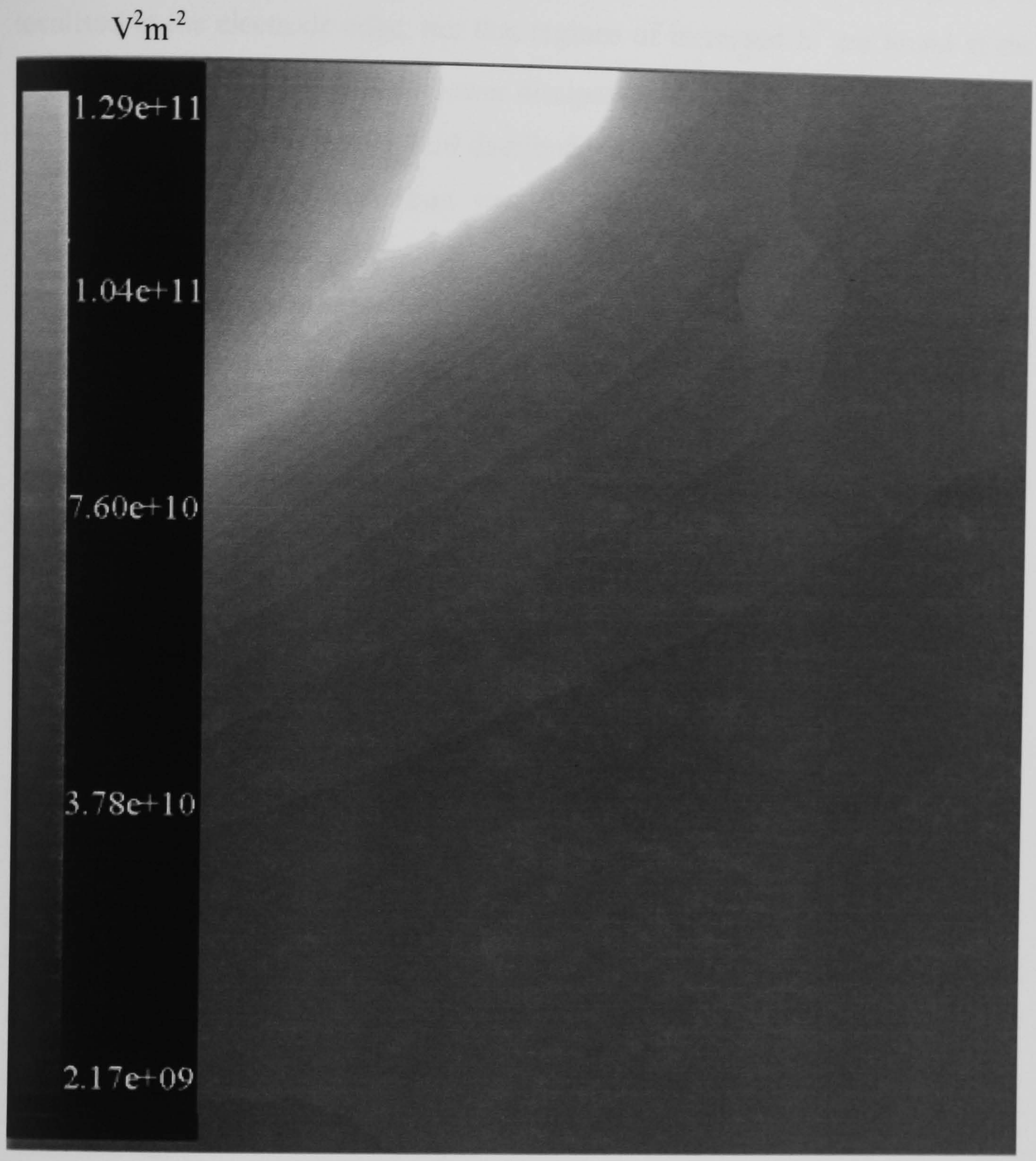

Figure 4(c): Simulation of the square of the electric field strength in the presence of a cell with the permittivity of a cell interior near the electrode edge in a sawtooth electrode, 6μm above the electrode surface. A voltage of $21V_{pk\text{-}pk}$ was applied to the electrodes. From the plot it can be seen that the electric field is consistent with the cell experiencing a net dipole moment.

Figure 4(c) shows E^2 within the cell and again it was approximately $5x10^{10}$ $V^2_{pk\text{-}pk}m^{-2}$ in magnitude, thus according to the simulation the potential drop across the cell is $2.8V_{pk\text{-}pk}$.

It can be seen from this simulation that the majority of the power dissipation is localised at the electrode edge, but that regions of increased E^2 are found at the poles of the cell. Time averaged power dissipation is given by $W = \sigma E^2$. On the basis of the simulated electric field distributions, and taking into account that the conductivity of a cell cytoplasm was $0.32 Sm^{-1}$, as compared to a medium conductivity of $0.01 Sm^{-1}$, the power dissipation inside cells will be higher than in the medium surrounding the cell. Because the membrane conductivity is very low, power dissipation in the plasma membrane can be neglected. Thus although the electric field is lower inside the cell, the power dissipation is higher owing to the high cytoplasm conductivity. On the basis of these calculations the total power dissipation in the cell amounts to 2.4pW.

These calculation assume that the electric field simulations are correct, however the finite element software does not take into account the free charge in the medium or in the cell. But as the conductivity of the cytoplasm of a cell was $0.32 Sm^{-1}$, it is a conductor that contains free charge, which means that such an approximation does not compute the correct field. It is likely that the electric field inside the cell should be smaller than the values obtained from the electric field simulation software. This means that both the potential dropped across the cell and the total power dissipation inside the cell should be smaller than the values calculated from the electric field simulations.

It was found that the power dissipation inside the cells was higher than in the suspending medium that surrounds it. Such a difference in power dissipation will lead to the cell experiencing a temperature rise that is greater than that of the suspension medium. Some time after the field is switched on the temperature of the cell will reach a steady state value at which the heat dissipated into the surrounding is the same as the heat generated by the electric field. An approximation of the temperature difference between the medium and the cell can be calculated using methods described by Ramos *et. al* [3]. According to which the increase in the temperature is given by:

$$\Delta T = \frac{\sigma V_{rms}}{k} \qquad (3)$$

where k is the thermal conductivity of water, V_{rms} is the *rms* voltage dropped across the cell and σ is the conductivity of the cell interior. Using this equation gives a value for the temperature increase within the cell of approximately 0.5°C. The temperature rise in the plasma membrane will be insignificant as a result of the low potential dropped across the membrane. The result obtained is likely to be too high as a result of the electric field simulations overestimating the electric field strength inside the cell. Further work is needed to clarify this could be undertaken with electric field simulation software capable of solving the full time dependent changes in the electric field in the presence of free charge.

8.4.3 Membrane potential calculations

The electrical potential dropped across the cell membrane was calculated from equation (1), using the minimum and maximum of electric field strengths in the electrode as given by figure 4(a). The data summarised in figure 5, this shows that at a frequency of 5MHz the potential across the cell membrane was in the range $8.6\mu V_{pk\text{-}pk}$to $68\mu V_{pk\text{-}pk}$. By contrast at lower frequencies the membrane potential is much higher, approaching $5V_{pk\text{-}pk}$, a potential that is sufficient to rupture cellular membranes

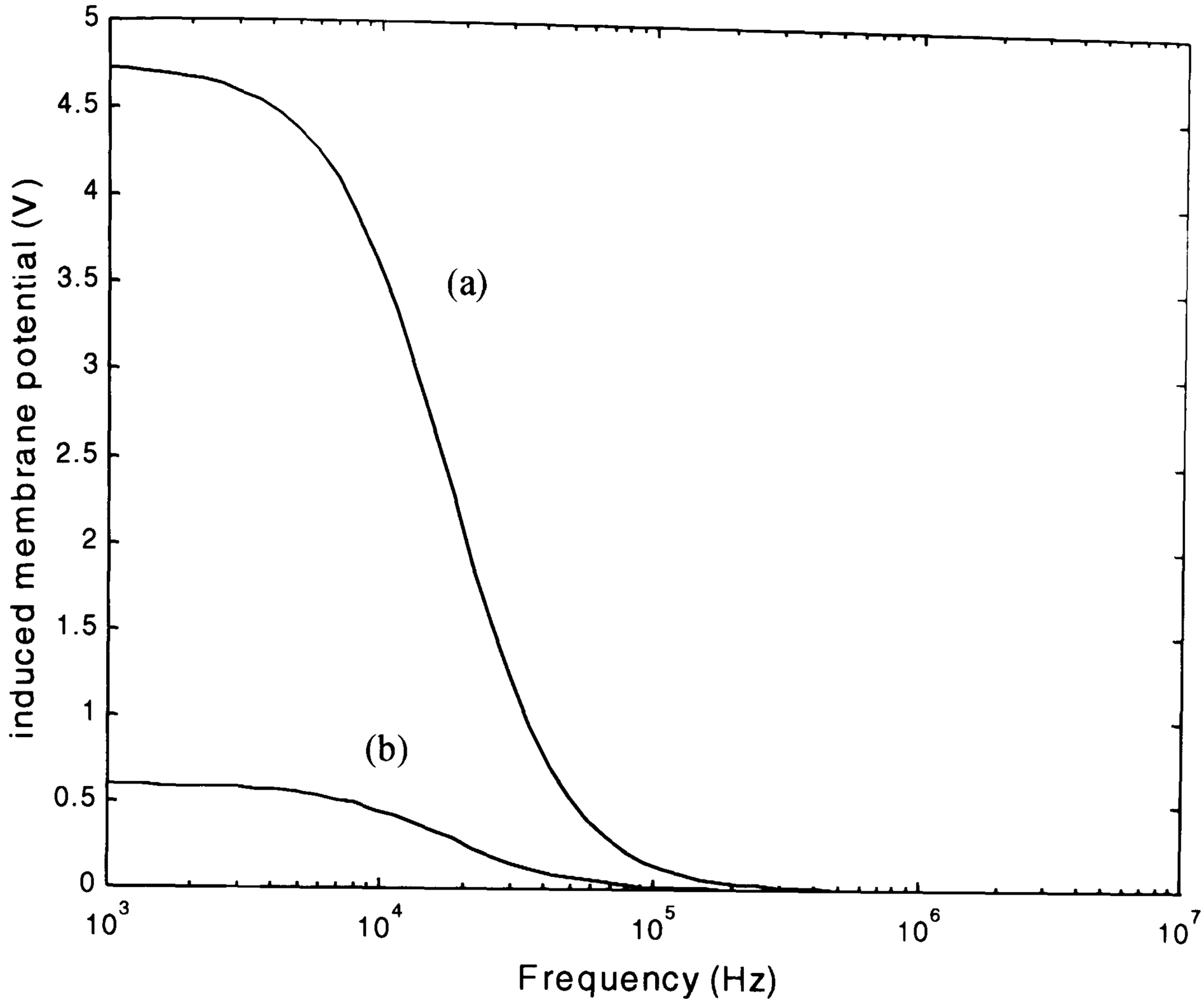

Figure 5: The frequency dependence of the induced membrane potential of a BHK21 C-13 cell suspended in $10mSm^{-1}$. The membrane potentials were calculated for the maximum (a) and minimum (b) electric field strength generated by the electrodes. At a frequency of 5MHz the maximum induced membrane potential was found to be 68μV.

8.4.4 Steady-state temperature measurements.

Steady-state temperature measurements were made in the medium using a thermocouple attached to a micromanipulator. 15 minutes after application of the electric field the temperature was measured at heights ranging from 0.5 to 5.5mm above the electrode surface. The data is shown in figure 6 and indicates that for this particular medium conductivity and applied potential the steady state temperature rise was less than one degree at all points in the bath after 15

minutes of field exposure. These data are consistent with other theoretical predictions and experimental observations [3].

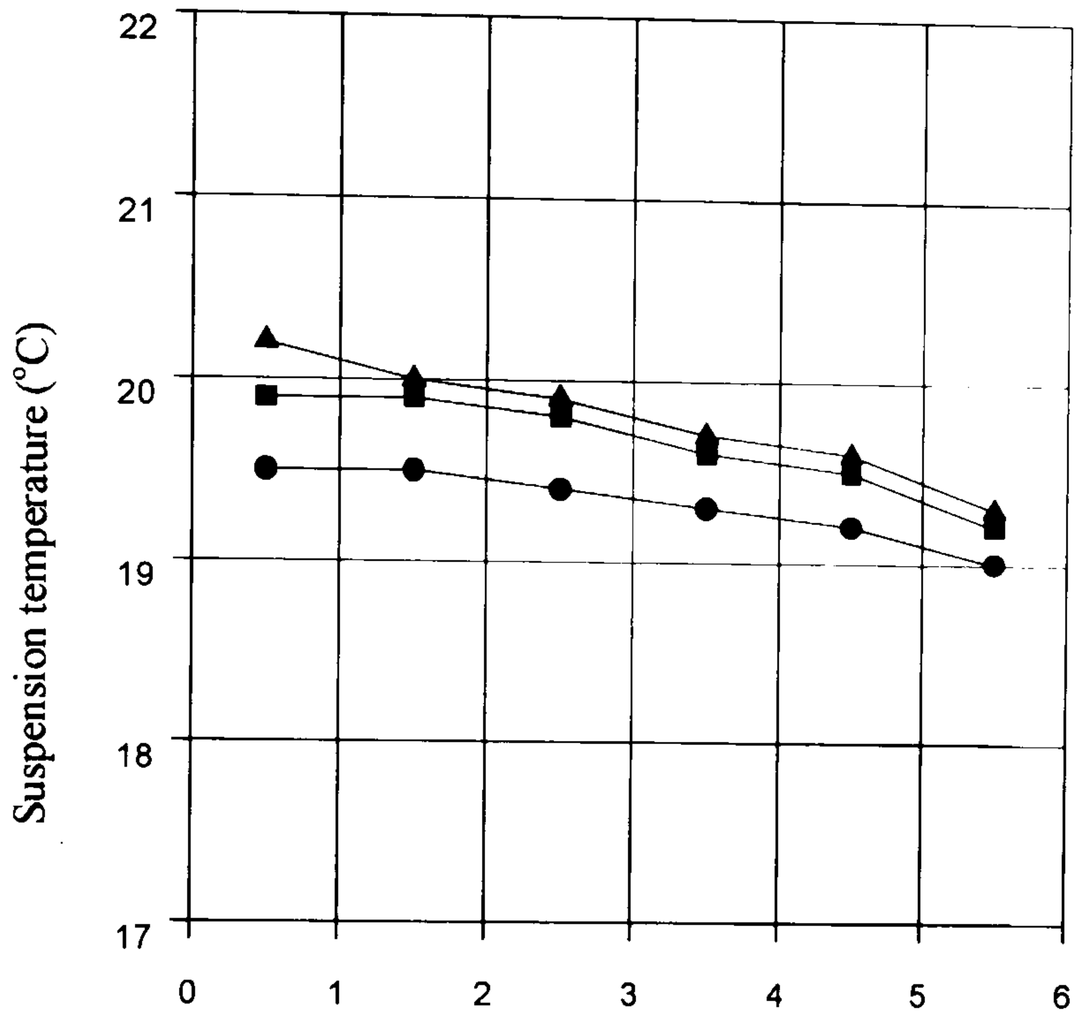

Figure 6: The dependence of the temperature of the suspension medium on the distance from the electrode pattern. The temperature was measured before the electric field was applied (•) after the electric field had been on for 15 minutes (■) and 15 minutes after the electric field had been switched off (▲).

8.4.5 Cell morphology

Following field exposure, scanning electron microscopy of the cells failed to reveal alterations in the morphology of the cells. SEM images of cells on electrodes are shown in figure 7(a) (unexposed) and figure 7(b) (field exposed). Phase contrast imaging also showed unremarkable morphology as shown in figure 7(c). (unexposed) and figure 7(d) (exposed). There was no evidence to

indicate possible galvanotropic alignment, such as aligned filopodial or lammelipodial protrusions, nor evidence of other atypical behaviours. The cell membrane appeared unremarkable with no obvious field-associated anomalies. Cells which were incubated in a mannitol solution but not exposed to the field also had unremarkable morphology.

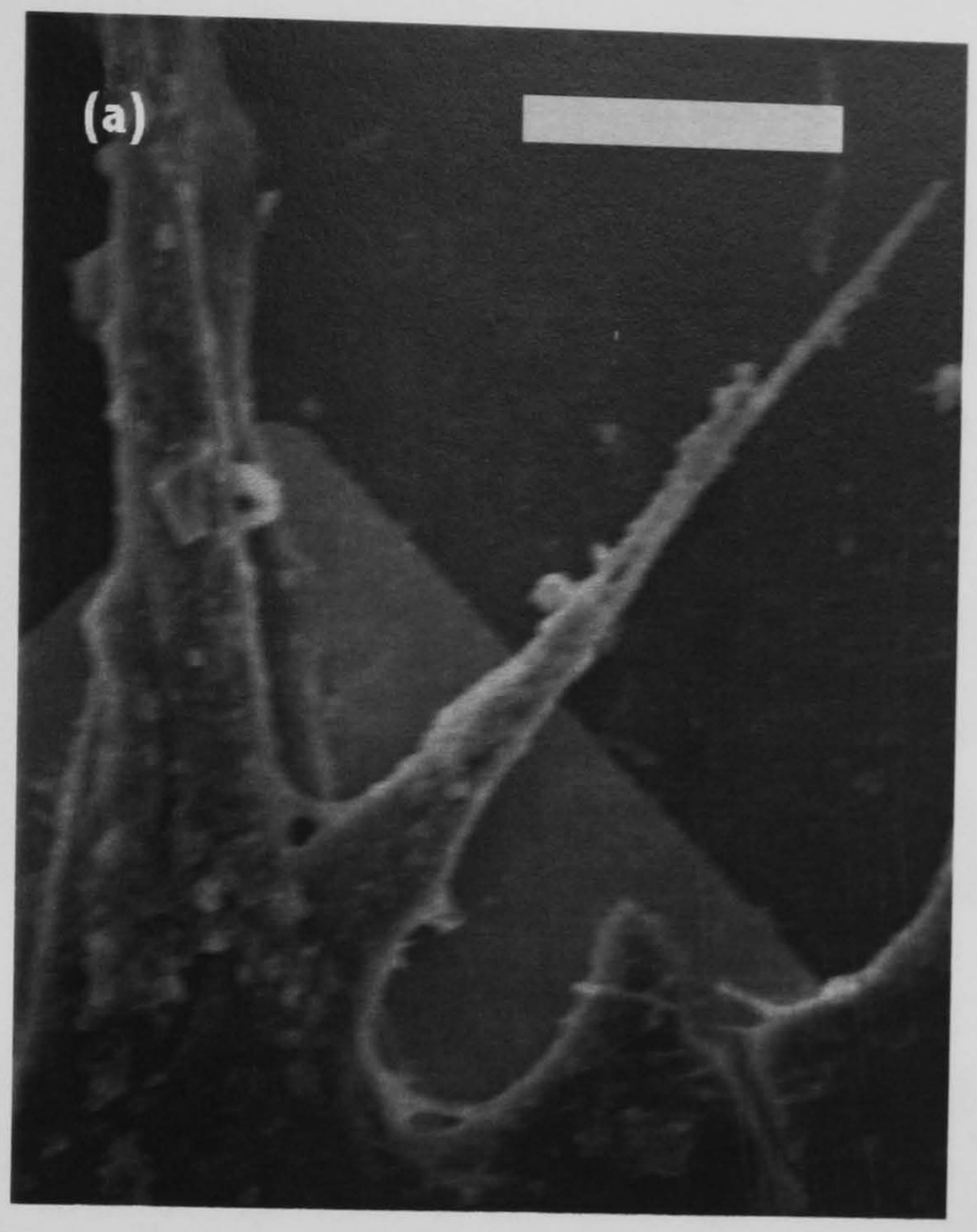

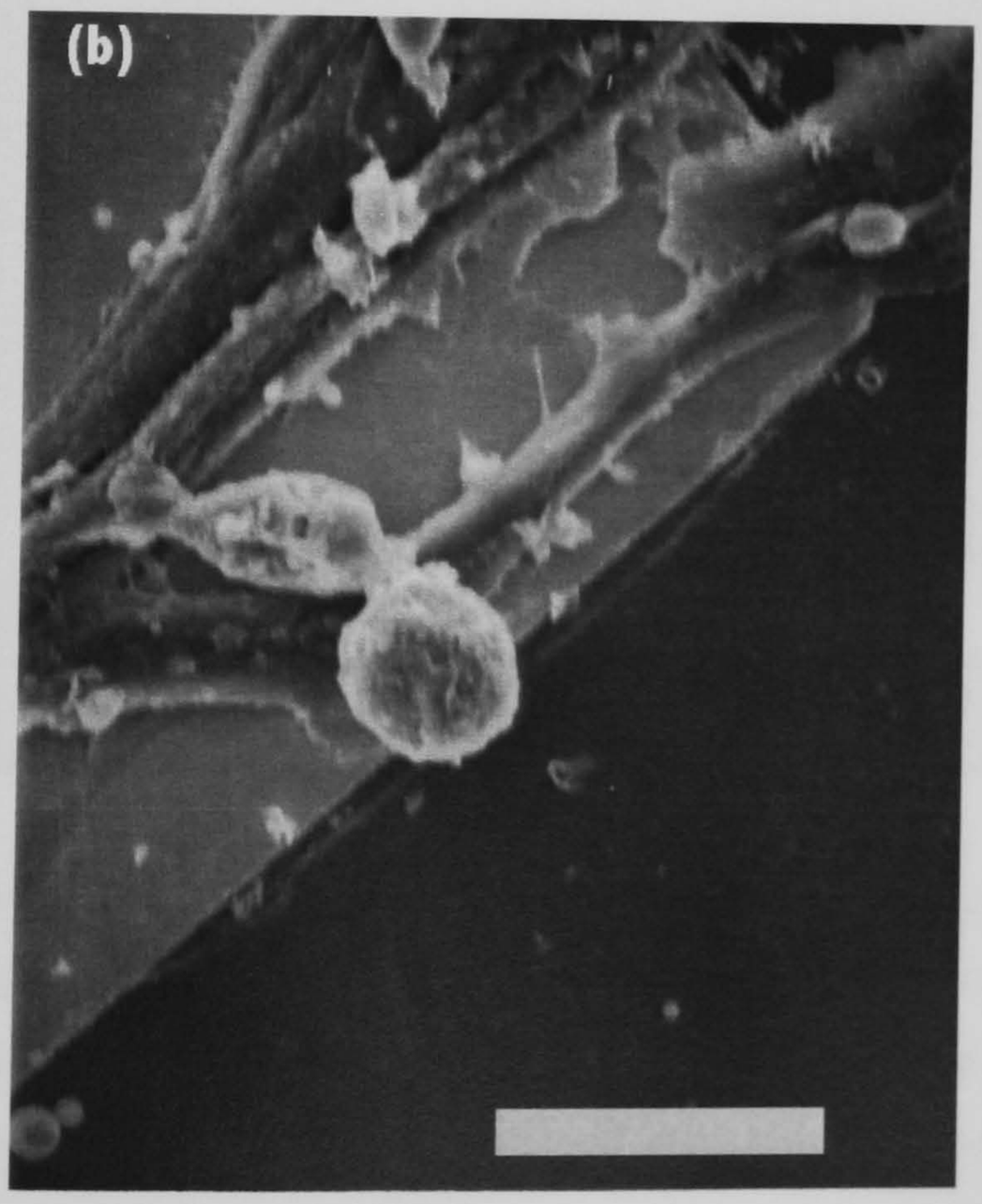

Figure 7: Scanning electron micrographs illustrating cell spread cell morphology of field-exposed cells (a) and non-exposed cells (b), the scale bar represents 15μm. Field exposed cells and cell incubated in Manitol have unremarkable morphology when compared with controls. No membrane abnormal membrane features could be identified in field- and non exposed cells.

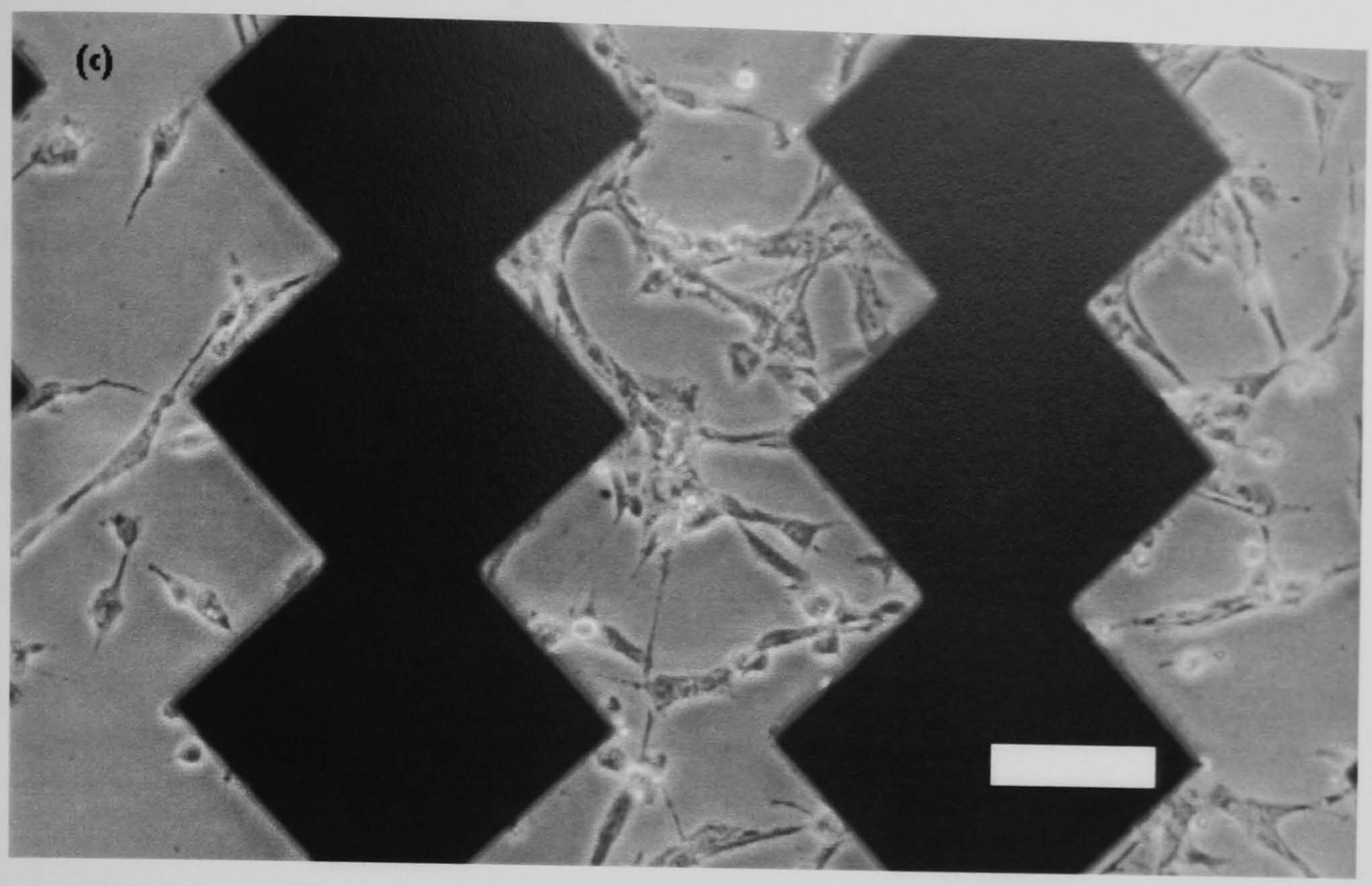

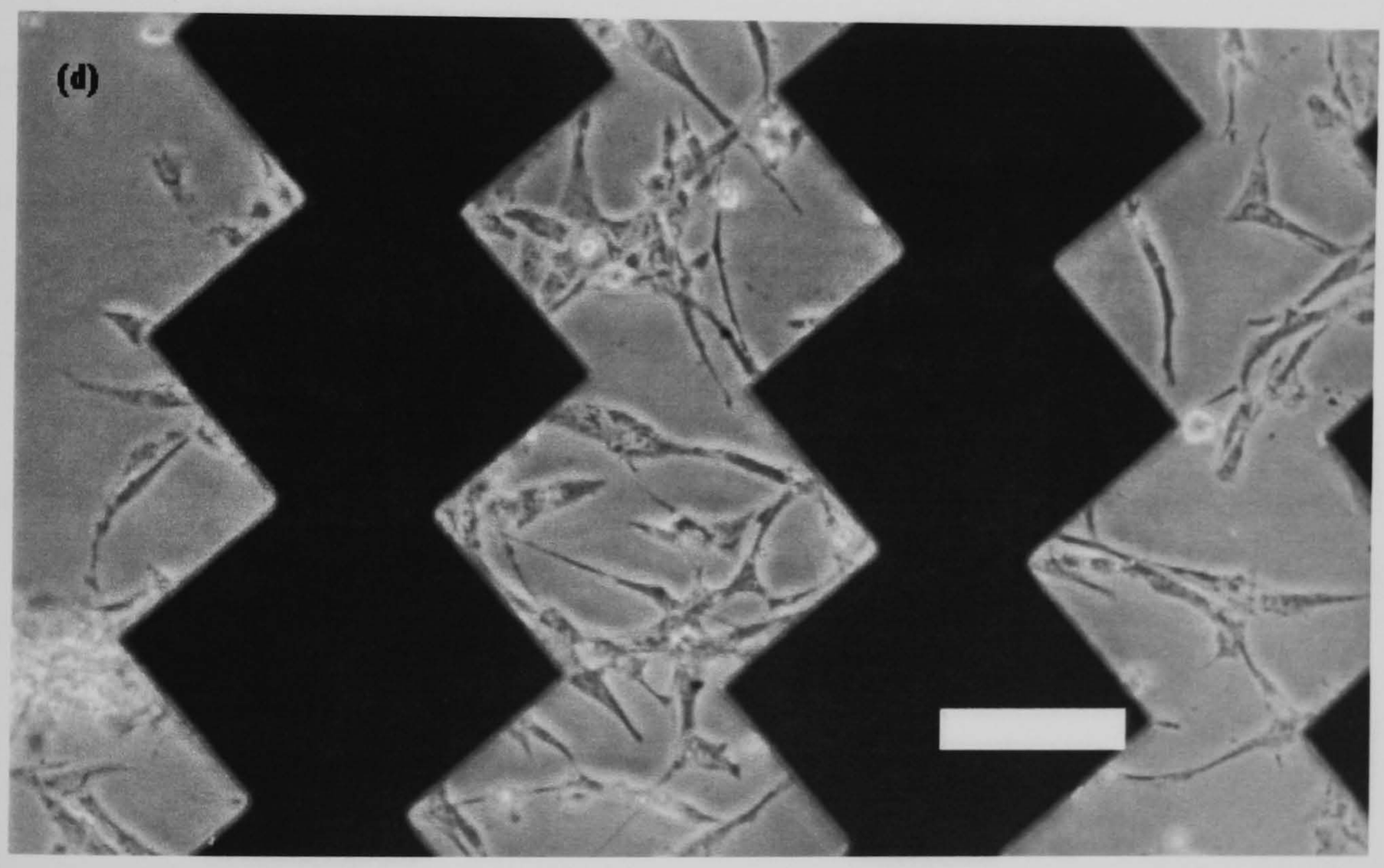

Figure 7: Phase contrast photomicrographs illustrating cell spread cell morphology of field-exposed cells (c) and non-exposed cells (d), the scale bar represents 15μm. Field exposed cells and cell incubated in Manitol have unremarkable morphology when compared with controls. No membrane abnormal membrane features could be identified in field- and non-exposed cells.

Studies on cell-doubling rates indicated that there was no difference between onset controls, exposed cells or cells with no field exposure. This data is summarised in figure 8.

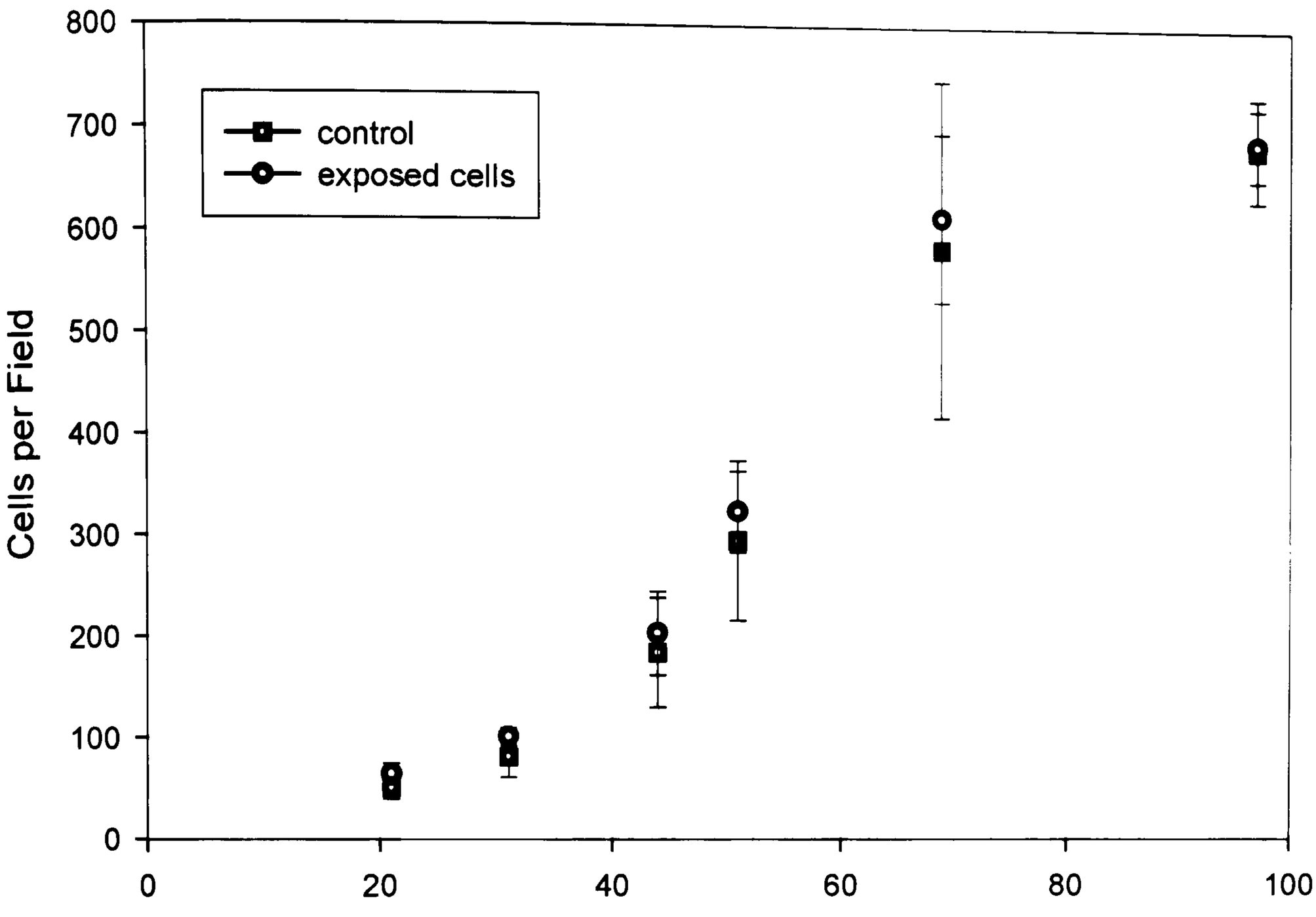

Figure 8: Growth curves for non-field-exposed cells (a), field-exposed cells (b) and non-exposed cell. Absence of any significant difference between the 2 growth curves suggests no lasting effect of the electric field or mannitol exposure on the cell cycle control system.

8.4.6 *Mitochondrial stress*

Spectrophotometric analysis of MTT solution revealed no difference in the rate of oxidative respiration between control and exposed cells (figure 9).

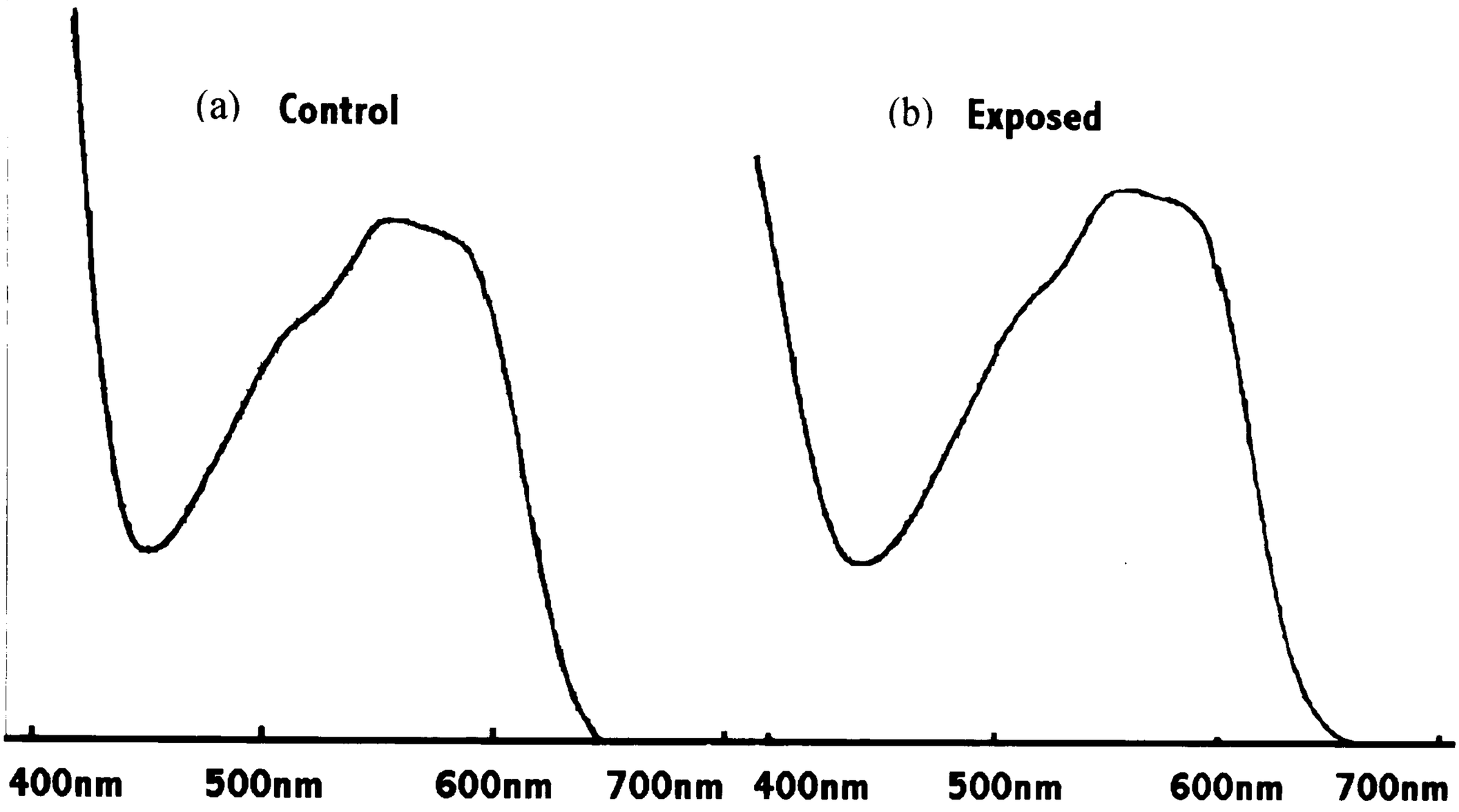

Figure 9: Spectrophotometric traces of MTT dye solution after incubation with control (a) and field-exposed cells (b). The traces were not different suggesting that field exposure had no effect on the rate of oxidative respiration with the suspension of BHK cells.

8.4.7 Expression of fos-protein.

Immunoprobing of Western blots of cell samples revealed a major reactive band at 45 - 50 kDa in both control (D and F) and exposed samples (C and E) consistent with the c fos protein product (figure 10). The staining is visually more intense in columns C and E. The fos-protein band was entirely removed by competition with the amino acid 4 - 17 peptide fragment of human c-fos in both exposed (a) and control (b) samples indicating that the bands did indeed represent fos-protein. Other bands reacting with the polyclonal antisera were not capable of being competed out, and therefore represent non-specific reactions.

This was further confirmed by semi-quantitative analysis of fos protein expression in the groups of manipulated cells was carried out by densitometric image analysis of band staining intensity on the Western blots using Paint Shop Pro version 5.01 (JASC Software). Bands correlating with fos expression in lanes A and B, the fos peptide blocked samples, showed staining intensities very similar to background levels. This confirmed the specificity of the anti-fos stain in lanes C-F. Densitomerty revealed an approximate 20-30% increase in fos protein expression in field-exposed lanes (lanes C,E) as compared to the respective non-exposed control lanes (lanes D, F). Staining intensity in both the field-exposed groups and both the non-exposed groups were very similar.

Peptite blocked 1	Peptite blocked 2	Exposed cells 1	Control cells 1	Exposed cells 2	Control cells 2
A	B	C	D	E	F

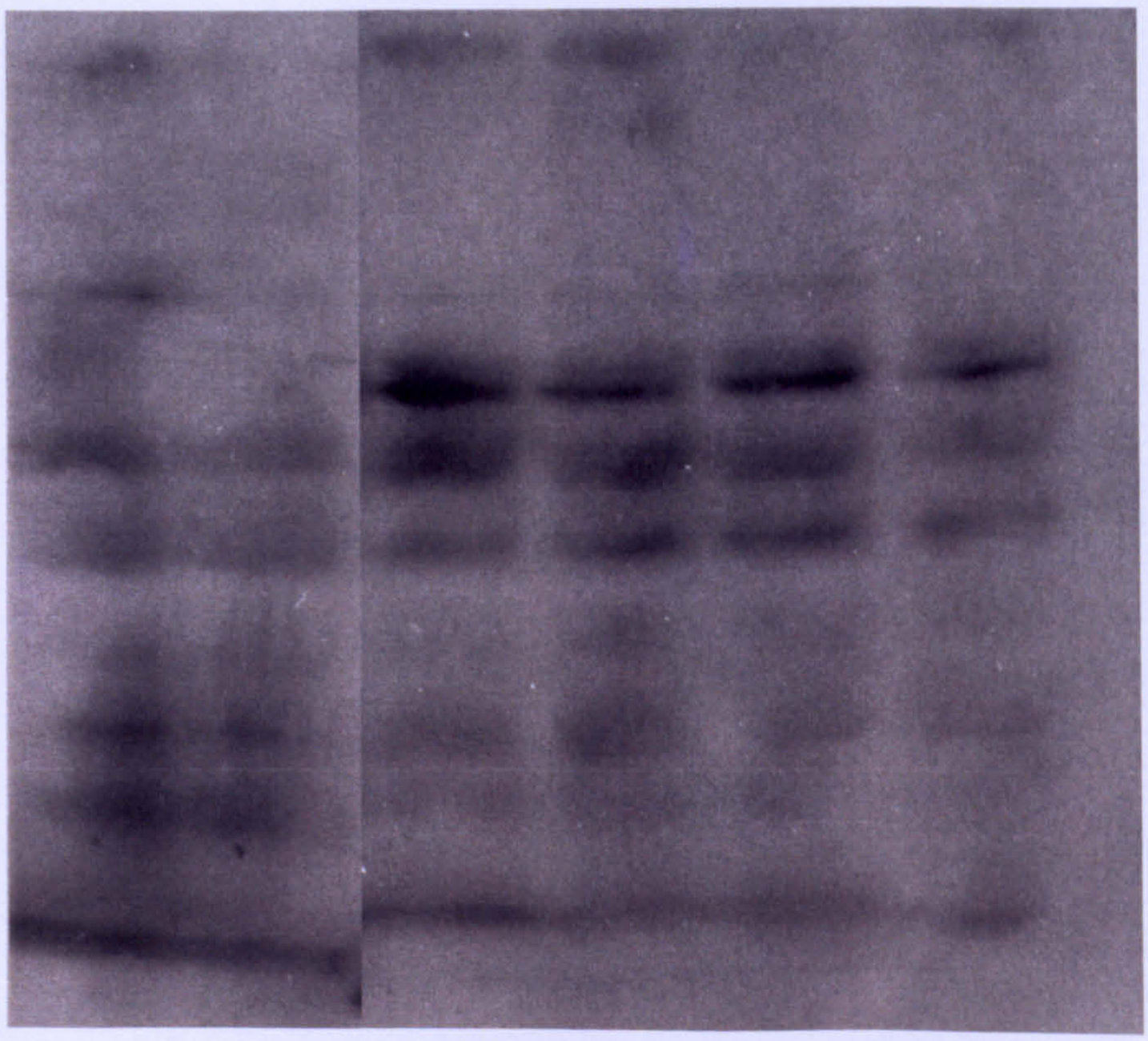

Figure 10: A Western blot of fos protein expression in two preparations of field-exposed and control cells. Qualitative comparison and densitometric analysis indicated increased fos protein staining intensity in lysate from field-exposed cells (C,E) when compared with their respective controls (D,F). The specificity of fos protein immunostaining is verified by co-incubation of anti-fos protein antisera with a 4-17 peptide fragment of human fos protein, in which case staining was illiminated (A,B).

8.4.8 *mRNA fingerprinting.*

In figure 11 panels A and B show cDNA gels obtained using two primers. Differentially expressed bands were found ranging from 0.3-2k bp in both cases. Columns 1 and 4 are control samples, 2 and 5 field-exposed cells, and 3 and 6 field-exposed cells processed after 0.5 hours. In the close up of panel A four bands of interest are highlighted. X_1 and X_2 in column 2 indicate gene upregulation in field-exposed cells. Bands Y_1 and Y_2, as well as Y_3 in column 5 highlight upregulated mRNA persisting in field-exposed cells 0.5 hours after cessation of the field. In panel B similar differentially expressed bands can be seen. Tags X_3, X_4 and X_5 in column 5 again show cDNA banding indicative of gene upregulation in field-exposed cells. Y_3 in column 6 indicates mRNA upregulation in cells 0.5 hours after cessation of the field.

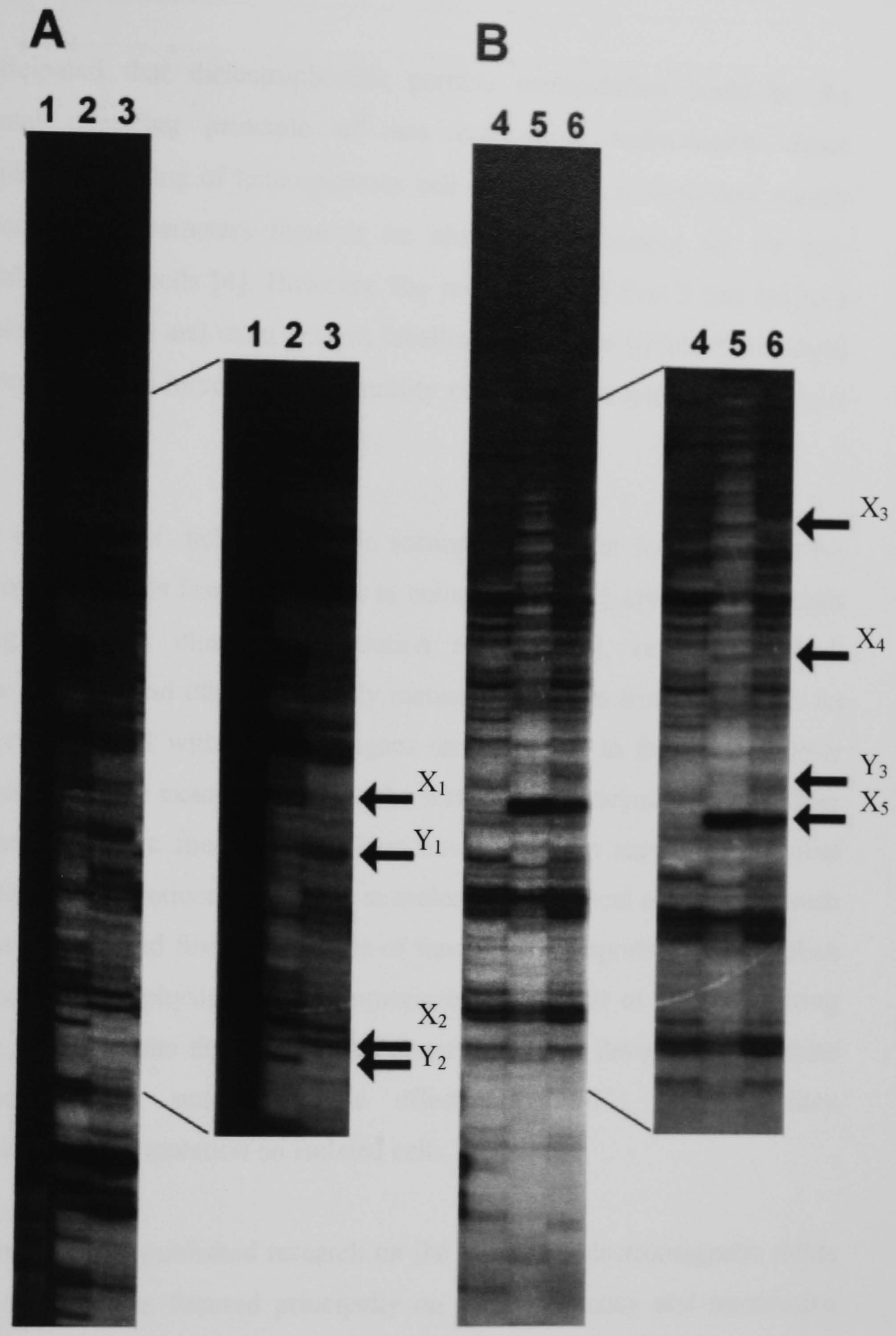

Figure 11: Panels A and B display cDNA bands reverse transcribed from mRNA extracted from control (lanes 1,4) and field-exposed cells processed immediately (2,5) and after a 0.5 hours delay (3,6) using two sets of random primers. Differentially expressed cDNA bands are seen in cells immediately after cells are removed from the field (X_1, X_2, X_3, X_4 andX_5) and 0.5 hours later (Y_1, Y_2, andY_3).

8.5 Discussion.

It is anticipated that dielectrophoretic particle manipulation could be the fundamental operating principle of new cell-sorting technologies. Since dielectrophoretic sorting of heterogeneous cell populations is dependent mainly upon phenotypic parameters there is no absolute requirement for the pre-immunolabelling of cells [4]. However, the routine use of FACS has led to a rapid evolution in CD and other antigen labelling techniques which, if employed in this context, could increase the versatility of the dielectrophoretic technique further.

Reported examples of dielectrophoretic sorting have so far included selective isolation of viable cells from lysed cells in culture media [5], enrichment of cells expressing particular cluster-differentiation antigens [6], removal of both leukaemic cells [7] and other potentially metastic cell-types from blood [8]. As well as cells infected with viral pathogens (as described in this work). Other biotechnology-related examples include the sorting of prokaryotes [9] and other non-human eukaryotic species [10]. There have also been reports of potential uses for dielectrophoretic manipulation in molecular biological applications such as cell fission [11] and fusion [12]. It is of fundamental importance to establish whether normal cell physiology is compromised as a result of any cell-sorting procedure. As a results the experiments undertaken were designed to examine the scope of any potential acute effects of 5MHz radio-frequency dielectrophoretic manipulation on isolated cells.

The vast majority of published research on the effects of electromagnetic fields on living systems has focused principally on radio-frequency and microwave fields, for example those with bandwidths commonly used for personal radiotelecommunications and power transmission. In fact, ambient RF fields can be derived from a number of sources; broadcasting, telecommunications, radar, industrial machinery, security equipment and also medical procedures such as diathermy and medical imaging [13]. The results of previous in vivo and in vitro investigations using different RF frequencies have suggested that radio-frequency fields may influence cellular processes, [14, 15]. It is thought that as

the frequency increases from 100kHz the dominant energy transfer process in biological systems is through localised heating. Cells would be expected to respond to local heating by upregulation of one or many heat shock proteins (HSPs), or chaperonins, which are also known to respond to other types of stress. Heat shock molecules display a broad phylogenetic distribution [16] and as such are known to mediate a variety of cellular functions.

The theoretical and experimental evidence presented suggests that thermal energy transfer into the cells from the culture medium or by direct heating of the cytosol was minimal. However, unidentified gene upregulation was detected in field-exposed cells. Since a specific examination of the levels of cytosolic HSPs was not conducted, the possibility that at least part of the differentially-expressed cDNA may have coded for HSP's in field-exposed cells cannot be excluded. It is possible that the field stimulus could have been transduced via a non-thermal mechanism. Indeed, this has been borne out by other workers who have reported changes in the steady-state levels of cellular HSP's and the expression of proto-oncogenes c-myc and c-jun in the absence of elevated temperatures [17]. These workers concluded that cells may respond to thermal and electromagnetic field stimulation by using similar transduction mechanisms. The results demonstrated that another stress marker for cells, fos protein was unregulated in cells exposed to the field. Once again, the possibility that the differentially-expressed cDNA in field-exposed cells may have coded for fos-protein or an associated gene regulatory protein could not be eliminated. Interestingly, it has been reported that c-fos transcription is not upregulated at 836.6Mhz at various power densities [18]. However, upregulation in another proto-oncogene, c-jun, the product of which combines with fos protein to produce the gene regulatory protein AP-1, has been reported after RF exposure. Intermediate early gene upregulation is consistent with our observation of differential cDNA expression, although adjustments in the cell-cycle control system were not highlighted by a quantitation of cell-doubling rates.

This contrasts with the only other study on the cellular effects of dielectrophoresis that was found in the literature. Fuhr *et al* [19], found that when cultivating mouse fibroblasts under the prolonged influence of electric field

the anchorage time and the lag phase of the cells dropped, while the average cell cycle time and speed of mobility was reduced. These results show that while exposing cells to electric field for 15 minutes is not sufficient to cause alterations in cell cycle dynamics, prolonged exposure to electric fields does cause changes in cell cycle dynamics.

The literature contains a number of reports of altered cell-cycle dynamics in response to field exposure. The consensus appears to be that cell division rates and other intracellular cytoplasmic and cytoskeletal events correlate with power level and duration of exposure [20]. This relationship has been found in human epithelial amnion cells [20], mast cells [21], human and rodent neuroblastoma cells [22] and osteoblasts [23]. Broude *et al* [24] suggested that there may correlation between the amplitude of cell membrane fluctuation in a RF field and the responses exhibited by the cell. This was based on a series of experiments using cytoskeletal disrupting agents. The real-time observations on spread cells on the devices did not show any apparent effect of field-exposure on the cell membrane under-phase contrast optics, nor retrospectively with SEM observations.

However, the data suggest that the potential drop across the cell membrane would have been a maximum of 68μV, a number that is considered physiological tolerable for mammalian cells [25]. The potential dropped over a whole cell was found to reach a maximum of $1.8V_{pk\text{-}pk}$, while the regions of joule heating were found to be in the cell interior, with heat being dissipated in the low conducting plasma membrane. An approximate calculation of the temperature difference between the cell and the surrounding medium found that the cell experienced a temperature increase of 0.5°C. Such a temperature rise would not be expected to cause damage to the cells but might induce production of heat shock proteins.

Studies on whole animals and humans at telecommunications RF frequencies have showed a variety of effects from field exposure. Fritze *et al* [26] recently reported that microwave fields were associated with upregulation of heat shock protein 70 and c-fos mRNA in the cerebellum, neocortex or piriform cortex of

acutely exposed rat brains. The levels of c-jun, and GFAP mRNA were not changed in any of the experimental groups. Immunocytochemical analysis of fos and jun proteins and HSP70 24 hours after exposure did not reveal any change from normal levels. After a further 7 days there was no evidence for glial proliferation. A recent report has suggested that these acute stress responses displayed by cells may not be manifest at the neurophysiological level. Roschke *et al* [27] did not find any effect of 3.5 minutes exposure to 900Mhz on the awake human electroencephalograph. However, a recent report has suggested that RF fields are associated with increased blood pressure in human [28] and impaired spatio-temporal co-ordination.

8.6 Conclusion

By screening a spectrum of possible resultant celullar effects of dielectrophoresis using a range of different biological investigations it was shown that dieletrophoretic manipulation of fibroblast like cells can be associated with pertubation of normal cellular events. Cell morphology, cell oxidative respiration and cell cycle dynamics each appeared to be unaffected by dieletrophoretic manipulation. However, exposure to the applied electric field was associated with an increased expression of fos-protein and upregulation in unidentified genes. The data also suggested that the process of gene transcription may have continued beyond the 0.5 hours refractory period set for this experiment. The results obtained were not considered to be predictive of genotoxic effects on the cells resulting from the field-exposure. The very subtle effects dielectrophoresis had on cell physiology were reflected by the effects being detected by the investigation of fos-protein and gene expression. While the cruder methods of qualitative examination of cell morphology and cell-doubling rates revealed little.

By screening a spectrum of possible resultant cellular effects of dielectrophoresis using a range of different biological investigations, it was found that increased expression of fos-protein and upregulation in unidentified genes occurred. In order to better understand the nature of these events, it will be necessary to extend the work presented here by conducting time-course observation on the detected alterations in cells physiology, in particular concentrating on the duration of field-associated gene transcription and fos-protein expression. Furthermore, a successful attempt at sequencing the differentially-expressed cDNA bands and thus elucidating the mechanism for field-induced gene expression could provide valuable information about the mechanism behind the upregulation of genes.

As dielectrophoresis and electrorotation are increasingly being used as methods for cell identification and cell sorting, it is becoming important to quantify the cellular effects of exposing cells to the electric fields required to manipulate the

cells. It is hoped that this work will provide a useful first step in such an undertaking

8.7 References.

1. Green, N.G., H. Morgan, and J.J. Milner, *Manipulation and trapping of sub-micron bioparticles using dielectrophoresis.* Journal of Biochemical and Biophysical Methods, 1997. **35**: p. 89-102.

2. Grosse, G. and H.P. Schwan, *Cellular membrane potentials induced by alternating field.* Biophysical Journal, 1992. **73**: p. 1632-1642.

3. Ramos, A., H. Morgan, N.G. Green, and A. Castellanos, *Ac electrokinetics: a review of forces in microelectrode structures.* Journal of Physics D: Applied Physics, 1998. **31**: p. 2338-2353.

4. Gascoyne, P.R.C., X.-B. Wang, Y. Huang, and F.F. Becker, *Dielectrophoretic Separation of Cancer Cells from Blood.* IEEE Transactions on Industry Applications, 1997. **33**: p. 670-678.

5. Docoslis, A., N. Kalogerakis, L.A. Behie, and K.V.I.S. Kalis, *A novel dielectrophoresis device for the selective isolation of viable cells in cell culture media.* Biotechnology and Bioengineering, 1997. **34**: p. 239-250.

6. Talary, M.S., K.I. Mills, T. Hoy, A.K. Burnett, and R. Pethig, *Dielectrophoretic separation and enrichment of CD34+ cell subpopulation from bone marrow and peripheral blood stem cells.* Medical and Biological Engineering and Computing, 1995: p. 235-237.

7. Becker, F.F., X.B. Wang, Y. Huang, P. R, J. Vykoukal, and P.R.C. Gascoyne, *The removal of human leukemic-cells from blood using interdigitated microelectrodes.* Journal of Physics D: Applied Physics, 1994. **27**: p. 2659-2662.

8. Becker, F.F., X.B. Wang, Y. Huang, R. Pethig, J. Vykoukal, and P.R.C. Gascoyne, *Separation of human breast cancer cells by differential dielectric affinity.* Proceedings of the National Academy of Science, 1995. **92**: p. 860-864.

9. Markx, G.H., P.A. Dyda, and R. Pethig, *Dielectrophoretic separation of bacteria using a conductivity gradient.* Journal of Biotechnology, 1996. **51**: p. 175-180.

10. Holzel, R., *Electrorotation of single yeast cells at frequencies between 100 Hz and 1.6 GHz.* Biophysical Journal. 1997. **73**: p. 1103-1109.

11. Marszalek, P. and T.Y. Tsong, *Cell fission and formation of mini cell-bodies by high frequency alternating electric field.* Biophysical Journal. 1995. **68**: p. 1218-1221.

12. Yamaha, E. and F. Yamazaki, *Electrically fused-egg induction and its development in the goldfish, Carassius-Auratus.* International Journal of Developmental Biology, 1993. **37**: p. 291-298.

13. Sienkiewicz, Z., *Biological effects of electromagnetic fields.* Engineering Science and Education Journal, 1998(June): p. 127-134.

14. Saunders, R.D., C.I. Kowlczuk, and Z.J. Sienkeinwics, *Biological effects of exposure to non-ionising electomagnetic fields and radiation. III. Radiowave frequency and radiation.* NRPB-R240. Chilton. Didcot. Oxfordshire, UK, 1991.

15. Tarricone, L., C. Cito, and G. D'Inzeco, *Ach receptor channels interaction with MW fields.* Bioelectrochemistry and Bioenergetics. 1993. **30**: p. 275-285.

16. Liang, P. and T.H. MacRae, *Molecular chaperones and the cytoskeleton.* Journal of Cell Science, 1997. **110**: p. 1431-1440.

17. Goodman, R. and M. Blank, *Biosynthetic stress-response in cells exposed to electromagnetic fields.* Advances in Chemistry Series, 1995. **250**(423-436).

18. Ivaschuk, O.I., R.A. Jones, T. Ishida-Jones, W. Haggren, W.R. Adey, and J.L. Philips, *Exposure of nerve growth factor-treated PC12 rat pheochromocytoma cells to a modulated radio-frequency field at 836.6 Mhz: Effects on c-jun and c-fos expression.* Bioelectromagnetics. 1997. **18**: p. 223-229.

19. Fuhr, G., H. Glasser, T. Muller, and T. Schnelle, *Cell manipulation and cultivation under a.c. electric field influence in highly conductive media.* Biochemica et Biophysica Acta, 1994. **1201**: p. 353-360.

20. Kwee, S. and P. Rasmask, *Changes in cell proliferation due to*

environmental non-ionising radiation 2. Microwave radiation. Bioelectrochemistry and Bioenergetics, 1998. **44**: p. 251-255.

21. Donellan, M., D.R. McKenzie, and P.W. French, *Effects of exposure to electromagnetic radiation at 835MHz on growth, morphology and secretory characteristics of a mast cell analogue, RBL 2H3.* Cell Biology International, 1997. **21**: p. 427-439.

22. Dutta, S.K., B. Watson, and K.P. Das, *Intensity dependence of enolase activity by modulated radiofrequency radiation.* Bioelectrochemistry and Bioenergetics, 1992. **27**: p. 170-189.

23. Zhuang, H.M., W. Wang, R.M. Seldes, A.D. Tahernia, H.J. Fan, and C.T. Brighton, *Electrical stimulation induces the level of TGF-beta 1mRNA in osteoblastioc cells by a mechanism involving calcium/calmodulin pathway.* Biochemical and Biophysical Research Communicatioons. 1997. **237**: p. 225-229.

24. Broude, N., R. Karabakhtsian, N. Shalts, R. Goodman, and A.S. Henderson, *Correlation between the amplitude of the plasma -membrane fluctuations and the response of cells to electric and magnetic fields.* Bioelectrochemistry and Bioenergetics, 1994. **33**: p. 19-23.

25. Hille, B., *Ionic Channels of Excitable Membranes.* 1984, Sunderland, Massachussetts: Sinauer Associates.

26. Fritze, K., C. Wissner, N. Kuster, C. Sommer, *et al.*, *Effect of global system for mobile communication microwave exposure on the genomic response of the rat brain.* Neuroscience, 1997. **81**: p. 627-639.

27. Roschke, J. and K. Mann, *No short-term effect of digital mobile radio telephone on the awake human electroencephalogram.* Bioelectromagnetics, 1997. **18**: p. 172-176.

28. Braune, S., C. Wrocklage, J. Raczek, T. Gailus, and C.H. Lucking, *Resting blood pressure increase during exposure to a radio-frequency electromagnetic field.* Lancet. 1998. **351**(9119): p. 1857-1858.

Chapter 9: Conclusion and future work

9.1. Conclusions

Electrorotational measurements of the time dependent changes in the dielectric properties of BHK(C-13) cells following infection with HSV-1 showed that electrorotation can be used as a method of probing the time-dependent biophysical changes that occur in cells as they undergo viral invasion, replication and release. It was found that the dielectric parameters of BHK(C-13) cells change as a result of HSV-1 infection. The membrane capacitance of the cells was found to reduce markedly, while the membrane conductivity remained unchanged, a reduction in the internal permittivity of the cells was also observed. It was possible to correlate the changes in the dielectric parameters to the known biophysical life cycle of the virus. This shows that electrorotation is a useful tool in probing changes in the gross biophysical properties of cells following infection by virions, the results also pointed to the potential for AC electrokinetic separation of infected cells from uninfected cells.

It was successfully demonstrated that HSV-1 could be complexed to polystyrene beads using antibodies specific to the virus. Probing the effect of complexing antibodies to beads using electrorotation showed that it was not possible to differentiate between HSV-1 complexed beads from beads without HSV-1. However, modelling beads of decreasing sizes suggested that as bead size decreases the relative difference in the **real** part of the Clausius-Mossotti factor increases, perhaps making it possible to detect the presence of virus on the surface of small beads with dielectrophoresis.

The electrodes used for electrorotation measurements generate non-uniform electric fields. As the rotation rate of a particle is proportional to the electric field, it is important to determine the effect that the non-uniformity of electric field has on the rotation rate of the particles. To this end, the rotation rates of latex spheres were measured across a polynomial electrode array in order to

determine the spatial variation in induced torque within the electrode. The results demonstrated that the torque varies by in excess of 50% depending on the position of a particle within the array.

The experimentally mapped spatial variation in the torque across the electrode chamber was found to closely match that predicted by numerical models in which both the variations in the electric field and phase distributions were taken into account.

When cells are manipulated using dielectrophoresis or electrorotation they are exposed to high electric fields. It is conceivable that such field could affect the physiology of the cells. Thus any possible resultant celullar effects of dielectrophoresis were screened for by using a range of different biological investigations. These investigations showed that dieletrophoretic manipulation of fibroblast like cells is associated with pertubation of normal cellular events. In summary, cell morphology, cell oxidative respiration and cell cycle dynamics each appeared to be unaffected by dieletrophoretic manipulation. However, exposure to the electric field was associated with increased expression of fos-protein and upregulation in unidentified genes. The results were not considered to be predictive of genotoxic effects on the cells. The very subtle effects that dielectrophoresis had on cell physiology were detected through investigation of fos-protein and gene expression, while the cruder methods of qualitative examination of cell morphology and cell-doubling rates revealed little.

9.2. Future work

It was successfully demonstrated that the changes that occurs in the biophysical properties of a cell as a result of virus infection could be detected using electrorotation. This points to the potential application of electrorotational methods as a means of non-invasive analysis of virus-host interactions. Further refinements to the technique, such as confinement of cells in electrical field cages as proposed by Fuhr *et al* [1] or in optical traps, such as laser tweezers [2, 3] would allow measurements to be made on a single cell for extended periods.

In this way data for the entire 24 hour life cycle of virus infectivity could be collected for a single cell. The results also suggests further biomedical applications and highlights the potential of dielectrophoretic separation techniques such as field-flow-fractionation [4] for the retrieval and separation of infected cells from uninfected cells.

It was not possible to use electrorotation to differentiate between beads either with or without HSV-1 on the surface. Mathematical modelling suggests that using beads of appropriate size could lead to the possibility of using dielectrophoresis as a method for detecting the complexing of virions to beads. This in turn could lead to a method where virus particles in solution are detected by beads complexed to beads which could then be detected and separated by dielectrophoretic methods [5-9]. Further developments of such a method could lead to real time separation of beads complexed with HSV-1 from uncomplexed beads using Field-Flow-Fractionation [10], or continuous separation [11]. This could give rise to a rapid advanced biosensor system.

Mapping the torque generated by polynomial electrodes showed that the torque profile closely matched that predicted by Hughes *et al* [12]. Recent work by De Gasperis *et al* [13] and Zhou *et al* [14] have led to the development of automated systems for the determination of rotation rates of cells using image processing techniques. Such systems could readily be adapted to automatically adjust the measured rotation rate of a particle depending on the position of the particle within an electrode chamber. This would increase the number of cells available for study by compensating for the position-related variations in torque away from the central region of an electrode pattern.

It has been shown that alterations in the physiology of cells occurred following exposure to dielectrophoresis. In order to better understand the nature of the changes, it will be necessary to extend the work. That could be done by conducting time-course observations of the detected alterations in cell physiology, a natural staring point would be to concentrate on the duration of field-associated gene transcription and fos-protein expression. Furthermore, a successful attempt at sequencing the differentially-expressed cDNA bands and

thus elucidating the mechanism for field-induced gene expression could provide valuable information about the mechanism behind the upregulation of the genes observed. It would also be of interest to obtain precise simulations of the electric field within a cell in order to be able to better understand the effect of the electric fields on cells.

9.3. References

1. Fuhr, G., T. Schnelle, R. Hagedorn, and S.G. Shirley. *Dielectrophoretic field cages: technique for cell, virus and macromolecule handeling.* Cellular Engineering, 1995. **1**: p. 47-57.
2. Ashkin, A., J.M. Dziedzic, J.E. Bjorkholm, and S. Chu. *Observations of a single-beam gradient force optical trap for dielectric particles.* Optics Letters, 1986. **11**: p. 288-290.
3. Uchida, M., M. Sato-Maeda, and H. Tashiro, *Whole-cell manipulation by optical trapping.* Current Biology, 1995. **5**: p. 380-382.
4. Gascoyne, P.R.C., X.-B. Wang, Y. Huang, and F.F. Becker. *Dielectrophoretic Separation of Cancer Cells from Blood.* IEEE Transactions on Industry Applications, 1997. **33**: p. 670-678.
5. Docoslis, A., N. Kalogerakis, L.A. Behie, and K.V.I.S. Kaler. *A novel dielectrophoresis device for the selective isolation of viable cells in cell culture media.* Biotechnology and Bioengineering, 1997. **34**: p. 239-250.
6. Green, N.G., H. Morgan, and J.J. Milner, *Manipulation and trapping of sub-micron bioparticles using dielectrophoresis.* Journal of Biochemical and Biophysical Methods, 1997. **35**: p. 89-102.
7. Hughes, M.P., H. Morgan, F.J. Rixon, J.P.H. Burt, and R. Pethig. *Manipulation of herpes simplex virus type 1 by dielectrophoresis.* Biochimica et Biophysica Acta, 1998. **1425**: p. 119-126.
8. Pethig, R., *Dielectrophoresis: Using Inhomogeneous AC Electrical Fields to Separate and Manipulate Cells.* Critical Reviews in Biotechnology, 1996. **16**(4): p. 331-348.
9. Pethig, R., Y. Huang, X.B. Wang, and J.P.H. Burt, *Positive and negative dielectrophoretic collection of colloidal particles using interdigitated castellated microelectrodes.* Journal of Physics D: Applied Physics, 1992. **24**: p. 881-888.
10. Wang, X.B., J. Vykoukal, F.F. Becker, and P.R.C. Gascoyne. *Separation of polystyrene microbeads using dielectrophoretic/gravitational field-flow-fractionation.* Biophysical Journal, 1998. **74**: p. 2689-2701.

11. Markx, G.H. and R. Pethig, *Dielectrophoretic separation of cells: continuous separation.* Biotechnology and Bioengineering. 1995. **45**: p. 337-343.

12. Hughes, M.P., X.B. Wang, F.F. Becker, P.R.C. Gascoyne, and R. Pethig. *Computer-aided analysis of electric fields used in electrorotation studies.* Journal of Physics D: Applied Physics, 1994. **27**: p. 1564-1570.

13. Gasperis, G.D., X.B. Wang, J. Wang, F.F. Becker, and P.R.C. Gascoyne. *Automated electrorotation: dielectric characterization of living cells by real time motion estimation.* Measurement Science and Technology. 1998.

14. Zhou, X.F., J.P.H. Burt, and R. Pethig, *Automatic cell electrorotation measurements: studies of the biological effect of low frequency electromagnetic fields and of heat shock.* Physics in Medicine and Biology, 1998.

Publications arising from this work

1. Archer, S., H. Morgan and F. Rixon, *Electrorotation of baby hamster kidney fibroblasts (C-13) following infection with herpes simplex virus, type 1.* Biophysical Journal, 1997. **72**(2): Pt2, p. TU381

2. Archer, S., F.J. Rixon and H. Morgan, *Dielectric investigation of the membrane properties of baby hamster kidney fibroblasts (C-13) following infection with herpes simplex virus, type 1.* Proceedings-20th Annual International Conference-IEEE/EMBS Oct. 29-Nov.1 1998, Hong-Kong.

3. Hughes, M.P., S. Archer and H. Morgan, *Mapping of the torque in planar microelectrode arrays.* Journal of Physics D: Applied Physics, 1999. **32**(13): p. 1548-1552.

4. Archer, S., H. Morgan and F.J. Rixon, *Electrorotational studies of baby hamster kidney fibroblasts infected with herpes simplex virus, type 1.* Biophysical Journal, 1999. **76**(5): p. 2833-2842.

5. S. Archer, T.T. Lee, S. Britland and H. Morgan. *The influence of radio frequency electric fields as used in dielectrophoresis on gene expression in Baby Hamster Kidney fibroblasts clone 13.* Biochemical Biophysical Research Communications, 1999. **257**: p. 687-698.